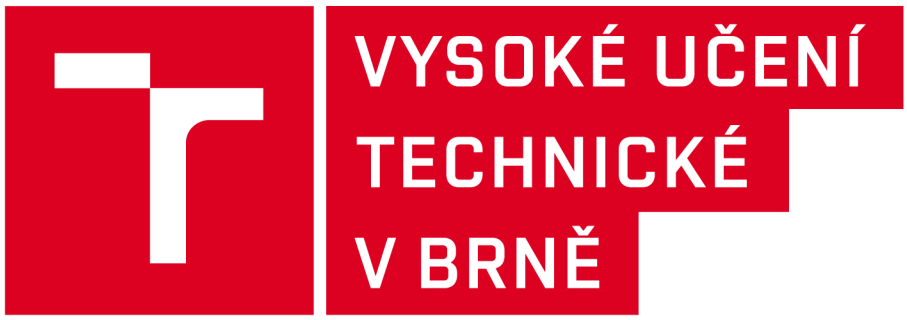

BRNO UNIVERSITY OF TECHNOLOGY
VYSOKÉ UČENÍ TECHNICKÉ V BRNĚ

CENTRAL EUROPEAN INSTITUTE OF TECHNOLOGY BUT
STŘEDOEVROPSKÝ TECHNOLOGICKÝ INSTITUT VUT

BRILLOUIN LIGHT SCATTERING CHARACTERIZATION OF NANOSCALE SPIN WAVES

CHARAKTERIZACE SPINOVÝCH VLN POMOCÍ BRILLOUINOVA ROZPTYLU SVĚTLA V BLÍZKÉM POLI

DOCTORAL THESIS
DIZERTAČNÍ PRÁCE

AUTHOR
AUTOR PRÁCE
Ing. Ondřej Wojewoda

SUPERVISOR
VEDOUCÍ PRÁCE
Ing. Michal Urbánek, Ph.D.

BRNO 2024

Abstract
Spin waves (and their quasi-particle magnons) have the potential to be used as a new platform for data transfer and processing, as they can reach wavelengths in the nanometer range and frequencies in the terahertz range. However, currently, the only technique enabling the spatial investigation of the nanoscale spin waves is time-resolved x-ray microscopy, requiring synchrotron radiation and making investigation of nanoscale-related phenomena time and resource demanding. On the contrary, Brillouin light scattering (BLS) is a common tabletop technique available in many magnonics laboratories. During my PhD research, I brought the possibility of measuring nanoscale spin waves to standard micro-focused BLS setup by utilizing Mie resonances in dielectric nanoresonators. I investigated this phenomenon by measuring thermally induced spin waves in NiFe layer using a single silicon disk as a Mie resonator. To analyze the obtained data, I developed a theoretical model for micro-focused BLS. Moreover, by introducing the periodical structures, I demonstrated the measurement of the nanoscale spin waves with in-plane wavevector resolution. I measured the dispersion relation of thermally excited spin waves down to the wavelengths of 50 nm, which is one order of magnitude improvement compared to the conventional BLS. Finally, I investigated coherently excited spin waves, where the phase-resolved measurements are demonstrated by measuring the spin-wave wavelength of 204 nm with the uncertainty of only 6 nm. In summary, the presented results open a new way of analyzing the micro-focused BLS data and measuring nanoscale spin waves. The presented approach is general and can revolutionize the field of condensed matter physics and mechanobiology in the same way as a plasmon-enhanced Raman spectroscopy.

Abstrakt
Spinové vlny (magnony) mají potenciál být použity jako nová platforma pro přenos a zpracování dat, protože mohou dosáhnout vlnových délek v rozsahu nanometrů a frekvencí v rozsahu terahertzů. Ovšem nyní je možné měřit spinové vlny s vlnovými délkami pod difrakčním limitem světla pouze pomocí rentgenové mikroskopie s použitím velkých urychlovačů částic. Toto razantně zpomaluje a zdražuje výzkum a vývoj zařízeních založených na spinových vlnách. Během svého doktorského studia jsem hledal možnosti, jak tento problém překonat. Využitím Mieho rezonancí v dielektrických strukturách můžeme měřit spinové vlny s srovnatelnými vlnovými délkami pomocí standardní optické sestavy určené pro měření mikroskopie Brillouinova rozptylu světla. Tento proces jsem studoval na silikonovém disku umístěném na vrstvě nikl-železa. Tato technika může být upravena pro získání rozlišení pro vlnové délky krátké až 50 nm v rovině vzorku pomocí pole silikonových proužků se subdifrakční periodou. V poslední části mé teze se věnuji měření koherentně vybuzených spinových vln, kde demonstruji fázové rozlišením změřením disperzní relace spinových vln. Prezentované výsledky můžou změnit výzkum v oblasti fyziky pevných látek a mechano-biologie.

Keywords
magnonics, spin wave, Brillouin light scattering, Mie resonances, light-matter interaction

Klíčová slova
magnonika, spinové vlny, Brillouinův rozptyl, Mieho rezonance, interakce světla a hmoty

WOJEWODA, Ondřej. *Brillouin light scattering characterization of nanoscale spin waves.* Brno, 2024. 138 p. Doctoral thesis. Brno University of Technology. Central European Institute of Technology BUT. Supervised by Michal URBÁNEK.

I hereby declare that I have written my treatise on the topic of *Brillouin light scattering characterization of nanoscale spin waves* independently, under the guidance of the PhD supervisor, Ing. Michal Urbánek, Ph.D., and using the technical literature and other sources of information which are all properly quoted in the thesis and detailed in the list of literature at the end of the thesis.

.....	.....
Place and date	Ing. Ondřej Wojewoda

Acknowledgment

My deepest gratitude goes to my PhD supervisor, Michal Urbánek, who created a supportive and professional environment inside the magnonics group at CEITEC. Moreover, he extensively contributed to my personal and scientific growth through endless discussions about (science) ethics, data management, leadership, communication, etc. He also provided me with many opportunities, including attending conferences and participating in interesting scientific collaborations. I have not forgotten to appreciate his physics intuition, which many times guided our research to the positive direction. Last but not least, I thank him for the careful proofreading (not only) of this thesis. I hope many other (PhD) students will have the same opportunity to work under Michal's supervision.

I am indebted to Martin Hrtoň, who guided me through the Green function formalism and shared his codes, which formed the backbone of the developed model. I want to acknowledge Filip Ligmajer, who helped me with all scattering experiments and depositions of the metallic nanospheres. I am grateful to Martin Hrtoň, Filip Ligmajer, Michal Kvapil, and Jakub Krčma, who performed FDTD calculations. I acknowledge Francesca di Croce for ellipsometry measurement of silicon layer. I thank Jan Klíma, Meena Dhankar, Jakub Krčma, Jakub Holobrádek, Kristýna Davídková, and Dominik Pavelka for sample fabrication. I am grateful to Jon Ander Arregi and Jan Čechal for many discussions on various physics topics. I acknowledge Jakub Zlámal for help with the multiphysics model in Comsol. I am grateful to Jakub Holobrádek for performing VSM measurements. I thank Andrii Chumak, Jan Čechal, and Eric Glowacki for helping me to navigate through the scientific environment. I am also very grateful to Ludovico Migliaccio, Jakub Holobrádek, Sebastian Knauer, Dominik Pavelka, Filip Ligmajer, Michal Staňo, Peter Kepič, Jakub Krčma, and Jan Klíma, who carefully proofread the thesis.

I want to thank all the people who supported me during my PhD journey. I thank the whole magnonics group (big Kuba, small Kuba, Honza, Dominik, Ekaterina, Jagan, Ludo, Ahmed), including former members (Mara, Flash, Igor, Kristýna, Véna, Lucka, Zdeněk, Meena, Xavi) for fostering a supportive and friendly atmosphere. It was an honor to work with you. I have to emphasize the role of Lukáš, who supervised me during my bachelor's and inspired me at the onset of my scientific career. I acknowledge my friends at CEITEC (and beyond) (Libor, Tomáš, Káťa, Bea, Peter, Joni, Michal, Říša, Vojta, Oleksii, Peter, Filip, Zdeněk, Ivoš, Tesy, Grim, Radek, Milan, Jiřina) for endless *coffee discussions* and running/biking sessions. I express my gratitude towards my parents and sister for their neverending support during my studies. Finally, I want to mention my fiancée Míša. Her kindness and unwavering love made me a better person than I would ever imagine, and her presence by my side always reminds me life's true priorities. She deserves my deepest gratefulness for all the support and understanding that she already gave me and will give me throughout our life journey.

Ondřej Wojewoda

CzechNanoLab project LM2023051 funded by MEYS CR is gratefully acknowledged for the financial support of the measurements/sample fabrication at CEITEC Nano Research Infrastructure.

Contents

Introduction **1**

1. Theory of spin waves **3**
1.1. Micromagnetic energies . . . 3
1.1.1. Exchange energy . . . 3
1.1.2. Zeeman energy . . . 4
1.1.3. Dipolar energy . . . 4
1.1.4. Anisotropy energy . . . 6
1.2. Effective field . . . 6
1.3. Equation of motion . . . 6
1.4. Spin waves . . . 7
1.4.1. What is a spin wave? . . . 7
1.4.2. Quantum description . . . 7
1.4.3. Mesoscopic description . . . 9
Numerical solution . . . 12
1.4.4. Spin wave's group velocity, decay length, and lifetime . . . 13
1.4.5. Bloch function of spin waves . . . 14
1.5. Materials used in spin-wave research . . . 15
1.5.1. Material parameters of YIG, Permalloy, and CoFeB . . . 15
1.5.2. Spin-wave characteristics of Permalloy layer . . . 16
Spin wave profiles in Permalloy layer . . . 17
Bloch function of spin waves in Permalloy layer . . . 18

2. Theory of inelastic light scattering **19**
2.1. Types of inelastic scattering processes . . . 19
2.1.1. Quasi-elastic scattering . . . 20
2.1.2. Raman scattering . . . 20
2.1.3. Brillouin light scattering . . . 21
2.2. Classical description of μ-BLS . . . 22
2.2.1. Structure of the model . . . 23
2.2.2. Semi-analytic modeling of the driving field . . . 25
Effect of the polarization . . . 28
Effect of the defocus . . . 28
Effect of the filling factor . . . 29
Focusing of higher-order laser modes . . . 30
2.2.3. Induced polarization . . . 32
Example of the induced polarization in a Permalloy layer . . . 33
2.2.4. Far-field transition . . . 35
Dipole radiation . . . 38

2.2.5. Resulting BLS spectra . . . 39
Thermal spin waves field sweep . . . 39
Influence of the film thickness on the thermal spin wave spectra . . . 40
Influence of the measurement geometry . . . 42
Influence of the numeric aperture and the filling factor of the objective lens . . . 43
Influence of the Cotton-Moutton effect . . . 44
2.3. Phenomenological model of the BLS signal . . . 45
2.4. BLS in the presence of a scattering center . . . 46
2.4.1. Mie theory . . . 46
2.4.2. Calculation of the BLS signal enhanced by Mie resonance . . . 48

3. Experimental methods **51**
3.1. Micro-focused Brillouin light scattering . . . 51
3.1.1. Light source . . . 51
3.1.2. Phase resolution . . . 54
Experimental realization . . . 56
3.1.3. Microscope . . . 57
Imaging system . . . 58
Magnetic field . . . 58
3.1.4. Tandem-Fabry-Perot interferometer . . . 58
3.2. Ferromagnetic resonance measurement . . . 60
3.2.1. Theory of FMR . . . 61
3.2.2. Experimental realization of FMR measurement . . . 61
3.3. Scattering measurements . . . 63
3.3.1. Cross-section terms . . . 63
3.3.2. Experimental setup . . . 63
3.4. Numerical solving of the differential equations . . . 64
3.4.1. Finite-differences-time-domain (FDTD) simulations . . . 65
Practical implementation of the FDTD simulations . . . 66
3.4.2. Micromagnetic simulations . . . 67
3.4.3. Multiphysics simulation of heat distribution around laser spot . . . 68
Procedure of multiphysics simulation of heat distribution around laser spot . . . 69
3.5. Extraction of dispersion relation from micromagnetic simulations . . . 70
3.5.1. Micromagnetic simulation and excitation of broadband spin waves . . . 70
3.5.2. Analysis of the simulation results . . . 71

4. Mie-enhanced Brillouin light scattering spectroscopy **73**
4.1. Basic concepts . . . 73
4.2. Plasmon-enhanced Brillouin light scattering . . . 74
4.2.1. Plasmon-enhanced BLS on 200 nm-wide silver sphere . . . 74
4.3. Sample design of silicon disks for Mie-enhanced BLS . . . 77
4.3.1. Sample fabrication . . . 77
4.3.2. Inspection of the sample . . . 78
4.4. Magnetic layer characterization . . . 79
4.4.1. Dynamic characterization . . . 79
4.4.2. Static characterization . . . 80

4.5. Mie enhancement of the BLS signal on the single silicon disk 81
4.5.1. Comparison of measurements on 175 nm-wide silicon disk and bare film 81
4.5.2. Sweep of the diameter of the silicon disks 84
4.5.3. Influence of the index of refraction of dielectric disk on Mie resonances 87
4.6. Simulation of the Mie-enhanced BLS signal 89
4.6.1. Theoretical description 89
4.6.2. Obtained spectra for various disk diameters 89
4.7. Heating of the magnetic layer under the nanoresonator 91
4.7.1. Multiphysics simulation 91
4.7.2. Measurement with different laser powers 93
4.8. Sweeps over the edges of the silicon disk with a diameter of 1500 nm 93
4.8.1. Measurement on the edges of the disk 93
4.8.2. Linescan across the edges of the disk 94
4.9. Versatility of the Mie-enhanced BLS 96
4.9.1. Measurement with laser wavelength of 457 nm 96
4.9.2. Enhancement on the 100 nm thick CoFeB layer 97

5. Mie-induced wavevector resolution in the micro-focused Brillouin light scattering spectroscopy 99
5.1. Basic concepts 99
5.2. Sample design and fabrication 100
5.3. Simulation of the electric field in the periodic structures 101
5.4. k-resolution in silicon stripes array 102

6. Mie-enhanced Brillouin light scattering microscopy 105
6.1. Coherent excitation 106
6.1.1. Theoretical description 106
6.1.2. Experiment on the single silicon disk 107
6.1.3. Two-dimensional spatial scanning of nanoscale spin waves 108
6.1.4. Polarization of BLS light from nanoscale coherent spin waves . . . 109
6.2. Phase-resolved measurement 110
6.2.1. Two wave interference linescans of nanoscale spin waves 110
6.2.2. Full-phase reconstruction of nanoscale spin waves 111
6.2.3. FDTD simulation of silicon disks array 113

Conclusion 115

References 117

Selected activities performed during doctoral studies 135

Introduction

Magnonics is a prospective beyond CMOS (complementary metal-oxide semiconductor) technology which uses magnons, the quanta of spin waves, for low-power information processing. Spin wave propagation does not involve the motion of electrical charges, hence it does not dissipate energy through the Joule heating mechanism. Thus, the overall losses are orders of magnitude smaller than in conventional circuits which employ electric currents [1–4]. Spin waves also provide an interesting computational framework, as both amplitude and phase can be used to encode information. Thus, spin waves can simplify logic gates and even perform complicated computing tasks such as Fourier transform with a single computational element [5]. Due to the quantum nature of magnon, the spin waves can also be utilized in quantum computing systems [6, 7].

Many magnonic concepts and devices have recently been demonstrated on macro and microscales. Nevertheless, magnonics practical implementation in computational elements is still missing. To achieve competitiveness of the proposed magnonic devices, the wavelength of the used spin waves has to be significantly shortened. However, these efforts are slowed down by the fact that there is no *table-top* technique capable of spatially mapping nanoscale spin waves. For mapping macro- and micro-scale spin waves, Brillouin light scattering (BLS) spectroscopy and microscopy is a commonly used technique. It enabled many pioneering magnonic experiments, however, due to its fundamental limit in a maximum detectable magnon momentum, the standard BLS cannot be used to characterize nanoscale spin waves.

This thesis shows an approach how to overcome this limitation. I show that Mie resonances hosted in dielectric nanoparticles extend the range of accessible spin-wave wavevectors beyond the BLS fundamental limit. The method is universal and can be used in many magnonic experiments dealing with thermally excited as well as coherently excited high-momentum, short-wavelength spin waves. This research can significantly extend the usability and relevance of the BLS technique for nanoscale magnonic and other condensed matter research.

Moreover, despite the fact that micro-focused BLS (μ-BLS) is used for more than twenty years, its full theoretical description was missing. This knowledge gap became apparent when I was analysing the data from Mie-enhanced BLS experiments. Thus, I developed a model describing the exact shape of the acquired BLS spectra. This model is based on the continuum theory of inelastic scattering applied to the micro-focused light. The model can be solved semi-analytically for the case of the bare film, and can be further extended to account for any spatial perturbation by employing Maxwell equations simulations. In combination with micromagnetic simulation, the model can be used to obtain micro-focused BLS signal in any scenario, such as measuring of magnons in nanostructures, or nonlinear phenomena. The spin-wave community will greatly benefit from this model, as it provides a whole new dimension for the analysis of the acquired BLS

spectra, as not only the frequency positions and intensities but also the exact shape of the BLS spectra can be analyzed.

This thesis is structured as follows: the first chapter deals with the basic theoretical background of the physics of spin waves needed for the understanding of μ-BLS spectra modeling and analysis described in the following chapters. In the second chapter, scattering processes are introduced, and the newly developed model for μ-BLS signal is presented. I show the implications of various parameters, such as numeric aperture, magneto-optical constants, and film thickness, and in the final part, the model is verified against the experimental data. The third chapter summarizes the experimental and simulation techniques used to achieve the results presented in this work. The main emphasis is on Brillouin light scattering (BLS) as it is the integral technique of the presented experiments. In the fourth chapter, the results obtained in the main topic of my PhD, BLS characterization of the nanoscale spin waves, are presented. In the first section, the geometry and fabrication of the samples are shown. Afterward, I investigate the enhancement of the BLS signal by Mie resonances. With the use of experiment and simulation, I also treat the different geometries of the resonators. Furthermore, I explore the heating of the underlying layer. The disks with big diameter of 1500 nm we fabricated to explore the role of the edges of the nanoresonator. I demonstrate the wavevector resolved measurement by utilizing a periodic array of silicon stripes. By using various periodicities, I reconstruct the dispersion relation of the fundamental and first-standing spin-wave modes. In the last chapter, I show the usage of the Mie resonators with coherently excited spin waves. I demonstrate the measurement of the dispersion relation to nanoscale wavelengths with the use of the phase-resolved BLS.

1. Theory of spin waves

This thesis deals with the Brillouin light scattering on spin waves. In order to fully understand the presented results, it is necessary to have fundamental insights into the theory of magnetism, and specifically into the dynamic eigenstates of magnetization, which are described by the dispersion relation. In this chapter, I aim to provide only a basic description of the spin waves in thin films, which is needed to understand the modeled and measured spectra. For a more in-depth review of spin waves, I recommend the books by Stancil and Prabhakar [8] and Melkov [9] and dissertation theses by Flajšman, Jungfleish, Bozhko, Schneider, and Vaňatka [10–14]. For the basic theory of micromagnetism, the reader can consult books by Coey, Blundell, Krishnan, or Guimaraes [15–18]. For a quick introduction to both topics, I recommend two courses given by Prof. Chumak recorded on the YouTube platform [19, 20].

The chapter is structured as follows: First, I start with the relevant micromagnetic energies. Then, I present the Landau-Lifschitz-Gilbert equation and its solution for dipole-exchange spin waves. In the last part, I formulate the Bloch function and discuss the impact of various parameters.

1.1. Micromagnetic energies

In the following text I describe the magnetization dynamics with the mesoscopic approach using the quantum properties of magnetism. However, they are applied to continuum approximation. This approximation is sufficient to properly describe all phenomena encountered in the scope of this thesis. I consider only the four most relevant energies: Zeeman, dipolar, exchange, and anisotropy. The energies in Fig. 1.1 are presented differently, in order to show the contribution of each individual energy. Other energy contributions, such as magnetostriction or Dzyaloshinskii–Moriya [15], can be considered, but they are not important for the results presented in this thesis.

1.1.1. Exchange energy

The exchange energy has its origin in quantum physics. The hand-wave explanation is given in Feynman lectures on physics [21], while more thorough derivation can be found in, e.g., Griffith's introduction to quantum mechanics [22]. This interaction prefers (energy is lowest) when the magnetization is aligned parallel to each other. The exchange energy density can be written as

$$e_{\mathrm{eq}} = A_{\mathrm{ex}} \left(\frac{\nabla \boldsymbol{M}}{M_{\mathrm{s}}} \right)^2 , \tag{1.1}$$

where A_{ex} is exchange constant, M is magnetization, and M_{s} is saturation magnetization. The $(\nabla \boldsymbol{M})^2$ is so-called Frobenius product and is calculated as follows

$$(\nabla \boldsymbol{M})^2 = \sum_{i,j} \left(\frac{1}{M_{\mathrm{s}}} \frac{\partial M_i}{\partial x_j} \right)^2, \tag{1.2}$$

where indices i,j run over all spatial coordinates.

The exchange interaction is significant only to tiny distances, typically comparable to the (tens of) inter-atomic distances (0.3546 nm for NiFe [23]). The characteristic exchange length, which defines the distance in which this interaction is prevailing, can be defined as

$$l_{\mathrm{ex}} = \sqrt{\frac{2A_{\mathrm{ex}}}{\mu_0 M_s^2}}, \tag{1.3}$$

where μ is permeability of vacuum. If only exchange energy is considered, the ordering of the magnetization would be entirely uniform, as is depicted in Fig. 1.1a.

1.1.2. Zeeman energy

The Zeeman energy (e_{Z}) represents the energy of magnetization in an external magnetic field, and its density can be expressed as (except the constant)

$$e_{\mathrm{Z}} = \mu_0 \boldsymbol{M} \cdot \boldsymbol{H}_{\mathrm{ext}}, \tag{1.4}$$

where $\boldsymbol{H}_{\mathrm{ext}}$ is external field. This energy is maximized when the magnetization is aligned anti-parallel in the direction of the applied field and minimized when the magnetization is parallel to the direction of the applied field. When the external field is increased, the energy is increased as well; however, if the field is uniform, no force will be exerted on the magnetization as potential energy does not depend on its position within the field.

1.1.3. Dipolar energy

The dipolar energy (e_{dip}) is the same as Zeeman, but the magnetization itself creates the external field. Its density can be calculated from the following equation

$$e_{\mathrm{dip}} = \frac{1}{2} \mu_0 \boldsymbol{M} \cdot \boldsymbol{H}_{\mathrm{dip}}, \tag{1.5}$$

where $\boldsymbol{H}_{\mathrm{dip}}$ is dipolar field. This field can be calculated using Maxwell's equation (Gauss law)

$$\nabla \cdot \boldsymbol{B} = 0, \tag{1.6}$$

where $\boldsymbol{B}$ is magnetic induction and is given by

$$\boldsymbol{B} = \mu_0 (\boldsymbol{M} + \boldsymbol{H}_{\mathrm{dip}} + \boldsymbol{H}_{\mathrm{ext}}). \tag{1.7}$$

By applying the divergence to the whole equation and using Eq. 1.6 we get

$$\nabla \cdot \boldsymbol{H}_{\mathrm{dip}} + \nabla \cdot \boldsymbol{H}_{\mathrm{ext}} = -\nabla \cdot \boldsymbol{M}. \tag{1.8}$$

This equation gives guidance on how to calculate the demagnetizing field ($\boldsymbol{H}_{\mathrm{dip}}$). From the above equation, it is visible that the magnetization avoids so-called magnetic charges. This is known as *avoidance principle* and results in *flux-closure* patterns, as can be seen in Fig. 1.1b, where the magnetization is parallel to the edges of the studied structure. Now the difference of Zeeman and exchange energy can be demonstrated. The domain in the direction of the applied field enlarges, as can be seen in Fig. 1.1c.

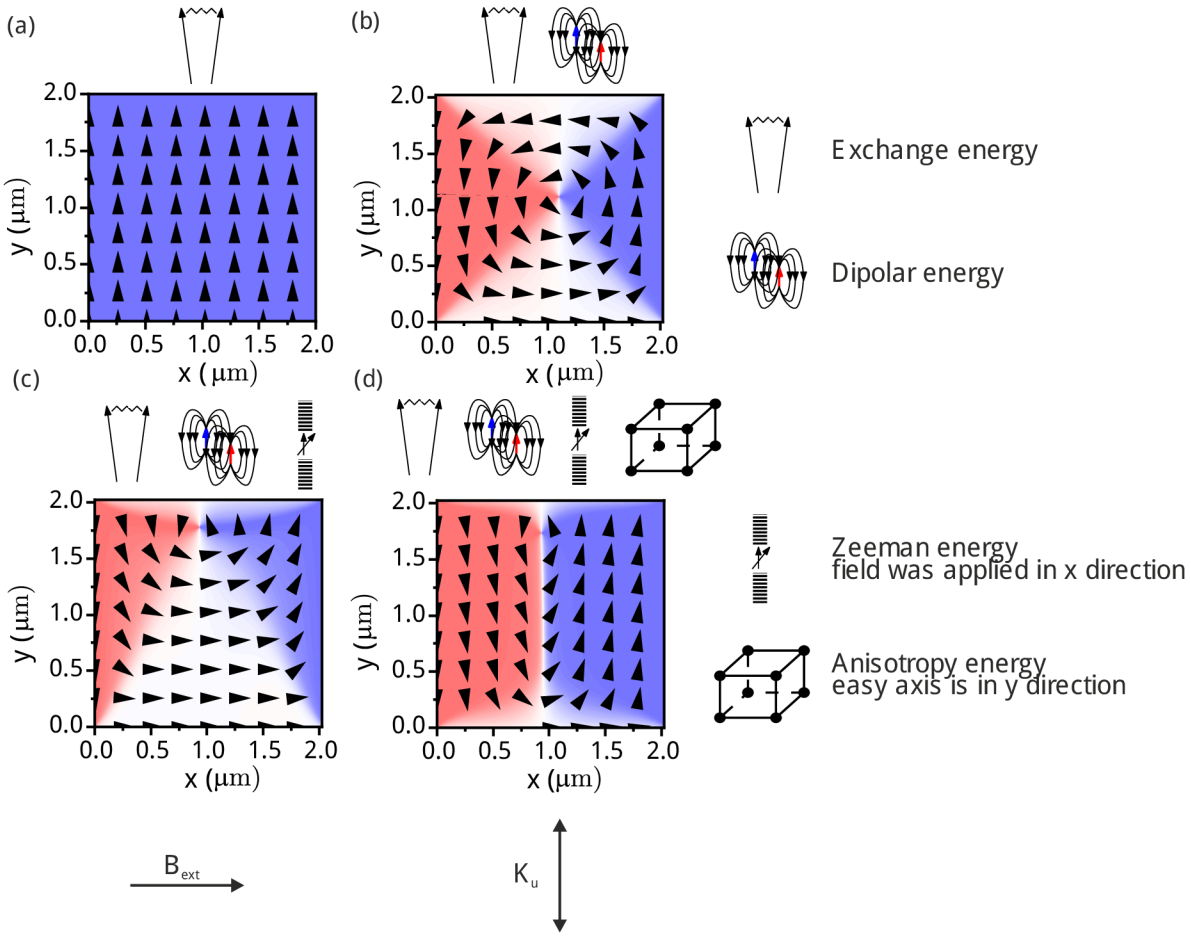

Figure 1.1: Magnetic energies at play. Results of micromagnetic simulations, where the energies are gradually taken into account. **a,** Exchange energy. **b,** exchange + dipolar energy. **c,** exchange + dipolar + Zeeman energy. **d,** exchange + dipolar + Zeeman + anisotropy energy. The contribution of the Zeeman energy is visible as the slight discrepancy between the sizes of top and bottom domain. The spatial distribution was obtained using MuMax3, with cell size 4^3 nm^3, total area 2^2 µm^2 and material parameters for permalloy.

1.1.4. Anisotropy energy

Due to the crystallographic properties, some materials can pose a preferable directions, where magnetization tends to align. In mesoscopic approximation, this is expressed as anisotropy energy contribution, which depends on the angle between the preffered crystallographic direction and magnetization. For simplicity, in the following, we will consider only uniaxial anisotropy with first-order approximation[1]

$$e_{\mathrm{uni}} = K_{\mathrm{u}} \sin^2 \vartheta, \tag{1.9}$$

where theta is an angle between the magnetization and easy axis (preferable direction), and K_{u} is a anisotropy constant. From the above equation, it can be seen that the magnetization energetically prefers to lay in the direction of the uniaxial anisotropy bi-vector. This is demonstrated in Fig. 1.1d, where the two domains in the bi-direction of the easy axis dominated the whole magnetization landscape.

1.2. Effective field

Once one finds all relevant energy terms and sums it up to total energy density ($\boldsymbol{e}_{\mathrm{tot}}$), the effective field ($\boldsymbol{H}_{\mathrm{eff}}$), which is felt by magnetization, can be calculated from the following equation

$$\boldsymbol{H}_{\mathrm{eff}} = -\frac{1}{\mu_0} \frac{\partial e_{\mathrm{tot}}}{\partial \boldsymbol{M}}, \tag{1.10}$$

where the e_{tot} is energy density. By inserting previously introduced energy terms to the Eq. 1.10, we obtain [18, 25]

$$\boldsymbol{H}_{\mathrm{eff}} = \frac{2}{\mu_0} \nabla \cdot (A_{\mathrm{ex}} \nabla \boldsymbol{M}) - \boldsymbol{H}_{\mathrm{ext}} + \boldsymbol{H}_{\mathrm{dip}} + \frac{2K_{\mathrm{u}}}{\mu_0 M_{\mathrm{s}}^2} (\boldsymbol{M} \cdot \boldsymbol{e}_{\mathrm{u}}) \boldsymbol{e}_{\mathrm{u}}, \tag{1.11}$$

where $\boldsymbol{e}_{\mathrm{u}}$ is a direction of easy axis. This field represents the effective field, which is felt by the magnetization. In other words, in the stationary case (with no applied time-dependent fields), the magnetization will align itself to the direction of the effective field after a sufficiently long time. The toque $\boldsymbol{\tau}$ exerted on the magnetization can be expressed as

$$\boldsymbol{\tau} = \mu \boldsymbol{M} \times \boldsymbol{H}_{\mathrm{eff}}. \tag{1.12}$$

1.3. Equation of motion

The motion (time-dependency) of magnetization is governed by torque equation with damping [26]

$$\frac{\mathrm{d}\boldsymbol{M}}{\mathrm{d}t} = -\gamma \mu_0 \boldsymbol{M} \times \boldsymbol{H}_{\mathrm{eff}} + \frac{\alpha}{M_{\mathrm{s}}} \boldsymbol{M} \times \frac{\mathrm{d}\boldsymbol{M}}{\mathrm{d}t}, \tag{1.13}$$

where γ is the gyromagnetic ratio, and α is Gilbert damping. This form of the damping term was first phenomenologically added by Gilbert in his PhD thesis and presented at the first MMM conference in Pittsburgh in 1955; however, it was not published in a peer-reviewed journal until 2004 [27]. It was intended to correct original form proposed by

[1] Another more complex form of anisotropy energies can be used, such as cubic [15, 24].

Landau and Lifshitz for high damping materials[2]. There are still discussions about the appropriate term for damping (energy dissipation) see, for example, [28, 29].

However, if energy dissipation is not of interest (e.g. when finding spin-wave eigenvalues), the simplified version (called the Landau-Lifshitz equation) can be formulated

$$\frac{\mathrm{d}\boldsymbol{M}}{\mathrm{d}t} = -\gamma\mu_0 \boldsymbol{M} \times \boldsymbol{H}_{\mathrm{eff}}. \tag{1.14}$$

1.4. Spin waves

A proper description of the spin waves is essential for the correct interpretation of the results obtained in this thesis. This section starts with the quantum description of the spin waves and derivation of the dispersion relation, which takes into account the forming of the Brillouin zone caused by the finite distances between the magnetic moments (atoms). However, the theory I used in this thesis is based on the mesoscopic approach [30]. In this approach, I assume that the magnetization is a continuum. This allows me to find an approximate zeroth perturbation solution of the dispersion relation. The problem is further reformulated in the form of an infinite matrix to allow for a numerical solution without neglecting off-diagonal terms. Afterward, the dispersion characteristics, group velocity, decay length, and lifetime are discussed. At the end of this section, I present my own approach to obtain the Bloch function (spectral density of states) of spin waves, based on the approximation of spin-wave resonances with Lorentzian shape.

1.4.1. What is a spin wave?

If we assume the solution of the Eq. 1.13 in the form of waves, we get the solution of eigenstates of spin waves. A spin wave is a collective excitation of the magnetization with a certain frequency and wavenumber. Bloch predicted them to explain the temperature dependence of the magnetization [31]. If the wavenumber is zero, thus the wavelength is infinite, and the magnetization oscillates in phase in the whole volume of the sample, it is called ferromagnetic resonance. Its depiction is shown in Fig. 1.2a.

If there is a certain wavenumber (wavelength) of the excitation (periodicity in spatial dimensions), we can talk about the spin waves. Its depiction is shown in Fig. 1.2b. The Brillouin zone of spin wave systems, spans to $\approx 10000\,\frac{\mathrm{rad}}{\mu m}$[3]. This is a 1000 times bigger wavevector than what is usually accessible in Brillouin light scattering experiments, so it is not necessary in the scope of this thesis to take this into account.

1.4.2. Quantum description

Hamiltonian for Heisenberg ferromagnet with external field in z-direction can be expressed as

$$\mathcal{H} = \frac{1}{2}\sum_{i,j} J_{i,j}\boldsymbol{S}_i \cdot \boldsymbol{S}_j - g\mu_B H_{\mathrm{ext}} \sum_i S_i^z, \tag{1.15}$$

where J is constant of exchange interaction between the spins, S is an operator of spin, g is a Lande g-factor, and μ_B is a Bohr magneton. The factor $\frac{1}{2}$ is to ensure that the

[2] Assuming frequency independent gyromagnetic ratio

[3] Brillouin zone boundary is given by $\frac{\pi}{a}$, where a is lattice parameter

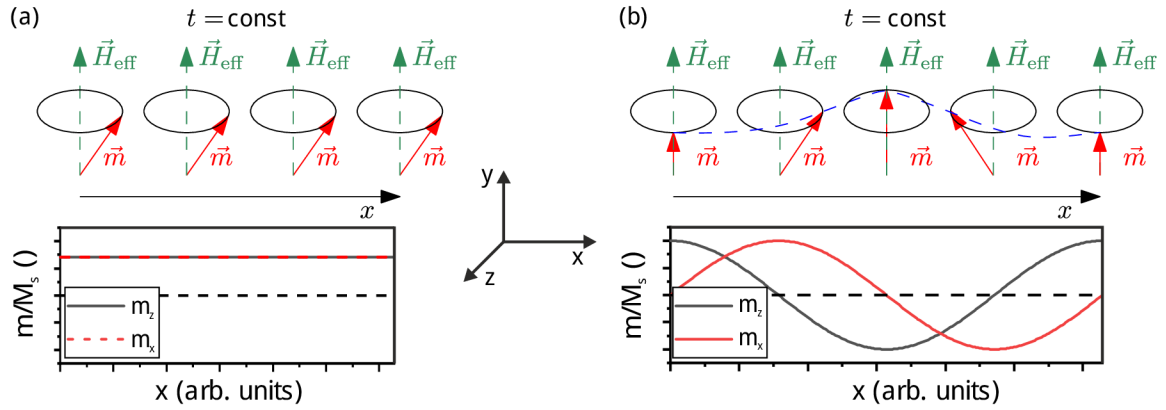

Figure 1.2: Ferromagnetic resonance and spin waves. **a,** Schematics of ferromagnetic resonance. The upper panel shows the oscillation of the magnetization of the ferromagnetic mode ($k = 0$). The lower panel shows a spatial evolution of the dynamic components of the magnetization. **b,** Schematic of a spin wave. The upper panel shows magnetization oscillations with $k \neq 0$. The lower panel shows the spatial evolution of dynamic components.

spins will not be accounted twice, as the summation runs along all spins. The Holstein-Primakoff transformation is used to go from this spin operator to bosonic one [32]. The transformation is expressed as follows

$$S_{x,j} + iS_{y,j} = a_j\sqrt{2S_j}\sqrt{1 - a_j^\dagger a_j/2S}, \tag{1.16a}$$

$$S_{x,j} - iS_{y,j} = \sqrt{2S_j}\sqrt{1 - a_j^\dagger a_j/2S}, \tag{1.16b}$$

$$S_{z,j} = S - a_j^\dagger a_j, \tag{1.16c}$$

where a_j and $a_j^\dagger$ are annihilation and creation of boson (magnon) operators, respectively. They obey the usual commutation rule

$$[a_j, a_j^\dagger] = \delta_{i.j}, \tag{1.17}$$

where $\delta_{i.j}$ is the Kronecker delta function. If only a small magnon density is assumed, we can expand the square root in 1.16. For example in 1.16a we get

$$S_{x,j} + iS_{y,j} = \sqrt{2S}\left(a_j - \left(a_j^\dagger a_j a_j/4S\right) + \dots\right). \tag{1.18}$$

The creation and annihilation operators can be defined in reciprocal space with respect to the wavenumber instead of real space using the Fourier transformation

$$a_j = \sqrt{\frac{1}{N}}\sum_q \exp\left(-i\boldsymbol{k}\cdot\boldsymbol{r}_j\right) a_{\boldsymbol{k}}, \tag{1.19a}$$

$$a_j^\dagger = \sqrt{\frac{1}{N}}\sum_q \exp\left(i\boldsymbol{k}\cdot\boldsymbol{r}_j\right) a_{\boldsymbol{k}}^\dagger, \tag{1.19b}$$

where N is the total number of magnetic sites, and $\boldsymbol{k}$ is spin wave wavevector. Now, the Hamiltonian (eq. 1.15) can be rewritten in terms of boson operators

$$\mathcal{H} = -NS(J_{z\circ}S/2 + g\mu_B H_{\text{ext}})\sum_{\boldsymbol{k}}\omega(\boldsymbol{k})a_{\boldsymbol{k}}^\dagger a_{\boldsymbol{k}} + \mathcal{H}_{\text{HO}}, \tag{1.20}$$

where $\mathcal{H}_{\mathrm{HO}}$ stands for higher order terms (nonlinear interactions), and $J_{z\circ}$ is exchange interaction to the nearest neighbor,

$$\omega(\boldsymbol{k}) = g\mu_B H_{\mathrm{ext}} + J_{z\circ} S(1 - \beta_{\boldsymbol{k}}), \tag{1.21}$$

where $\beta_{\boldsymbol{k}}$ is structural factor and is given by

$$\beta_{\boldsymbol{k}} = \frac{1}{z\circ} \sum_{\boldsymbol{d}} \exp\left(i\boldsymbol{k} \cdot \boldsymbol{d}\right), \tag{1.22}$$

where $z\circ$ is a number of the nearest neighbors, and $\boldsymbol{d}$ is a vector of the nearest neighbor. These equations give the dispersion relation of the magnons, assuming only exchange interaction and external field in bulk magnets. Near the center of the Brillouin zone, the dispersion can be approximated with quadratic dependency on the wavevector. The treatment based on the Landau-Lifshitz equation (Eq. 1.14) can lead to the dispersion relation for more complicated geometries and description of nonlinear processes such as three- and four-magnon scattering [33].

1.4.3. Mesoscopic description

This section aims to provide the dispersion relation of spin waves in thin films, which is rather cumbersome to achieve with quantum description. The dispersion relation is of high interest, as its proper knowledge is crucial to solving some fundamental questions and designing devices for spin wave applications. If one is interested in spin waves with either long wavelengths (typically larger than $\approx 1\,\mu\mathrm{m}$), or short wavelengths (shorter than $\approx 100\,\mathrm{nm}$), simple solutions exist and can be found e.g. here [8]. However, the intermediate region is the most relevant to the topics presented in this thesis. To tackle this challenge, the linearized Landau-Lifshitz equation (Eq. 1.14) has to be solved together with the Maxwell equations employing standard electrodynamics and exchange boundary conditions.

Two main theoretical approaches to solve this problem were formulated. The first is based on plane waves. Here, the magnetization, magnetic fields, and magnetic potential are formulated as a sum of plane waves. They are plugged into the Landau-Lifshitz equation inside the medium and Laplace equation outside the magnetic medium. This leads to a system of linear conditions, and by requiring vanishing determinant, resulting in a 8×8 matrix. Such matrix does not have an analytical solution. Thus, this method is only solvable by using numerical methods. This approach was used in e.g. [34–37]. This method can also be applied to the multi-layer systems (mostly known as *Hillebrands method*) [38].

The second approach is based on formulating an integro-differential equation and assuming the solution in form of spin-wave modes. The advantage of this approach is that an approximate analytical solution can be found[4]. At the same time, it can be used to obtain exact dispersion by numerical means. In the coming text, we follow the simplified derivation given in [30].

The assumed geometry is shown in Fig. 1.3a, b. Usage of the two coordinate system simplifies the notation of all formulated equations, as z axis coincides with the static magnetization direction, and ζ axis coincides with the propagation direction. In such notation, angle φ (ϑ) defines the in-plane (out-of-plane) angle between the static magnetization and

[4]The solution can be formulated with desired accuracy using perturbation theory

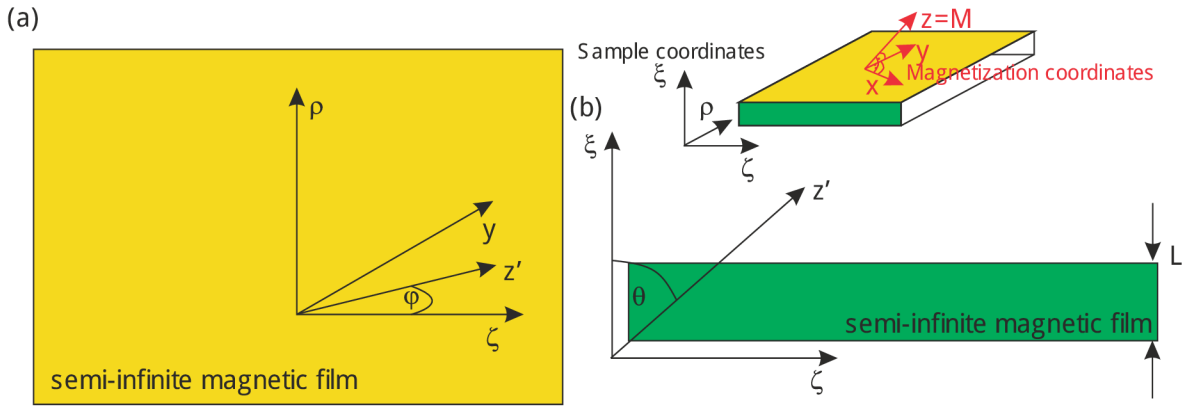

Figure 1.3: Geometry for calculation of dispersion relation. a, b, Geometry in in-plane (**a**) and cut through thin film (**b**). The axis with *x'*,*z'* shows only projection to the current view-plane. The coordinate system *x, y, z* is chosen to coincide with the static magnetization direction (axis *z* is in the direction of the static magnetization and axis *y* is in the plane of the sample). The coordinate system ζ,ϱ,ξ is aligned with the sample axis, and the axis ζ coincides with the direction of propagation of the spin wave.

propagation direction (sample plane), respectively. The magnetization is assumed to be in the form of propagating wave

$$\boldsymbol{m}(\zeta,\xi) = \boldsymbol{m}_Q(\xi)\exp\left[i\left(\omega t - Q\zeta\right)\right], \tag{1.23}$$

where ω is a spin wave angular frequency, Q is an in-plane wavevector, and $\boldsymbol{m}_Q$ is the amplitude of magnetization distribution connected to the specific in-plane wavevector. The created dipole field can be expressed as

$$\boldsymbol{h}(\zeta,\xi) = \boldsymbol{h}_Q(\xi)\exp\left[\right]i\left(\omega t - Q\zeta\right)\right], \tag{1.24}$$

where $\boldsymbol{h}_Q$ is the amplitude of field distribution connected to the specific in-plane wavevector. Now, by using Maxwell's theory, this two equations can be rewritten in integral form

$$\boldsymbol{h}_Q(\xi) = \int_{-\infty}^{\infty} \hat{\boldsymbol{G}}_{\zeta\varrho\xi}(\xi\xi')\boldsymbol{m}_Q(\xi)\mathrm{d}\xi', \tag{1.25}$$

where $\hat{\boldsymbol{G}}_{\zeta\varrho\xi}$ is dyadic Green function

$$\hat{\boldsymbol{G}}_{\zeta\varrho\xi}(\xi\xi') = \begin{pmatrix} G_\mathrm{P} - \delta(\xi-\xi') & 0 & iG_\mathrm{Q} \\ 0 & 0 & 0 \\ iG_\mathrm{Q} & 0 & -G_\mathrm{P} \end{pmatrix}, \tag{1.26}$$

where

$$G_\mathrm{P} = \frac{Q}{2}\exp\left(-Q|\xi-\xi'|\right), \tag{1.27a}$$

$$G_\mathrm{Q} = \begin{cases} G_\mathrm{P}\ \mathrm{sgn}\ (\xi'-\xi) & \xi \in (0,L) \\ -G_\mathrm{P}\ \mathrm{sgn}\ (\xi) & \xi \in (-\infty,0)\cup(L,\infty). \end{cases} \tag{1.27b}$$

We assume only small amplitudes, i.e. static magnetization[5] is not changing, the Eq. 1.26 can be geometrically transformed to the 2×2 ($\hat{\boldsymbol{G}}_{xy}$) matrix in x, y, y coordinate system (there will be non-zero dynamic magnetization components only in the direction of x, y axes). Now, the obtained results ($\hat{\boldsymbol{G}}_{xy}$), together with the Landau-Lifshitz equation (Eq. 1.14) give the integro-differential equation

$$\hat{\boldsymbol{F}}\boldsymbol{m}_Q(\xi) = \int_0^L \hat{\boldsymbol{G}}_{xy}(\xi,\xi')\boldsymbol{m}_Q(\xi')\mathrm{d}\xi', \tag{1.28}$$

where $\hat{\boldsymbol{F}}$ is a matrix differential operator

$$\hat{\boldsymbol{F}} = \begin{pmatrix} \frac{\omega_\mathrm{H}}{\omega_\mathrm{M}} + l_\mathrm{ex}^2 Q^2 + l_\mathrm{ex}^2 \nabla_\xi^2 & \frac{i\omega}{\omega_\mathrm{M}} \\ -\frac{i\omega}{\omega_\mathrm{M}} & \frac{\omega_\mathrm{H}}{\omega_\mathrm{M}} + l_\mathrm{ex}^2 Q^2 + l_\mathrm{ex}^2 \nabla_\xi^2 \end{pmatrix}, \tag{1.29}$$

where $\omega_\mathrm{M} = \mu_0 \gamma M_\mathrm{S}$, and $\omega_\mathrm{H} = \mu_0 \gamma H_\mathrm{ext}$. The boundary conditions are given by mixed exchange boundary condition [39]

$$\frac{\mathrm{d}m_x}{\mathrm{d}\xi} + \nu_{1,2} m_x(\xi) \cos(2\vartheta) = 0, \tag{1.30a}$$

$$\frac{\mathrm{d}m_y}{\mathrm{d}\xi} + \nu_{1,2} m_y(\xi) \cos(\vartheta)^2 = 0, \tag{1.30b}$$

where $\nu = \frac{K_\mathrm{s}}{A_\mathrm{ex}}$ is pinning parameter, K_s is surface anisotropy, and the subscript numbers denote different boundaries. To simplify the further derivation, we will focus only on cases without surface anisotropy, i.e., totally unpinned surface spins. Next step to proceed is to find the *spin wave modes* (i.e., spin wave profiles in ξ direction). To obtain them one has to find the eigenfunction of matrix differential operator from Eq. 1.29, assuming only diagonal elements ($\hat{\boldsymbol{F}}_\mathrm{diag}$) of the matrix operator $\hat{\boldsymbol{F}}$

$$\hat{\boldsymbol{F}}_\mathrm{diag}\boldsymbol{S}(\xi) = \boldsymbol{F}\boldsymbol{S}(\xi), \tag{1.31}$$

with boundary condition given by Eq. 1.30. This is the so-called Sturm–Liouville problem [40]. For the completely unpinned surface spins, one obtains

$$\begin{pmatrix} S_x \\ S_y \end{pmatrix} = \begin{pmatrix} \frac{1}{\sqrt{1+\delta_{0n}}} \cos\left(\frac{n\pi\xi}{L}\right) \\ \frac{1}{\sqrt{1+\delta_{0n}}} \cos\left(\frac{n\pi\xi}{L}\right) \end{pmatrix}, \tag{1.32}$$

where $n = 0,1,2,3,\cdots$. Now, by knowing *spin-wave modes*, the Eq. 1.23 can be rewritten to the form of infinite sum

$$m_Q(\xi) = \sum_n \boldsymbol{m}\boldsymbol{S}(\xi). \tag{1.33}$$

Now, substituting this to integro-differential equation Eq. 1.29 and after some further transformation, we get

$$\hat{\boldsymbol{H}}_{nn}\boldsymbol{m}_n + \sum_{n \neq n'} \hat{\boldsymbol{W}} m_{n'} = 0. \tag{1.34}$$

Now, in a zero-order approximation, we may neglect off-diagonal elements, and by the requirement of the vanishing determinant, we can solve the eigenvalue problem and obtain dispersion relation for non-degenerate spin waves

$$\omega^2 = \left(\omega_\mathrm{H} + l_\mathrm{ex}^2 \omega_\mathrm{M} k^2\right)\left(\omega_\mathrm{H} + l_\mathrm{ex}^2 \omega_\mathrm{M} k^2 + \omega_\mathrm{M} F_n\right), \tag{1.35}$$

[5] Projection of magnetization into the z-axis direction

where

$$F_n = P_\mathrm{n} + \sin(\vartheta)^2 \left(1 - P_\mathrm{n}\left[1 + \cos(\varphi)^2\right]\right) + \frac{\omega_\mathrm{M} P_\mathrm{n}\left(1 - P_\mathrm{n}\right)\sin(\varphi)^2}{\omega_\mathrm{H} + l_\mathrm{ex}^2 \omega_\mathrm{M} k^2}, \tag{1.36}$$

where

$$P_\mathrm{n} = \begin{cases} \frac{Q^2}{k^2} - \frac{Q^4}{k^4}\frac{1}{2}\left[\frac{2}{QL}\left(1 - \exp\left(-QL\right)\right)\right] & n = 0 \\ \frac{Q^2}{k^2} - \frac{Q^4}{k^4}\left[\frac{2}{QL}\left(1 - \exp\left(-QL\right)\right)\right] & n \neq 0 \end{cases}. \tag{1.37}$$

Here, We stress one more time that this solution is only approximate and does not work for cases where one branch of spin-wave mode crosses another (degenerate state). Moreover, this zeroth order approximation does not provide modification in the spin-wave profile, and calculated profiles strictly follow cosine without any modification, which is not consistent with experiments. The correction can be made using perturbation theory to get a more precise solution, but it is rather cumbersome. For example, the second perturbation theory for degenerate states was implemented to model avoided crossing in 100 nm thick CoFeB layer [14, 41].

Numerical solution

In my opinion, currently, a more convenient way to calculate dispersion relation is to numerically solve the eigenvalue problem [42]. For this purpose, the Landau-Lifshitz equation (Eq. 1.14) can be expressed in the matrix notation

$$\omega \boldsymbol{m}_Q = C_Q \boldsymbol{m}_Q, \tag{1.38}$$

where C_Q is an infinite matrix

$$C_Q = \begin{pmatrix} -(a_{0Q} + C_{00}) & -(b + p_{00}) & 0 & -q_{10} & -C_{20} & -p_{20} & \cdots \\ (b + p_{00}) & -(a_{0Q} + C_{00}) & -q_{10} & 0 & p_{20} & C_{20} & \cdots \\ 0 & -q_{01} & -(a_{1Q} + C_{11}) & -(b + p_{11}) & 0 & -q_{21} & \cdots \\ -q_{01} & 0 & (b + p_{11}) & (a_{1Q} + C_{11}) & -q_{21} & 0 & \cdots \\ -C_{02} & -p_{02} & 0 & -q_{12} & -(a_{2Q} + C_{22}) & -(b + p_{22}) & \cdots \\ p_{02} & C_{02} & -q_{12} & 0 & (b + p_{22}) & (a_{2Q} + C_{22}) & \cdots \\ \cdots & \cdots & \cdots & \cdots & \cdots & \cdots & \cdots \end{pmatrix}, \tag{1.39}$$

where

$$a_{nQ} = \Omega_{nQ} + \frac{\omega_\mathrm{M}}{2}, \tag{1.40a}$$

$$b = \frac{\omega_\mathrm{M}}{2}, \tag{1.40b}$$

where

$$\Omega_{nQ} = \omega_\mathrm{H} + \omega_\mathrm{M} l_\mathrm{ex}^2 \left(Q^2 + \left(\frac{n\pi}{L}\right)^2\right). \tag{1.41}$$

The other coefficients are

$$C_{nn'} = -\frac{\omega_\mathrm{M}}{2}\left(1 - \sin^2\varphi\right) P_{nn'}, \tag{1.42a}$$

$$p_{nn'} = -\frac{\omega_\mathrm{M}}{2}\left(1 + \sin^2\varphi\right) P_{nn'}, \tag{1.42b}$$

$$q_{nn'} = -2\omega_\mathrm{M}\left(1 + \sin\varphi\right) Q_{nn'}, \tag{1.42c}$$

where

$$Q_{nn'} = \frac{Q^2}{k_{n'}^2}\left(\frac{\left(\frac{n'\pi}{L}\right)^2}{\left(\frac{n'\pi}{L}\right)^2 - \left(\frac{n\pi}{L}\right)^2}\frac{2}{QL} - \frac{Q^2}{2k_n^2}F_n\right)\frac{1}{\sqrt{(1+\delta_{0n})(1+\delta_{0n'})}}\left(\frac{1-(-1)^{n+n'}}{2}\right), \tag{1.43}$$

and $P_{nn'}$ defined by Eq. 1.37. The found eigenvalues of the matrix C_Q (Eq. 1.39) represent the dispersion relation of the three lowest energy modes (each mode is represented two times, by positive and negative frequency), and the eigenvector represents mode amplitudes for x and y components. The mode profiles can be calculated using Eq. 1.32. All presented models are implemented in own-made open-source code available at GitHub platform [41]. The resulting dispersion relation and mode profiles for Permalloy layer are discussed in Section 1.5.2.

1.4.4. Spin wave's group velocity, decay length, and lifetime

From the dispersion relation, one can obtain more spin wave characteristics. The rate of wave energy transfer is described by the group velocity ($\boldsymbol{v}_\mathrm{g}$). This quantity can be obtained from the dispersion relation

$$\boldsymbol{v}_\mathrm{g} = \frac{\partial\omega}{\partial\boldsymbol{k}}. \tag{1.44}$$

As the dispersion relation of the spin waves is highly anisotropic, the spin-wave wavevector and group velocity do not have to point in the same direction. In the limiting case of in-plane magnetized thin film ($\Theta = \frac{\pi}{2}$), two pronounced geometries can be defined: Damon-Eshbach geometry (DE, wavevector perpendicular to the static magnetization direction, $\varphi = \frac{\pi}{2}$) and backward-volume (BV, wavevector parallel to the static magnetization direction, $\varphi = 0$). In the case of DE geometry, the group velocity has the same direction as a wavevector, but in the case of BV, each faces the opposite direction. In between these two limiting cases ($0 < \varphi < \frac{\pi}{2}$)) the angle between them continuously evolve. This behavior gives rise to interesting phenomena, such as caustic beams [43–46].

Another characteristic, which can be phenomenologically obtained from the dispersion relation, is spin-wave lifetime (τ) [8, 47]

$$\tau = \left(\left(\alpha\omega + \gamma\mu_0 H_\Delta\right)\frac{\partial\omega}{\partial\omega_\mathrm{H}}\right)^{-1}, \tag{1.45}$$

where H_Δ is so-called inhomogeneous broadening. The contribution of this inhomogeneous broadening to the lifetime is typically significant only for Yitrium-Iron-Garnet (YIG). Usually, the spin-wave lifetime is not strongly dependent on the wavevector or thickness of the magnetic layer.

If one knows the group velocity and lifetime, then the spin wave decay length (Λ), a distance where the spin-wave amplitude is decreased to $\frac{1}{e} \approx 0.38$, can be calculated as

$$\Lambda = \tau v_\mathrm{g}. \tag{1.46}$$

The decay length is very important for the design of the experiments or functional devices. The propagation of the spin waves can be measured only to several multiples of the decay length. In a typical experiment, reliable measurement is only possible within $\approx 3\Lambda$, which means that only 5 % of the original spin-wave amplitude is left.

1.4.5. Bloch function of spin waves

This section introduces the procedure for obtaining *Bloch spectral density of states* of thermally excited spin waves. The term *Bloch spectral density of states* or *Bloch function* $[\mathcal{D}(\omega,\boldsymbol{k})]$ is often used for function describing the density of states in frequency-wavevector space, i.e. [48, 49]. Another terms, used throughout the literature are *power spectral density*, or *spectral density* [8, 50, 51]. In this thesis we use the term *Bloch function*. We present here phenomenological approach, which can be used together with any method for obtaining dispersion relation together with calculated (or estimated) lifetime of the spin waves. This Bloch function is then used later in Chapter 2 to obtain the Brillouin light scattering signal.

A complex circular magnetization is assumed (the possible ellipticity of the spin wave mode will be accounted for later)[6]

$$\mathcal{M}(\omega,\boldsymbol{k}) = M'_x(\omega,\boldsymbol{k}) + iM'_y(\omega,\boldsymbol{k}). \tag{1.47}$$

This complex circular magnetization now describes the possible spin-wave resonances. If we assume only one spin wave mode, on the given in-plane wavevector, the frequency-dependent complex magnetization will have Lorentzian shape [9],

$$\mathcal{M}(\omega,\boldsymbol{k}) \propto \frac{1}{(\omega_0-\omega)^2+\left(\frac{2}{\tau}\right)^2} + i\frac{1}{(\omega_0-\omega)^2+\left(\frac{2}{\tau}\right)^2}, \tag{1.48}$$

where the width of the resonance is given by the spin-wave lifetime τ. To obtain the Bloch function we take the absolute value out of the complex magnetization and, as we are interested in thermally excited spin waves, correct the resulting function for Bose-Einstein distribution

$$\mathcal{D} \propto \sqrt{2}n_{\mathrm{BE}}(\omega)\frac{1}{(\omega_0-\omega)^2+\left(\frac{2}{\tau}\right)^2}, \tag{1.49a}$$

where the Bose-Einstein distribution is given by

$$n_{\mathrm{BE}} = \frac{1}{\exp\left(\frac{\hbar(\omega-\mu)}{k_{\mathrm{b}}T}\right)-1}, \tag{1.50}$$

μ is a chemical potential, k_{b} is the Boltzman constant, $\hbar$ is the reduced Planck constant, and T is a thermodynamic temperature.

To obtain the out-of-plane and in-plane magnetization (this transformation will be useful for calculating the interaction with light in Chapter. 2)[7], we need to multiply the solution by the spin-wave profile amplitude

$$M_{\mathrm{IP}}(\boldsymbol{Q},\omega,\xi) = m_{Q,\varrho}(\boldsymbol{Q},\omega,\xi)\mathcal{D}(\boldsymbol{Q},\omega), \tag{1.51a}$$
$$M_{\mathrm{OOP}}(\boldsymbol{Q},\omega,\xi) = im_{Q,\xi}(\boldsymbol{Q},\omega,\xi)\mathcal{D}(\boldsymbol{Q},\omega). \tag{1.51b}$$

[6] For more information refer to Bogoluibov transformation, e.g., [8, 9].

[7] In the limiting case of magnetization pointing out of the plane ($\vartheta = 0$), a similar procedure to acquire two in-plane dynamic components can be used.

1.5. Materials used in spin-wave research

To support spin-wave propagation, a ferromagnetic or ferrimagnetic material with reasonably high saturation magnetization and low damping has to be used. Several materials fulfill these demands. I have selected the three most used materials in spin wave research, namely Yttrium Iron Garnet, Permalloy, and CoFeB and summarized them in Table 1.1. However, the material research is searching for novel material systems, such as half-metallic Heusler alloys, which can provide low damping and high saturation magnetization at the same time [52, 53].

1.5.1. Material parameters of YIG, Permalloy, and CoFeB

The first material shown is a nm-thick Yttrium Iron Garnet (YIG). It is a magnetic insulator and single-crystal. It has one of the lowest damping of all materials, making it the ideal candidate for future application in devices for telecommunication technologies. The disadvantage of this material is its requirement of a single crystal substrate. For this purpose, gadolinium gallium garnet (GGG) is usually used. This material is also extensively used for research because long decay lengths simplify performed experiments [69–71].

The second material is Permalloy, a poly-crystalline alloy of nickel and iron, hence is often called NiFe. It was specifically designed to provide a low anisotropy field. However, it has approximately one order of magnitude higher damping than YIG. On the other

Table 1.1: Three materials commonly used in spin-wave research. The material parameters and spin wave characteristic for $k = 10\,\mathrm{rad/\mu m}$ ($\lambda \approx 2\,\mu\mathrm{m}$), external field of $B_{\mathrm{ext}} =$ $= 50\,\mathrm{mT}$ and film thickness of $t = 30\,\mathrm{nm}$ are given for each material. Inspired by [47, 54].

	nm-thick Yttrium Iron Garnet (YIG)	Permalloy (Py, NiFe)	CoFeB
Chemical composition	$Y_3Fe_5O_{12}$	$Ni_{80}Fe_{20}$	$Co_{40}Fe_{40}B_{20}$
Gilbert damping α ($\cdot 10^{-4}$)	2	70	40
Sat. magnetization M_s, (kA/m)	140	800	1250
Exchange constant A_{ex}, (pJ/m)	3.6	16	15
Typical thickness (nm)	5-100	5-100	5-100
Anisotropy field (mT)	$< 1\,\mathrm{mT}$	$< 1\,\mathrm{mT}$	$< 1\,\mathrm{mT}$
Frequency DE/BV	3.6	12.0	18.4
(GHz)	3.0	6.4	8.2
Group velocity DE/BV	0.4	2.1	3.5
(km/s)	0.1	-0.05	-0.1
Lifetime DE/BV (ns)	25.5	1.4	1.6
	23.6	1.6	1.52
Decay length DE/BV	10.0	3.0	0.2
(µm)	2.9	0.07	0.09
References	[55–61]	[62–65]	[66–68]

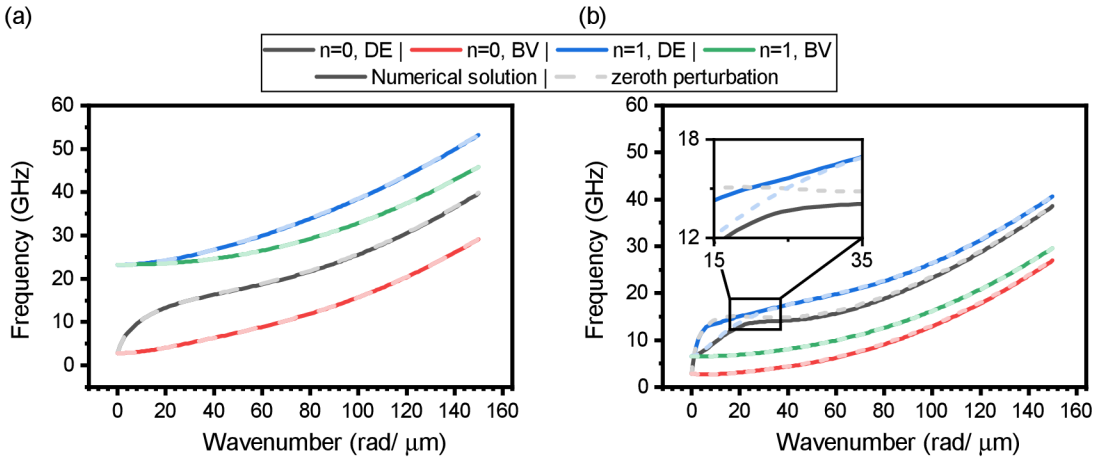

Figure 1.4: Dispersion relation calculated with zeroth perturbation approximation and numeric solving of eigenvalues. a, b, Dispersion relation for first two modes of 30 nm **(a)** and 100 nm **(b)** thick Permalloy layer. Faint dashed lines show zeroth perturbation approximation and solid lines show the numeric calculation.

hand, this is compensated by higher saturation magnetization. However, decay lengths are still comparatively shorter in permalloy than in nm-thick YIG. The integration of the Permalloy to the existing CMOS is technologically viable, as it can be easily grown on the silicon substrate. However, it is not optimal for telecommunication technologies, as higher damping causes lower quality factors. Due to its easiness of fabrication of micro/nano-structures and longevity of the produced samples, it is as well often used in research [43, 62, 72–75].

The third material is an alloy of cobalt, iron, and boron (CoFeB). This material is widely used in spintronic research and applications [76, 77], especially in magnetic tunnel junction structures. Due to this extensive use, the fabrication and deposition technologies are thoroughly researched. Thus any potential implementation of spin wave devices based on CoFeB would be prompt. Moreover, it has lower damping in comparison to Permalloy and higher saturation magnetization. However, in our laboratory experience, it is not as persistent as Permalloy layers, and thus Permalloy can provide advantages for the easiness of experimental work.

1.5.2. Spin-wave characteristics of Permalloy layer

In this section, I show the dispersion characteristics of the 30 nm-thick Permalloy (NiFe) layer, which is used in the majority of the presented result in Chapters 4,5, and 6. The NiFe layer with a thickness of 100 nm is shown for comparison. First, I show the dispersion characteristics, followed by a discussion of the spatial profiles of various spin-wave modes. At the end of this section, the spin wave Bloch function, which is essential in calculating BLS spectra of 30 nm-thick layer, is shown.

In Fig. 1.4a, b the dispersion relations of 30 nm and 100 nm thick permalloy layers are shown. For the case of 30 nm thick permalloy layer, the full analytical calculation, which uses zeroth perturbation theory (Eq. 1.35) is in full agreement with semi-analytical calculation (Eq. 1.38). On the other hand, in the case of 100 nm thick Permalloy layer, there is a significant deviation in the region, where the two modes get close to each other, see especially crossing around 20 $\frac{\text{rad}}{\mu m}$ in Fig. 1.4b. This is caused by the interaction between

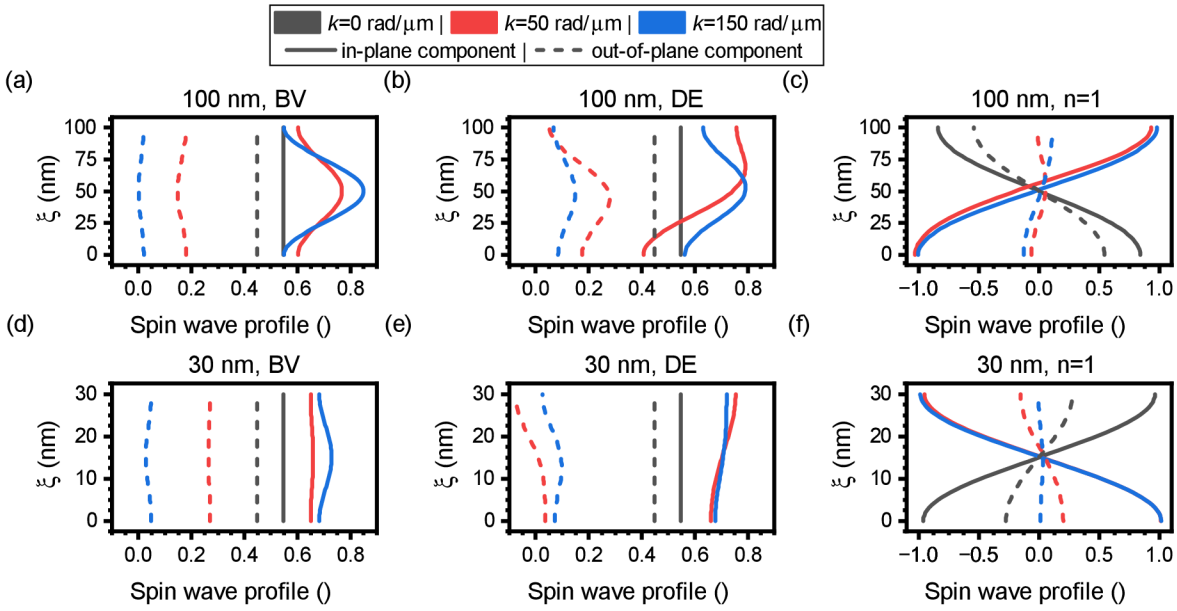

Figure 1.5: Spin wave profiles for in-plane magnetized thin film. a, b, c, d, e, f Spin-wave profiles of 100 nm (**a, b, c**) and 30 nm (**d, e, f**) thick Permalloy layer. The backward volume geometry is in panels (**a, d**), Damon-Eshbach in panels (**b, e**), and n=1 mode in Damon-Eshbach like geometry is in panels (**c, f**). Dashed curves represent out-of-plane components, while solid curves represent in-plane components. The k-vector is encoded to color, see legend. The external magnetic field was set to 10 mT.

the modes represented by off-diagonal elements in Eq. 1.34, which were omitted in the zeroth perturbation approach.

Spin wave profiles in Permalloy layer

We calculated the spin-wave profiles (Fig. 1.5) for three different modes: backward volume, Damon-Eshbach, and first perpendicular standing spin wave mode propagating perpendicularly to the static magnetization direction (n=1, Damon-Eshbach like). In the case of $k = 0$ the situation is straightforward: spin wave mode is always homogeneous across the thickness of the layer for $n = 0$ modes, see black curves in Fig. 1.5a,b,d,e. For the case of perpendicular standing spin wave mode ($n = 1$), cosine profile without any disturbances can be observed, see black curves in Fig. 1.5c, f.

If the wavenumber is increased the situation gets more complex. In BV geometry, the spin-wave in-plane amplitude is increased in the middle of the layer, see Fig. 1.5a,d. This behavior is more pronounced for the thicker layer. Interestingly, there is very weak opposite behavior for the out-of-plane component. In DE geometry, we can observe localization of the spin-wave in-plane amplitude to the upper boundary[8], see Fig. 1.5b,e. Again, for the out-of-plane component, the behavior is opposite. For very high wavenumber, the exchange energy dominates (which is isotropic), and the spin-wave profile resembles a very similar shape as in BV geometry, compare blue solid curve in Fig. 1.5a and Fig. 1.5b.

The ratio between the in-plane and out-of-plane components defines the ellipticity. One can observe that with $k = 0$, $n = 0$, the ellipticity is not significantly dependent on the layer thickness. In DE geometry, the ellipticity increases with increasing wavenumber

[8]The boundary on which spin wave is localized depends on the direction of the propagation.

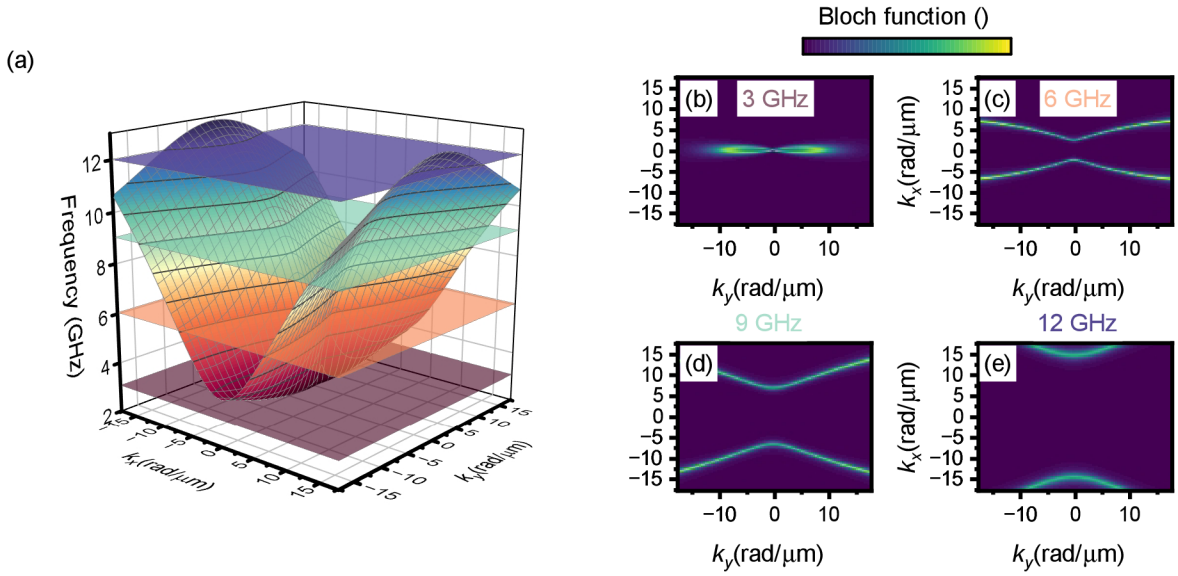

Figure 1.6: Full in-plane dispersion and Bloch functions of spin waves. **a** Spin wave dispersion relation for all propagation directions for in-plane magnetized 30 nm-thick Permalloy film. The transparent planes depicts the frequency positions of the calculated Bloch functions. **b, c, d, e,** Calculated Bloch functions for 3 GHz (**b**), 6 GHz (**c**), 9 GHz (**d**), and 12 GHz **(e)**. The external field was set to 10 mT and chemical potential −1 THz.

(see Fig. 1.5b,e); however, in BV geometry, the trend is weakly opposite. In the case of $k = 0$, $n = 1$ the ellipticity is increased with decreased layer thickness, see Fig. 1.5c,f.

Bloch function of spin waves in Permalloy layer

These examples only dealt with spin waves in two specific geometries (spin waves propagating parallel and perpendicular to the magnetization direction). However, the spin waves can propagate in all in-plane directions. In Fig. 1.6a, the dispersion relation for all directions in the in-plane magnetized Permalloy layer is shown. In Fig. 1.6b,c,d,e, Bloch functions are shown for selected frequencies. At 3 GHz (Fig. 1.6b), the resonance is only in the BV direction, i.e., on the cut through k_y, there is not any intensity. For higher frequencies (above ferromagnetic resonance frequency) the resonance for DE geometry appears, see Fig. 1.6c,d,e. With increasing frequency, one can observe that the linewidth in k_x,k_y space becomes wider. This is especially visible for the spin-wave modes with low wavenumber, see Fig. 1.6b,c,d.

2. Theory of inelastic light scattering

Inelastic scattering refers to the type of light scattering where the frequency of the scattered light differs from the frequency of the incident light, i.e. exhibits so-called frequency shift. It is a useful tool in condensed matter physics, as it can provide insight to the properties of the excitations of matter, such as magnons or phonons. The frequency, amplitude and phase of the scattered light can be analysed, and thus the otherwise inaccessible information about excitation of matter can be investigated. However, to correctly interpret measured data it is essential to fully understand the mechanism of scattering.

The chapter is structured in the following way. First, I introduce different types of inelastic scattering and their simplified description using a quantum-mechanical approach. However, this approach is unsuitable for obtaining quantitative values, especially in spatially non-homogeneous cases, such as focused light. For this purpose, I have developed a model based on continuum approximation (classical approach) [78] for a description of micro-focused Brillouin light scattering (BLS). The description of this model starts by showing its structure, and afterward, individual steps are discussed more closely. I use the developed theory to model micro-focused BLS spectra and show various dependencies. At the end of the chapter, I introduce a simple phenomenological model and compare it with developed theory and experimental data.

2.1. Types of inelastic scattering processes

In this section, I discuss different types of inelastic scattering. Here, for a simplified description, I use the quantum approach. In the case of this approach, the light is considered as a particle with momentum and energy. This allows me to find the frequency shift value solely based on the conservation laws of momentum and energy in the system of interacting particles and quasi-particles.

All the described processes of the inelastic light scattering are the same from the physical point of view. However, in the scope of this thesis, I divide them to three categories based on the absolute value of the frequency shift of the scattered light. The first process is called quasi-elastic scattering. This term is used for the process where frequency shifts of the scattered light do not exceed 1 GHz. Second process, Raman scattering, usually describes the process, where frequency shifts of the scattered light are above 500 GHz. The last process is called Brillouin scattering, and is integral for the presented thesis. Usually the term Brillouin scattering is used to describe the scattering processes in between the quasi-elastic and Raman scattering.

2.1.1. Quasi-elastic scattering

The quasi-elastic light scattering happens on either particles in solution, or particles of solid matter. First, we start with the equations of conservation of energy and momentum. Let's consider the energy of the incident photon and the kinetic energy of the particle on which the photon is scattered. By applying the conservation laws of momentum and energy, we can derive a set of equations that describe the relationship between the incident and scattered photon and particle (with given momentum and kinetic energy)

$$\hbar\omega_\mathrm{l} + \frac{1}{2}mv_\mathrm{p}^2 = \hbar\omega_\mathrm{l}' + \frac{1}{2}mv_\mathrm{p}'^2, \tag{2.1a}$$

$$\hbar\boldsymbol{k}_\mathrm{l} + m\boldsymbol{k}_\mathrm{p} = \hbar\boldsymbol{k}_\mathrm{l}' + m\boldsymbol{k}_\mathrm{p}', \tag{2.1b}$$

where $\hbar$ is the Planck constant, ω_l is the frequency of light, and m (v_p) is the mass (velocity) of the particle on which the light is scattered, $\boldsymbol{k}_\mathrm{l}$ is a wavevector of light. Typically, the kinetic energy of the particles is much lower than the energy of the incident light, so this interaction results in a small broadening (less than 500 MHz) of the spectral width of the scattered light. This type of scattering is known as quasi-elastic scattering. The total cross-section is proportional to [79]

$$\sigma_\mathrm{QES} \sim \frac{\gamma}{(\omega_i - \omega_s)^2 + \gamma^2}, \tag{2.2}$$

where ω_i is the incident frequency of light, ω_s is the frequency of scattered light, and γ is a broadening parameter that depends on e.g. thermal energy, entropy, heat capacity of the sample material. One can see that the highest scattering efficiency is reached when the scattered light has the same frequency as the incident light. This type of scattering is used for analysis of e.g. particle sizes in liquids [80, 81].

2.1.2. Raman scattering

This process usually involves scattering on intrinsic vibrational, rotational, or higher excited states of matter. There is no clear distinction between the Brillouin and Raman light scattering, but usually the scattering is called Raman, if the frequency shift is at least above 1 THz. This scattering is also ruled by the equations of conservation of energy and momentum of the whole system of all relevant particles. When the photon inelastically scatters on the excitation of matter, it is transferred to the state with the energy difference equal to the energy of that excitation. However, this assumes that scattering involves only one transition, there is no absorption (thus, all wavevectors are real), and the sample is infinite. The reality is usually much more complex and exact description of all involved energies and momenta is cumbersome. The cross-section for particular transition is proportional to [82, p. 379],

$$\sigma_\mathrm{R-aS} \sim \sum_{\omega_t} \frac{\omega_l(\omega_l + \omega_\mathrm{t})^3}{(\omega_l - \omega_\mathrm{s})^2 + \gamma_\mathrm{R}^2}, \tag{2.3a}$$

$$\sigma_\mathrm{R-S} \sim \sum_{\omega_t} \frac{\omega_l(\omega_l - \omega_\mathrm{t})^3}{(\omega_l - \omega_\mathrm{s})^2 + \gamma_\mathrm{R}^2}, \tag{2.3b}$$

where ω_t is the frequency of transition and γ_R^2 is damping parameter. The Raman resonances can occur for several frequencies, depending on the number of allowed transitions.

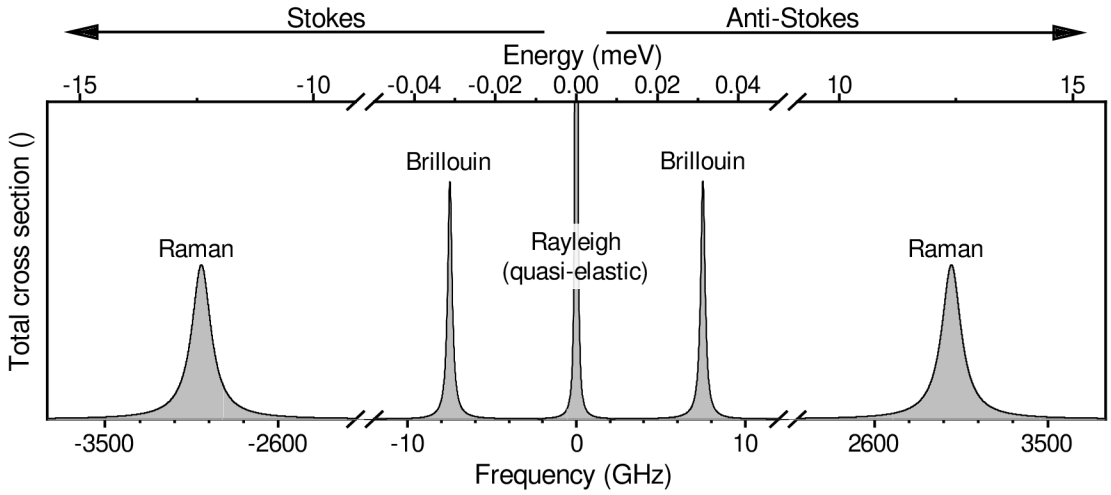

Figure 2.1: Schematical overview of the scattering processes.

Typically, the frequencies of transitions in Eq. 2.3 are in the terahertz range, as can be seen in Fig. 2.1.

Raman scattering is used to analyze substances, because transition frequencies are intrinsic properties of molecules. Also, the number of layers in graphene or binding parameters between layers could be determined [83]. The Raman scattering is also widely used in biology and pharmaceutical research for e.g. estimation of the molecular activity [84, 85].

2.1.3. Brillouin light scattering

Now, we consider the case where the photon is scattered on a quasi-particle, e.g., a phonon or a magnon. This scattering happens in a frequency range between hundreds of megahertz to hundreds of gigahertz. A schematic of a typical Brillouin light scattering (BLS) spectrum is shown in Figure 2.1. In this case, we get a set of energy and momentum conservation equations

$$\hbar\omega_{\mathrm{l}} + \hbar\omega_{\mathrm{qp}} = \hbar\omega'_{\mathrm{l}} + \hbar\omega'_{\mathrm{qp}}, \tag{2.4a}$$

$$\hbar\boldsymbol{k}_{\mathrm{l}} + \hbar\boldsymbol{k}_{\mathrm{qp}} = \hbar\boldsymbol{k}'_{\mathrm{l}} + \hbar\boldsymbol{k}'_{\mathrm{qp}}, \tag{2.4b}$$

where $\hbar$ is the Planck constant, ω_{l} is the frequency of light and ω_{qp} is the frequency of the quasi-particle. To conserve both the energy and the momentum, two main processes are present. In the first one, the quasi-particle's final energy is zero (the quasi-particle is annihilated). Subsequently, the scattered light's energy is increased, resulting in a shift towards a higher frequency. This is called the Anti-Stokes process, and it is schematically shown in Fig. 2.3a. In the second case, the initial energy and momentum of the quasi-particle are equal to zero, then the energy and the momentum of the incident light are transformed to the quasi-particle. Thus, the frequency of the scattered light is lower. This is called the Stokes process, and it is shown in Fig. 2.3b. Both processes can generally include more quasi-particles or photons, such as scattering on two or three magnons, but these processes become important only if the process between three particles is prohibited [86].

Two main experimental approaches to measure BLS spectra are being used: k-resolved BLS (also called conventional) and μ-BLS (micro-focused BLS). Both of them are depicted

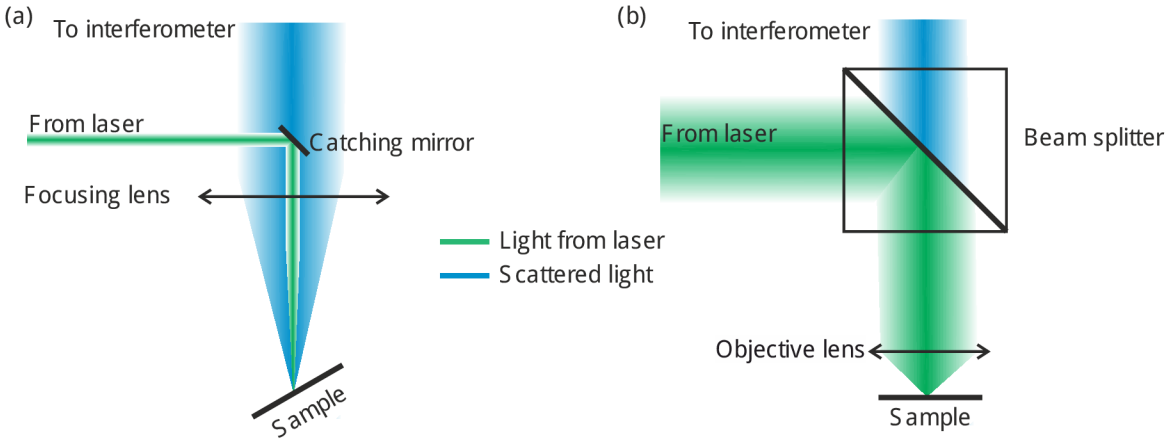

Figure 2.2: Experimental realization of the BLS. **a,** Schematics of the k-resolved BLS where the sample is tilted in respect to the incident light. **b,** Schematics of the μ-BLS with objective lens with high numerical aperture.

in Fig. 2.2a, b. The main difference between the two approaches is the numeric aperture of the lens. In k-resolved BLS it is beneficial to use the focusing lens with small numeric aperture in order to achieve good wavevector resolution[1]. On the other hand, in μ-BLS the spatial resolution is usually of the main interest, thus the objective lens with high numeric aperture is usually used. Due to this difference, the spatial resolution in k-resolved BLS is limited to spot sizes in order of tens of microns, and there is no wavevector resolution in μ-BLS of thermally excited spin waves.

Typically, in the k-resolved BLS the back-scattering geometry is used in experiments, as shown in Figure 2.3c. In the thin film, the probed quasi-particle wavenumber is then equal to twice the in-plane component of the wavenumber[2] of the incident light. The limit of maximum probed k-vector versus angle of incidence using 532 nm laser is shown in Figure 2.3d. The maximum value of wavenumber is reached in the case where the laser beam is parallel with the surface of the sample and is $23.6\,\mathrm{rad}\cdot\mu\mathrm{m}^{-1}$, which is equal to the wavelength of 266 nm.

Due to the typically low frequencies of the quasi-particles involved in BLS (see Fig. 2.1), the shift of the magnitude of free-space momentum (given by $\Delta\omega_\mathrm{l} = c\Delta k_\mathrm{l}$) between the incident and scattered light is negligible, and conservation of momentum is satisfied by only slight changes in the angle of the scattered light.

2.2. Classical description of μ-BLS

In this section, I present my own model developed for the calculation of the μ-BLS spectra. During the development of this theory, I was helped by Martin Hrtoň, who introduced me to Green function formalism. The structure is as follows. First, I show the general design of the model. Then, the semi-analytic theory for calculating the electric field focused by a thin lens is introduced. I discuss the consequences of various parameters on the electric field distribution. Next, I elaborate on the mechanism of inducing polarization and show an example calculated for the NiFe layer. Afterward, the far-field transition is discussed

[1] On the contrary, the lower numeric aperture means lower signal strength, thus typically some sweet spot is targeted during designing the experimental setup.

[2] I.e. projection of the light to the sample plane.

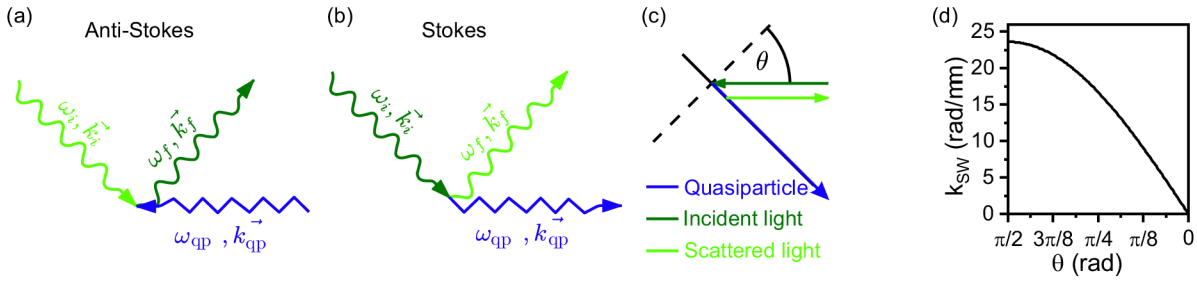

Figure 2.3: The Stokes (a) and anti-Stokes (b) processes are schematically shown. (c) The schematic of back-scattering geometry. (d) Detectable spin-wave wavenumber depending on the angle of incidence of light with a wavelength of 532 nm.

and demonstrated on the dipole radiation. Finally, I use this theory to show the influence of various parameters on the calculated spectra.

Although the quantum approach can give some general insight into the inelastic light scattering, the classical approach is far more convenient to get quantitative values of the acquired signal. This is especially true for the μ-BLS, where the quantum mechanical model would be cumbersome. In this section the model is built with μ-BLS in mind, however it can also be used to calculate k-resolved spectra just by decreasing the numeric aperture of the focusing lens [86–89]. Inelastic scattering can originate from all kinds of excitation, but here we solely focus on inelastic scattering on spin waves. In order to cover e.g. light scattering on phonons, the coupling mechanism between the excitation and light has to be adjusted (i.e. adjust the calculation of the time-dependent susceptibility tensor).

This section presents only the case of simple magnetic film with linearly excited spin waves, however current research usually investigates much more complicated situations. Fortunately, using numerical simulations of Maxwell equations, the model can be extended to include spatial perturbation such as optical resonators to, e.g., extend the range of measurable wavevectors or measure only specific wavevectors. In the same manner, the model can be easily extended also by using micromagnetic simulation, to obtain the BLS intensities from the magnetic structures, which cannot be modelled analytically, such as complicated 3D structures (e.g. helix, disk with hollow center), nonlinear phenomena (e.g. parametric pumping, three-magnon scattering), or non-homogeneous landscapes (e.g. heated magnetic layer by laser spot, corrugated waveguides).

2.2.1. Structure of the model

To model the μ-BLS spectra we use the approach of Landau and Lifshitz presented in [78, p. 413] applied to micro-focused light. First, the structure of the presented model is discussed, and later in this section, each step is carefully described. The model can be divided to four steps, as is shown in Fig. 2.4.

Obtaining the electric field distribution in the magnetic layer

The first step is to compute electric field in the sample ($\boldsymbol{E}_\mathrm{d}$). Usually, this is easier to perform in real space coordinates. However, for the subsequent calculation it is far more convenient to transform it into the Fourier space

$$\boldsymbol{E}_\mathrm{d}(\omega_l,\boldsymbol{k}') = \mathcal{F}\left(\boldsymbol{E}_\mathrm{d}(\omega_l,\boldsymbol{r}')\right). \tag{2.5}$$

The electric field shape is dependent on e.g. the used objective lens (especially on its numeric aperture), used light wavelength, or defocus of the light. Futhermore, the sub-

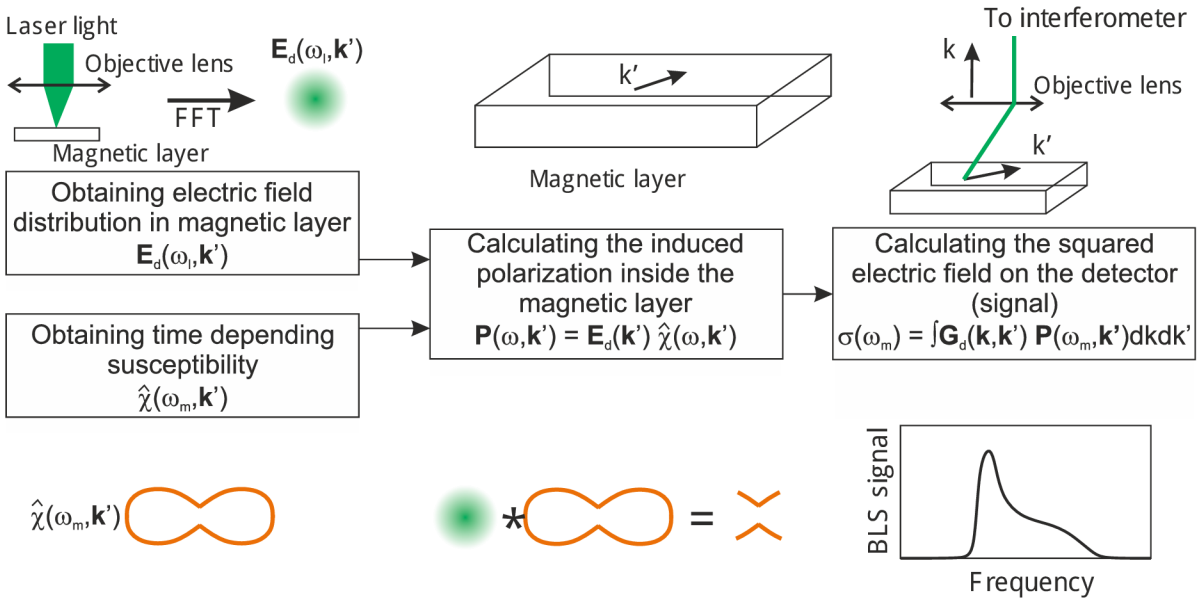

Figure 2.4: Schematics of the structure of the calculation of BLS signal within classical approach. The k' represents the wavevectors in plane of a magnetic layer, while k represents the wavevectors of scattered free light. The schematics provides simplified view and is not completelly correct. For more detailed discussion please follow explanation given in the text.

strate, magnetic layer material or some capping layers (e.g. antireflecting coating) can modify the electric field distribution, however in the presented approach we neglect these contributions. If needed, full Maxwell simulation can account for these effects.

Obtaining the time-dependent susceptibility

The time-dependent susceptibility ($\hat{\chi}$) is integral part of the model for calculating BLS spectra. This quantity represents the mechanism of interaction between the light and excitation of matter. In the specific case of the interaction between the spin waves and light, this interaction is called magneto-optical coupling. To calculate the time-dependent susceptibility, one has to know the magnetization distribution dependent on the wavevector and frequency of the spin waves

$$\hat{\chi} \propto \boldsymbol{M}(\omega_{\mathrm{m}},\boldsymbol{k}'). \tag{2.6}$$

Calculation of the polarization

The driving field and time-dependent susceptibility are used to calculate induced polarization in the magnetic layer by their convolution

$$\boldsymbol{P}(\omega,\boldsymbol{k}) = \boldsymbol{E}_{\mathrm{d}}(\omega,\boldsymbol{k}) * \hat{\chi}(\omega,\boldsymbol{k}). \tag{2.7}$$

Generally, the polarization with wavevectors double of the incident driving field can be induced[3]. However, the possible states of the polarization in the k-space are still limited by the eigenstates of the spin waves, i.e. can occur only at the positions of the spin-wave resonance.

Transition to the far field and calculation of the BLS signal

Now, the polarization has to be propagated to the far field. In order to do that, we use Green function formalism[4]. In the studied case, the polarization source can be regarded

[3] See the convolution in Eq. 2.7.

[4] In simple words, Green function represents the impulse response to the point source.

as a sum of the dipoles (point sources); thus, by integrating over them, the overall electric field can be obtained. This can be expressed as

$$\mathbf{E}_{\mathrm{FF}}(\omega,\mathbf{k}_{\mathrm{p}}) = \hat{\mathbf{G}}(\omega,\mathbf{k}_{\mathrm{p}},\mathbf{k}'_{\mathrm{p}})\mathbf{P}(\omega,\mathbf{k}'_{\mathrm{p}}). \tag{2.8}$$

However, this equation describes all emission of all wavevectors, including those which are not able to reach the detector. For this reason, subsequent trimming of the electric field has to be done, such as trim by numeric aperture of the objective lens, or assuming only wavevectors parallel to the optical axis after passing through the objective lens.

To get the resulting BLS signal, one has to square the electric field. The obtained quantity can then be fitted or compared to the acquired BLS signal.

2.2.2. Semi-analytic modeling of the driving field

In this section, I use the semi-analytical method developed by Richards and Wolf [90, 91] to obtain electric field on the surface. I follow the notation given by Novotny and Hecht in [92]. The geometry of the calculation is depicted in Fig. 2.5. The collimated beam is clipped by the back aperture of the objective lens and is focused on the sample. For convenience, the spherical coordinate system is used after the objective lens is used. This calculation is based on the two basic principles:

- **Sine condition** - each ray that converges to the focus intersects its conjugate ray (ray in the collimated beam) in the position of the lens.
- **Intensity law** - the energy flux along each ray needs to stay constant.

The electric field $\boldsymbol{E}(\varrho,\varphi,z)$ can be expressed as

$$\boldsymbol{E}(\varrho,\varphi,z) = \frac{\mathrm{i}k_0 f \exp(\mathrm{i}k_0 f)}{2\pi} \int_0^{\Theta_{\max}} \int_0^{2\pi} \boldsymbol{E}_\infty(\Theta,\Phi) \exp \mathrm{i}k_0 z \cos\Theta \exp \mathrm{i}k_0 \varrho \sin\Theta \cos(\Phi-\varphi) \mathrm{d}\Phi\Theta, \tag{2.9}$$

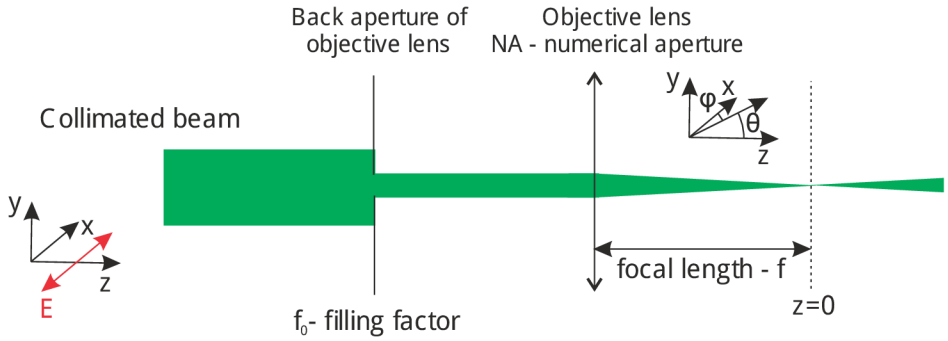

Figure 2.5: Schematics of the calculation geometry for focal fields. In the region of the collimated beam, we use cartesian coordinates as depicted in the sketch. The filling factor is the ratio between the beam waist and back aperture (entrance pupil) of an objective lens. The beam profile in Cartesian coordinates can be calculated in arbitrary z-plane.

where the electric field in far-field $\boldsymbol{E}_\infty(\Theta,\Phi)$ reads

$$\boldsymbol{E}_\infty(\Theta,\Phi) = \boldsymbol{E}_{\mathrm{inc},x}(\Theta,\Phi)\frac{1}{2}\begin{pmatrix} 1+\cos\Theta-(1-\cos\Theta)\cos 2\Phi \\ -(1-\cos\Theta)\sin 2\Phi \\ -2\cos\Phi\sin\Theta \end{pmatrix}\frac{n_1}{n_2}(\cos\Theta)^{1/2}, \tag{2.10}$$

k_0 is the wavelength of the free-space light, f is the effective focal length of the objective lens[5], and $\boldsymbol{E}_{\mathrm{inc},x}(\Theta,\Phi)$ is the field incident on the objective lens, which we assume to be the lowest Hermite-Gaussian mode

$$\boldsymbol{E}_{\mathrm{inc},x}(\Theta,\Phi) = E_0 f_w(\Theta), \tag{2.11a}$$

$$f_w(\Theta) = \exp\left(\frac{-1}{f_0^2}\frac{\sin^2\Theta}{\sin^2\Theta_{\max}}\right), \tag{2.11b}$$

where f_0 is a filling factor of the lens and is given by the ratio between the waist of the beam and the back aperture of the objective lens, and E_0 is the amplitude of the light. Integration through the angle Φ can be carried out by analytic means using the following relations

$$\int_0^{2\pi}\cos n\Phi\exp\left(\mathrm{i}x\cos\left(\Phi-\varphi\right)\right)\mathrm{d}\Phi = 2\pi\left(\mathrm{i}^n\right)J_n(x)\cos n\varphi, \tag{2.12a}$$

$$\int_0^{2\pi}\sin n\Phi\exp\left(\mathrm{i}x\cos\left(\Phi-\varphi\right)\right)\mathrm{d}\Phi = 2\pi\left(\mathrm{i}^n\right)J_n(x)\sin n\varphi, \tag{2.12b}$$

where $J_n(x)$ is the *Bessel* function of the nth-order. The focal field can now be expressed in cylindrical coordinates as

$$\boldsymbol{E}(\varrho,\varphi,z) = \frac{\mathrm{i}k_0 f^2}{2}\sqrt{\frac{n_1}{n_2}}E_0\exp\left(-\mathrm{i}kf\right)\begin{pmatrix} \mathrm{I}_{00}+\mathrm{I}_{02}\cos 2\varphi \\ \mathrm{I}_{02}\sin 2\varphi \\ -2\mathrm{i}I_{01}\cos\varphi \end{pmatrix}, \tag{2.13}$$

where

$$\mathrm{I}_{00} = \int_0^{\Theta_{\max}} f_w(\Theta)\left(\cos\Theta\right)^{1/2}\sin\Theta\left(1+\cos\Theta\right)J_0\left(k\varrho\sin\Theta\right)\exp\left(\mathrm{i}k_0 z\cos\Theta\right)\mathrm{d}\Theta, \tag{2.14a}$$

$$\mathrm{I}_{01} = \int_0^{\Theta_{\max}} f_w(\Theta)\left(\cos\Theta\right)^{1/2}\sin^2\Theta J_1\left(k\varrho\sin\Theta\right)\exp\left(\mathrm{i}k_0 z\cos\Theta\right)\mathrm{d}\Theta, \tag{2.14b}$$

$$\mathrm{I}_{02} = \int_0^{\Theta_{\max}} f_w(\Theta)\left(\cos\Theta\right)^{1/2}\sin\Theta\left(1-\cos\Theta\right)J_2\left(k\varrho\sin\Theta\right)\exp\left(\mathrm{i}k_0 z\cos\Theta\right)\mathrm{d}\Theta. \tag{2.14c}$$

These integrations have to be carried out numerically[6].

The magnitude of the x-component (Fig. 2.6a) have full polar symmetry, while the y-component (Fig. 2.6b), and z-component (Fig. 2.6c) resembles four-fold and two-fold

[5]The focal length only affects the phase factors in the field.

[6]In our code, we used *Trapezoidal numerical integration* implemented in Matlab 2021a [93]

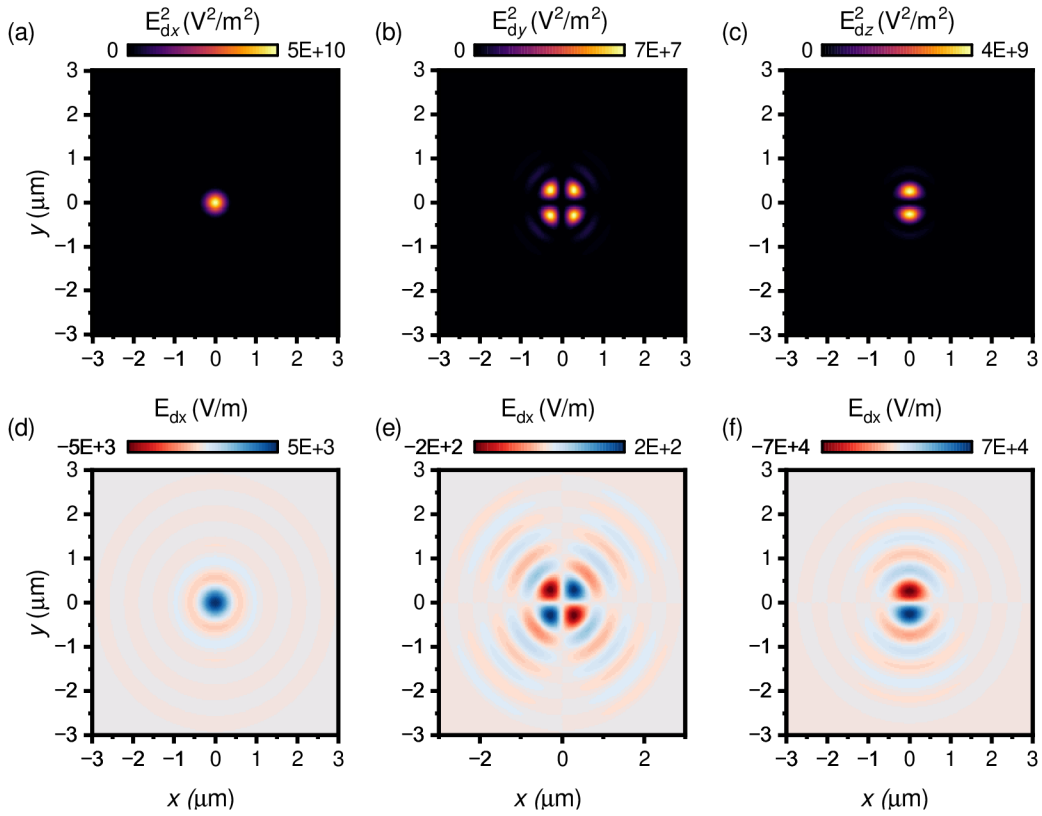

Figure 2.6: Semi-analytically calculated magnitude and real part of the focal field of Gaussian beam. a,b,c The squared x- **(a)** y- **(b)** and z- **(c)** component of the focal field of 00 Hermite-Gaussian mode. **d, e, g** The real part of x- **(d)** y- **(e)** and z- **(f)** component of the focal field of 00 Hermite-Gaussian mode.

symmetries, respectively. The magnitude of the x-component is the largest. The maximum value of the squared field in the z-component is ≈ 12.5 and the y-component is ≈ 715 smaller than the x-component. Thus, the x-component (along the polarization axis) is the most important for the calculation of the BLS signal in most scenarios. However, in specific geometries (e.g. for out-of-plane magnetized thin film) its contribution can cancel out and other components can become significant. From the images of the real parts of the electric field vector (Fig. 2.6d, e, f), one can see phase differences between the parts of the intensity distribution. This implies, that the non-zero net intensity is present only in the x-component. In the other two components (y and z), the regions of high intensity have exactly opposite phases and cancel each other out. This can possibly further decrease obtained signal in specific scenarios.

After the Fourier transformation to reciprocal space these results can be used in calculation using Eq. 2.21. In the calculation, we neglect the effect of the substrate on the beam shape, i.e., the reflection and refraction on a possible multilayer stack. However, in the studied cases this approximation leads to the qualitatively same results as the full simulation of the Maxwell equations (without any approximation). The semi-analytical formulation for the driving fields, including the effects of the boundaries, can be achieved by using *transfer-matrix method* and following the approach given in section 3.9 in [92].

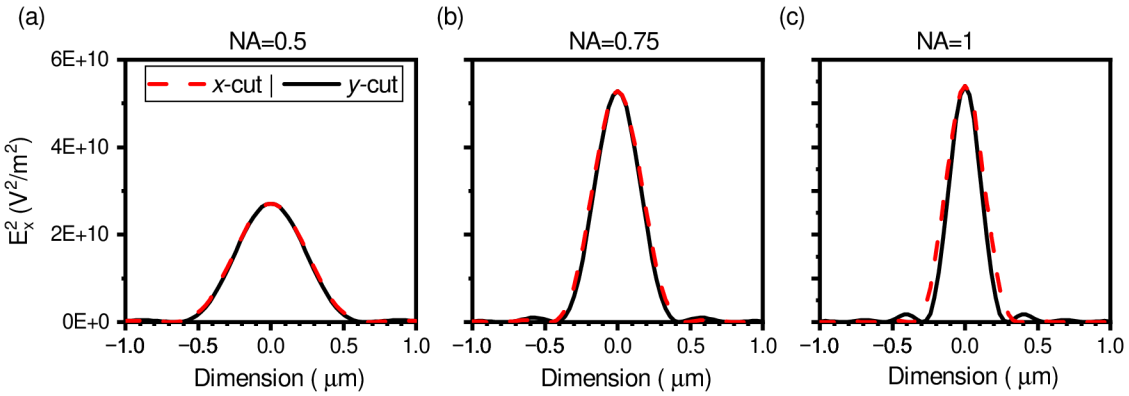

Figure 2.7: Effect of the polarization axis on the beam waist. a,b,c The cut through squared x-component of the electric field in the x- and y-direction for objective lens with numeric aperture NA=0.5 **(a)**, NA=0.75 **(b)**, and NA=1 **(c)**. The red dashed line shows the cut along the linear polarization direction, and the black solid line shows the cut perpendicular to the linear polarization direction.

Effect of the polarization

The polarization effects affect the shape of the beam even in the component along the polarization axis (x-component in our geometry). The beam spot is slightly enlarged in the direction of the polarization and thus it is not circular but elliptical. This effect becomes more pronounced when the beam dimensions reach the diffraction-limited sizes. For the objective lens with NA= 0.5 there is no difference in beam shape for both perpendicular directions, see Fig. 2.7a. The waist of the spot is 464 ± 1 nm. The increase of the numeric aperture to NA= 0.75 causes the shrinking of the beam spot to 295 ± 1 nm in y-direction, and the difference is now clearly visible and is 20 ± 2 nm, see Fig. 2.7b. The highest possible numerical aperture with non-immersion objective lens NA= 1 gives the beam spot waist of 204 ± 1 nm in the y-direction. The difference between the two orthogonal cuts now becomes 44 ± 2 nm, see Fig. 2.7c.

Another effect that becomes more pronounced with the tighter focus of the beam, here achieved by increase in numeric aperture, is the formation of the side peaks, so-called *Airy disc* [94]. In the case of the objective lens with NA= 0.5 (Fig. 2.7a), we can observe only Gaussian distribution in both cross sections. As the numerical aperture increases, the formation of the side peaks becomes apparent, see Figs. 2.7b, c. Interestingly, these peaks occur only in the direction perpendicular to the incident polarization.

Effect of the defocus

We have so far calculated only the fields directly in the focus ($z = 0$, see Fig. 2.5). However, in the experiment, the z-direction can be changed by the out-of-plane movement of the sample stage. This movement can be done on purpose (to enlarge the measurement spot) or, more commonly, unintentionally by thermal fluctuations or vibrations. The calculated beam shapes in dependence on the z-direction (defocus) are shown in Fig. 2.8. The summed magnitude of electric field along the polarization axis (x-axis) is shown in Fig. 2.8a, b, c. The region of z-coordinate, where the waist width is relatively constant, is called the *depth of focus*. For our set of parameters, this region has depth of roughly 500 nm. In the case of x-component, we can observe focusing to only a single beam spot, while for the case of y- and z- component, we observe two maxima, which is in agreement with

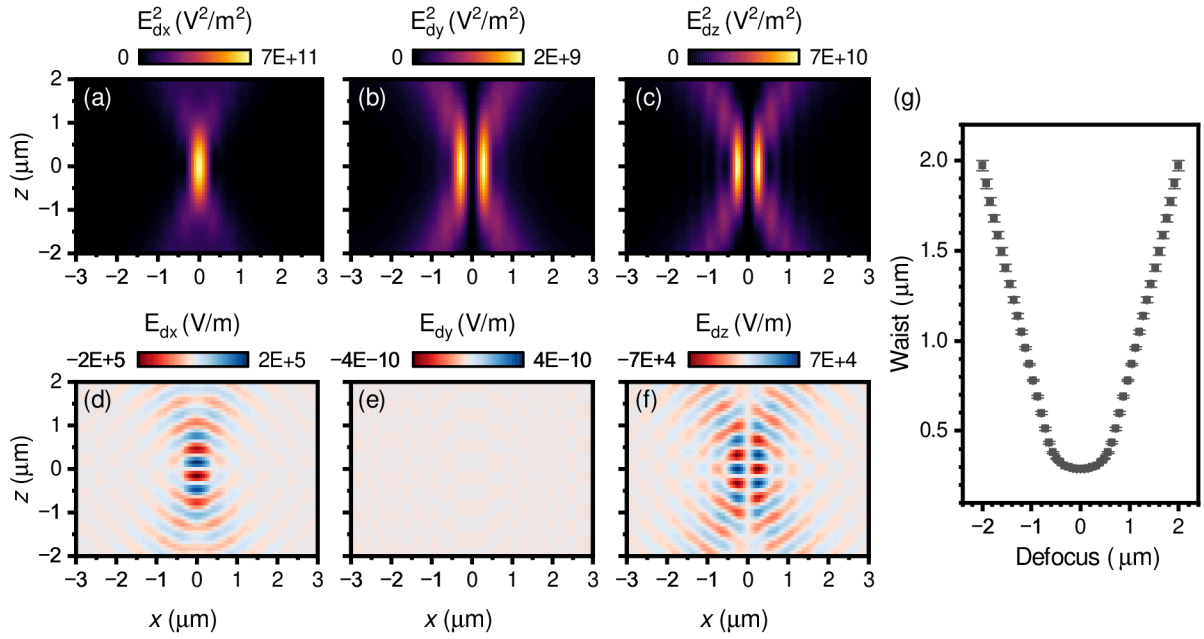

Figure 2.8: Effect of the defocus on the beam spot shape. a,b,c The integrated squared x- **(a)**, y- **(b)**, z- **(c)** component of the electric field in xz plane. The integration is done along the y-direction. **d, e, f** Real part of the cut in $y = 0$ of x- **(d)**, y- **(e)**, z- **(f)** component of the electric field. **g** The fitted waist of the squared x-component of the electric field in $y = 0$ cut for different values of z (defocus).

Fig. 2.6. In the cross-section of real parts of the electric field along direction perpendicular to polarization ($x = 0$) (Fig. 2.8d, e, f), phase evolution in z-direction can be observed. In the cross-section of the y-component, there is no intensity, as there is no electric field in the central plane (see Fig. 2.6e).

To get more insights into the behavior of the beam shape, we fitted the Gaussian function to squared x-component of the electric field in $y = 0$ cut for different values of z. The result is plotted in Fig 2.8g. Near the $z = 0$, we can observe relatively constant width of the waist, so-called *depth of focus*. For our parameters, this is $\approx 500\,\text{nm}$ wide, i.e., if the sample is moved by 250 nm in either out-of-plane direction from the ideal position, there will not be any significant change in the beam spot shape. The dependence of the beam spot width becomes quickly linear once it is out of *depth of focus*, see Fig. 2.8g. The increase in the width of the beam spot with the defocused distance is 1.126 ± 0.002 in linear regime. This means that if the beam is focused 1 μm above the focus on the surface of the studied film, its width is increased by $\approx 1\,\mu\text{m}$.

Effect of the filling factor

Another important parameter for beam waist is the filling factor of the objective lens. Contrary to the naive view[7], if the incident beam to the back aperture of the objective lens (see Fig. 2.5) is narrower, the resulting beam waist will be broader. In Fig. 2.9a dependence of the magnitude of the y-cut from x-component of the driving field on the filling factor is shown. We can observe, that with small filling factors (narrow beam incidence to

[7]By naive view we mean expectation that resulting beam would be narrower, if the incident beam to the objective lens is narrower as well.

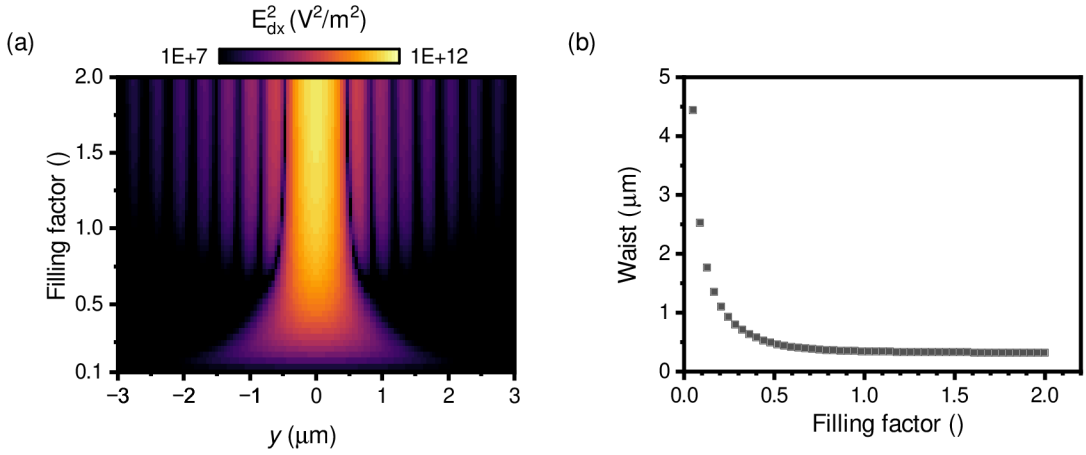

Figure 2.9: Effect of the filling factor on the beam shape and waist. **a** Magnitude of the y-cut of x-component of the electric field in dependence on filling factor. **b** Extracted beam waist.

the back aperture of the objective lens), the beam spot is very wide (above 2 μm). With the increasing filling factor, the Gaussian beam becomes narrower. This comes at the cost of losing the total incidence power, but this is not captured by the semi-analytical modeling. When the filling factor reaches values above 0.7, we can observe the formation of the *Airy disc* [94].

The extracted beam waists are shown in Fig. 2.9b. For the lowest calculated filling factor value ($f_0 = 0.05$), the beam waist is 4.4376 ± 0.0002 μm. When the filling factor is $f_0 = 2$, the waist is 0.3159 ± 0.0009 μm, which is 10 % broader than the waist with infinite filling factor, i.e. 0.287 ± 0.001 μm.

Focusing of higher-order laser modes

The previously developed theory allows us to consider also focusing of spatially more complicated laser modes. The radially and azimuthally polarized doughnut modes get a lot of attention, as they can provide, e.g., tighter focuses or beams with orbital angular momentum for application in light tweezers [95, 96]. We focus here on the so-called Laguerre-Gaussian modes, namely on the radially and azimuthally polarized doughnut modes.

The radially and azimuthally polarized doughnut mode can be generated by, e.g., laser cavity with conical mirrors [97–99], or by interferometric techniques [100, 101]. However, the most common technique nowadays is the use of so-called *vortex plates* [102, 103]. Then, one can freely switch between radially and azimuthally polarized doughnut modes just by rotating the vortex plate. The intensity in the center is equal to zero, and there is cylindrical symmetry. The polarization bivector always points to/out of the center for the radially polarized doughnut mode and is axially symmetrical for the azimuthally polarized doughnut mode.

The electric field can be obtained in from of superposition of the Hermite-Gaussian fields as

$$\boldsymbol{E}(\varrho,\varphi,z) = \frac{\mathrm{i}k_0 f^2}{2}\sqrt{\frac{n_1}{n_2}}E_0 \exp\left(-\mathrm{i}kf\right)\begin{pmatrix} \mathrm{i}I_{\mathrm{rad}}\cos\varphi \\ \mathrm{i}I_{\mathrm{rad}}\sin\varphi \\ -4\mathrm{i}I_{10} \end{pmatrix}, \tag{2.15}$$

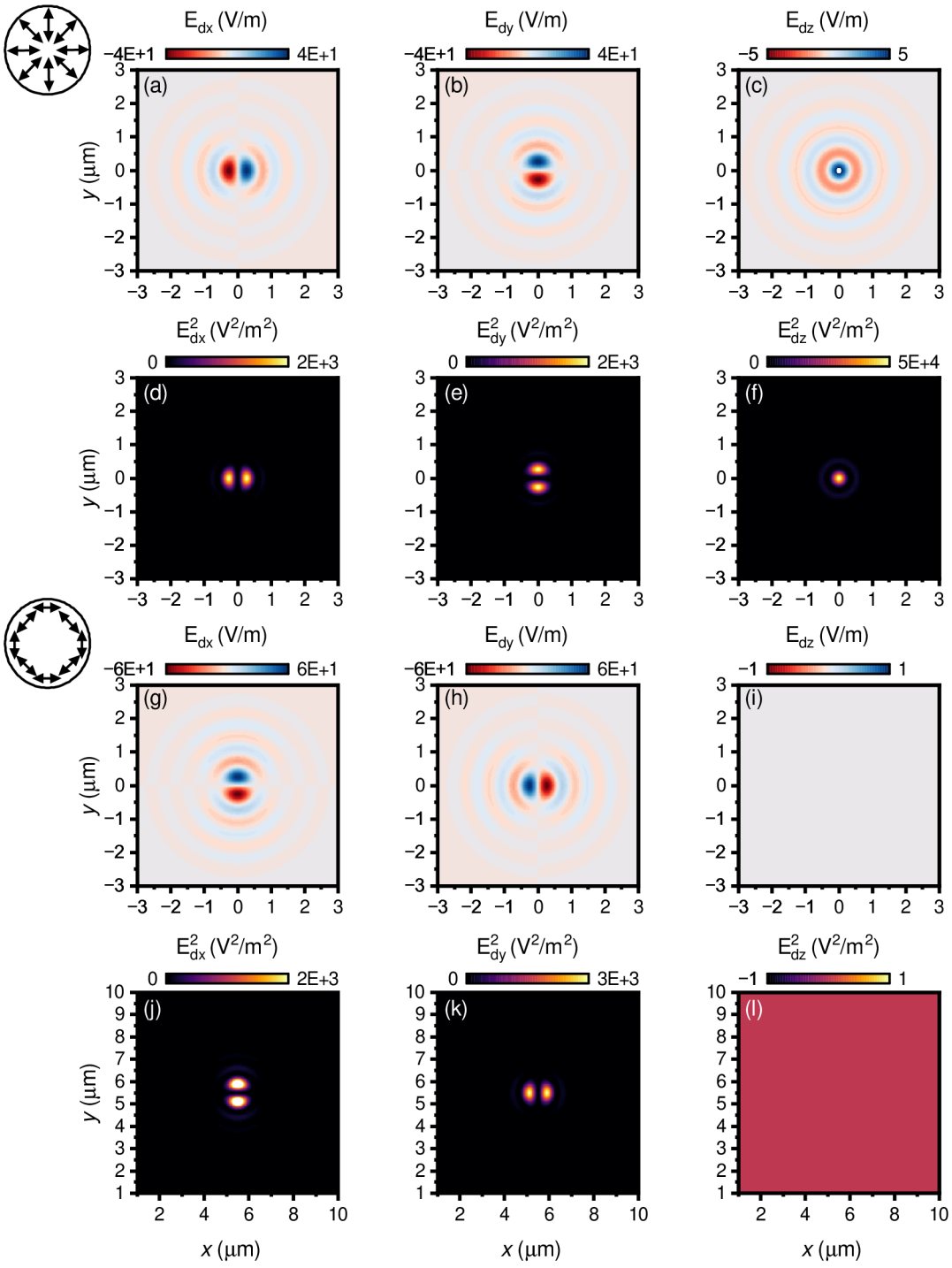

Figure 2.10: Focusing of the higher order laser modes. a, b, c The x- **(a)**, y- **(b)**, z- **(c)**, of the real part of the focal electric field of radially polarized doughnut mode. **d, e, f** The x- **(d)**, y- **(e)**, z- **(f)**, of the squared focal electric field of radially polarized doughnut mode. **g, h, i** The x- **(g)**, y- **(h)**, z- **(i)**, of the real part of the focal electric field of azimuthally polarized doughnut mode. **j, k, l** The x- **(j)**, y- **(k)**, z- **(l)**, of the squared focal electric field of radially polarized doughnut mode. The sketches of the incident field on the objective lens are depicted on the left side for both modes.

where

$$\mathrm{I_{rad}} = \int_0^{\Theta_{\max}} f_w(\Theta)\,(\cos\Theta)^{3/2}\sin^2\Theta J_1\left(k\varrho\sin\Theta\right)\exp\left(\mathrm{i}k_0 z\cos\Theta\right)\mathrm{d}\Theta, \tag{2.16a}$$

$$\mathrm{I_{10}} = \int_0^{\Theta_{\max}} f_w(\Theta)\,(\cos\Theta)^{1/2}\sin^2\Theta J_1\left(k\varrho\sin\Theta\right)\exp\left(\mathrm{i}k_0 z\cos\Theta\right)\mathrm{d}\Theta. \tag{2.16b}$$

The electric field for azimuthally polarized doughnut mode can be expressed as

$$\boldsymbol{E}(\varrho,\varphi,z) = \frac{\mathrm{i}k_0 f^2}{2}\sqrt{\frac{n_1}{n_2}}E_0\exp\left(-\mathrm{i}kf\right)\begin{pmatrix}\mathrm{iI_{azm}}\sin\varphi\\ -\mathrm{iI_{azm}}\cos\varphi\\ 0\end{pmatrix}, \tag{2.17}$$

where

$$\mathrm{I_{azm}} = \int_0^{\Theta_{\max}} f_w(\Theta)\,(\cos\Theta)^{1/2}\sin^2\Theta J_1\left(k\varrho\sin\Theta\right)\exp\left(\mathrm{i}k_0 z\cos\Theta\right)\mathrm{d}\Theta. \tag{2.18}$$

In Fig. 2.10, we can see the results of Eq. 2.15. In Figs. 2.10a-f are results for radially polarized doughnut mode. In this case, the majority of the intensity is in the out-of-plane direction, compare Figs. 2.10d-f. The intensity in the in-plane direction is completely symmetrical, see Figs. 2.10a, b, d, e around one symmetry axis. The out-of-plane intensity has rotational symmetry and a Gaussian shape.

Figs. 2.10a-f show the results for azimuthally polarized doughnut mode. In this case, all intensity is concentrated in-plane, see Figs. 2.10f-l. The symmetry in the in-plane direction is reversed with respect to radially polarized mode, compare Figs. 2.10a, b and 2.10g, h. For the radially polarized doughnut mode, there is no out-of-plane magnetic field, while for the azimuthally polarized mode, the majority of the magnetic field intensity is in the out-of-plane direction, which is opposite behavior to the electric field. This can be used in designing experiments where there is need for specific electric of magnetic component. For more detailed discussion, see [92].

2.2.3. Induced polarization

In the continuum model, the inelastic scattering (shift of the frequency of the scattered light) is caused by the time-dependent susceptibility. This mechanism can be, e.g., acusto-optic (photoelastic effect), electro-optic (Pockels and Kerr effect), or in the case of spin waves magneto-optical coupling [104, 105]. This mechanism is usually described by two contributions: the so-called Voigt effect, which is linear in magnetization, and the Cotton-Mouton effect, which is quadratic in magnetization. The susceptibility induced by the magneto-optical coupling ($\hat{\boldsymbol{\chi}}_{\mathrm{MO}}$) can be written as

$$\hat{\boldsymbol{\chi}}_{\mathrm{MO}} = \left(\begin{pmatrix}0 & iM_zQ & -iM_yQ\\ -iM_zQ & 0 & iM_xQ\\ iM_yQ & -iM_xQ & 0\end{pmatrix} + \begin{pmatrix}B_1M_x^2 & B_2M_xM_y & B_2M_xM_z\\ B_2M_xM_y & B_1M_y^2 & B_2M_yM_z\\ B_2M_xM_z & B_2M_yM_z & B_1M_z^2\end{pmatrix}\right), \tag{2.19}$$

where M_x,M_y,M_z denote the magnetization vector components, B_1,B_2 are Cotton-Mouton magneto-optical constants, and Q is Voigt magneto-optical constant.

In this model, the incident electric field $\boldsymbol{E}_\mathrm{d}$ probes the dynamic modulation of the susceptibility via magneto-optical coupling, which gives the polarization inside the magnetic material in the form [86, 87, 106]

$$\boldsymbol{P}(t,\boldsymbol{r}) = \boldsymbol{E}_\mathrm{d}(t,\boldsymbol{r})\hat{\boldsymbol{\chi}}(t,\boldsymbol{r}), \tag{2.20}$$

where $\hat{\boldsymbol{\chi}} = \hat{\boldsymbol{\chi}}_\mathrm{mat} + \hat{\boldsymbol{\chi}}_\mathrm{SW}(t,\boldsymbol{r})$ is a sum of the static material susceptibility $\hat{\boldsymbol{\chi}}_\mathrm{mat}$ and of the additional dynamic contribution caused by spin waves $\hat{\boldsymbol{\chi}}_\mathrm{SW}(t,\boldsymbol{r})$. It should be stressed out that the modulations in the susceptibility caused by magnons are on a vastly different time scale than the optical cycle of the probing photons. Thus, from the light's point of view the situation is somehow similar to the scattering on a static grating. As a consequence, there is a mixing of the frequencies both in temporal and spatial domains, namely

$$\boldsymbol{P}(\omega,\boldsymbol{k}_\mathbf{p},z) = \hat{\boldsymbol{\chi}}(\omega_\mathrm{m},\boldsymbol{k}_\mathrm{m},z)\boldsymbol{E}_\mathrm{d}(\omega-\omega_\mathrm{m},\boldsymbol{k}_\mathbf{p}-\boldsymbol{k}_\mathbf{m},z), \tag{2.21}$$

where ω denotes the frequency of the induced polarization, $\boldsymbol{k}_\mathbf{p}$ stands for its in-plane wavevector (parallel to the magnetic layer), while ω_m and $\boldsymbol{k}_\mathrm{m}$ represent their magnon counterparts. This equation represents the convolution of the Fourier images of the susceptibility $\hat{\boldsymbol{\chi}}$ and the driving field $\boldsymbol{E}_\mathrm{d}$. The vertical profile of the dynamic magnetization (along z) depends on the exact geometry and mode of the spin wave and should be considered for precise calculations. In the presented analysis, we disregard this dependency. However, this approximation can be insufficient in the case, where there is strong dependency of mode profile on z-coordinate comparable to the penetration depth of the light. This can especially be true for transparent materials like Ytrium-Iron-Garnet (YIG), where the penetration length can be longer than the sample thickness. Another approximation, which can be safely made, since $\omega \gg \omega_\mathrm{m}$, is to drop the exact dependence of the driving field on ω_m. Thanks to this approximation, the driving field $\boldsymbol{E}_\mathrm{d}$ can be calculated numerically, or in simple geometries even by analytic formulas.

Example of the induced polarization in a Permalloy layer

We present a semi-analytical calculation of the induced polarization in reciprocal space (Eq. 2.20) in the 30 nm thick NiFe slab on the silicon substrate with magnon frequency of $\omega_\mathrm{m} = 27$ GHz. The calculation starts with the semi-analytic calculation of the electric driving field ($\boldsymbol{E}_\mathrm{d}$), see Fig. 2.11a, b, c. The x-component (in polarization axis of the incident light, Fig. 2.11a) has intensity higher by approx. two orders of magnitude in comparison to y- and z- components. While x-component has polar symmetry, the y-component has four-fold (see 2.11b) and z-component has two-fold symmetry in the polarization axis (see 2.11c).

To calculate the magneto-optical part of the susceptibility tensor ($\hat{\boldsymbol{\chi}}$), we have to obtain all magnetization components. We have done this by following Bloch function calculation described in Chapter 1. The x-component of the magnetization (Fig. 2.11d) has no dynamics since the static magnetization points in this direction. In the y- and z-component (Fig. 2.11e, f) are visible allowed states at the studied frequency. The magnitude is roughly similar, which can be interpreted as a nearly circular precession of the magnetic moments. There is a phase delay of 90 degrees ($\pi/2$) between these two components, but since we show squared value, this is not directly visible on the presented plots.

We calculated the resulting polarization using a built-in 2-dimensional convolution function in Matlab 2022b and considering only linear Voigt contribution. The code is available on the code-sharing platform [107]. The polarization currents are then calculated by

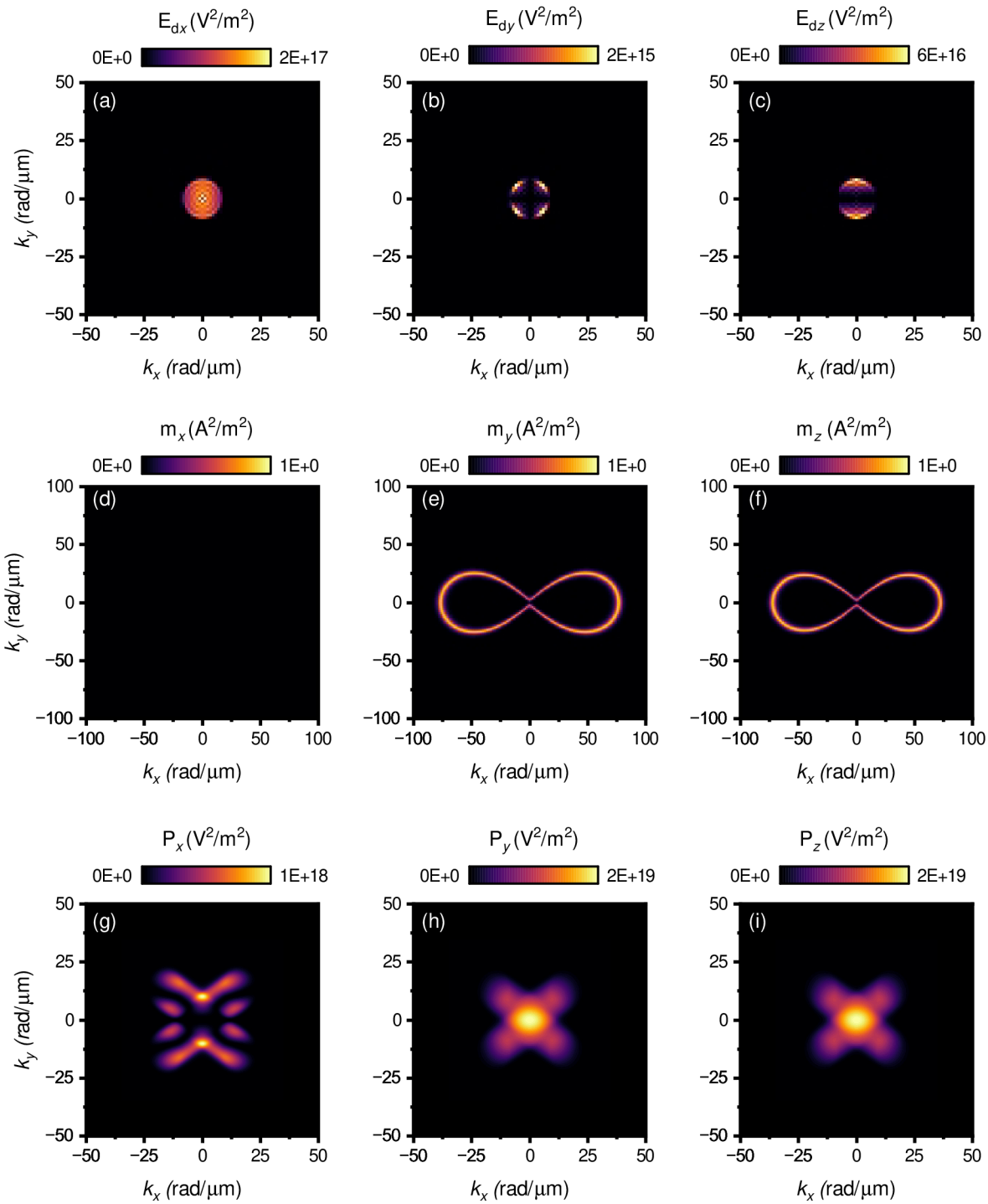

Figure 2.11: The calculation of the induced polarization. a, b, c The squared Fourier-transformed x- **(a)**, y- **(b)**, and z **(c)** component of the electric driving field $\boldsymbol{E}_{\mathrm{d}}$. **d, e, f** The squared Fourier-transformed magnetization x- **(d)**, y- **(e)**, and z **(f)** component. **g, h, i** The squared Fourier-transformed induced polarization x- **(g)**, y- **(h)**, and z-component **(i)**.

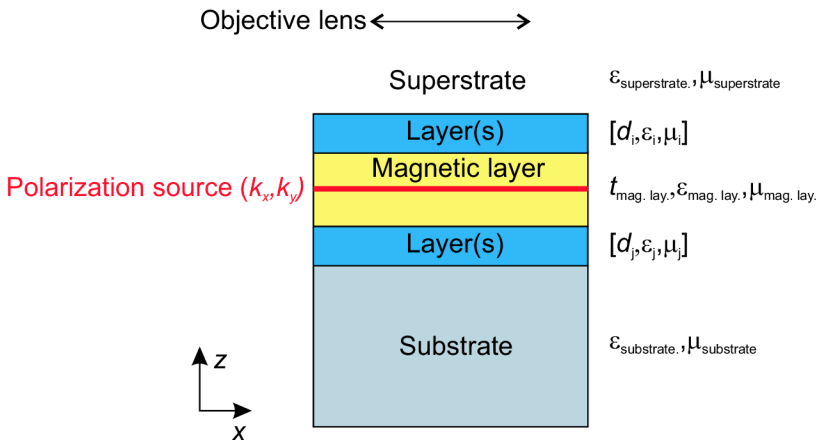

Figure 2.12: Schematics of the geometry for far-field transition. The light is focused on the magnetic layer by the objective lens, which is in the superstrate (usually air). We can assume an arbitrary number of layers above (coating) and beneath the magnetic layer. The polarization (radiation source) is placed in the middle of the magnetic layer. For simplicity, we assume for all materials $\mu = 1$.

the equation Eq. 2.21. We can observe that the current in x-component (Fig. 2.11g) has one order of magnitude lower intensity in comparison to the y- and z-components (Fig. 2.11h, i). Also note that polarization currents with free light inaccessible wavevectors are formed (in this case $k > 10\,\mathrm{rad/\mu m}$).

2.2.4. Far-field transition

The polarization vector in (2.21) acts as a local radiation source that eventually forms the detected BLS signal. The contribution of a particular spatial frequency to this signal is determined by its ability to efficiently couple to the free space continuum and pass through the optical setup towards the detector. In the case of the so-called k-resolved BLS, the spatial frequencies are given by the wavevector of the incident light and its angle with respect to the sample normal. In the case of the micro-focused BLS, the range of spatial frequencies that can reach the detector is mainly limited by the numerical aperture of the used objective.

The transition from polarization source to far-field can be mathematically expressed using Green's function formalism

$$\mathbf{E}_{\mathrm{FF}}(\omega,\mathbf{k}_{\mathrm{p}}) = \hat{\mathbf{G}}(\omega,\mathbf{k}_{\mathrm{p}},\mathbf{k}'_{\mathrm{p}})\mathbf{P}(\omega,\mathbf{k}'_{\mathrm{p}}). \tag{2.22}$$

The dyadic Green's function[8] $\hat{\mathbf{G}}(\omega,\mathbf{k}_{\mathrm{p}},\mathbf{k}'_{\mathrm{p}})$ embodies the response of a system to a local source and it can account fully for the presence of any scattering object, substrate effects or complex geometries. The term dyadic means here that it relates the spatial frequencies of polarization $(\omega,\mathbf{k}'_{\mathrm{p}})$ to the spatial frequencies in the far field $(\omega,\mathbf{k}_{\mathrm{p}})$.

Here, we present a representation of the Green function for (possibly) multilayer continuous film[9] with Gaussian illumination by the objective lens. We use the theory devel-

[8]This approach is general and can also be used for solving complex anisotropic cases (such as the presence of the resonator, see chapter 4).

[9]This is commonly called stratified medium.

oped by Sommerfield [108] and further extended by Weyl [109]. The approach follows the explanation in the book *Principles of Nano-Optics* [92].

We assume infinite layers in xy plane with broken symmetry in z-direction, as depicted in Fig. 2.12. The superstrate (in our calculation air) and substrate are semi-infinite also in z-direction. Between them, we assume a stack of optically active layers, of which at least one is magnetic[10].

Now, the dyadic Green function can be formulated as follows:

$$\hat{\boldsymbol{G}}(\boldsymbol{k}_\mathrm{p}) = \frac{\mathrm{i}}{8\pi^2} \iint_{\infty}^{\infty} \mathrm{d}^2 k'_p \hat{\boldsymbol{M}} \exp\left(\mathrm{i} k_\mathrm{zs} t_\mathrm{mag.lay.}\right), \tag{2.23}$$

where

$$\hat{\boldsymbol{M}} = \frac{1}{k_s^2 k_\mathrm{zs}} \begin{pmatrix} k_\mathrm{s}^2 - k_x^2 & -k_x k_y & \pm k_x k_\mathrm{zs} \\ -k_x k_y & k_\mathrm{s}^2 - k_y^2 & \pm k_y k_\mathrm{zs} \\ \pm k_x k_\mathrm{zs} & \pm k_y k_\mathrm{zs} & k_\mathrm{s}^2 - k_z^2 \end{pmatrix}, \tag{2.24}$$

$t_\mathrm{mag.lay.}$ is a thickness of the magnetic layer, k_s is a wavevector in the magnetic material, and $k_\mathrm{zs} = \sqrt{k_\mathrm{s}^2 - k_x^2 - k_y^2}$ is its longitudinal projection. The sign $\pm$ at some terms in 2.24 is for back-scattered waves $(+)$ and for forward-scattered $(-)$ waves. This dyadic Green function allows us to calculate propagating and evanescent waves originating from all orientations of polarization $\boldsymbol{P}$. To properly calculate the field that is back-scattered to the far field, we have to include the refraction and reflection on all involved boundaries. We can calculate transmission and reflection on all boundaries for p- and s- polarization by using the following set of equations

$$r^s(k_x,k_y) = \frac{k_\mathrm{zs1} - k_\mathrm{zs}}{k_\mathrm{zs1} + k_\mathrm{zs}} \tag{2.25a}$$

$$t^s(k_x,k_y) = \frac{2k_\mathrm{zs1}}{k_\mathrm{zs1} + k_\mathrm{zs}} \tag{2.25b}$$

$$r^p(k_x,k_y) = \frac{\varepsilon_2 k_\mathrm{zs1} - \varepsilon_1 k_\mathrm{zs}}{\varepsilon_2 k_\mathrm{zs1} + \varepsilon_1 k_\mathrm{zs}} \tag{2.25c}$$

$$t^p(k_x,k_y) = \frac{2\varepsilon_2 k_\mathrm{zs1}}{\varepsilon_2 k_\mathrm{zs1} + \varepsilon_1 k_\mathrm{zs}} \sqrt{\frac{\varepsilon_1}{\varepsilon_2}} \tag{2.25d}$$

Now, by employing the *transfer-matrix method*, we can calculate effective transmission and reflection coefficient for s- and p- polarized light for both direction (back-scattered and forward-scattered) light [110, 111]. However, to apply this *transfer-matrix method* to our dyadic Green function, we have to decompose it to the s and p parts. This decomposition can be accomplished by splitting the matrix $\hat{\boldsymbol{M}}$ to

$$\hat{\boldsymbol{M}}^s = \frac{1}{k_\mathrm{zs}\left(k_x^2 + k_y^2\right)} \begin{pmatrix} k_y^2 & -k_x k_y & 0 \\ -k_x k_y & k_x^2 & 0 \\ 0 & 0 & 0 \end{pmatrix} \tag{2.26a}$$

$$\hat{\boldsymbol{M}}^p = \frac{1}{k_s^2\left(k_x^2 + k_y^2\right)} \begin{pmatrix} k_\mathrm{zs} k_x^2 & k_\mathrm{zs} k_x k_y & \pm k_x\left(k_x^2 + k_y^2\right) \\ k_\mathrm{zs} k_x k_y & k_\mathrm{zs} k_y^2 & \pm k_y\left(k_x^2 + k_y^2\right) \\ \pm k_x\left(k_x^2 + k_y^2\right) & \pm k_y\left(k_x^2 + k_y^2\right) & \left(k_x^2 + k_y^2\right)/k_\mathrm{zs} \end{pmatrix}. \tag{2.26b}$$

[10] In our practical examples, we assume only a single NiFe layer between air and silicon.

.

Now, by multiplying $\hat{\boldsymbol{M}}^s$ and $\hat{\boldsymbol{M}}^p$ by appropriate reflection and transmission coefficient, we can obtain a full electric field in the far field. However, for practical calculation, we transform the above result to spherical coordinates [110]. In spherical coordinates in the far field, the radial component must be zero, simplifying the problem only to the 2×3 matrix. For transferring to spherical coordinates, we use the following substitution

$$M_{\varphi\beta} = -\sin\varphi M_{x\beta} + \cos\varphi M_{y\beta}, \tag{2.27a}$$
$$M_{\vartheta\beta} = -\sin\varphi\cos\vartheta M_{x\beta} + \sin\varphi\cos\vartheta M_{y\beta} - \sin\vartheta M_{z\beta}. \tag{2.27b}$$

Using 2.27 and 2.26 we get

$$\hat{\boldsymbol{M}}^s = \frac{1}{k_{\mathrm{zs}}\left(k_x^2+k_y^2\right)^{3/2}}\begin{pmatrix} k_y\left(k_x^2-k_y^2\right) & -k_x^3+k_xk_y^2 & 0\\ 0 & 0 & 0\end{pmatrix} \tag{2.28a}$$

$$\hat{\boldsymbol{M}}^p = \begin{pmatrix} 0 & 0 & 0\\ \pm\frac{k_x}{k_{\mathrm{s}}\sqrt{k_x^2+k_y^2}} & \pm\frac{k_y}{k_{\mathrm{s}}\sqrt{k_x^2+k_y^2}} & \frac{\sqrt{k_x^2+k_x^2}\left(1+k_{\mathrm{zs}}^2\right)}{k_{\mathrm{s}}^3k_{\mathrm{zs}}}\end{pmatrix}. \tag{2.28b}$$

.

By inserting (2.21) into (2.22) and integrating over all spatial frequencies supplied by the driving electric field, the far-field angular spectrum becomes

$$\mathbf{E}_{\mathrm{FF}}(\omega_{\mathrm{m}}\mathbf{k}_{\mathrm{m}},\omega,\mathbf{k}_{\mathrm{p}}) = \int \mathrm{d}^2k'_{\mathrm{p}}\ \hat{\mathbf{G}}(\omega,\mathbf{k}_{\mathrm{p}},\mathbf{k}'_{\mathrm{p}})\hat{\boldsymbol{\chi}}(\omega_{\mathrm{m}},\mathbf{k}_{\mathrm{m}})\mathbf{E}_{\mathrm{d}}(\omega,\mathbf{k}'_{\mathrm{p}}-\mathbf{k}_{\mathrm{m}}). \tag{2.29}$$

Another important aspect of the BLS detection process is the limited area from which the signal is collected. This is equivalent to the statement that only rays virtually parallel to the microscope's optical axis can successfully reach the detector. Assuming that the collection spot has a Gaussian spatial profile $h(x,y) = \mathrm{e}^{-(x^2+y^2)/w_{\mathrm{c}}^2}$, the detectable portion of the far-field radiation amounts to

$$\mathbf{E}_{\mathrm{FF}}(\mathbf{r}_{\parallel}) = h(\mathbf{r}_{\parallel}) \int\limits_{k_{\mathrm{p}}\le k_0\mathrm{NA}} \mathrm{d}^2k_{\mathrm{p}}e^{\mathrm{i}\mathbf{k}_{\mathrm{p}}\cdot\mathbf{r}_{\parallel}}\mathbf{E}_{\mathrm{FF}}(\mathbf{k}_{\mathrm{p}}), \tag{2.30}$$

where the integration limits reflect the restrictions placed on the spatial frequencies by the numerical aperture of the objective lens.

Finally, to estimate the strength of the BLS signal at a particular frequency ω_{m}, one has to sum up the contributions from all magnons (i.e., integrate over $\mathbf{k}_{\mathrm{m}}$). The exact nature of this summation depends on the coherence properties of the magnon population. In the case of thermal magnons (which are inherently incoherent), the proper procedure is to add intensities originating from individual magnon contributions. In the case of coherent magnons (e.g., excitation by vortex core motion), one must account appropriately for the phase and sum of all waves before calculating intensities. The modeled BLS signal for thermal magnons (integration after squaring) reads

$$\sigma(\omega_{\mathrm{m}}) = \int\mathrm{d}^2r_{\parallel}\int\mathrm{d}^2k_{\mathrm{m}}\left| h(\mathbf{r}_{\parallel}) \int\limits_{k_{\mathrm{p}}\le k_0\mathrm{NA}}\mathrm{d}^2k_{\mathrm{p}}\,e^{\mathrm{i}\mathbf{k}_{\mathrm{p}}\cdot\mathbf{r}_{\parallel}}\int\mathrm{d}^2k'_{\mathrm{p}}\hat{\mathbf{G}}(\mathbf{k}_{\mathrm{p}},\mathbf{k}'_{\mathrm{p}})\,\hat{\boldsymbol{\chi}}(\omega_{\mathrm{m}},\mathbf{k}_{\mathrm{m}})\mathbf{E}_{\mathrm{d}}(\mathbf{k}'_{\mathrm{p}}-\mathbf{k}_{\mathrm{m}})\right|^2, \tag{2.31}$$

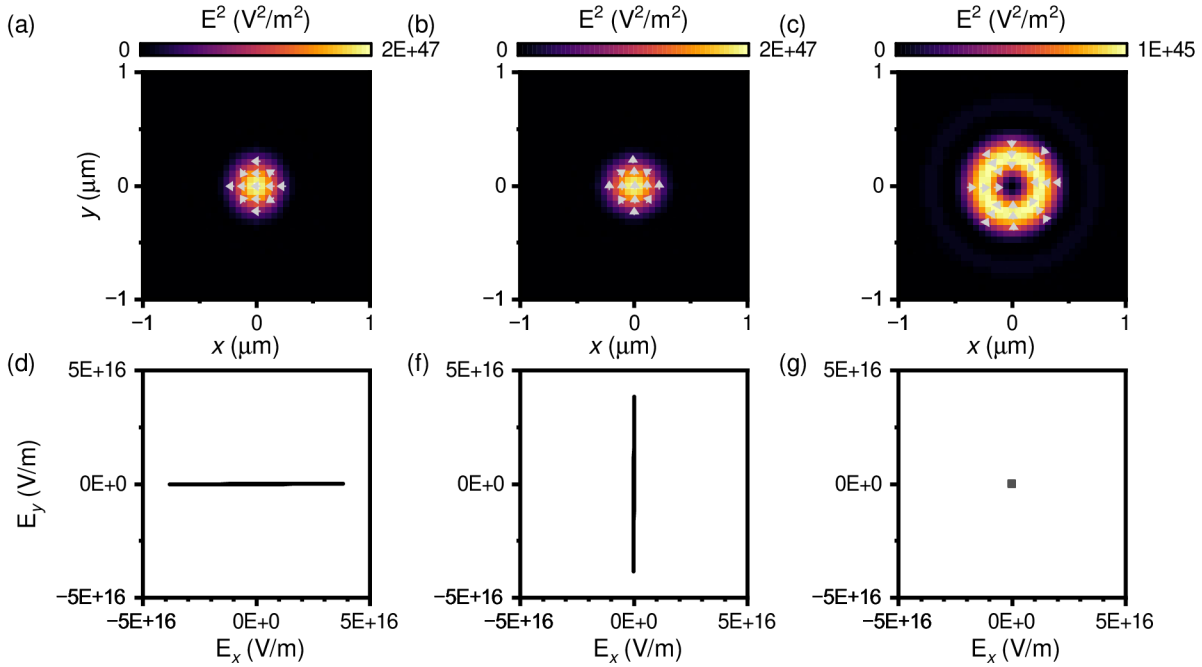

Figure 2.13: Radiation of the dipole oriented along Cartesian axis. **a, b, c** Magnitude of the electric field, which is able to arrive at the detector, in the plane of dipole oriented along x- **(a)**, y- **(b)**, and z- (**c**) axis. The arrows show the orientation of the electric field at a certain moment in time and help to visualize polarization. **d, e, f** Representation of the summed electric field intensity using Lissajous curves. The dipole is oriented along x- **(d)**, y- **(e)**, and z- (**f**) axis. Due to the rotational symmetry in **(c)**, there is no net electric field in **(f)**.

while for coherent magnons (integration before squaring), we get

$$\sigma(\omega_{\mathrm{m}}) = \left| \int \mathrm{d}^2 r_{\parallel} \int \mathrm{d}^2 k_{\mathrm{m}}\; h(\mathbf{r}_{\parallel}) \int\limits_{k_{\mathrm{p}} \leq k_0 \mathrm{NA}} \mathrm{d}^2 k_{\mathrm{p}}\, e^{\mathrm{i}\mathbf{k}_{\mathrm{p}}\cdot\mathbf{r}_{\parallel}} \int \mathrm{d}^2 k'_{\mathrm{p}} \hat{\mathbf{G}}(\mathbf{k}_{\mathrm{p}},\mathbf{k}'_{\mathrm{p}})\, \hat{\boldsymbol{\chi}}(\omega_{\mathrm{m}},\mathbf{k}_{\mathrm{m}}) \mathbf{E}_{\mathrm{d}}(\mathbf{k}'_{\mathrm{p}} - \mathbf{k}_{\mathrm{m}}) \right|^2 . \tag{2.32}$$

Dipole radiation

To see the behavior of the developed theory, we calculated the resulting far-field of the dipoles with $k = 0$ oriented along the direction of all three axes (x, y, and z), see Fig. 2.13.

The in-plane oriented dipole radiation (Fig. 2.13a, b) creates identical results, which are just rotated by 90 degrees. The resulting net electric field in the perpendicular axis to dipole radiation is near the numerical error (approximately 13 orders of magnitude smaller than the net polarization in the axis parallel to the dipole orientation). This is caused by the compensation of the perpendicular electric field (see the mirror symmetry along $y = 0$ in Fig. 2.13a, or $x = 0$ in Fig. 2.13b). The polarization state is visualized by the use of Lissajous curves. These curves show the E_x and E_y values through one period of oscillation. The straight lines correspond to perfectly linearly polarized light, which is the case for Fig. 2.13d, f.

In the case of the out-of-plane oriented dipole radiation, we get a rotationally symmetrical shape, with the polarization axis aligned to the center (see Fig. 2.13c). The electric

field magnitude forms a doughnut shape with zero intensity in the center. Due to the rotational symmetry, the net electric field (polarization) is equal to zero (see Fig. 2.13f).

2.2.5. Resulting BLS spectra

In this section, we use the built theory to show the effects of the various factors on the resulting μ-BLS spectra. We investigate thermal spin waves in various external fields and thicknesses of the magnetic layers. The consequences of the different geometries, numerical aperture, filling factor, and Cotton-Moutton effect is investigated on the coherent spin waves.

Thermal spin waves field sweep

Zeeman energy is one of the factors that contribute to the spin wave frequency. If the magnetization is saturated to the direction of the applied magnetic field, then with higher applied field, the spin wave frequency is increased, i.e., the spin wave dispersion is shifted to higher frequencies. The increase of this energy also changes the slope of the dispersion and the lifetime of magnons.

In Fig. 2.14a, the BLS spectra are calculated according to Eq. 2.31 for NiFe 30 nm thin film. In all fields, we can observe two peaks. The one with lower frequencies corresponds to the fundamental mode, while the one with higher frequencies corresponds to the first perpendicular standing spin wave mode. The decrease of the BLS signal with higher fields can be observed, which is caused by the decreased spin wave population (the chemical potential −1 THz is assumed). The used theory assumes that there is no evolution in spin wave amplitude across the thickness of the magnetic layer, which is not fulfilled for perpendicular standing spin waves. Due to this, the presented theoretical treatment can not precisely estimate the ratio between these two peaks. This may be solved by

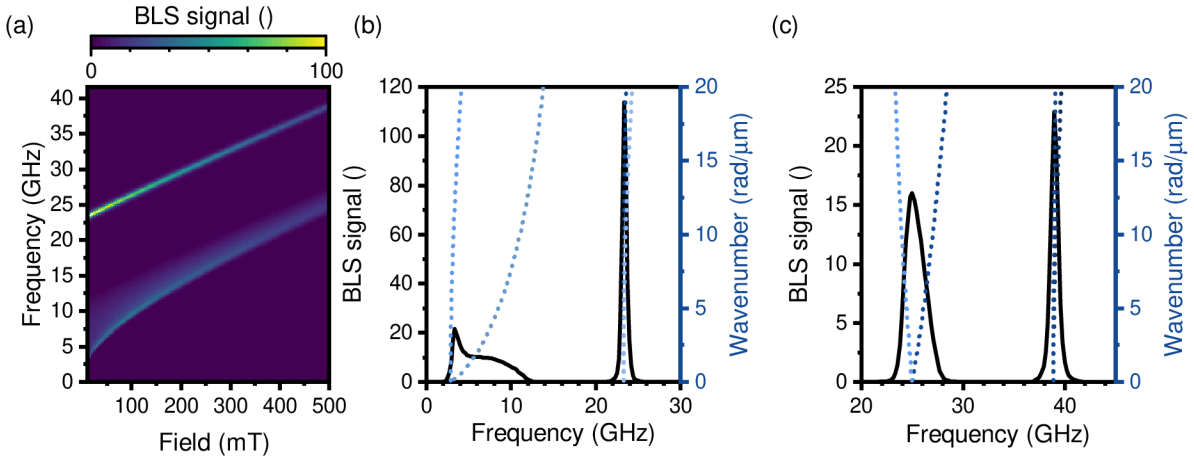

Figure 2.14: BLS spectra in different external magnetic fields. **a,** Calculated BLS spectra using Eq. 2.31 in external magnetic fields from 10 mT to 500 mT. We used parameters for NiFe and calculated the signal for fundamental and first thickness modes. The chemical potential is −1 THz. **b, c,** Slices of the panel **(a)** in the lowest (10 mT, **(b)**) and the highest (500 mT, **(b)**) magnetic field. The dispersion relations in the direction of high symmetry (Damon-Eshbach and Backward volume) are shown as blue dotted curves for fundamental and fist thickness modes.

calculating the induced polarization in many planes inside the magnetic layer. It would require calculating the focal fields with semi-infinite metallic films and amplitude profiles of the spin waves in the out-of-plane direction, as done in Sec. 1.5.2.

The linewidth of the first perpendicular thickness mode is solely determined by the lifetime of these spin waves (for the given parameters). This statement is only valid for the calculation following the Eq. 2.31. In experiments with the Sandercock type tandem Fabry-Perot interferometer [112], the frequency linewidth is usually determined by the instrumental transmission function, as it ranges from several hundreds of megahertz to a few gigahertz and increase with higher measurement frequencies.

The decrease of the BLS signal towards the higher fields is caused by the fact that the spin wave frequencies are increased, and as a result (as spin waves obey Bose-Einstein distribution, as considered in Sec. 1.5.2), their population is decreased.

In the low fields, the fundamental mode exhibits distinct peaks in its lowest frequencies. This peak is caused by the low group velocity (and the resulting high density of states) of spin waves in backward volume geometry, see Fig. 2.14b, light blue dotted curve). The group velocity of BV spin waves is very low, as there is competition between dipolar interaction, which tends to have a negative contribution to the group velocity, and exchange interaction, which has a positive contribution with higher wavenumbers. As the field increases, the importance of the dipolar interaction increases as well. In turn, the absolute value of the group velocity increases, and the minimum frequency (point with zero group velocity) is moved towards the inaccessible wavenumbers, see Fig. 2.14c, light blue dotted curve. The resulting spectra then resemble a Gaussian shape.

Influence of the film thickness on the thermal spin wave spectra

The change in the thickness of the film does not affect the frequency of ferromagnetic resonance ($k = 0$). However, it dramatically affects spin wave dispersion, particularly spin wave group velocities. Also, the spin-wave signal is proportional to the interaction volume, which is decreased when the thickness of the film is low. The light propagation in the magnetic medium is assumed to be uniform, with just exponential attenuation on the way to and out of the material. This introduces the power of two to the volume factor $\mathfrak{F}$. This approach is a good approximation as long as the thickness of the magnetic layer is not larger than the *depth of focus* of the used objective lens. To account for this we introduced a factor ($\mathfrak{F}$),

$$\mathfrak{F} = \int_0^{t_{\mathrm{mag}}} \exp\left(-k_{\mathrm{exc}} k_0 z\right)^2 \mathrm{d}z, \tag{2.33}$$

where t_{mag} is thickness of the magnetic layer, k_{exc} is the extinction coefficient of the magnetic material, and k_0 is free space wavenumber of the used light. The whole equation for the BLS signal then reads as

$$\sigma(\omega_{\mathrm{m}}) = \int \mathrm{d}^2 r_{\parallel} \int \mathrm{d}^2 k_{\mathrm{m}} \left| \mathfrak{F}\, h(\mathbf{r}_{\parallel}) \int_{k_{\mathrm{p}} \leq k_0 \mathrm{NA}} \mathrm{d}^2 k_{\mathrm{p}}\, e^{\mathrm{i}\mathbf{k}_{\mathrm{p}} \cdot \mathbf{r}_{\parallel}} \int \mathrm{d}^2 k'_{\mathrm{p}} \hat{\mathbf{G}}(\mathbf{k}_{\mathrm{p}}, \mathbf{k}'_{\mathrm{p}})\, \hat{\boldsymbol{\chi}}(\omega_{\mathrm{m}}, \mathbf{k}_{\mathrm{m}}) \mathbf{E}_{\mathrm{d}}(\mathbf{k}'_{\mathrm{p}} - \mathbf{k}_{\mathrm{m}}) \right|^2 . \tag{2.34}$$

This equation approximates magnetization dynamics with a uniform precession angle across the thickness of the magnetic layer. This is quite a strong approximation, especially in the case of the quantized thickness modes. But it also neglect the case of non-zero wavenumbers or non-zero spin pinning on the layer boundaries.

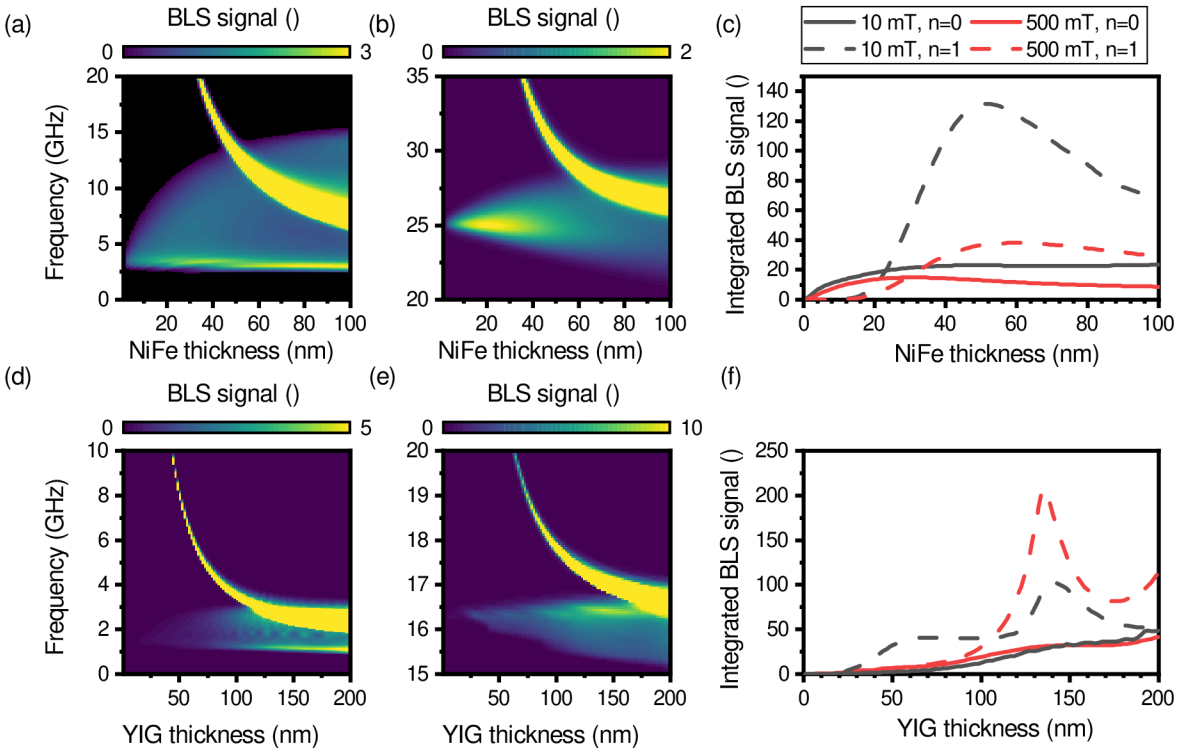

Figure 2.15: BLS spectra of NiFe and YIG with different thicknesses. **a, b** Calculated BLS spectra of NiFe using Eq. 2.34 in 10 mT **(a)**, and 500 mT **(b)** of thicknesses ranging from from 1 nm to 100 nm. We used parameters for NiFe and calculated the signal for fundamental and first thickness modes. The chemical potential is −1 THz. **c,** Integrated signal of all four shown peaks. **d, e** Calculated BLS spectra of YIG using Eq. 2.34 in 10 mT **(a)**, and 500 mT **(b)** of thicknesses ranging from from 1 nm to 200 nm. **f,** Integrated signal of all four shown peaks.

The resulting BLS spectra for NiFe and YIG layers are shown in Fig. 2.15. The NiFe is metallic and thus has strong attenuation of the light in the material, with an extinction coefficient of $k_{\text{exc}} = 3.842$. On the other hand, the YIG is almost transparent and has extinction coefficient $k_{\text{exc}} \approx 1 \cdot 10^{-6}$. On these two examples, we can see the consequences of different light attenuation in magnetic material. Note, that it is not possible to compare the strength of the calculated signal between the two materials, as it depends mostly on the *Voigt* constant Eq. 2.19, which we assumed $Q = 1$ in both cases.

As shown in Fig. 2.14 in low magnetic fields ($B_{\text{ext}} = 10\,\text{mT}$), the *turning point* in BV geometry is accessible by the μ−BLS, and this exhibits itself as strong signal in the lowest detected frequency as can be seen across all thicknesses in Fig. 2.15a. With increasing thickness, we can observe broadening to both lower and higher frequencies. This is caused by the increase in the group velocity of the spin waves in all directions. This increase is more steep in the so-called Damon-Eshbach geometry, thus the spectrum is more broadened towards the higher frequencies. In the high magnetic field ($B_{\text{ext}} = = 500\,\text{mT}$), the BLS spectrum is much more symmetrical, see Fig. 2.15b.

In both magnetic fields, when the thickness of the layer increases, the frequency of the first thickness mode decreases and is slowly reaching the value of ferromagnetic resonance. The higher thickness modes were not considered.

In Fig. 2.15c, the intensities of all four peaks are integrated. In integrated intensities a fundamental spin-waves (solid lines), we can see that the signal strength reaches the

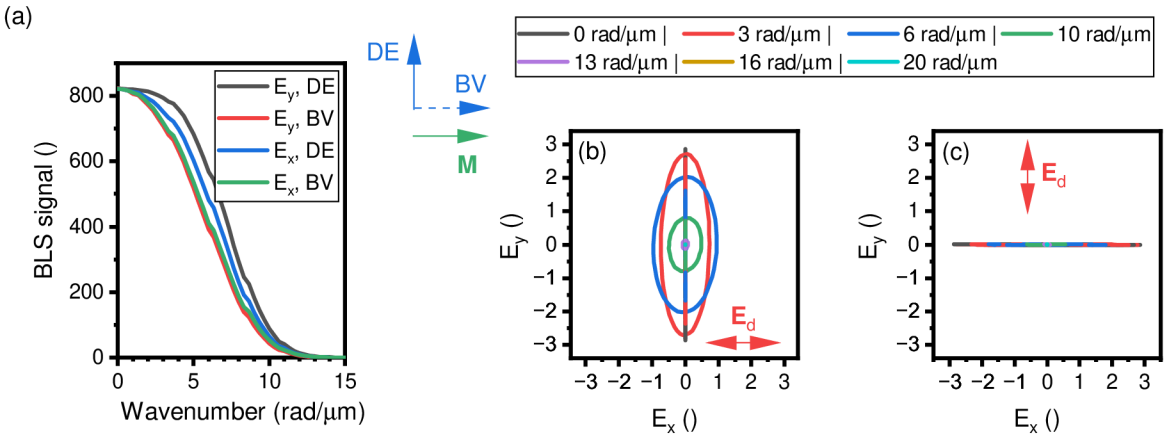

Figure 2.16: BLS spectra of coherently excited spin waves in different measurement geometries. **a** Calculated BLS spectra by using Eq. 2.32 for polarization along y-axis (black and red curves) and x-axis (blue and green curves). The spin waves are propagated in Damon-Eshbach-like geometry (black and blue curves) and backward-volume-like geometry (red and green curves). **b, c** The Lissajous curves represent the polarization state for light scattered on coherent spin-waves with different wavenumbers. The polarization axis of the driving field $\boldsymbol{E}_\mathrm{d}$ was in x-axis **(b)**, and y-axis **(c)**. The solid (dashed) curves show Damon-Eshbach (backward-volume)-like geometry.

maximum for thickness of the magnetic layer around 25 nm for field of 500 mT, and 50 nm for field of 10 mT. This position of maximum signal is determined by the interplay between the contribution of larger interaction volume and from lower group velocity in thinner NiFe layers. However, the interaction volume does not increase linearly with the increasing thickness, and after reaching $\approx$ 70 nm is not increased at all due to the fast decay of the light in the NiFe layer.

In the case of the first thickness mode (dashed lines), the intensity is almost zero for low thicknesses as the frequencies of these modes reach several terahertz. Due to the Bose-Einstein distribution, the population of the magnons on these frequencies is very low in comparison to the frequencies in the order of several gigahertz. On the other hand, as the group velocity is increased in the range of the accessible wavevectors for thicknesses above 40 nm, this results in the decrease of the signal. These two factors cause formation of the optimal thickness for the signal strength at $\approx$ 50 nm.

The results for YIG films are shown in Figs. 2.15d, e, f. The attenuation of the light in these layers is minimal, and thus, the signal increases for all calculated thicknesses of the fundamental modes as the volume factor $\mathcal{F}$ increases practically linearly with the thickness of the YIG layer. In the first thickness mode, we can observe a pronounced maximum of signal strength at 150 nm of YIG layer thickness. This is caused by the increase of the group velocity in the *backward-volume-like* geometry of the spin waves in first thickness mode after it reaches approx. 150 nm.

Influence of the measurement geometry

The BLS signal is also affected by the exact mutual orientation of the wavevector of coherently excited spin waves, driving field polarization, and static magnetization orientation. These effects are investigated in Fig. 2.16.

If we assume only the perpendicular orientation of the spin-wave wavevector, static magnetization, and driving field polarization there are four possible configurations. Let's assume that the static magnetization always points in the direction of the x-axis. The highest detection sensitivity for coherent spin waves is reached when the driving field is perpendicular to the static magnetization (electric field is along y-axis), and parallel to the wavevector (in so-called Damon-Eshbach-like geometry), see black line in Fig. 2.16a. On the other hand, the lowest detection sensitivity is reached when magnetization and propagation direction are pointing in the x-direction and electric field in the y-direction, see red line in Fig. 2.16a.

The resulting BLS signal is linearly polarized for three configurations – when the driving field is along y-axis, and when the driving field is along x-axis, and spin-waves propagates in backward-volume-like geometry. This can be checked in Lissajous curves representation of the electric field in far-field in dashed curves in Fig. 2.16b and Fig. 2.16c. Nevertheless, the driving field along x-axis and spin waves propagating in Damon-Eshbach-like geometry give rise to ellipticity. The major axis of the ellipse is rotated by 90 degrees with respect to the incident polarization axis. Depending on the magnitude of the spin-wave wavevector, one can observe the change in the ellipticity parameter.

Influence of the numeric aperture and the filling factor of the objective lens

The numeric aperture has a pronounced effect on the formed polarization in the material through the change of the driving field $\boldsymbol{E}_\mathbf{d}$ (see Eq. 2.20, Fig. 2.7), but it also affects the far-field transition (see Eq 2.30). On the other hand, the change of the beam waist before the back aperture of the objective lens (filling factor) only affects the formation of the polarization and does not directly influence the radiation process.

Fig. 2.17 illustrates the effects of both previously mentioned factors. In Fig. 2.17a, b, one can observe that with a higher numeric aperture, higher wavenumbers can be detected. This increase is linear, with the slope of $(15.9 \pm 0.2)\,\mathrm{rad/\mu m}$ and intercept of

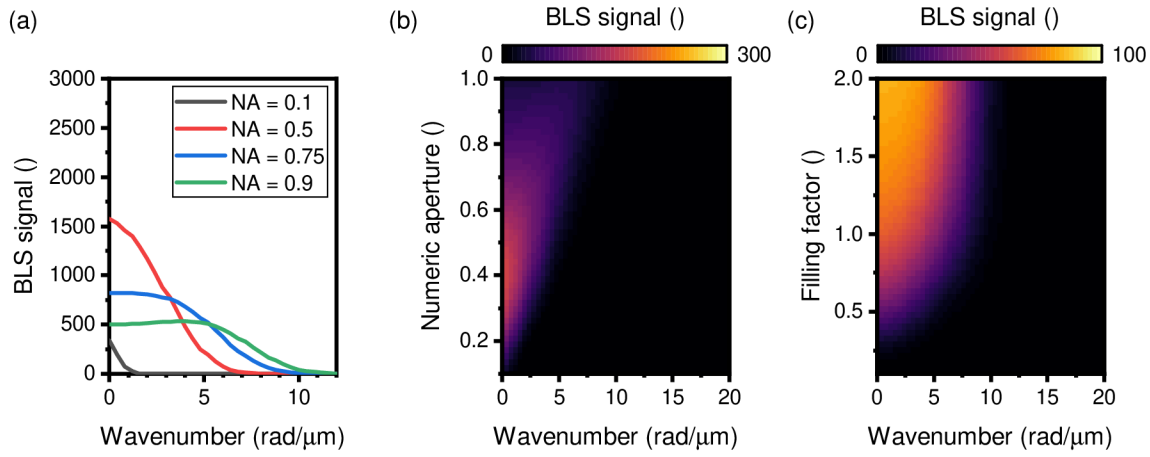

Figure 2.17: BLS spectra calculated for objective lenses with different numeric apertures and filling factors. **a** Calculated BLS spectra by using Eq. 2.32 for objective lenses with different numeric aperture (NA) and filling factor of 2. **b** 2D map of BLS signal in dependence to numeric aperture and wavenumber. **c** BLS spectra in dependence on the filling factor of the objective lens with a numeric aperture of 0.75. All panels assume the 30 nm thick NiFe layer on a silicon substrate.

(0.9 ± 0.1) rad/μm. Also the strength of the signal and shape of the spectra are changed as well, see Fig. 2.17a.

In the cases of the varying filling factor, the situation is different. In the range from 0.7 to 2, there is only a small variation of the highest detectable wavenumber (from ≈ 9.5 to 10.5 rad/μm). In the cases of lower fillings factor (0.01→0.5) we can observe linear increase with the slope of (8.1 ± 0.2) rad/μm and intercept of (5.33 ± 0.09) rad/μm.

Influence of the Cotton-Moutton effect

In all previous calculations, we assumed that the Cotton-Moutton effect does not contribute to the formed BLS signal. However, in reality, there could be a small contribution from this second-order magneto-optical effect. If there is a product of the two dynamic magnetization components (e.g. in geometry where the static magnetization is along x-axis products of M_y, and M_z), the resulting signal would be present on the double of the frequency of spin waves. However, if there is the product of the dynamic and static components, the resulting signal would be on the same (spin wave) frequency [86].

The case of the increasing Cotton-Moutton constant (relative to the Voigt constant Q, see Eq. 2.19) is investigated in Fig. 2.18 for spin waves propagating in backward-volume-like geometry. In the case of the electric field parallel to the static magnetization, we can observe an increase in the detected BLS signal, see Fig. 2.18a. On the other hand, when the electric field is perpendicular to the static magnetization, the BLS signal decreases with increasing Cotton-Moutton constant, see Fig. 2.18b.

In geometries, where the driving field is parallel with the static magnetization, the change of the polarization state of the far-field light is possible. However, the exact influence depends on many factors and needs to be investigated separately for each case, and general discussion is beyond the scope of this thesis.

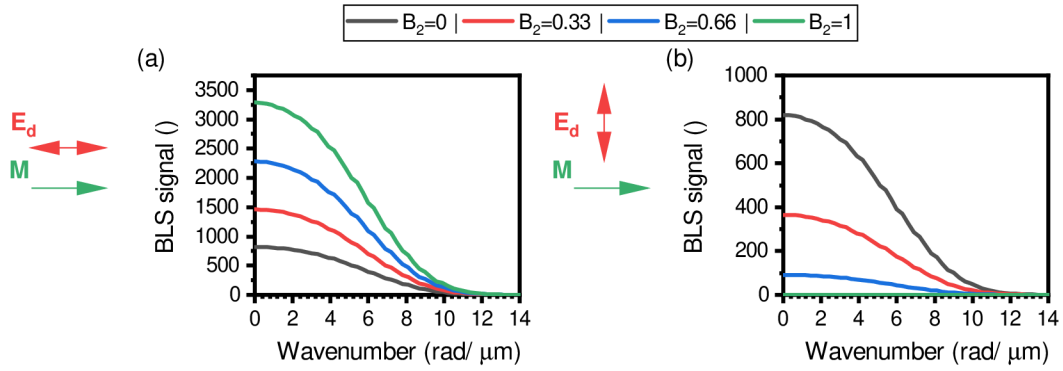

Figure 2.18: BLS spectra with different Cotton-Moutton constants. **a, b** Calculated BLS spectra by using Eq. 2.32 for different Cotton-Moutton constants (while $Q =$ $= 1$) for geometry where driving field is parallel **(a)**, and perpendicular **(b)** to the static magnetization. The other parameters are: NA=0.75, $f = 2$, $t_{\mathrm{NiFe}} = 30$ nm. The spin waves are propagated in backward-volume-like geometry.

2.3. Phenomenological model of the BLS signal

The theory developed in the previous sections is robust and, with modification, can account for various discussed effects but also for, e.g., the presence of the scattering center [113], nonlinear phenomena [114], or different optical properties. However, it is not suitable for quantification of the detection efficiency of the BLS setup. For this task, I developed a simple phenomenological model based on the following equation

$$\sigma_{\mathrm{BLS}}(f) = \iint\limits_{k_x,k_y} \mathcal{D}(f,k_x,k_y)\,\Gamma(k_x,k_y)\,dk_x dk_y + \mathrm{bg}, \tag{2.35}$$

where $\mathcal{D}(f,k_x,k_y)$ is the density of states of spin waves, bg stands for the background signal, which could be caused by a dark current in the detector, inelastic scattering on the phonon modes or by stray light, $\Gamma(k_x,k_y)$ is an instrumental detection function and $\sigma_{\mathrm{BLS}}(f)$ is the measured signal. We assume that the detection function Γ has a Gaussian form

$$\Gamma = A\exp\left(\frac{-k_x^2}{2\left(\mathrm{HWTM}_x/\sqrt{2\ln 10}\right)^2}\right)\exp\left(\frac{-k_y^2}{2\left(\mathrm{HWTM}_y/\sqrt{2\ln 10}\right)^2}\right), \tag{2.36}$$

where A is the strength of the measured signal, k_x (k_y) is the spin-wave k-vector in x (y) direction, and HWTM_x (HWTM_y) is half width at tenth of maximum of the detection sensitivity for spin-wave k-vectors in x (y) direction. To quantify the enhancement of the BLS signal in our data, we only fit two parameters A, and HWTM.

This phenomenological model was used to fit experimental data from 30 nm thick NiFe layer at 50 mT and 550 mT, see Fig. 2.19a, b. Even with this simple model, we can achieve perfect agreement with the experimental data in both measured fields. The advantage of this approach is that it does not require input parameters of the setup and thus can be used to quantify the detection efficiency with respect to the specific wavenumber. Note, that the analytic BLS model (Eq. 2.31) was not fitted but calculated based on the known

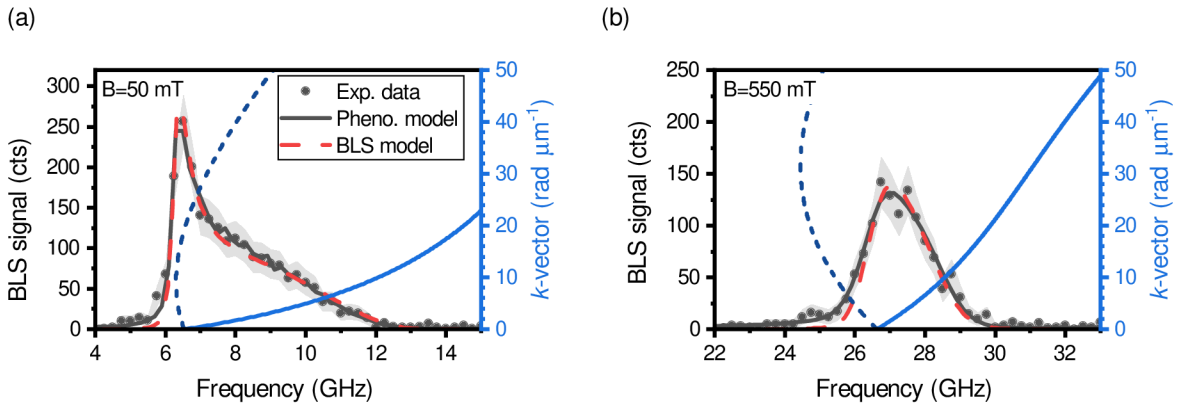

Figure 2.19: Comparison between Phenomenological model, BLS model, and experimental data. **a, b** Calculated BLS spectra by using Eq. 2.35, and Eq. 2.32 for 30 nm thick NiFe layer in 50 mT (**a**) and 550 mT (**b**). Blue curves represent backward-volume (dashed line) and Damon-Eshbach (solid line) dispersion.

set of parameters. The advantage of this approach is that it can predict the behavior of the detected signal with respect to various instrument-related parameters.

In order to achieve good agreement between the analytic model and experimental data, the numeric aperture of the lens had to be lowered by 0.1 to NA = 0.65. This is caused by inherent aberration to the used objective lens and imperfection in the alignment of the setup during the measurement.

2.4. BLS in the presence of a scattering center

In this section, I lay theoretical foundations for the description of the main topic of this PhD thesis: enhancement of the BLS signal by the presence of the scattering center. First, I divide the materials based on their optical response into two classes: metallic and dielectric. Afterward, the Mie theory of scattering of electromagnetic waves on the spherical particle in a homogeneous medium is introduced together with a simulated disk on the NiFe layer. The differences between the electromagnetic field distributions between the case of metallic and dielectric particles are discussed. Finally, I present the calculation procedure developed by Martin Hrtoň for obtaining the BLS signal in the presence of the scattering center with a discussion of the role of electromagnetic field shaping, induced polarization, and transition to the far field.

2.4.1. Mie theory

The theory of scattering of light on particles was first introduced by Gustav Mie [115]. The theory calculates scattering and absorption cross-section depending on the material of the sphere, its diameter, and the medium in which the sphere is immersed. From the perspective of optics, the most important material parameter is its dielectric function (ε). Dielectric function is connected to the index of refraction (n) by following relation

$$\mathrm{n}^2 = \varepsilon. \tag{2.37}$$

Please note, that dielectric function and index of refraction are complex. The imaginary part represents the optical losses of the material.

In general, dielectric function depends on the light frequency. Based on this dependency, we can (crudely) divide materials into two groups: dielectric and metallic. Metallic materials have free charge carriers - electrons. Their behavior (complex dielectric function) is described by the so-called Drude model [116]

$$\varepsilon(\omega) = \varepsilon_\infty - \frac{\omega_\mathrm{p}^2}{\omega^2 + \gamma^2} + i\frac{\gamma\omega_\mathrm{p}^2}{\omega^3 + \gamma^2\omega}, \tag{2.38}$$

where ε_∞ is the dielectric constant, γ is the damping collision frequency, and ω_p is the plasma frequency of the free electron gas.

For the dielectric materials with bounded charge carriers, the Lorentz model can be used. This model is based on the sum of the Lorentz oscillators, which can be formulated as written as [117]

$$\varepsilon(\omega) = \varepsilon_\infty - \sum_{j=1}^{N} \frac{f_j\omega_\mathrm{p}^2(\omega_{0,j}^2 - \omega^2)}{(\omega_{0,j}^2 - \omega^2)^2 + (\gamma_j\omega)^2} + i\sum_{j=1}^{N} \frac{f_j\omega_\mathrm{p}^2\gamma_j\omega}{(\omega_{0,j}^2 - \omega^2)^2 + (\gamma_j\omega)^2}, \tag{2.39}$$

where j is number of oscillator, N is the overall number of oscillators, $\omega_{0,j}^2$ is the resonance frequency of given oscillator, γ_j is the damping frequency of oscillator, f_j is strength of oscillator. We note here that these two are only basic models and are sufficient only for a handful of materials. Some materials even require more complicated descriptions consisting of more models combined [117].

Mie's theory assumes that the incident wave is planar, and the scattered one is spherical. Depending on the material of the sphere, we can talk about plasmonic resonance in the case of metallic materials or dielectric resonance in the case of insulating materials. The total cross section (σ_{MS}) is expressed in the form of infinite series [118, 119]

$$\sigma_{\mathrm{MS}} = \frac{\lambda}{2\pi n_0^2} \sum_i^{\infty} \left[\left(2\frac{n}{n_0} + 1 \right) \left(|a_i(2\pi n_0 r/\lambda)|^2 + |b_i(2\pi n_0 r/\lambda)|^2 \right) \right], \tag{2.40}$$

where a_i and b_i are spherical Hankel functions and spherical Bessel functions, respectively. However, the original Mie theory is not very applicable, as it is restricted to spherical particles in uniform medium. As the *real-world* particles with various shapes are often fabricated by lithography processes on top of a (semi-finite) substrate, numerical solving of the Maxwell equations is used to predict their optical response to arbitrary shaped light.

We present the results of the original Mie theory applied to a 180 nm-wide sphere in the air made out of silicon and silver in Fig. 2.20a, and 180 nm-wide disk out of silicon and silver as well on top of a 30 nm thick NiFe layer on silicon substrate Fig. 2.20b. First, we discuss the case of silver (metallic) particle. We can observe that for the silver sphere and for silver disk, for wavelengths ranging from 200 nm to 300 nm, the scattering is kept

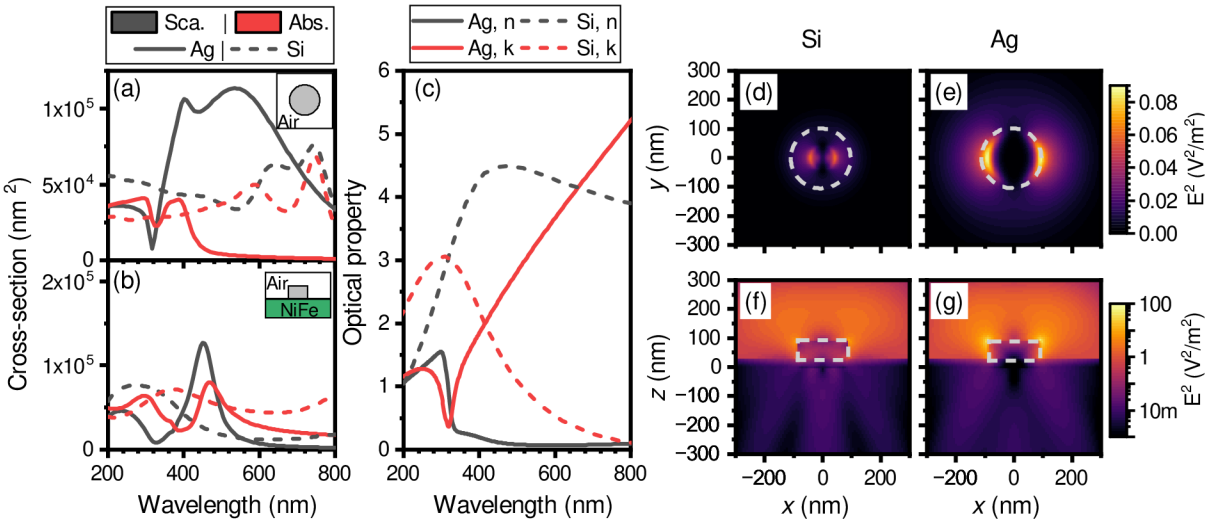

Figure 2.20: Mie scattering. **a, b,** Scattering and absorption cross sections. The panel **(a)** shows calculation employing the original Mie theory (sphere in homogeneous medium). The panel **(b)** shows calculation employing simulation of Maxwell equations of silicon disk on the NiFe layer. **c,** Index of refraction and absorption of silver and silicon. **d, e,** Squared electric field distribution for wavelength of 532 nm in middle of NiFe layer under silicon (**d**) and silver (**e**) disks. The disc circumference is shown as a gray dashed line. Both panels share the same linear scale. **f, g,** Squared electric field distribution for wavelength of 532 nm in XZ-cross section for silicon (**f**) and silver **(g)** disks. The profiles of the disks are depicted by gray dashed lines. Both panels share the same logarithmic scale.

relatively constant. This is caused by the relatively constant index of refraction, see Fig. 2.20c. Above 300 nm the absorption of the silver sphere slightly falls. This is caused by crossing the absorption edge of silver, and thus, no light penetrates inside the sphere, see quick rise in absorption and fall of the index of refraction for silver in Fig. 2.20c. With further increase of the wavelength, and moving outside the resonance, the absorption further deacreses. A similar behavior is also visible in the case of a silver disk. However, it is not pronounced so much because part of the light is absorbed by the NiFe layer and silicon substrate. At approx. 450 nm the resonance peak is visible for the case of a silver disk on NiFe. This resonance is most likely caused by the electric dipole resonance, but for proper analysis, the multipolar decomposition would be necessary [120].

In the case of silicon, the situation is much more constant across the studied wavelengths. This is caused by the fact, that there is not so much variation in the index of refraction (for all wavelengths it is above 1), see Fig. 2.20c. In the case of the sphere in air, only a small increase in resonance is visible around the wavelength of 700 nm. In the case of silicon disk on NiFe substrate, we can observe a slight drop in scattering cross section after wavelength of 400 nm, which is connected to the silicon absorption edge, see Fig. 2.20c.

Now, we discuss the spatial profile of the electromagnetic field in the case of silicon and silver discs and their differences. The cross-section in the middle of the NiFe layer is shown in Fig. 2.20d for the silicon disk and in Fig. 2.20e for the silver disk. We can observe that in the case of the silicon disk, the majority of the electric field is concentrated under it. On the other hand, under the silver disk, the situation is completely reversed, and the majority of the electric field is around the disk. This is caused by the huge difference in the transparency between the two materials. The silicon disk is at this wavelength (532 nm) absorbing, but transparent medium ($n > 1$). In the case of silver, the index of refraction is below 1, and absorption is approx. four times larger than in the case of silicon, see Fig. 2.20c. Both electric field distributions dominantly resemble characteristics of the electric dipole resonance. In the case of silver disk, the maximum magnitude of the squared electric field is higher by approx. 30 % in comparison with silicon disk. Fig.2.20f, g shows XZ-cross section for silicon and silver disks. In this view, a similar trend can be observed. The silver disk has squared electric field intensity concentrated to its edges, while in the case of silicon disk, we can observe electric field distribution inside the disk.

So far, the discussion has focused on the specific case of a disk placed on the top of the NiFe layer. However, in a more general description, we can summarize that Mie resonances in dielectric materials (such as silicon) are better suited for far-field applications, where the penetration of the light into the material is desirable. Moreover, they can have much more pronounced magnetic resonances (enhance more magnetic field) in comparison to the metallic particles. These properties allow them to be used in, e.g., so-called metasurfaces [121]. On the other hand, resonances in metallic (plasmonic) particles provide higher electric field enhancement and can be miniaturized to smaller sizes.

2.4.2. Calculation of the BLS signal enhanced by Mie resonance

Here, we present the calculation of the BLS signal obtained on the sample with a dielectric nanoresonator. The calculation is performed in a similar way as previously discussed in this chapter, however to account for the scattering center, the simulations of Maxwell equations had to be used.

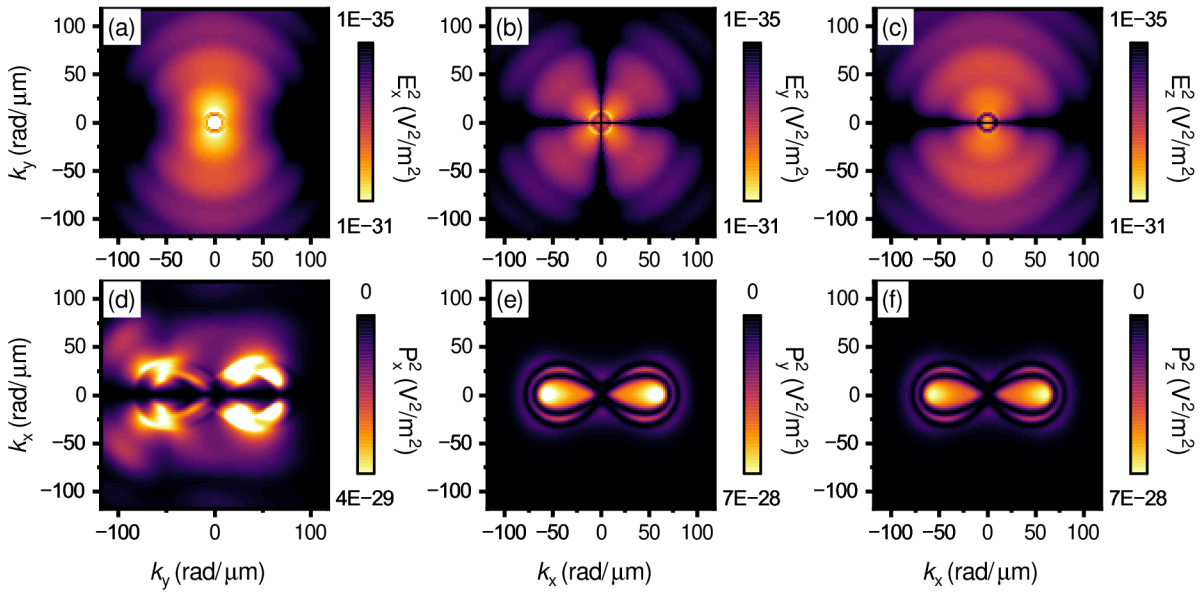

Figure 2.21: Induced polarization in case of presence of scattering center. a, b, c Squared electric field profiles in reciprocal space of each electric field component. The scale of colorbar is logarithmic. **d, e, f,** Squared induced polarization in the NiFe layer. The polarization was calculated for spin waves in 30 nm-thick Permalloy layer in external magnetic field of 550 mT. The isofrequency surface for 28 GHz is shown. The colorbar scale is linear.

To calculate the polarization vector in the presence of the scattering center, we solved the Maxwell equation in time and space and obtained the electric field in the middle of the NiFe layer. The squared electric field profiles in reciprocal space are shown in Fig. 2.21a-c. We can observe that in all electric field components, the electric field distributions span into much higher wavevectors in comparison to the case of illumination of the bare film, see Fig. 2.11a-c, where it was limited to approx. 10 $\frac{\text{rad}}{\mu\text{m}}$. Also note that x-component has no longer full polar symmetry, while the y-component keeps the four-fold symmetry, and z-component keeps the two-fold symmetry. All three components have comparable squared electric field strengths. This electric field is subsequently used for the calculation of the polarization vector by using Eq. 2.20, see Fig. 2.21d-f. We can observe that in the case of the presence of the scattering center (Fig. 2.21d-f) polarization with much higher wavevectors is induced, in comparison to the case of the bare film (Fig. 2.11g-i), where it was limited only to approx. 20 $\frac{\text{rad}}{\mu\text{m}}$. However, we again stress out, that inducing the polarization is only the first step. For actual measurement, it is necessary that the polarization is able to emit towards the far-field and be collected by the objective lens. The emission of the free-light inaccessible wavevectors (above approx. 10 $\frac{\text{rad}}{\mu\text{m}}$) is not possible in the case of bare film. This emission (as stated before) is described by the dyadic Green function. In the case of the presence of the scattering center (silicon disk in this case), the light's wavevectors are *fliped-over* to the free-light accessible range, which allows them to propagate towards the detector and form a BLS signal.
The whole process can be summarized by following equation

$$\sigma(\omega_\text{m}) = \int \text{d}^2 r_\parallel \int \text{d}^2 k_\text{m} \left| h(\mathbf{r}_\parallel) \int\limits_{k_\text{p} \leq k_0 \text{NA}} \text{d}^2 k_\text{p}\, e^{\text{i}\mathbf{k}_\text{p}\cdot\mathbf{r}_\parallel} \int \text{d}^2 k'_\text{p} \hat{\mathbf{G}}(\mathbf{k}_\text{p}, \mathbf{k}'_\text{p})\, \hat{\boldsymbol{\chi}}(\omega_\text{m}, \mathbf{k}_\text{m}) \mathbf{E}_\text{d}(\mathbf{k}'_\text{p} - \mathbf{k}_\text{m}) \right|^2 . \tag{2.41}$$

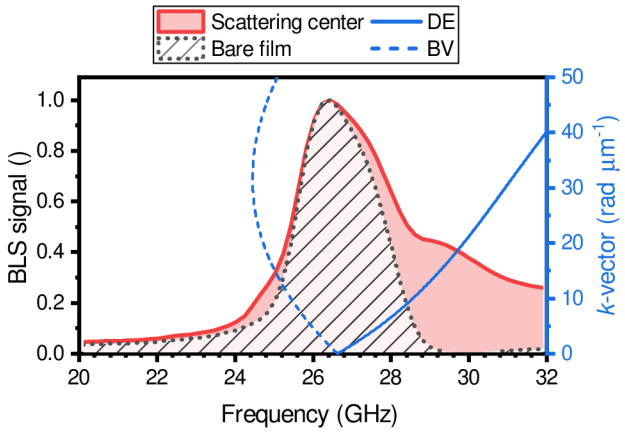

Figure 2.22: Resulting BLS signal in the presence of the scattering center. The normalized BLS signal was calculated for the case of 180 nm-wide silicon disk and on bare film for comparison. Both calculations are done for 30 nm-thick NiFe layer external field of 550 mT. The blue lines show the dispersion relation of the spin waves in Damon-Eshbach (DE) and backward-volume (BV) geometry.

By solving this equation, with use of numerical tools, we can obtain the BLS spectra in the presence of the scattering center, see Fig. 2.22. We can observe that the peak has broadened to both higher and lower frequencies. This suggests that the spin-waves with higher wavevectors were measured. The broadening towards the higher frequencies is caused by the increased sensitivity to the spin waves propagating in Damon-Eshbach geometry, whereas the broadening towards the lower frequencies is caused by the increased wavevector sensitivity to spin waves propagating in backward geometry.

3. Experimental methods

This chapter describes used setups and experimental techniques. The most important technique for this work is Brillouin light scattering. The inelastic scattering theory has already been described in previous chapters, so the following section only deals with experimental technicalities. Furthermore, I briefly discuss ferromagnetic resonance measurement for magnetic characterization, scattering measurement for optical characterization, numerical solving of the differential equations for modeling the investigated systems, and method for extracting dispersion relation from micromagnetic simulation.

3.1. Micro-focused Brillouin light scattering

For experiments, I used a micro-focused Brillouin light scattering setup [123, 124], which is located at CEITEC Nano research infrastructure. The setup was originally designed and built by Lukáš Flajšman [10]. Most of the optical parts were ordered from Thorlabs, Inc., microscope was ordered from THATec Innovation GmbH i.L. and interferometer from The Table Stable Ltd. In the scope of my master thesis, I rebuilt the setup to make the alignment more convenient, cover the optical path to improve stability and safety, and upgraded it with the possibility to perform phase-resolved measurements. [122]. During my PhD, I added the time-resolved functionality.

The schematics of the setup is shown in Fig. 3.1. In the following text, we go through the individual parts and sections of the used setup. We start at the light source (laser) and follow the laser beam through Faraday isolator, Fabry-Perot etalon, beam-splitter for reference beam, polarizer and lambda half plate, electro-optical modulator, microscope, and interferometer.

3.1.1. Light source

In order to get stable system with minimum noise a single mode laser is necessary. The light source has to deliver sufficient power to the sample and, at the same time, provide coherent light without any undesirable modes[1]. We use two types of laser sources in our setup, both with wavelength of 532 nm. The first one is Torus from the Laser Component. The maximal output power from this laser is 200 mW. The second option is Samba by Cobolt. This laser provides 300 mW of output power and was used for all experiments presented in the scope of this thesis. Both lasers provide very similar performance, and currently inactive laser mainly serves as a back-up.

The stability over prolonged period of time, is necessary over the long BLS measurement (e.g. 2D spatial mapping). To test this, we measured the output power over the span of two hours, see Fig. 3.2a. From the measured data, one can see, that the both lasers

[1] By undesirable mode we mean light shifted in frequency in respect to the main output.

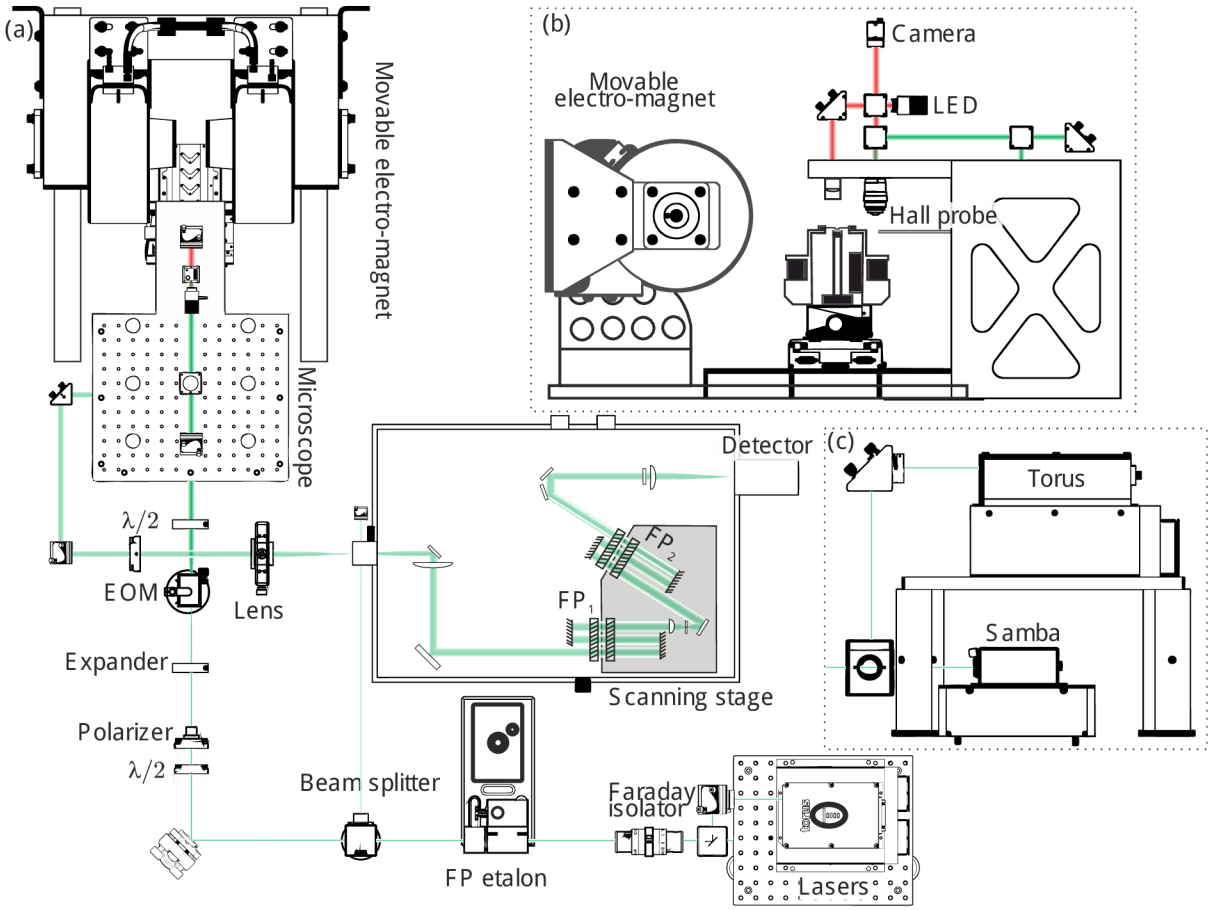

Figure 3.1: (a) Schematic of the used BLS setup. (b) Side-view of the microscope module and electromagnet. (c) The side-view of the two used lasers. Reproduced from [122].

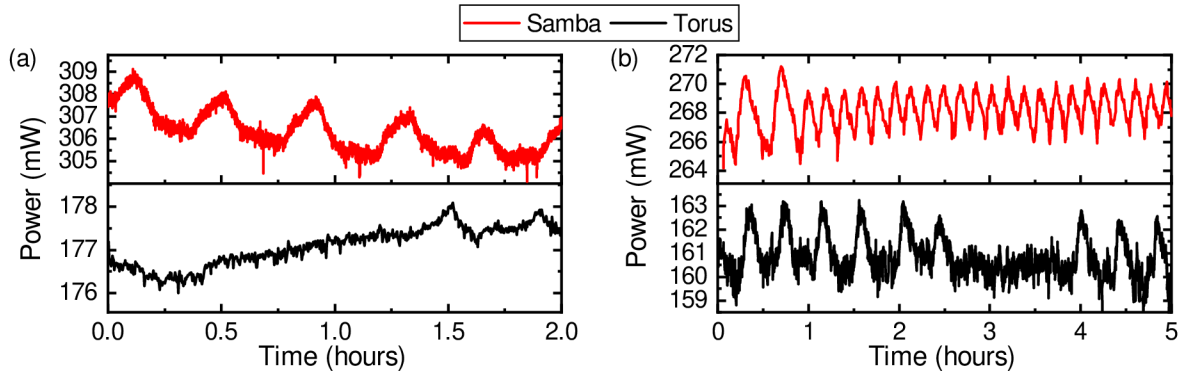

Figure 3.2: Stability of the used lasers. **a,** The power measured directly after the output of the lasers in time-span of two hours. **b,** The power measured after the Fabry-perot etalon (mode filter) in time-span of five hours. Reproduced from [122].

oscillate within the 3 mW ($\approx$ 1.5 %). Such stability is sufficient for the measurements presented in Chapters 4, 5, 6.

If the light is reflected back to the output pinhole of the laser, it can interfere with the feedback loop of the laser and decrease the stability or damage the laser. To prevent that, a device called Faraday isolator is employed. This device uses the fact that the Faraday rotation is nonreciprocal, which means that it depends on the direction of propagation of the light. Nevertheless, the setup can be safely operated even without the Faraday isolator, if a tiny misalignment of the Faraday isolator is introduced. In that case, the reflected light can not pass through the output pinhole of the laser, and thus can not affect its operation. The Faraday isolator was used for all the presented experiments, but currently the setup is being operated without it.

Next device in laser path, Fabry-Perot etalon[2], can be used to further enhance the spectral purity of the laser light. In our setup we use the solution provided by Table Stable ltd. [125]. The cavity length is stabilized based on the feedback loop by the thermal expansion of the metal plate, on which one of the cavity mirror is mounted. The feedback loop is based on the optimization of the light signal which passes through the cavity.

The attenuation of the light in the cavity is approximately 8 %. The stable state of the feedback loop is reached after roughly two hours of operation. The oscillations of the laser power are increased to $\approx$ 2 % after the etalon, see Fig. 3.2b.

Next, a small fraction of the light (about 10%) is split in the beam splitter and guided towards the Tandem-Fabry-Perot interferometer (TFPi), where it is used for stabilization.

To control the incident power, the combination of the lambda-half plate and polarizer is employed. The ability to change the incident power on sample is essential, as in most experiment the heating of the sample is undesirable as it can change e.g. effective saturation magnetization, or affect the shape of the spectra by changing the spin-wave population. The angle of the polarizer is fixed, and the lambda half plate is in automatic rotational mount. In this setting the polarization axis of the incident light can be freely changed without any regard to the incident power, and at the same time the power can be freely changed without any dependence to the incident polarization.

[2]Etalon consists of the two reflecting glass plates, which allows transmission only of the light with wavelength that equals to an integer multiples of the cavity length.

In Fig. 3.3a, the dependence of the incident power on angle of lambda half plate is shown. The powers in range from near zero (0.1 mW) to 15 mW can be achieved. The incident power exhibits the four-fold symmetry, as the rotation of the polarization angle by lambda half plate is double the rotation of its axis [126]. The BLS signal strength has a linear trend in dependence to the incident power, see Fig. 3.3b. This is in agreement with developed theory in Chapter 2, see Eq. 2.31.

3.1.2. Phase resolution

To allow phase investigation, and thus the wavevector measurement, signal with constant phase, sufficient coherency, and the same frequency as is the frequency of the studied spin wave has to be introduced. This is usually done by modulating part of the laser beam by electro-optic modulator (EOM) [72, 122, 127–129], see Fig. 3.4a. Introduction of such reference signal with constant phase allows to observe the interference between this modulated reference signal and the light undergoing BLS process. As the BLS process conserves the overall phase (the phase of the light is shifted by the phase of the spin wave), a constructive or destructive interference between the reference and light which undergoes BLS process can be observed.

In order to get the information about the phase of spin waves, we need to perform five separate measurements (usually, only four measurements are performed, but the presented approach gives better sensitivity when the signal from coherent spin waves becomes comparable to the thermal background [122]), see Fig. 3.4b. In the first measurement $[E(x)]$, only the EOM is pumped and we get only the combination of the elastic scattering of light, which already has the frequency upshifted by EOM, and background signal, which is incoherent and mostly originates from the thermally excited spin waves. In the second measurement $[R(x)]$, only the microstrip antenna, which serves for the excitation of the spin waves, on the sample is pumped, and in this setting only information about coherent spin waves and background signal is gathered. In the third measurement $[T(x)]$ pumping is completely turned off and the gathered signal represents only incoherent background. In the fourth and fifth measurements $[r_0(x), r_{\frac{\pi}{2}}(x)]$ both, EOM and microstrip antenna, are pumped and the signal represents interference between EOM and BLS. The thermal incoherent background is present in these two cases as well. The disparity between the

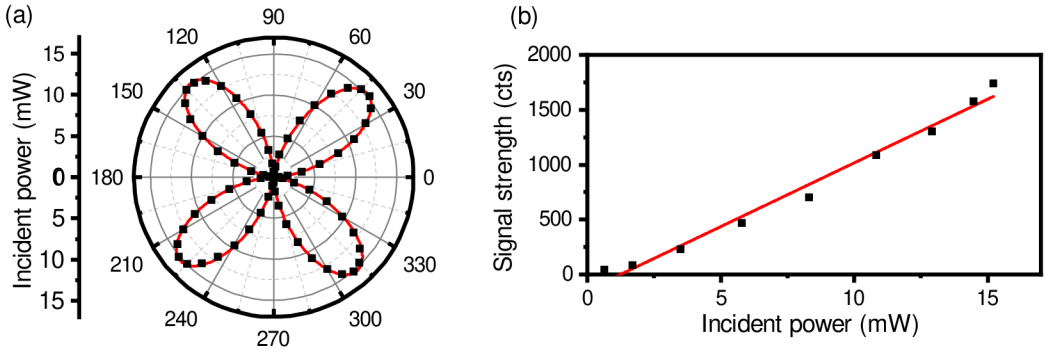

Figure 3.3: Adjusting the incident laser power by changing the angle of lambda half plate. a, The incident intensity versus the half-wave plate angle. The measured data (squares) were fitted with the sin2 (red line). **b,** Signal strength in dependence on the incident intensity. The measured data (squares) were fitted with a linear function (red line). Reproduced from [122].

fourth and fifth measurement is in the phase-difference between the EOM pumping. This difference has to be set exactly to the $\pi/2$ rad.

Once we measure all five signals, the complex spin-wave function can be calculated as

$$\mathrm{Re}\left\{\Psi_{\mathrm{SW}}(x)\right\} = \frac{r_0(x) - R(x) - E(x) + T(x)}{2\sqrt{E(x) - T(x)}}, \tag{3.1a}$$

$$\mathrm{Im}\left\{\Psi_{\mathrm{SW}}(x)\right\} = \frac{r_{\frac{\pi}{2}}(x) - R(x) - E(x) + T(x)}{2\sqrt{E(x) - T(x)}}. \tag{3.1b}$$

From this complex spin-wave function (Ψ_{SW}), the spin wave phase (Φ_{SW}) can be calculated as

$$\Phi_{\mathrm{SW}} = \mathrm{atan}\left(\frac{\mathrm{Im}}{\mathrm{Re}}\right) + s\pi, \tag{3.2}$$

where $s = 0, \pm 1$ and it depends on the quadrant of the complex spin wave. In homogeneus media, the dependency of the phase on distance from the spin wave source (in our case microstrip antenna) can be used to get the value of the wavevector of measured spin wave. The wrapped phase exhibits noncontinuous jumps, where the spacing between them is equal to the wavelength of the studied spin wave, see Fig. 3.4c. If the phase is unwrapped, the slope of the linear evolution is equal to the spin-wave wavenumber. Although this technique is quite straightforward, some precautions should be taken into account. The BLS signal should be given only by a single coherent wave, the wave should be in linear regime, and there should be no change of the wavelength/frequency with propagation distance. In cases with good signal-to-noise ratio and decay length-to-wavelength ratio, the wavelength can be also measured with single interference measurement by fitting experimental data by following equation

$$r(x) = R(x) + E(x) + \sqrt{2R(x)E(x)}\cos\left(2\pi\frac{x}{\lambda} + \Phi_0\right), \tag{3.3}$$

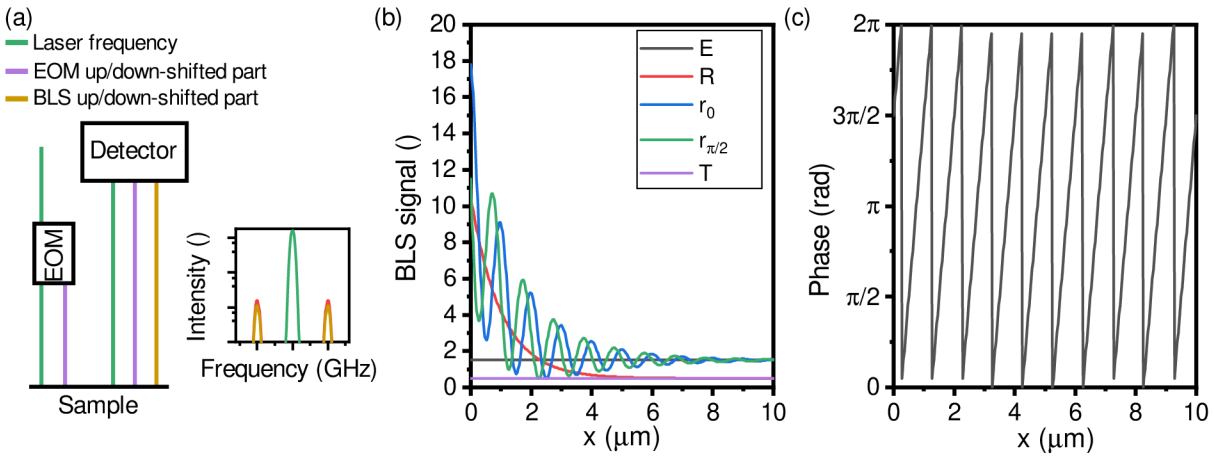

Figure 3.4: Principle of the phase reconstruction using micro-focused BLS. a, Schematics of the partition of light present in phase-resolved micro-focused BLS. **b,** Model of all-five necessary signals to reconstruct the full-phase of spin waves. **c,** Calculated wrapped phase of the spin waves from modeled signals in panel **(b)**.

where $E(x)$ is assumed as a constant (for homogeneous samples), λ is the wavelength of spin waves, Φ_0 is the phase offset and the $R(x)$ is exponentially decaying function

$$R = R_{\max} \exp\left(-\frac{x}{l_{\text{att}}}\right), \tag{3.4}$$

where $R_{\max}$ is the maximum of spin wave intensity and l_{att} is the propagation length. This expression is shown in Fig. 3.4b as green and blue solid lines. By fitting the Eq. 3.3 to experimental data, one can obtain wavelength (wavenumber), amplitude ($R_{\max}$), and decay length. But usually, from this fit only the wavelength is of interest, as other fitting parameters does not give reliable results, and it is generally better to obtain these parameters from fitting the intensity measurement $[R(x)]$.

Experimental realization

In our setup the EOM is placed in the focal point of the beam expander to achieve good throughput, see Fig. 3.1. The beam expander consits of the two lenses with focal lengths of 100 mm and 300 mm. This ratio expands the beam by a factor of 3 to approx. 5 mm in diameter.

The schematics of the radio-frequency (RF) elements is shown in Fig. 3.5. The RF signal is formed in signal generator R&S SMB100A. This signal is split by Narda-ATM P214H 3 dB power divider. To allow for full automation of the measurement, the PC controlled RF switches Teledyne CCR-33S8E-T are employed.

First, let's discuss the right branch (connected to the antenna on sample). After the switch, the amplifier can be optionally placed. The SMB100A signal generator can provide max 10 dBm of RF power. This is usually insufficient for investigation of the non-linear phenomena in metallic samples, as e.g. parametric pumping. In our setup, we usually use Nextec-RF NB00441, or NB00616 amplifiers. The NB00441 works in the frequency range of 2-20 GHz and can achieve the power up to 20 dBm. The second amplifier, NB00616, can achieve higher powers up to 32 dBm. but is limited to narrower frequency range of 8-14 GHz.

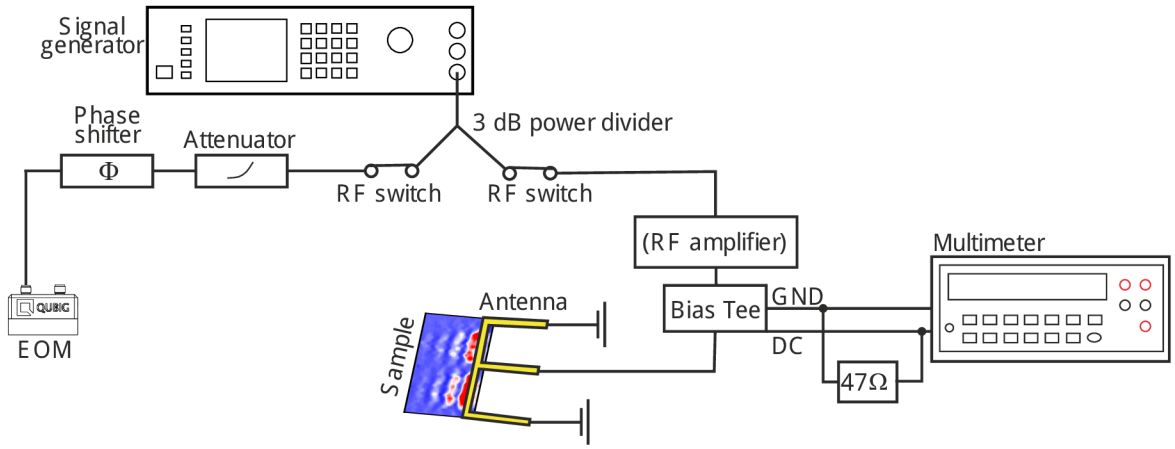

Figure 3.5: Schematics of the phase-resolved RF setup. This schematics only shows the parts of the setup related to the RF. For the light part see Fig. 3.1. The RF amplifier (in schematics in brackets) is only optional, and is used when the high RF power is needed. The resistor with resistance of 47 Ω is connected parallel to the investigated antenna to protect it from burn by measurement current.

To check proper electrical contact between the contacting RF probe and fabricated antenna we can measure DC resistance. To protect the delicate (nano) antenna structures on the sample a resistor with resistance of $R_{47} = 47\,\Omega$ is connected parallel to the contacted antenna. In such setting the current is flowing constantly through this resistor, and thus the structures on sample are protected from sudden peaks caused by e.g. static discharge. The resulting resistance of contact and antenna structure (R_a) is then calculated from the measured resistance (R_m) as

$$R_\mathrm{a} = \frac{R_{47} R_\mathrm{m}}{R_{47} - R_\mathrm{m}}. \tag{3.5}$$

Now, we discuss the left branch (connected to the EOM). To suppress uncertainties caused by the noise one has to balance the signal strengths between the EOM and BLS. For this purpose the attenuator AV884H-10-ITI by Impulse Technologies Inc. is employed. Usually, the output power is set on signal generator to provide the highest spin-wave amplitude in linear regime. Then the operator needs to investigate the approximate distance where the signal becomes undetectable due to the thermal background. Then roughly in the middle between this point, both signal strengths are equalized with use of the attenuator.

To change the phase of EOM signal, for acquisition of the signals $r_{\frac{\pi}{2}}(x)$, and $r_0(x)$, the motorized phase shifter Narda-ATM P1507-28 is used. Due to the motorization, operator is able to precisely set the number of required steps to achieve the phase shift of 90 degrees ($\pi/2$), thus the experimental systems with signal strength comparable to thermal background can be easily measured[3]. After this, the signal finally reaches the EOM QUBIG TW-15M1-VIS. The output port of the EOM is terminated by $50\,\Omega$ terminator.

3.1.3. Microscope

To allow for precise navigation on the sample and sharp focus, a reflective microscope is built on a rigid aluminum construction. To guide the light to top platform, a periscope is used, see Fig. 3.1b. The light then goes through 90:10 beam splitter cube, where 90 % of light is damped and only 10 % passes through. In this way, we are able to recover 90 % of the BLS signal, and as the laser provides sufficient power, this configuration is optimal. Above the objective lens, a dichroic mirror is placed. This mirror is tuned to reflect the green light, but pass through red light. This behavior is used to separate lights used for imaging (red) and for measurement (green).

In majority of the experiments we use an objective lens with the high numerical aperture of 0.75 (Zeiss LD EC Epiplan-Neofluar 100x/0.75 BD). The combination of the imaging system and nano-positioning stage is utilized to position the laser spot on the sample. The *xyz*-stage by Physik Instrument is used (V-551, and V-501), which allows positioning with precision down to 1 nm and also has long travel range enabling the automatized transfer from contacting microscope (large view-field) to measurement objective lens. Amortization of this transfer makes it easier to find the areas of interest with big view-field.

The same objective lens collects the back-scattered light. The light then shares the same path with the incident light until the 90:10 beam splitter cube. Now the 90 % of light

[3]Typically, in setups where the non-motorized phase shifter is used, the procedure is as follows: operator puts the laser spot near the antenna to get high signal. Then, maximizes the signal with phase shifter. After that, the operator moves the phase shifter to either direction while counting the revolutions until the minimum is reached. Afterwards it is necessary to divide the count by two and move the phase shifter by this count in opposite direction.

is reflected to the periscope. After two more mirrors, the optional 90:10 beam splitter cube can be included to use part of the light for maintaning focus. This cube is placed in a way, that 90 % of light is transmitted and 10 % of light is reflected. The reflected light then passes through the lens with small focal distance at which an aperture is placed. After the light passes through the aperture, it hits a photo-diode. If the sample is in the focus, the backscattered light will be focused to infinity, and transmission through the aperture would be maximized. By sweeping the z-position of the sample, one can find this maximum. Such procedure can be performed several times in between the measurements to maintain good performance e.g. through long 2D scans. In this approach, the 10 % of signal is lost. The preferable option is to use focusing using the imaging system.

Imaging system

The system is equipped with both, bright field and dark field imaging systems. The bright field system uses the red light generated in LED. This light is divergent; thus, we use a system of lenses to focus the light on the back aperture of the objective lens. The bright field imaging system is also used to navigate the sample and contact the RF probes. For this purpose, we split the red light on the beam splitter (see Figure 3.1) and guide it towards the lens with a focal distance of 150 mm. The view-field of this navigation system is in order of millimeters, while the system with an objective lens has a view-field of 60 μm.

The dark field option is available only with the objective lens. This is realized by the white LED with an output power of 2 W. The light is also collimated by the lens and its angle of incidence is around 70 degrees from normal incident, so the reflected light is not directly collected by the objective lens.

The autofocus routine is implemented in similar fashion as with laser light. The z-position of the sample is swept. In each z-position, Fourier transform of image is performed, and region with higher reciprocal wavevector (details) is summed and saved as a scalar value. These scalar values then resembles Gaussian shape in dependancy to the z-position of the sample. Then the position with the maximal value is selected. The necessary ingredient for this routine is, that some structures with details (i.e. lithographically prepared or dirts) are present on the sample.

Magnetic field

To create a magnetic field in the sample plane, we use electromagnet GMW5403 on the rail system (see Figure 3.1). The power to the magnet is supplied by the two bipolar current sources KEPCO BOP20-DL, which are connected in parallel. The maximum available field is approximately 670 mT. The field is measured with hall probe LakeShore 450, placed slightly off center and corrected by a linear factor of 0.96.

3.1.4. Tandem-Fabry-Perot interferometer

To analyze the frequency of the scattered light, the so-called Fabry-Perot interferometer is utilized. It consists of the two high reflectivity mirrors, with perfectly flat surfaces mounted parallel to each other. Due to the constructive and destructive interference,

only the light with specific wavelength can pass through it. The transmission function of single Fabry-Perot interferometer can be expressed as

$$T = T_0 \frac{1}{1 + (4F^2/\pi^2)\sin^2(2\pi L/\lambda)}, \tag{3.6}$$

where T_0 is the maximal transmission (limited by the absorption of the mirrors and the system in general), F is a finesse of the mirrors, L is the cavity length, and λ is a wavelength of the used light. From the Eq. 3.6, it can be seen that the transmission function have several transmission peaks separated by multiplies of the wavelength. The finesse F defines the quality of the interferometer transmission and is defined as [112]

$$F = \frac{\pi\sqrt{R}}{1-R}, \tag{3.7}$$

where R is a reflectivity of the Fabry-Perot mirrors. Thus a higher reflectivity would result into the better transmission characteristic.

In BLS experiments, one has to achieve the resolution in the order of hundreds of megahertz and at the same time free-spectral range at least in the order of gigahertz. Knowing the fact, that the frequency of the used light is approximately 563 THz, the interferometer has to be able able to resolve changes in the order of $\approx 10^{-6}$. Also, as the cross-section of the BLS process is very low, the desired contrast has to be higher then 10^{16} [112].

To tackle these challenges, one can use the two Fabry-Perot interferometers with different cavity lengths in series, so-called vernier arrangement [112, 130–132]. In this design the change in the cavity lengths has to obey the following relation

$$\frac{\Delta L_1}{\Delta L_2} = \frac{L_1}{L_2}, \tag{3.8}$$

where L (ΔL)is length (change) of the first and second cavity.

Such design is really cumbersome, as the cavity lengths have to stay perfectly synchronized during the scanning. One of the first approaches was to change the air pressure in both cavities simultaneously, and thus the resulting optical length was changed synchronously. However, this approach cannot provide long scan ranges [132, 133]. The Sandercock's design of tandem Fabry-Perot interferometer (TFPi) consists of the two Fabry-Perot cavities. The lengths of both cavities are different but are bounded by the following geometrical relation, where ϑ is the angle between both cavities and is given by the construction geometry (see Fig. 3.1)

$$L_2 = L_1 \cos\vartheta. \tag{3.9}$$

The multiplication of the transmission function of individual cavities then gives the overall transmission function. The demonstration of this principle is shown in Figure 3.6. In Fig. 3.6a, b, the transmission functions of the two Fabry-Perot cavities are shown. Both cavity lengths are aligned in a way, that light with wavelength exactly 532 nm can pass through it. We can see, that the single cavity cannot provide sufficient free spectral range[4], see Fig. 3.6d,e. Now, if we multiply these two transmission function we get much larger free spectral range, see Fig. 3.6c, f.

[4]Free spectral range is frequency (wavelength) distance between the two transmission maxima, and effectively defines the largest possible continuous scanning range.

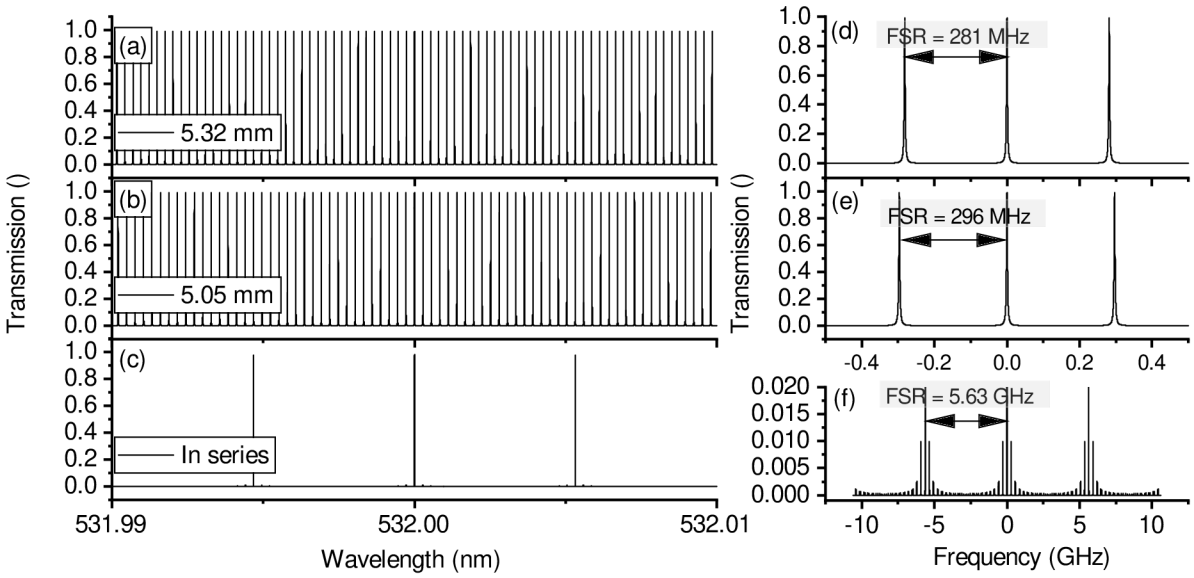

Figure 3.6: Transmission characteristic of the tandem Fabry-Perot interferometer.a, b, c, Transmission depending on the wavelength for FPis with **(a)** $L_1 = 5.32\,\mathrm{mm}$, **(b)** $L_1 = 5.05\,\mathrm{mm}$ and **(c)** both in tandem operation. **d, e, f,** details of **(a)**, **(b)** and **(c)**.

In the Sandercock's type of TFPi, the free spectral range (FSR) can be calculated as [134]

$$\mathrm{FSR} = \frac{c}{2L_1} \approx \frac{150}{L_1}, \tag{3.10}$$

where c is speed of light. The calculated free spectral range is shown in Fig. 3.7a. The FSR of $\approx 1\,\mathrm{THz}$ can be achieved, with the mirror spacing of $50\,\mu\mathrm{m}$. But it does not mean, that the measurement is limited only to this values, as one can also measure in between the higher transmission maxima (in second, third, ..., FSR window). Note, with shorter mirror spacing, the resolution is decreased. This can be calculated by the following formula [12, 134]

$$\mathrm{FWHM} = \mathrm{FSR}/F. \tag{3.11}$$

Fig. 3.7b shows calculated FWHM of the transmission function for mirrors with finesse of 100. For short L_1 the FWHM is improving rapidly. In 3 mm, which was setting for most of the experiments in this thesis, the FWHM is around 0.5 GHz. At 20 mm, which is still achievable with reasonable operator's persistence, the FWHM is below 0.1 GHz.

3.2. Ferromagnetic resonance measurement

The setup used for ferromagnetic resonance (FMR) measurement was developed by Václav Roučka and Marek Vaňatka [14, 135]. During my PhD, I improved the setup by using a bigger water-cooled magnet with much larger pole pieces providing a homogeneous external field. Moreover, the magnet provided higher fields (up to approx. 1.7 T), allowing the proper analysis of magnetic damping. The analysis procedure is based on the codes written by Marek Vaňatka [136].

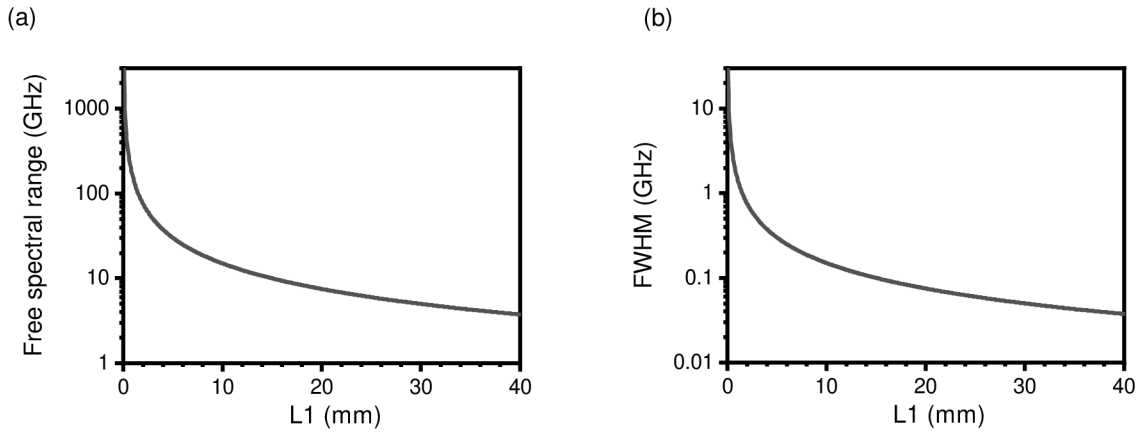

Figure 3.7: Characterization of TFPi depending on the mirror distance L_1.a, b, Free spectral range **(a)**, and FWHM **(b)** in dependence to the mirror distance L_1.

3.2.1. Theory of FMR

The ferromagnetic resonance is a state when the magnetization of a sample is in precession with the same phase. Also, it can be understood as the limiting case of spin waves for $k = 0$. The theoretical description for the simplest case (without any anisotropy and for the external field applied in the in-inplane direction) is given by [137]

$$\omega_{\mathrm{FMR}}^2 = \omega_{\mathrm{H}}(\omega_{\mathrm{M}} + \omega_{\mathrm{H}}), \tag{3.12}$$

where $\omega_{\mathrm{H}} = \mu_0\gamma H_{\mathrm{ext}}$, $\omega_{\mathrm{M}} = \mu_0\gamma M_{\mathrm{S}}$, μ_0 is permeability of vacuum, γ is gyromagnetic ratio, H_{ext} is external field, and M_{S} is saturation magnetization. By analysis of the mutual dependency of the terms in the Eq. 3.12, one can see that if applied external field is comparable in magnitude with $\mu_0 M_{\mathrm{s}}$, the gyromagnetic ratio and saturation magnetization can be deduced from a single dataset.

Historically, the FMR was measured using the microwave cavities tuned to the specific frequency [138, 139]. With advent of the more sensitive instrumentation the so-called broadband FMR became possible. In such setup, we usually sweep both, external magnetic field and frequency[14, 139, 140].

3.2.2. Experimental realization of FMR measurement

In presented experiments we used the setup shown in Fig. 3.8. To measure scattering parameters the vector network analyzer (VNA) Rohde&Schwarz ZVA50 is used. From these scattering parameters, the power absorbed by the so-called device under test (DUT)[5] can be calculated. Scattering parameters relate the reflected and transmitted powers from the two independent ports

$$\begin{pmatrix} b_1 \\ b_2 \end{pmatrix} = \begin{pmatrix} S_{11} & S_{12} \\ S_{21} & S_{22} \end{pmatrix} \begin{pmatrix} a_1 \\ a_2 \end{pmatrix}, \tag{3.13}$$

where a_i (b_i) is the generated (measured) wave from port i, and S_{ij} is a scattering parameter between the port i and j. The scattering parameters are complex numbers, which represent the both, magnitude and the phase of the measured signal. Usually, the VNA

[5] In described case magnetic sample.

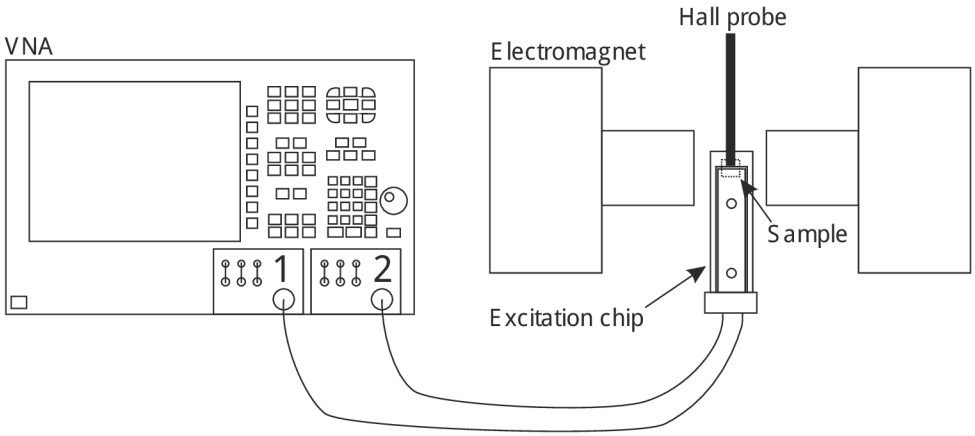

Figure 3.8: Sketch of the experimental setup used for FMR measurements. the electromagnet is placed on the rail, so the sample can be placed without changing the RF path

outputs S-parameters in form of magnitude expressed in dB and phase in radians. To calculate the absorbed or transmitted power, one can convert this output to real and imaginary representation with linear scale

$$S_{ij,\mathrm{lin}} = 10^{\frac{S_{ij,\mathrm{mag}}}{10}} \exp\left(iS_{ij,\mathrm{mag}}\right). \tag{3.14}$$

The transmitted power (for S_{12} and S_{21}) or absorbed power (S_{11} and S_{22}) can be calculated

$$P = S_{ij} P_{\mathrm{inp}}, \tag{3.15}$$

where P is a absorbed or transmitted power, P_{inp} is input power.

The measured signal is influenced by a lot of factors, e.g. bends in the connection cables, not perfect contact, etc., which results in the not completely flat transmission characteristic. This background signal can be such high, that especially in samples with lower signal, can hide all the spin-wave related signal. To get rid of the unwanted contribution one can apply median background subtraction [14, 136]. For this, the scattering parameter has to be acquired for all frequencies across various externals fields. The field and frequency range has to be chosen in a way, that in the lowest and highest fields the spin wave spectra will not overlap (even with broadening taken into the account). The median subtraction can be expressed as

$$S_{ij,\mathrm{sub}} = S_{ij} - \mathrm{Med}_B\left(S_{ij}\right), \tag{3.16}$$

where Med_B is median dependent on frequency (taken in accordance to external field for each measured frequency).

The analysis in the scope of this thesis is focused to the S_{21} parameter, which describes the transmission from the first to the second port. The resonance frequency can be described by following function

$$S_{12,\mathrm{sub}} = y_0 + \frac{2A}{\pi} \frac{w}{4(f - f_{\mathrm{FMR}})^2 + w^2}, \tag{3.17}$$

where A is a area of the peak, w is full-width-at-half-maximum, f_{FMR} is the position of the ferromagnetic resonance, y_0 is the background level.

In the presented experiments, we used the so-called flip-chip technique. In this technique, the thin film is placed on the excitation antenna with the magnetic layer facing down [141].

3.3. Scattering measurements

To optically characterize any scattering center, one can measure relative scattering intensity. For this type of measurement, I used the existing setup Nanonics Imaging MV 4000 maintained by the group of Prof. Tomáš Šikola. The setup can serve as a scanning near-field optical microscope, but here, it was used only for scattering measurement. During all measurements, I was helped by Filip Ligmajer.

3.3.1. Cross-section terms

Depending on the shape, dimensions, or material, the particles have different optical responses to the light with different wavelengths, see Chapter 4. The response can be described by so-called cross-section terms. These terms represent ratio between total light and scattered (C_{sca}), extinct (C_{exc}), and absorbed (C_{abs}) light. The extinct light is the light which cannot pass through the studied medium

$$C_{\mathrm{exc}} = C_{\mathrm{sca}} + C_{\mathrm{abs}}. \tag{3.18}$$

The sum of the all ratio should give 1

$$C_{\mathrm{exc}} + C_{\mathrm{sca}} + C_{\mathrm{abs}} = 1. \tag{3.19}$$

3.3.2. Experimental setup

Used setup allows measurement of scattering coefficient of individual particles using dark-field confocal spectroscopy, see schematics in Fig. 3.9. As a source of a white light a halogen lamp is used. By employing spectrometer, the scattering coefficient can be directly measured in dependency to wavelength of light.

The light from halogen lamp is guided to hollow elliptical mirror. In such setting, only outer ring is illuminated, as central part of the beam passes through the hollow elliptical

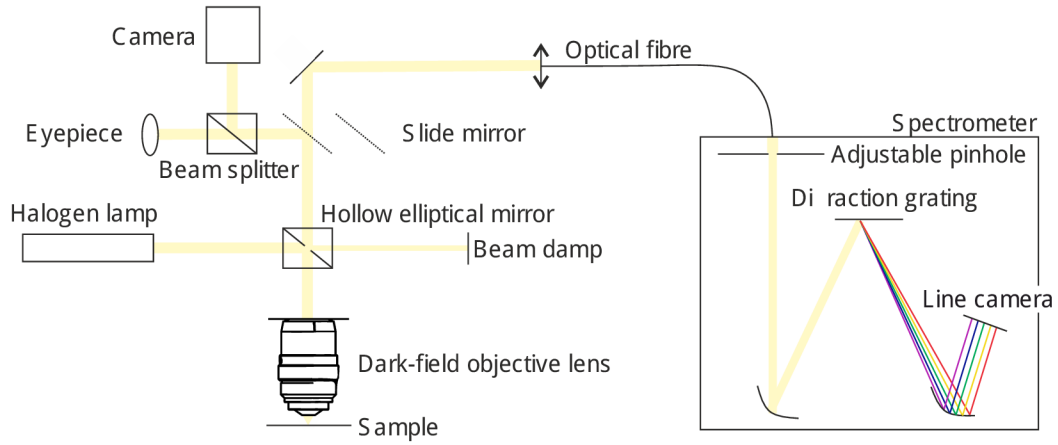

Figure 3.9: Sketch of the setup used for scattering measurements. Adapted from [142].

mirror and is attenuated in beam damp, see Fig. 3.9. The light is focused to sample by a dark-field objective lens (Olympus LMPLANFLN 100× NA=0.8). The backscattered light is collected by the same objective lens, but in central ring and passes through hollow in elliptic mirror. The slide mirror can be positioned either to the path of reflected light, or away. If the slide mirror is in the path, the image of nanoparticles can be directly seen in either eyepiece or on camera. Based on the position of resonance of the nanoparticle, it appears with different colors, i.e. nanoparticle with resonance centered around 530 nm appears green. Also, the live image from camera can be used for precise positioning. To measure spectral response of individual nanoparticle, the collection spot has to be precisely aligned to its position. To do this, a optical fibre is connected to the white light source with fibre-ready output. The slide mirror is put to the position with 50:50 beam splitter. This results in formation of white light spot in the image, formed by the light from optical fiber. By reciprocal arguments, one can assume that this spot is similar to a collection spot. By precise positioning of the fibre, one can align the spot to cross-hair. Once this aligment is done, the nanoparticles are selected by positioning of the sample stage in a way, that nanoparticle overlaps with the cross-hair. The width of the collection spot can be tuned by changing the width of optical fiber.

Once everything is aligned, the sliding mirror is completely removed. The light is spatially filtered by a 200 µm pinhole of a multimode optical fiber. Then the reflected light is directly guided to the spectrometer (Andor Shamrock 303i). In the spectrometer the individual wavelengths are angularly decomposed by diffraction grating and guided by parabolic mirrors to a CCD camera (Andor iDus DU420A-BU). The image recorded by the camera is averaged in vertical coordinates and the horizontal coordinates are recalculated to the light's wavelength.

The resulting relative scattering intensity is calculated as

$$I_{\mathrm{sca}} = \frac{I_{\mathrm{nd}} - I_{\mathrm{bg}}}{I_{\mathrm{ref}} - I_{\mathrm{bg}}}, \tag{3.20}$$

where I_{nd} is the dark-field signal collected from a nanoparticle, I_{bg} is the background, and I_{ref} is the signal from a spectrally uniform diffuse reflectance standard (Labsphere Inc.).

3.4. Numerical solving of the differential equations

This section introduces used numerical techniques. All techniques use available simulation tools, namely Lumerical's FDTD Solutions software for finite-differences-time-domain (FDTD), MuMax3 for micromagnetic simulations, and Comsol for multiphysics simulations. All FDTD simulations were performed by Martin Hrtoň, Filip Ligmajer, Michal Kvapil, and Jakub Krčma, and I have only analyzed the resulting electric field. The micromagnetic simulations were solely performed by me. During the development of the Comsol model, I was helped by Jakub Zlámal.

Solving the differential equation is usually needed to get a better insight into the experiments. Unfortunately, analytically this can be typically done only for a limited set of cases, especially with elementary geometries. Numerical calculations are essential for solving the differential equation in complex geometries, which are required to simulate experimental conditions. To solve spatially dependent differential equations, the space has to be divided to the so-called evaluation points. These divisions can be done in two ways. The first one uses regular elements and is called finite differences, see Fig. 3.10a.

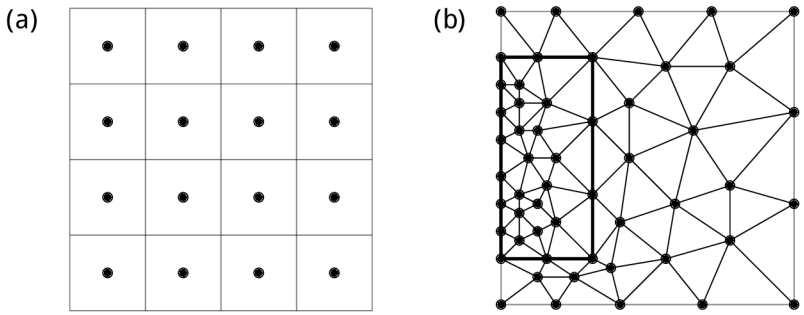

Figure 3.10: Comparison between finite differences and finite elements meshing method. a, Sketch of the regular rectangular grid of finite differences. **b,** Sketch of the grid of finite elements.

The advantage of this method is its simplicity. The second method uses irregular elements and is called finite elements method, see Fig. 3.10b. The advantage of this method is that the finesse of the mesh can be tuned locally. On the other hand, to use Fast Fourier transform (FFT) for analysis of the simulation, one has to interpolate results into the regular grid.

3.4.1. Finite-differences-time-domain (FDTD) simulations

Finite-differences-time-domain (FDTD) method is usually used for numerical solving of the Maxwell equations. The method was discovered by Yee in 1966 [143]. However it was named *Finite-differences-time-domain* and vastly popularized by Taflove in 1980 [144, 145]. This method is widely used in photonics research [146, 147].

The space is discretized into a regular grid (finite-differences method). The primary cell in this discretization is called Yee cell [143], see Fig. 3.11. On the first sight, it seems that it complicates the calculation, but the opposite is true. By using this cell the calculation is divergence free

$$\nabla \cdot (\varepsilon \boldsymbol{E}) = 0, \tag{3.21a}$$

$$\nabla \cdot (\mu \boldsymbol{H}) = 0, \tag{3.21b}$$

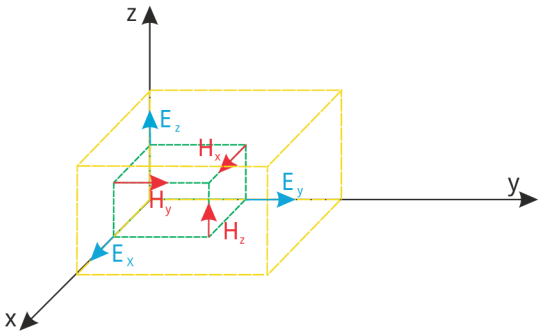

Figure 3.11: Sketch of Yee cell used for discretization in FDTD simulations. The electric and magnetic field are staggered in space.

where $\boldsymbol{E}$ is a electric field, $\boldsymbol{H}$ is a magnetic field, ε is a permittivity, and μ is a permeability. Calculation is not divergence free if all vector components are placed to origin of the cell on the boundaries between the two materials. Moreover, the physical boundary condition on the interface between two materials is naturally preserved. These properties then reduce the problem only to solving the two curl equations [143]

$$\frac{\partial \boldsymbol{B}}{\partial t} + \nabla \times \boldsymbol{E} = 0, \tag{3.22a}$$

$$\frac{\partial \boldsymbol{D}}{\partial t} - \nabla \times \boldsymbol{H} = \boldsymbol{J}, \tag{3.22b}$$

where $\boldsymbol{J}$ is a current vector, and

$$\boldsymbol{B} = \mu \boldsymbol{H}, \tag{3.23a}$$

$$\boldsymbol{D} = \varepsilon \boldsymbol{E}. \tag{3.23b}$$

Now the spatial derivation of the magnetic and electric field is very convenient, as the central differences gives the value directly in the desired position.

For the calculation to be valid, a proper cell size has to be chosen, so that the electromagnetic field does not change significantly. It is necessary to have dimensions of the cell well below the studied wavelengths. Moreover, if some objects with dimensions smaller than the studied wavelength are introduced, one has to make the cell smaller than size of these objects. As the finite-differences method requires uniform discretization in the whole simulation area, this requirement can quickly make simulation unfeasible. For example, if one wants to investigate an interaction between a beam with size of several tens of microns and a small sphere with a diameter of 100 nm, one has to use cell size with dimensions in order of tens of nanometers in whole simulation area.

As the theory of electromagnetic waves is linear, the principle of superposition can be used. Usually, in simulation the electrodynamics is excited via broadband pulse. Typically, the pulse has shape of the sinc function, therefore all the studied wavelengths are equally distributed in the simulation. Then, by performing Fourier transformation and filtering in reciprocal domain, the dynamics of individual wavelengths can be imaged. This significantly speeds up the simulation, where the dependency on wavelength is of interest, as all information can be extracted from single simulation.

Practical implementation of the FDTD simulations

In the scope of this work, calculations were performed using Lumerical's FDTD Solutions software.

The 3D simulation region spanned $5.3 \times 5.3 \times 1.36\,\mu\text{m}^3$, with the shorter side oriented along the optical axis (out-of-plane direction). Each model included a semi-infinite silicon substrate covered by a 30 nm thick permalloy thin film, on top of which was a 60 nm thick silicon disk of varying diameter located at the simulation center, see Fig. 3.12. Staircase meshing (mesh order 3) was adopted everywhere except in the vicinity of the silicon disk, where it was fixed to 3 nm cells in all directions. Boundary conditions in the form of perfectly matched layers were used at all simulation boundaries while applying appropriate symmetry conditions accelerated the computation. Gaussian source, implemented using the scalar approximation, was focused onto the disk-permalloy interface from the air side with the waist diameter set to 500 nm. The dielectric function of permalloy was taken from [148] and the dielectric function of silicon was taken from [149]. The resulting electric field

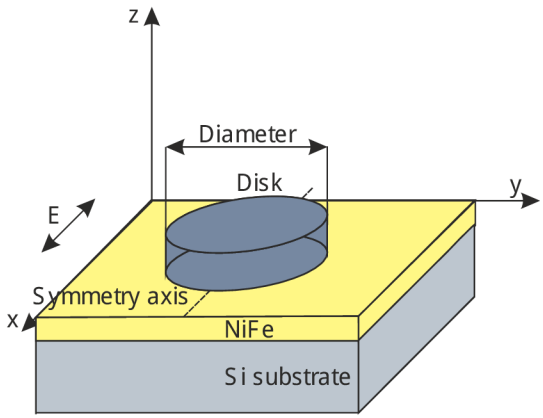

Figure 3.12: Sketch of the simulation setting.

vector components were recorded by field monitors and further processed in Matlab2021a [107].

3.4.2. Micromagnetic simulations

The Landau-Lifschitz-Gilbert equation (LLG) governs the motion of the magnetic moments. In scope of this thesis, we use MuMax3 which is finite difference solver of LLG. LLG reads as [27, 150, 151]

$$\frac{\partial \boldsymbol{m}}{\partial t} = \gamma \frac{1}{1+\alpha^2} \left(\boldsymbol{m} \times \boldsymbol{B}_{\text{eff}} + \alpha \left(\boldsymbol{m} \times \left(\boldsymbol{m} \times \boldsymbol{B}_{\text{eff}} \right) \right) \right), \tag{3.24}$$

where $\boldsymbol{m}$ is magnetization vector, α is Gilbert damping parameter, γ is gyromagnetic ratio, and $\boldsymbol{B}_{\text{eff}}$ is an effective field. This effective field in MuMax3 composes of several contributions, namely:

- $\boldsymbol{B}_{\text{ext}}$ - Externally applied field
- $\boldsymbol{B}_{\text{demag}}$ - Magnetostatic field
- $\boldsymbol{B}_{\text{exch}}$ - Heisenberg exchange field
- $\boldsymbol{B}_{\text{DM}}$ - Dzyaloshinskii-Moriya exchange field
- $\boldsymbol{B}_{\text{anis}}$ - magneto-crystalline anisotropy field
- $\boldsymbol{B}_{\text{therm}}$ - thermal field

The challenge now, is to calculate all relevant contributions to the effective field, and then integrate the Eq. 3.24. In the following three paragraphs we describe calculation of the three most important field terms for the case studied in the scope of this thesis, namely externally applied field, magnetostatic field, and Heisenberg exchange field.

The externally applied field $\boldsymbol{B}_{\text{ext}}$ is usually defined by the simulation script. In spin-wave calculation, this quantity usually contains a bias field ($\boldsymbol{B}_{\text{bias}}$) and excitation field ($\boldsymbol{B}_{\text{exc}}$), thus

$$\boldsymbol{B}_{\text{ext}} = \boldsymbol{B}_{\text{bias}} + \boldsymbol{B}_{\text{exc}}. \tag{3.25}$$

Bias field is usually spanning across the whole simulation area and does not have any time or spatial dependence. The excitation field usually has both, time and spatial dependency.

The magnetostatic field is calculated with the use of so-called demagnetizing kernel $\hat{\boldsymbol{K}}$. In this way, the magnetostatic field can be calculated by performing the convolution

$$\boldsymbol{B}_{\text{demag}} = \hat{\boldsymbol{K}} \cdot \boldsymbol{m} M_{\text{sat}}, \tag{3.26}$$

where M_{sat} is saturation magnetization. The convolution is performed with use of Fast Fourier transform which significantly speeds up all the calculations. The demagnetizing kernel is calculated by assuming that the magnetization is pointing to x-direction in all simulation cells.

The exchange field is calculated with use of the six-neighbour approximation [151–153]

$$\boldsymbol{B}_{\text{exch}} = 2\frac{A_{\text{ex}}}{M_{\text{sat}}} \sum_i \frac{\boldsymbol{m}_i - \boldsymbol{m}}{\Delta_i^2}, \tag{3.27}$$

where A_{ex} is exchange constant, i is index of the six nearest neighbouring cells, and Δ_i is a distance between the evaluated cells.

As the next step, the Eq. 3.24 has to be integrated. In the scope of this thesis, we used Runge-Kutta method with 5th oreder of convergence and 4th order of error estimation commonly called Dormand-Prince method [93, 151, 154]. The Dormand-Prince is known, to provide the best convergence from available methods in MuMax3. The time step in the simulation is adaptive, which can considerably speed up the simulations in cases, where the error of calculation (difference between the 5th and 4th evaluation) is approaching zero.

3.4.3. Multiphysics simulation of heat distribution around laser spot

The laser light carries energy, which can become very dense if it is focused to small spots. The absorption of the light can then results to the locally elevated temperatures of the surface, where the light is focused. Such rise in temperature can then affect material properties such as index of refraction. This change of index of refraction in turn then affects again the propagation of light. This forms challenging scenario, where both these phenomena have to be modeled simultaneously.

The calculation scheme is shown in Fig. 3.13. Initially the value of room temperature is set in all simulated regions. Afterwards, the distribution of electromagnetic field of a Gaussian spot is calculated. From this subsequent calculation step generated heat is deduced. This is then used as the input for calculation of a temperature distribution. After obtaining the temperature distribution, the space-dependent index of refraction is calculated and computation proceeds to calculation of electromagnetic distribution again. The whole procedure is repeated until there is no significant difference between the iterations.

The temperature distribution is governed by the following differential equation [155]

$$\varrho C_p \boldsymbol{u} \cdot \nabla T + \nabla \cdot \boldsymbol{q} = Q, \tag{3.28}$$

where ϱ is density, C_p is specific heat capacity at constant pressure, $\boldsymbol{u}$ is fluid velocity vector, T is a temperature, $\boldsymbol{q} = -k\nabla T$ is a conductive heat flux, k is a thermal conductivity, and Q is a heat source, which in the studied case was laser spot. The first term

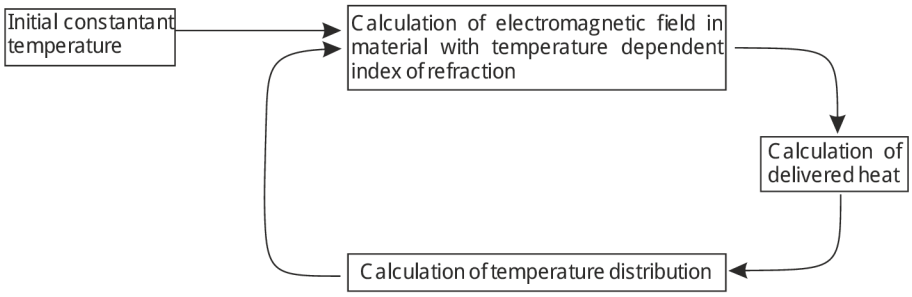

Figure 3.13: Schematics of the calculation procedure.

in Eq. 3.28 represents the heat transfer by convection and is equal to zero in the studied case. The second term represents the heat conduction and it is a mechanism responsible for resulting temperature distribution.

The electromagnetic field distribution is obtained by solving following form of wave equation in the frequency domain

$$\nabla \times \frac{1}{\mu} (\nabla \times \boldsymbol{E}) + \left(\boldsymbol{j}\omega\sigma - \omega^2 \varepsilon \right) \boldsymbol{E} = 0, \tag{3.29}$$

where μ is permeability, $\boldsymbol{E}$ is electric field vector, $\boldsymbol{j}$ is free current, ω is angular frequency, and ε is permittivity.

Procedure of multiphysics simulation of heat distribution around laser spot

We used COMSOL Multiphysics 6.0 [156]. The packages *Electromagnetic waves* and *Heat transfer in solids* were used. In practical implementation, the calculation consisted of these four steps:

1) Calculation of the Gaussian beam in the air.

In the background, a Gaussian beam with E_x polarization is excited. The solution is transferred to the next step using *General Extrusion*, where it generates the Gaussian beam at the *in* interface.

2) Calculation of the Gaussian beam passing through the permalloy layer and the substrate.

This wave serves as the background wave in the calculation of Gaussian beam scattering. The electric field strength of the Gaussian beam determined in Part 1 is prescribed at the *in* interface. The *Scattering Boundary Condition* is prescribed at the *out* interface, ensuring that the wave is transmitted out of the domain without reflection. The boundary condition *Perfect Electric Conductor* is prescribed on the vertical boundaries (they are far enough away from the spatially limited Gaussian beam). The solution, extended to the perfectly matched layer (PML) domain (where zero electric intensity is artificially prescribed), is used as the *Background Field* for the next calculation step.

3) Calculation of the Gaussian beam scattering on the silicon disk on the permalloy layer and the substrate.

PML is used to attenuate the scattered wave. *Total Power Dissipation Density* is used as the heat source in the next calculation step.

4) Calculation of the temperature field in the silicon substrate, permalloy layer and silicon disk.

Temperature of 20 °C is prescribed at the *out* interface, the other interfaces are isolated (zero heat flux), and radiation to the surroundings is not considered either. The

temperature field is again artificially extended to air and PML, where a temperature of 20 °C is prescribed. The temperature field affects the value of the dielectric function (real and imaginary part) of the silicon.

These 4 steps are solved using the *Frequency-Stationary Solver*. Quadratic elements are used in all calculations. The tetrahedral mesh in each domain has a step of $\lambda/5$, where λ is the wavelength of the wave in that domain.

3.5. Extraction of dispersion relation from micromagnetic simulations

Usually, the micromagnetic simulators works in time domain and real space coordinates. However, for analysis of spin wave behavior, or calculation of the BLS spectra by following the approach introduced in Chapter 2, it is often beneficial to transform the results into frequency and wavevector domain. In this section I show this transformation on the easist example of obtaining the linear dispersion relation of spin waves in 30 nm-thick NiFe layer. I developed the methodology and codes presented here during my Bachelor's and further improved it during my PhD [157]. The methodology follows standard procedure [158]. However, it brings several innovations, such as using a 3-dimensional excitation function or correcting for thermal distribution.

3.5.1. Micromagnetic simulation and excitation of broadband spin waves

The simulations in this work were done in order to obtain dispersion relation, more precisely Bloch function (density of states in respect to frequency and two-dimensional wavenumber) $\mathcal{D}\left(f,k_x,k_y\right)$. Results shown in the following graphs use material parameters of NiFe[6]

The initial magnetization $\boldsymbol{m}$ and the external field pointed in the x direction. The energy of the system was then minimized by using the relax command of MuMax3.

In order to get the characterization of all spin-wave wavelength out of single simulation we used similar trick as used in FDTD simulation. All possible spin wave frequencies and wavevectors were excited by a 3D sinc pulse $\boldsymbol{B}_{\mathrm{exc}}\left(x,y,t\right)$. The spatial mask ($\boldsymbol{B}_{\mathrm{mask}}$) is depicted in Fig. 3.14a. This mask was generated by sinc function

$$\boldsymbol{B}_{\mathrm{mask}} = \mathrm{sinc}\left(k_{\mathrm{c}} \cdot \sqrt{(x-x_0)^2 + (y-y_0)^2}\right)\boldsymbol{z}, \tag{3.30}$$

where k_{c} is a cut-off wavenumber, which was set to 150 $\frac{\mathrm{rad}}{\mu m}$, x, and y are in-plane spatial coordinates, x_0, and y_0 are center of the pulse (here set to 0 for both), and $\boldsymbol{z}$ is a unit vector in out-of-plane direction. The evolution of the sinc pulse is depicted in Fig. 3.14b for center of the simulation. Again, the time evolution B_{time} is governed by the sinc function

$$B_{\mathrm{time}} = A \cdot \mathrm{sinc}\left(2\pi f_{\mathrm{c}}(t-t_0)\right), \tag{3.31}$$

where $A = 1\,\mathrm{mT}$ is the amplitude of the pulse, t is the time of simulation, $t_0 = 100\,\mathrm{ps}$ is the time offset of the pulse, and f_{c} is the cut-off frequency, which was set to 60 GHz.

[6] Saturation magnetization ($M_{\mathrm{s}} = 741\,\mathrm{kA\,m^{-1}}$), gyromagnetic ratio ($\gamma = 29.5\,\mathrm{GHz\,T^{-1}}$), and exchange constant ($A_{\mathrm{ex}} = 16\,\mathrm{pJ\,m^{-1}}$).

Now, by multiplying both parts (spatial and temporal) we can get the overall excitation field ($\boldsymbol{B}_{\text{exc}}$) as

$$\boldsymbol{B}_{\text{exc}} = \boldsymbol{B}_{\text{mask}} B_{\text{time}}. \tag{3.32}$$

The simulation size was set to $7680 \times 7680 \times 34.8\,\text{nm}^3$ with a cell size of 3.75 nm in the in-plane and 4.35 nm in the out-of-plane direction. This allows to investigate spin-wave wavelengths in the range from 7.5 nm to approx. 7.5 µm, according to Nyquist theorem [159]. This is way above and below the wavelengths of interests (see cut-off wavenumber in Eq. 3.30), which relaxes the needs of filtering. Periodic boundary conditions with 32 repetitions in both in-plane directions were used. This ensures proper calculation of the magnetostatic field (see Eq. 3.26), and thus subsequent match between the analytical models and results from the micromagnetic simulation.

While applying the excitation pulse ($\boldsymbol{B}_{\text{exc}}$) we let the magnetization evolve for 5 ns with the sampling interval of 8 ps. This, according to Nyquist theorem, is equal to 62.5 GHz (which is above the frequency cut-off, see Eq. 3.31), and minimal frequency of 200 MHz.

3.5.2. Analysis of the simulation results

All three magnetization components were taken from the top-most layer, so we acquired a 3D array $\boldsymbol{m}(x,y,t)$. The obtained out-of-plane magnetization component m_z in time of 3 ns is shown in Fig. 3.15a. The anisotropic dispersion relation of spin waves, can be seen there as the lack of rotational symmetry. The spatio-temporal cut through data is depicted in Fig. 3.15b. The fading of the spin-wave amplitude in later times is visible. Please note, that only 6 ns are shown, while the simulation lasted till 10 ns, which is above lifetime of all investigated spin waves.

To obtain the spin wave dispersion and the amplitudes of the individual modes in the reciprocal space (which can be used in calculation of BLS signal according to Eq. 2.32, or 2.31) the Fourier transform needs to be perfromed

$$\boldsymbol{m}(k_x,k_y,f) = \mathcal{F}(\boldsymbol{m}(x,y,t)). \tag{3.33}$$

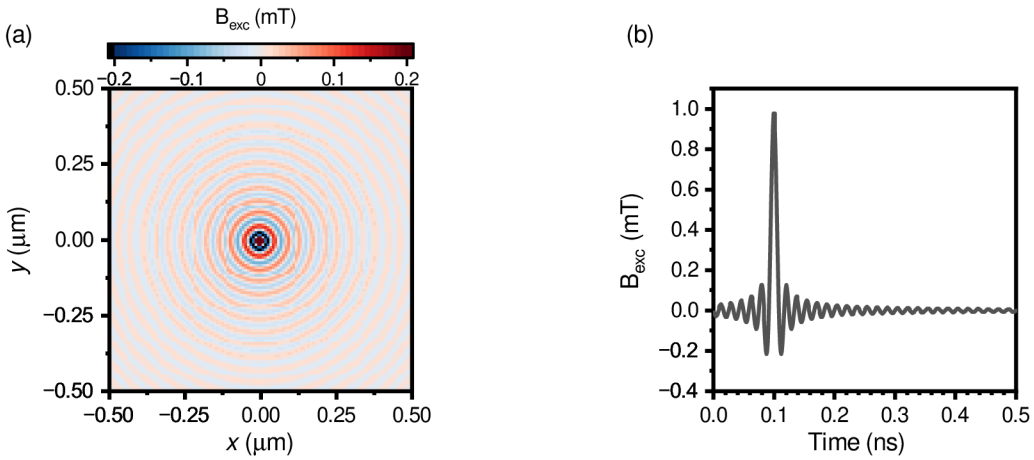

Figure 3.14: Used 3D $\boldsymbol{B}_{\text{exc}}(x,y,t)$ sinc pulse for excitation of micromagnetic dynamics. **a,** Spatial mask of the external field. The panel shows only the central part of the simulation. Outside the shown region the external field was practically zero. **b,** Time dependency of the sinc pulse in the center of simulation area. The panel shows only the first 0.5 ns of simulation. After this time the external field is practically zero.

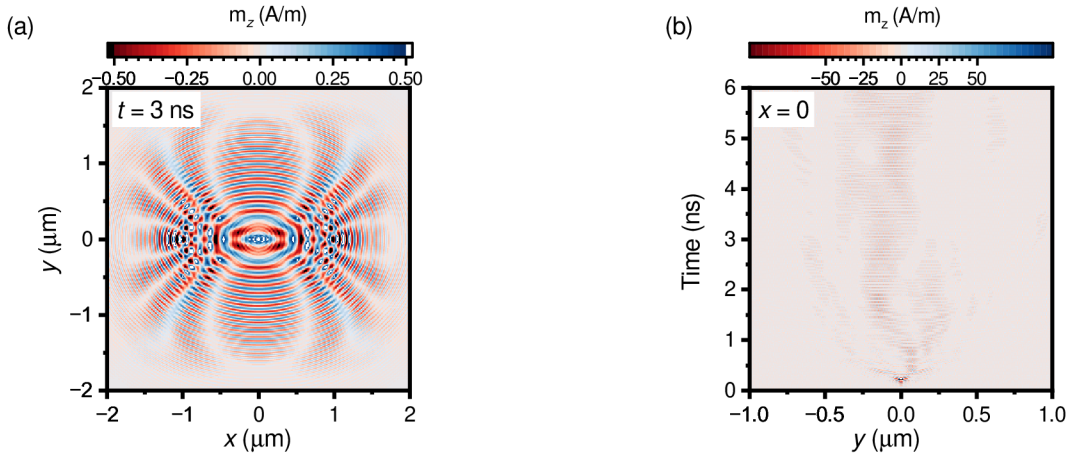

Figure 3.15: Simulated magnetization dynamics. a, Snapshot of the z-component of the magnetization at t=3 ns. **b,** Spatio-temporal evolution of the z-component of magnetization at $x = 0$.

The used script code is available at [107]. The m_z component is transformed to the reciprocal space using a built-in FFT function in Matlab2021a. The obtained dispersion relation was compared with analytical calculation [30, 41], as shown in Fig. 3.16a, b. No windowing nor detrending is used. The resulting density of states is then obtained as

$$\mathcal{D}\left(f,k_x,k_y\right) = \frac{1}{\exp\left(\frac{2\pi\hbar f+\mu_{\text{chem}}}{k_B T}\right)-1}\, m_z\left(f,k_x,k_y\right)^2 ,$$

where the first fraction is the Bose-Einstein distribution at room temperature with chemical potential $\mu_{\text{chem}} = -1$ THz, see in Fig. 3.16c.

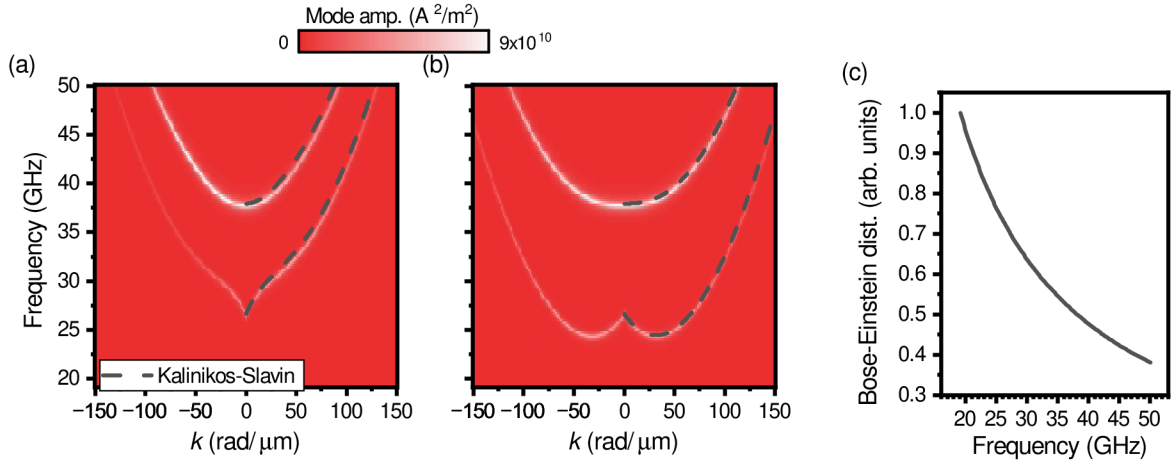

Figure 3.16: Extracted dispersion relation from micromagnetic simulations. a, b Squared Fourier transform of $m_z(x,y,t)$. Panel **(a)** shows DE spin waves, and panel **(b)** shows BV spin waves. Dashed lines show the analytically calculated dispersion relations [30, 41]. **c,** Normalized Bose-Einstein distribution calculated for a range of frequencies relevant to spin waves in the magnetic field of 550 mT.

4. Mie-enhanced Brillouin light scattering spectroscopy

This chapter describes the enhancement of the μ-BLS detection sensitivity to spin waves with high wavenumber exploiting the electromagnetic resonances in individual nanoresonators. This chapter is mainly based on the results published in [113]. Martin Hrtoň and Jakub Krčma performed the FDTD simulations. I was helped with vibrating sample magnetometry by Jakub Holobrádek. I have performed all μ-BLS, and FMR experiments, analyzed all acquired data, and planned all experiments.

This chapter is structured as follows: it starts with the introduction to near-field mediated BLS, followed by the description of plasmon-enhanced BLS and its limitations. Next, the sample geometry and fabrication for Mie-enhanced BLS are presented, followed by magnetic layer characterization. The enhancement of the BLS signal on individual disks is discussed, followed by a discussion of nanoresonator's material influence. Thereafter, a theoretical description of the observed phenomena is given. Afterward, the heating caused by the dissipation of laser power and subsequent change of refractive index are discussed. Now, the measurement of the disk's edge is discussed. The influence of the wavelength of probing light is discussed. Finally the universality of the method is demonstrated on the different material system, namely 100 nm thick CoFeB layer.

4.1. Basic concepts

Until now, the BLS techniques fell short in the detection of nanoscaled spin waves due to their fundamental limit in maximum detectable magnon momentum [53, 160–163]. This limit is given by the law of conservation of momentum in the Stokes process

$$\boldsymbol{k}_\mathrm{i} = \boldsymbol{k}_\mathrm{r} + \boldsymbol{k}_\mathrm{mag}, \tag{4.1}$$

where $\boldsymbol{k}_\mathrm{i}$ and $\boldsymbol{k}_\mathrm{r}$ are k-vectors of the incident and reflected light and $\boldsymbol{k}_\mathrm{mag}$ is the k-vector of the magnon on which the light is being scattered. It means that in a typical BLS experiment in back-scattering geometry, the maximal detectable k-vector of spin waves equals twice the k-vector of the incident light. For the laser wavelength $\lambda_\mathrm{i} = 532\,\mathrm{nm}$, for example, the maximum k-vector which can be theoretically detected is $k_\mathrm{mag}^\mathrm{max} = 23.6\,\mathrm{rad\,\mu m^{-1}}$. This corresponds to a minimum spin-wave wavelength $\lambda_\mathrm{mag}^\mathrm{min} = \lambda_\mathrm{i}/2 = 266\,\mathrm{nm}$ [123, 124].

Taking inspiration from tip- and surface-enhanced Raman scattering spectroscopy [164–166], nanosized apertures or other plasmonic structures made of metals have been used to locally enhance the electromagnetic field and increase the range of the accessible k-vectors [167–169]. Unfortunately, the efficiency of the plasmonic approach is severely limited by high optical losses in metallic structures, which makes it unsuitable for convenient magnon measurements. A detailed discussion of this phenomenon is given in

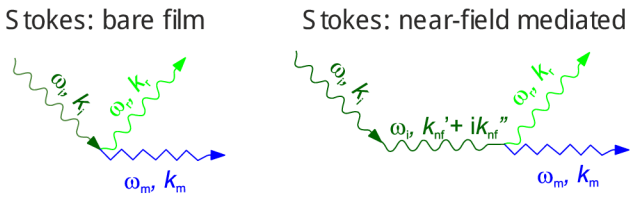

Figure 4.1: Principle of the near-field enhanced Brillouin light scattering. Comparison of the conventional and near-field enhanced (Stokes) BLS processes. Near-field converts an incoming photon into a photon with complex momentum. The real part of the converted photon can be larger than the momentum of the incident free-space light. This way, the limit of conventional BLS can be overcome, and high-k magnons can be optically detected.

section 4.2. However, recent advances in nanophotonics suggest that plasmonic structures made of metals can be substituted by structures made of dielectric materials. Such dielectric nanoresonators have an advantage in reduced dissipative losses and associated heating, while their high refractive index still enables comparatively strong light confinement [170–176].

We use simple geometry consisting only of silicon disks, which support Mie resonances [121, 177–179]. The Mie resonance creates strong and localized electric fields (hot spots). When the incident light with momentum k_i is restricted to the sub-diffraction hot spots, its momentum becomes complex

$$k_\mathrm{nf} = k'_\mathrm{nf} + ik''_\mathrm{nf}, \tag{4.2}$$

and thus its real part k'_nf can be larger than the momentum of the free-space light [180] (see Fig. 4.1). This way, the fundamental limit of BLS in maximum detectable magnon momentum can be overcome.

4.2. Plasmon-enhanced Brillouin light scattering

Plasmon resonances have been the first choice for researchers to enhance the BLS signal for many years. However, all these attempts resulted only in three publications [167–169]. Quite naturally, when I started to work on my PhD topic, enhancement of the BLS signal, I also chose plasmon resonances. I have tried many geometries such as bow-ties, diabolos, disks, apertures, etc [181, 182]. However, most approaches based on the plasmon resonances drastically reduce the obtained BLS signal. Here, I show the most promising one, silver spheres. I deposited nanoparticles Michal Kvapil did the FDTD simulations presented here.

4.2.1. Plasmon-enhanced BLS on 200 nm-wide silver sphere

The light can be focused on sub-diffraction focal spots with the use of localized surface plasmon resonances (LSPR) [183–185]. These resonances are the collective motion of free electrons in noble metals. Typically, the nanostructure made of noble metal is either deposited from solution or fabricated by, e.g., e-beam lithography. They can be used e.g. for sensing [186, 187], or to increase resolution [188, 189].

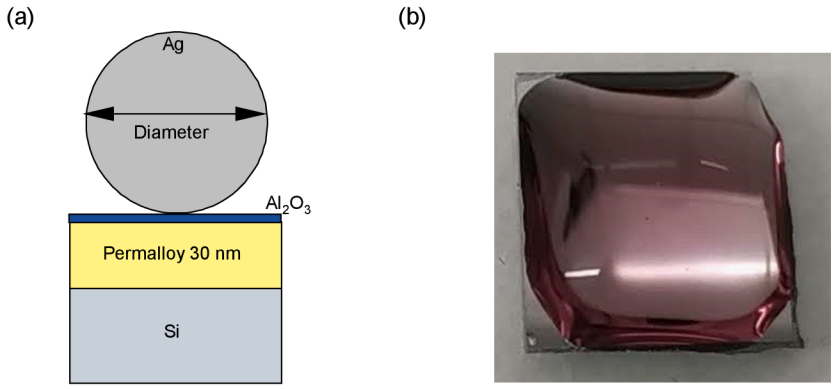

Figure 4.2: Geometry of plasmon-enhanced Brillouin light scattering. a, The sketch of the geometry of the plasmonic nanoresonator used in presented BLS experiments. The spacer layer was 2 nm thick and the diameter of the silver sphere was 200 nm. **b,** Photo of the sample during the deposition (drop-casting) of the silver spheres with a diameter of 200 nm.

The easiest approach to getting plasmonic nanoresonators on a thin magnetic film is to deposit them from the solution. The material of choice for these nanoresonators is silver, as gold has poor performance at the wavelength of 532 nm due to inter-band transitions [190, 191]. The sample was prepared by drop-casting from a commercial solution (nanoComposix) to a 30 nm thick permalloy layer covered by 2 nm of an insulating Al_2O_3 spacer prepared by atomic layer deposition, see sketch in Fig. 4.2a.

We deposited 30 µl droplet of the solution containing silver nanospheres with the diameter of 200 nm to the sample surface and let the sample dry for 120 min, see Fig. 4.2b. After that, the solution was rinsed in deionized water and blow-dried with clean, dry air. This is the typical procedure used in e.g. [192–194].

The silver spheres with a diameter of approx. 140 nm provides the resonance at wavelength of 532 nm (see Fig. 4.3a), which is wavelength used in our BLS setup. The commercially available solutions are only suplied with 100 nm, or 200 nm spheres. As 200 nm spheres provided better results in the following discussion we focus only on them.

The FDTD simulations of the studied geometry (see Fig. 4.3a) were performed by Michal Kvapil. The results are shown in Figs. 4.3b, c. The localization and enhancement of the light intensity can be observed between the sphere and the magnetic layer. This is improved by the rather large diameter of the silver sphere, which is enabled by the relatively high plasma frequency of silver. As there is only a single contact point between the sphere and spacer layer, the distance between the *equator* of the sphere and magnetic layer is enlarged, resulting in further improvements.

Nevertheless, the resonance is constricted only *below* the sphere. Thus, the light that is emitted by induced polarization (see Chap. 2) can be reabsorbed by the sphere. This process is called quenching, and its consequence is a significant lowering of the BLS signal.

The BLS spectra were measured on the individual silver nanosphere and bare film. The results are shown in Fig. 4.4a. The obtained results were fitted by the phenomenological model (see Eq. 2.35). The resulting detection function is shown in Fig. 4.4b. The overall signal strength is reduced from $A = (89 \pm 5)$ cts for the bare film to $A = (84 \pm 4)$ cts for the silver sphere. This is likely caused by the absorption and quenching. The signal-to-noise ratio is further reduced by the elevated background signal from bg$= (1.6 \pm 0.8)$ cts for the

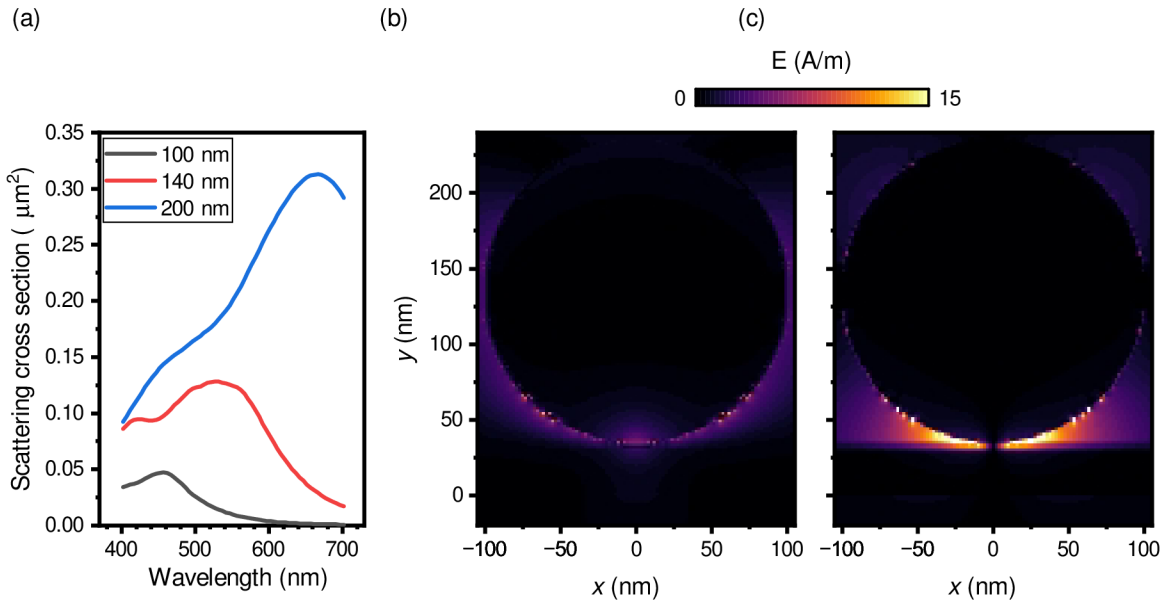

Figure 4.3: Scattering of silver nanospheres. a, Calculated scattering cross-section of the silver nanosphere with a diameter of 100 nm (black solid line), 140 nm (red solid line), and 200 nm (blue solid line) placed on the 30 nm of NiFe. **b, c,** Distribution of the *x- (b)* and *z-* **(c)** component of the electric field around the sphere. The bottom boundary of NiFe is placed to 0 nm in *z*-direction, i.e., the interface between the Al_2O_3 and NiFe is in 30 nm.

bare film to bg= (19 ± 2) cts for the silver sphere. The half-width-at-tenth-of-maximum (HWTM) of the detection, which defines the maximum detectable wavevector, is slightly increased from HWTM= (11.2 ± 0.8) rad/μm for bare film to HWTM= (13 ± 2) rad/μm for silver sphere.

The spheres also introduce the exponentially decaying background to the signal [195–197]. In Fig. 4.4c, this is shown as a blue exponentially decaying line. Moreover, the spheres are allowed to vibrate. The first description of the vibrational modes of free standing spheres were given by Lamb [198]. The modes are acquired by solving the Navier elastic equation [199, 200]

$$v_{\mathrm{L}}^2 \nabla \cdot (\nabla \cdot \boldsymbol{u}) - v_{\mathrm{T}}^2 \nabla \times (\nabla \times \boldsymbol{u}) = \frac{\mathrm{d}^2 \boldsymbol{u}}{\mathrm{d}^2 t}, \tag{4.3}$$

$\boldsymbol{u}$ is a displacement vector, v_{L}^2 (v_{T}^2) is a longitudinal (transversal) velocity of sound, and t is time. This equation can be solved for simple geometries (e.g., discussed spheres) that are positioned in free space, i.e., no forces are applied to them. The rough position of the fundamental vibrational modes can be estimated by using these simple formulas [199]

$$f_{l=0}^{n=1} = 0.9 \frac{v_{\mathrm{L}}}{D}, \tag{4.4a}$$

$$f_{l=2}^{n=1} = 0.84 \frac{v_{\mathrm{T}}}{D}, \tag{4.4b}$$

where D is a diameter of sphere, and n,l are quantization numbers. If the sound velocities for silver are used ($v_{\mathrm{L}} = 3747 \frac{\mathrm{m}}{\mathrm{s}}$ and $v_{\mathrm{T}} = 1740 \frac{\mathrm{m}}{\mathrm{s}}$ [200]) the resulting frequencies are 16.8 GHz and 7.3 GHz which coincides with first and third measured vibrational peaks.

To precisely associate each peak in the acquired spectra (see Fig. 4.4c) with specific vibrational mode, one has to perform numerical simulations of the Eq. 4.3 [195, 199, 201].

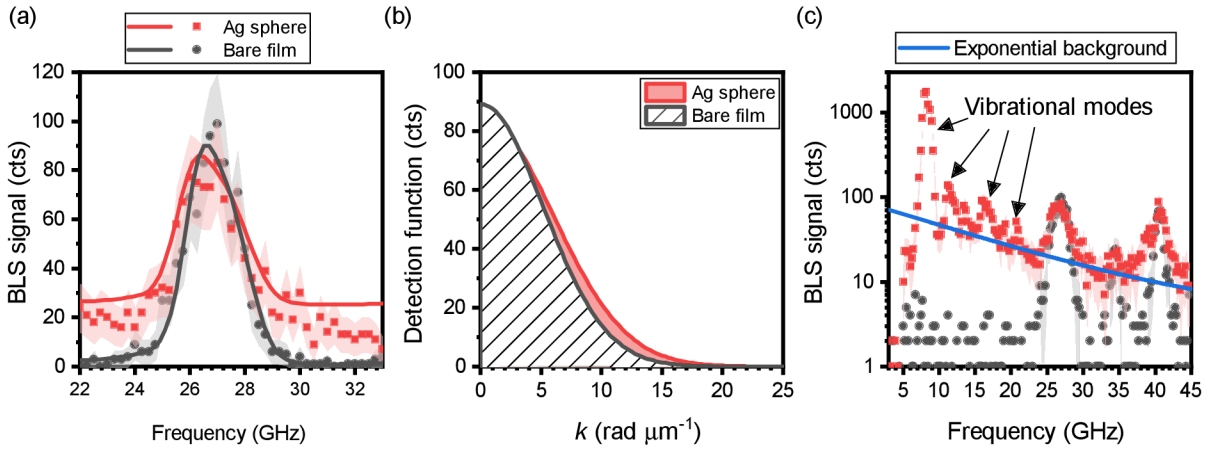

Figure 4.4: Resulting Brillouin light scattering spectra acquired on a silver sphere with a diameter of 200 nm. a, Thermal spin-wave spectra obtained by μ-BLS on the bare permalloy film (black squares) and on the permalloy film with the silver nanosphere (red circles) and their corresponding fits (lines). The error margins represent the 95% confidence interval. **b,** Detection function extracted from the fits to the data shown in panel **(a)**. **c,** The whole frequency spectrum is acquired on the silver sphere (red dots) and bare film (black circles). The blue line represents the fit of the exponentially decaying background signal acquired on the silver sphere. The arrows show the vibrational modes of the sphere. The magnetic signals are present around 27 GHz and 41 GHz. The signal around 35 GHz is a so-called ghost and is caused by the secondary transmission of TFPi, see Chap. 3.

Nevertheless, these peaks caused by the vibrational modes of the sphere interfere with the magnetic signal and further complicate a proper analysis of the acquired signal.

4.3. Sample design of silicon disks for Mie-enhanced BLS

Now, I move from plasmon (metallic) resonances to Mie (dielectric) resonances. In the presented experiments, I have investigated spin waves in a 30 nm thick permalloy film, on top of which 60 nm thick silicon disks were fabricated, see Fig. 4.5a. The sample was measured on a standard μ-BLS, using a microscope objective lens with NA = 0.75 to illuminate it by $\lambda_i = 532$ nm coherent laser light (see chapter 3). The sample used in this investigation was fabricated by Jan Klíma (who also made a design in kLayout), Meena Dhankhar, Kristýna Davídková, and Jakub Holobrádek.

4.3.1. Sample fabrication

To allow the investigation of the influence of the geometry, namely the diameter of the disk, the design with different disk diameters was prepared, see Fig. 4.5b. The diameters of the disks ranged from 100 nm to 300 nm in 5 nm steps and from 350 nm to 1500 nm in 50 nm steps. Each disk was prepared five-times in one *fabrication cell* and the whole design shown in Fig. 4.5b was repeated four times on each sample. Thanks to this, the repeatability and influence of the small fabrication imperfection to enhancement of the BLS signal could be checked. Moreover, the acquisition of the BLS spectra was fully

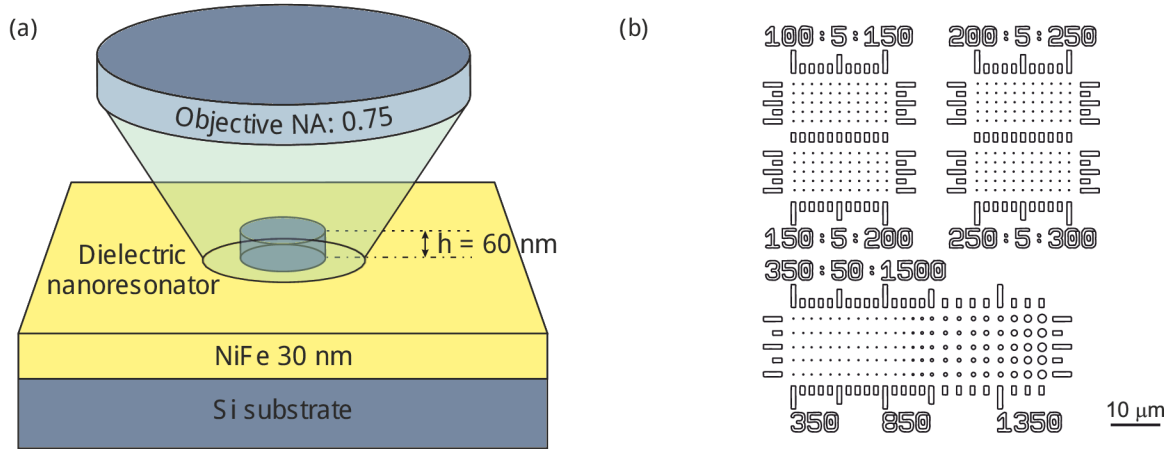

Figure 4.5: Geometry of the experiment. **a,** Schematics of our µ-BLS setup. Laser light (532 nm) is focused onto a silicon disk by a high numerical aperture objective lens. The disk is placed on the top of a permalloy layer, in which the spin waves are probed. The inelastically back-scattered light is then analyzed in the tandem Fabry-Perot interferometer (TFPi) and collected with a single-photon detector. **b,** Schematics of the design of the silicon deposited layer.

automatized as the presented design provides features with good visibility that were used for automatic stabilization and positioning.

Sample was fabricated by electron beam lithography and a lift-off process. We started with room temperature deposition of a 30 nm thick permalloy film onto a Si(100) substrate using e-beam evaporation from $Ni_{80}Fe_{20}$ (at. %) pellets with purity of 99.95 %. Then we spin-coated a double-layer polymethyl methacrylate resist (200 nm thick Allresist AR-P 649.04 200K and 60 nm thick AR-P 679.02 950K, this resist combination provides sufficient undercut for lift-off). The pattern was written with RAITH 150-two e-beam writer. Silicon film with a thickness of 60 nm was consequently deposited onto the patterned sample by RF magnetron sputtering or by ion beam sputtering system with Kaufmann source from a crystalline silicon target at room temperature. The lift-off procedure consisted of immersing the sample in acetone for approx. 8.5 h, followed by 30-second isopropanol rinse and blow-drying by nitrogen gas.

4.3.2. Inspection of the sample

After the fabrication, sample were checked for its exact shape, size and uniformity by scanning electron microscopy (Tescan Lyra and Thermofisher Verios 460L) and atomic force microscopy (Bruker Dimension Icon). The scanning electron microscope image of the sample with 0 deg tilt is shown in Fig. 4.6a. One can observe that the shape of the disk is circular, and there are no significant aberrations. The bright outer ring is formed around the disk. This is caused by the *ears*, which resulted from the deposition of the silicon on the substrate walls. This is confirmed by doing scanning electron microscope image under the tilt of 45 deg, see Fig. 4.6b[1]. The acceleration voltage of 30 keV was used, which resulted in partial transparency of these *ears*. On some predefined positions, these *ears* were removed by rough scanning in an atomic force microscope, and spectra BLS

[1]Please note that disk with different diameter (450 nm) is shown.

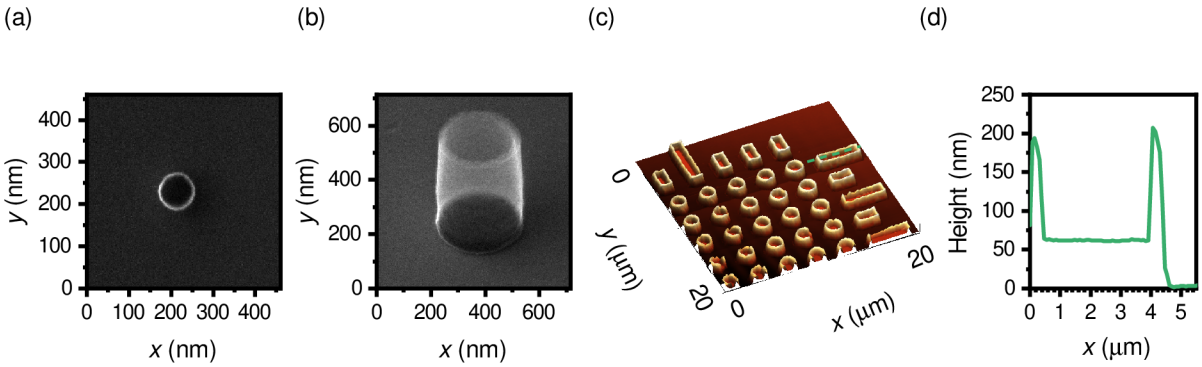

Figure 4.6: Inspection of the sample used for thermal BLS measurements. a, Scanning electron microscope image of silicon disk with diameter of 200 nm taken under 0 deg tilt. **b,** Scanning electron microscope image of silicon disk with a diameter of 450 nm was taken under 45 deg tilt. **c,** Atomic force microscopy image of the corner of silicon disks array. The green dashed line indicates the region taken for height profile in **(d)**. **d,** Line profile taken from a two-dimensional scan along the green dashed line.

spectra acquired on disks with and without *ears* were compared. We did not find any measurable effect, which was further confirmed by the FDTD simulations.

Atomic force microscopy measurement was performed to precisely judge the height of the deposited silicon layer. The two-dimensional scan of the corner of the disk array (see design in Fig. 4.5b) is shown in Fig. 4.6c. The formation of the *ears* is visible. To assess the height, the line profile was extracted (see green dashed line in Fig. 4.6c). This line profile is shown in Fig. 4.6d. The height of the disk is 62 ± 1 nm, and the height of the *ears* is 195 ± 5 nm.

4.4. Magnetic layer characterization

To get material and magnetic constants of the fabricated permalloy layer, I performed flip-chip ferromagnetic resonance (FMR) (see chapter 3) and vibrating sample magnetometry (VSM) measurements. The fitted values were then used in the micromagnetic, electrodynamic, and analytical modeling of the spin-wave systems. The same values are also used in chapter 6, where a layer from the same deposition is employed. In chapter 5, all parameters except of thickness are used.

4.4.1. Dynamic characterization

The experimentally measured S12 parameter is shown in Fig. 4.7a. The experimental data were fitted with the Lorentzian function to find peak's position, which was used in the subsequent fitting of the Herring-Kittel formula. The Fig. 4.7b shows BLS thermal spectra taken on bare NiFe film in different external fields[2]. From this data set, we fit only the first perpendicular standing spin-wave mode. The fitting of FMR frequency from this data is not trivial since there is a strong dependence of the frequency on the k-vector within the accessible range by the μ-BLS, although full BLS model (eq. 2.31) can be used.

[2]The constant signal at approx. 34 GHz originates from a so-called ghost, which is higher-order transmission of the tandem-Fabry-Perot interferometer, see chapter 3.

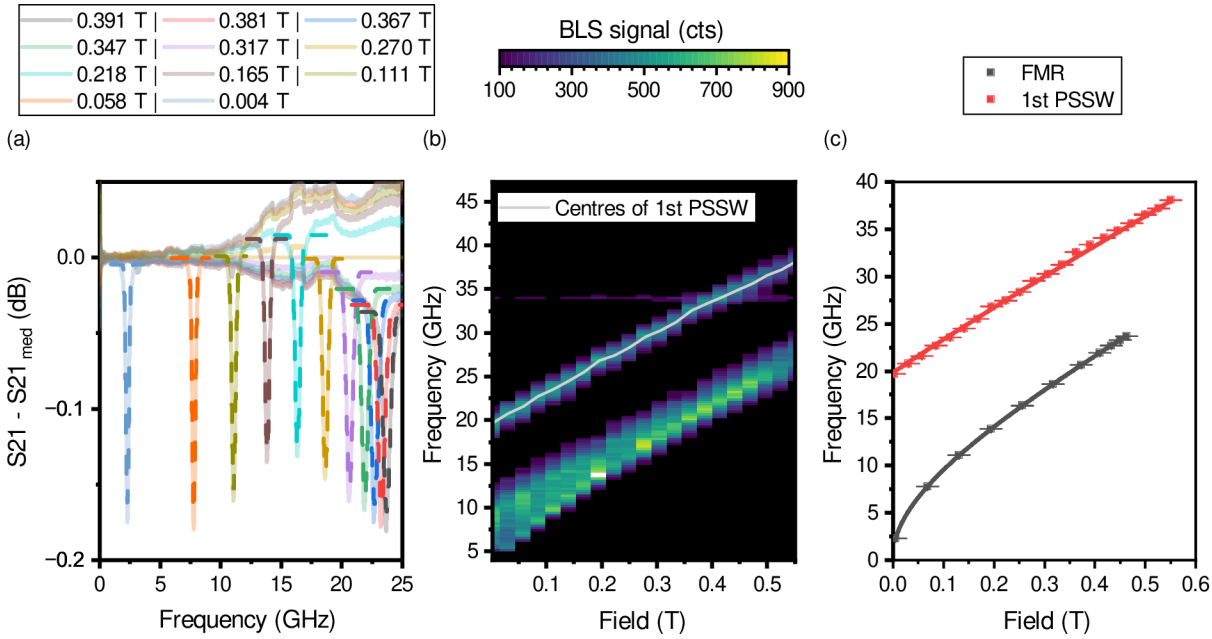

Figure 4.7: Magnetic characterization of the permalloy film used in the experiments. **a,** Scattering parameter acquired by a broadband ferromagnetic resonance technique. Different color lines represent different external magnetic fields (see legend). Dashed lines are Lorentzian fits of the resonance peak. **b,** Thermal magnon spectra measured by μ-BLS microscopy. The light gray line shows the centers of the Lorentzian functions. **c,** Fits of the data from **(a)** FMR and **(b)** PSSW. Magnetic properties extracted from the fit are shown above the graph.

Again, we used Lorentzian fitting to get the frequency position of the first perpendicular standing spin-wave mode; see the gray solid line in Fig. 4.7b. In Fig. 4.7c, these positions were fitted. The fitted material and sample properties are summarized in Tab. 4.1.

4.4.2. Static characterization

Vibration sample magnetometry (VSM) measurements were conducted to confirm the experimental findings from the VNA-FMR. The Fig. 4.8a shows the out-of-plane measurement. The saturation magnetization can be deduced from this type of measurement by finding the field in which the sample becomes saturated or by finding the overall magnetic moment and dividing it by the magnetic sample volume. The saturation magnetization deduced from the saturation field (the first mentioned method) is $750 \pm 10 \frac{\mathrm{kA}}{\mathrm{m}}$ and from the overall magnetic moment and volume is $730 \pm 60 \frac{\mathrm{kA}}{\mathrm{m}}$. Both methods are in agreement with their uncertainty with the VNA-FMR measurement.

Fig. 4.8b shows a single hysteresis in-plane loop in the external field of 20 mT. Again, the value of saturation magnetization is in agreement with previous measurements. The last panel 4.8c depicts the value of the saturation magnetization in dependence on the

Table 4.1: Obtained parameters by fitting of the FMR and 1st PSSW of the studied NiFe layer.

$M_\mathrm{s}(\frac{\mathrm{kA}}{\mathrm{m}})$	$\gamma(\frac{\mathrm{GHz}}{\mathrm{T}})$	d(nm)	$A_\mathrm{ex}(\frac{\mathrm{pJ}}{\mathrm{m}})$	B_ani(mT)
740 ± 10	29.5 ± 0.1	34.8 ± 0.3	16 (fixed)	1.4 ± 0.1

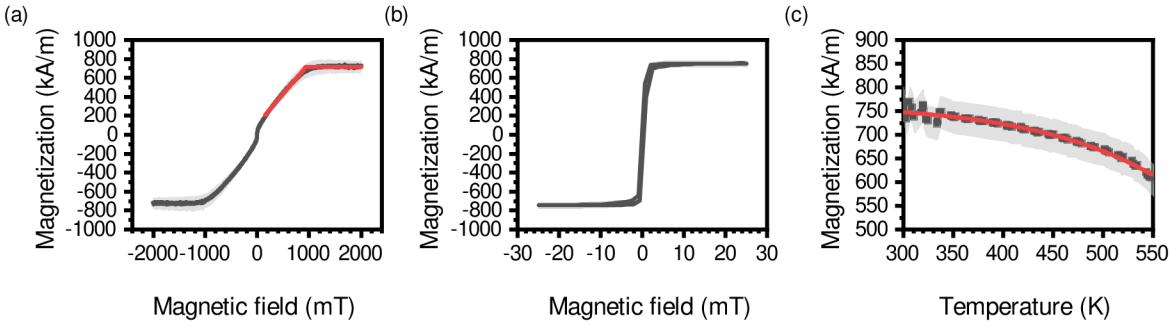

Figure 4.8: VSM characterization of the magnetic layer. a, Out-of-plane vibrating sample magnetometry (VSM) measurement of a 20 nm thick permalloy film (black solid line). The value obtained from the overall magnetic moment and measurement of the volume of the sample is $M_s = 730 \pm 60$ kA/m. The red solid line represents a piece-wise fit of the saturating field which gives $M_s = 750 \pm 10$ kA/m. **b,c,** In-plane VSM measurement of the permalloy layer used in our experiments. Temperature-dependent measurement of the magnetization in **(c)** was performed in the field of 20 mT. The red solid curve is a fit.

temperature of the magnetic layer. One can observe a slight decrease of approx. 200 kA/m with the increase of temperature by 150 K. These data were fitted by a model based on the Bloch's model modified by Kuz'min [202]

$$M(T) = M_0 \left(1 - \left(\frac{T}{T_C}\right)^p\right)^{\frac{1}{3}}, \tag{4.5}$$

where M_0 is saturation magnetization at 0 K, T is a temperature, T_C is a critical temperature, and p is a empirical parameter. The fitted values are $M_0 = 760 \pm 30$ kA/m, $T_C = 670 \pm 10$ K, and $p = 3.8 \pm 0.3$.

4.5. Mie enhancement of the BLS signal on the single silicon disk

In this section, the main outcome of my PhD research is shown. The enhancement of both amplitude and maximal detectable wavevectors is demonstrated in two external magnetic fields on a single silicon disk fabricated on top of a permalloy layer. The phenomenological model introduced in chapter 2 is used to assess the achieved enhancement.

4.5.1. Comparison of measurements on 175 nm-wide silicon disk and bare film

The dramatic improvement of high-k[3] magnon detection sensitivity in the presence of a 175 nm wide silicon disk is visible in Figure 4.9. One can see that at low magnetic field of 50 mT (Fig. 4.9a the BLS signal increases, and the spin wave band broadens towards higher frequencies. At higher magnetic field of 550 mT (Fig. 4.9b, BLS signal increases, and the spin wave band now broadens to both sides.

[3]Here, by high-k magnon we mean magnons with wavevector, which cannot be detected by standard μ-BLS.

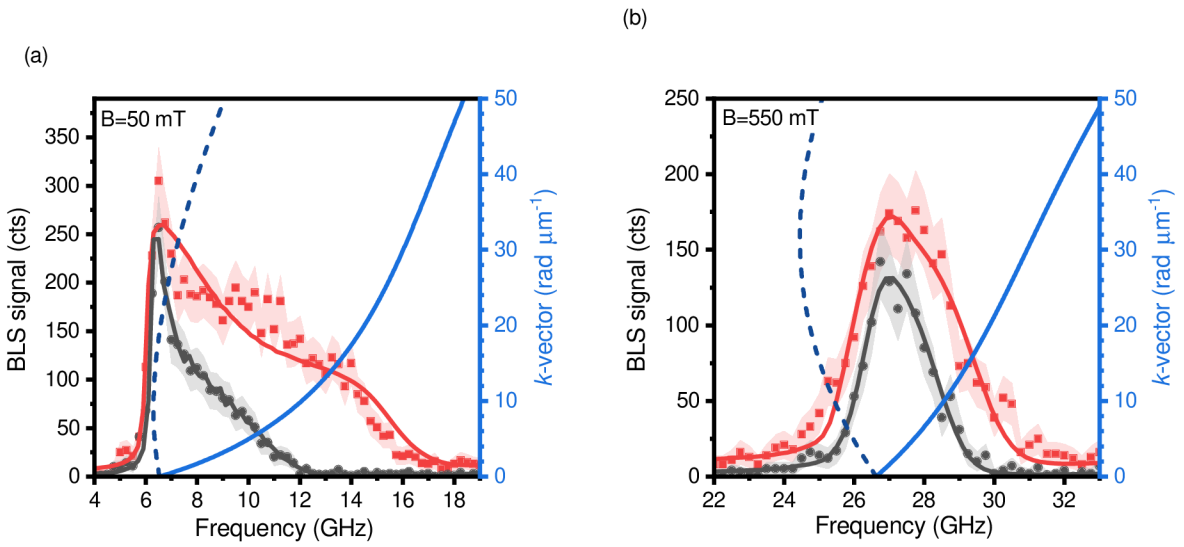

Figure 4.9: Enhancement of the BLS spectra. a, b, BLS spectra acquired on a bare permalloy film (black circles) and on the same film with a 60 nm thick, 175 nm wide silicon disk on top (red squares). The black and red solid lines represent fits to the experimental data assuming the Gaussian detection function. The error margins of the experimental data are estimated on the basis of the Poisson distribution. The blue lines show spin wave dispersions for Damon-Eshbach (DE) and backward volume (BV) modes.

Different broadening of the spin wave band at high and low magnetic fields can be explained by different shapes of the spin wave dispersion relations of the permalloy thin film for different directions of k-vector $\boldsymbol{k}$ with respect to the direction of magnetization vector $\boldsymbol{M}$ [30, 203]. The upper part of the spin wave band is limited by the Damon-Eshbach mode ($\boldsymbol{k} \perp \boldsymbol{M}$, DE, Figs. 4.9a, b, light blue solid line), which rises at both values of the external field, and for exchange dominated (high-k) spin waves converges towards quadratic dependence of frequency $f \propto k^2$. Hence, the shift of the right edge of the detected spin-wave band towards higher frequencies always means an enhanced sensitivity to spin waves with higher k-vectors. The left edge of the spin wave band is limited by the backward volume mode ($\boldsymbol{k} \parallel \boldsymbol{M}$, BV, Figs. 4.9a, b, dark blue dashed line), which first decreases in frequency for dipolar (low-k) spin waves and then increases for exchange dominated (high-k) spin waves (and again converges towards quadratic dependence $f \propto k^2$). In the low magnetic field, the exchange interaction prevails already for the spin waves with $k \approx 10\,\frac{\text{rad}}{\mu\text{m}}$ and the drop in the frequency for the BV mode is only 0.2 GHz. This results in a sharp increase of the BLS signal at the left edge of the spin wave band. The sharp increase is the same for both measured spectra (with the silicon disk and on the bare film). The μ-BLS even without the presence of the dielectric nanoresonator can still detect spin waves with k-vectors around the mode minimum at $k \approx 10\,\frac{\text{rad}}{\mu\text{m}}$ and thus the complete lower part of the spin wave band is captured in both cases. In the case of high magnetic field, the onset of the exchange dominated spin waves occurs at much higher values of k, at approx. $30\,\frac{\text{rad}}{\mu\text{m}}$. Here, the BV mode is very pronounced, and the mode frequency decreases approx. 1.5 GHz down from the ferromagnetic resonance frequency (FMR, $k = 0\,\frac{\text{rad}}{\mu\text{m}}$) before it starts rising again (Fig. 4.9b, dark blue dashed line). In this case, the μ-BLS on the bare film cannot detect spin waves above $k = 10\,\frac{\text{rad}}{\mu\text{m}}$ and capture the whole lower part of the spin wave band.

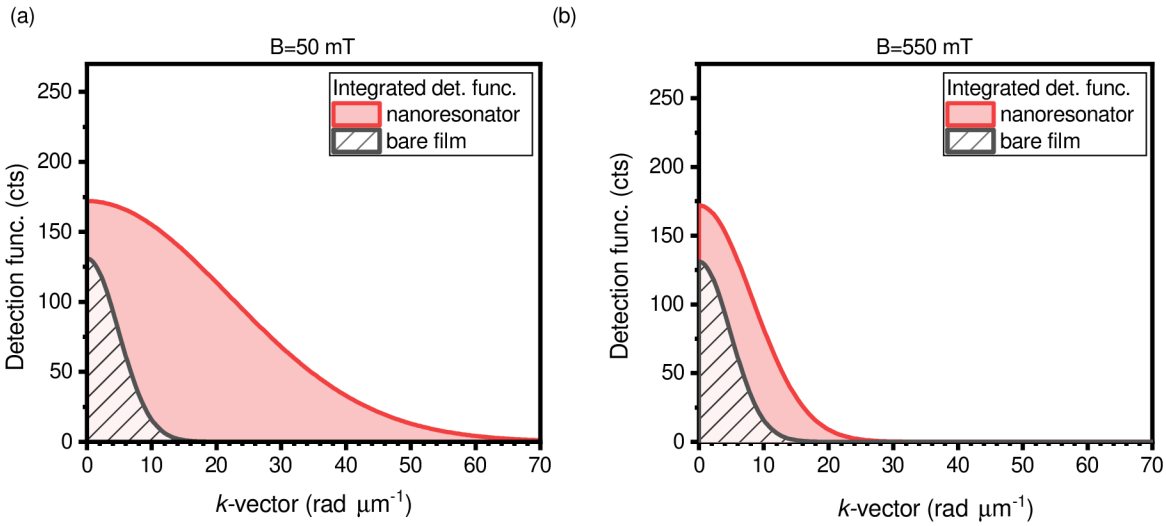

Figure 4.10: Gaussian detection functions extracted from the fits. a, b, Extracted Gaussian detection from experimental data shown in Fig. 4.9 using phenomenological model (Eq. 2.35). The panel **(a)** shows the data extracted from data acquired in 50 mT, and panel **(b)** from data acquired in 550 mT.

By fitting the parameters A and HWTM, we can obtain very good agreement between the model and the experimentally measured spectra for both the bare film and the silicon-disk-enhanced measurement (see black and red solid lines in Fig. 4.9a, b. In Fig. 4.10 the detection function $\Gamma(k_x)$ resulting from the fit to the experimental data measured at 50 mT (Fig. 4.10a), and 550 mT (Fig. 4.10b) are plotted for the bare film (black line) and for the measurement on the silicon disk (red line). This figures give us a direct visualization of the enhancement of the detection sensitivity caused by the presence of the dielectric nanoresonator extracted in each field. In 50 mT, the HWTM (i.e. the maximum detectable k) increased from $9.5 \pm 1.0 \frac{\text{rad}}{\mu\text{m}}$ for bare film to $47 \pm 3 \frac{\text{rad}}{\mu\text{m}}$ for silicon disk, whereas the A increased from 245 ± 6 cts to 259 ± 19 cts. Note that the increase in the amplitude of the Gaussian function does not represent the total increase of the integrated signal. After integration of the detection function, the value of $2720 \pm 170 \,\text{cts} \frac{\text{rad}}{\mu\text{m}}$ is obtained for the case of the bare film and the value of $14300 \pm 1600 \,\text{cts} \frac{\text{rad}}{\mu\text{m}}$ for the silicon-disk-enhanced signal. This gives us an enhancement factor of 5.3.

In 550 mT the widening of the detection function is significantly lower, due to the following two effects. Firstly, in 50 mT, this widening is a bit overestimated, see the modeled curve and experimental data around 16 GHz. On the other hand, in 550 mT the widening is underestimated, see model around both detection edges ($\approx$ 25 GHz and $\approx$ 31 GHz). This big uncertainty in fitting is caused by the strong assumption of the Gaussian shape of detection function. This assumption is valid for simple geometry of bare film (see comparison between the full BLS model and phenomenological model in chapter 2), but for the case of Mie-enhanced BLS the situation is more complicated and simple Gaussian shape of detection function does not completely describe observed BLS spectrum. The comparison of the main parameters of the fitted detection function for both fields is shown in Table 4.2.

Table 4.2: Summary of the fitted parameters of the detection function

	Field	A	HWTM	bg
bare film	50 mT	245 ± 6 cts	$9.5 \pm 1.0 \frac{\text{rad}}{\mu\text{m}}$	3 ± 1 cts
	550 mT	131 ± 7 cts	$11.4 \pm 1.0 \frac{\text{rad}}{\mu\text{m}}$	2 ± 1 cts
Mie-enhanced	50 mT	259 ± 19 cts	$47 \pm 3 \frac{\text{rad}}{\mu\text{m}}$	10 ± 2 cts
	550 mT	172 ± 13 cts	$18 \pm 2 \frac{\text{rad}}{\mu\text{m}}$	8 ± 4 cts

4.5.2. Sweep of the diameter of the silicon disks

Mie resonances are strongly dependent on the geometry of nanoresonators. To investigate this dependency, we measured a serie of silicon disks with diameters ranging from 100 to 1500 nm. First, we introduce the results obtained in the field of 50 mT, which deals only with diameters ranging from 100 nm to 300 nm. This is followed by similar analysis performed in field of 550 mT. We connect the trends in the analysed data with changes of the resonance modes calculated by FDTD simulations.

Fig. 4.11a shows relative scattering intensities acquired by dark-field optical spectroscopy, see chapter 3. A characteristic red shift (shift of the resonances towards the longer wavelengths) of the Mie resonances with increasing disk diameter can be observed. For 175 nm disk the peak resonance wavelength perfectly matches with the laser in our μ-BLS setup (532 nm). To quantify the dependence of the enhancement of the measured BLS spectra on the disk diameter at 50 mT, we fitted the HWTM (Fig. 4.11b) and A (Fig. 4.11c) parameters for each disk diameter. From these data, we can see that the enhancement of both parameters starts appearing for disk diameters beyond approx. 125 nm and reaches its maximum for the diameters between 170 and 200 nm. When the disk diameter exceeds 200 nm, we observe a sharp decrease of both parameters.

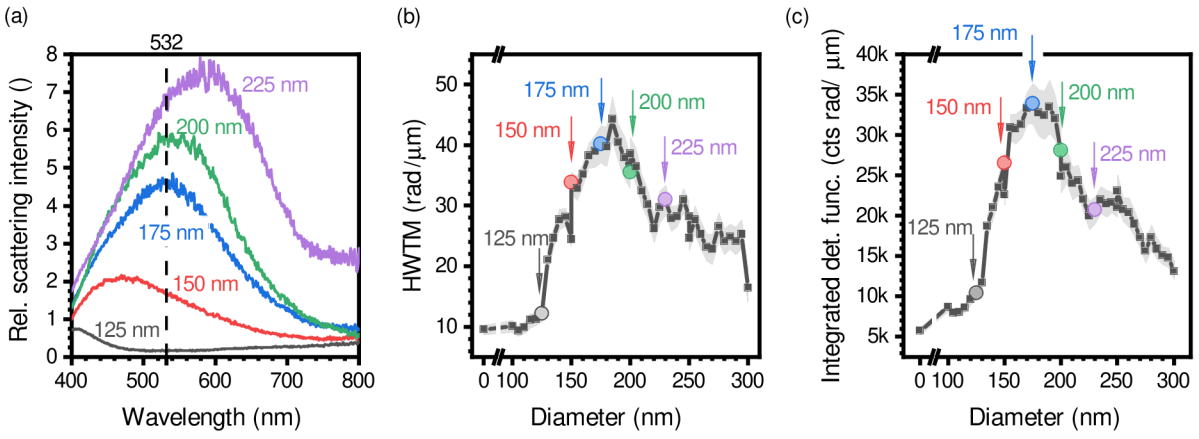

Figure 4.11: Dependence of the BLS enhancement on the silicon disk diameter at 50 mT. a, Relative scattering intensities of five selected silicon disks measured using dark-field optical spectroscopy. The dashed line marks the 532 nm wavelength of the μ-BLS laser. **b, c,** Dependence of HWTM (half-width-at-tenth-maximum, maximum detectable k-vector) and integrated detection function (BLS signal enhancement) on the diameter of the silicon disk. The arrows and colored points refer to the diameters with elastic scattering spectra shown in panel **(a)**.

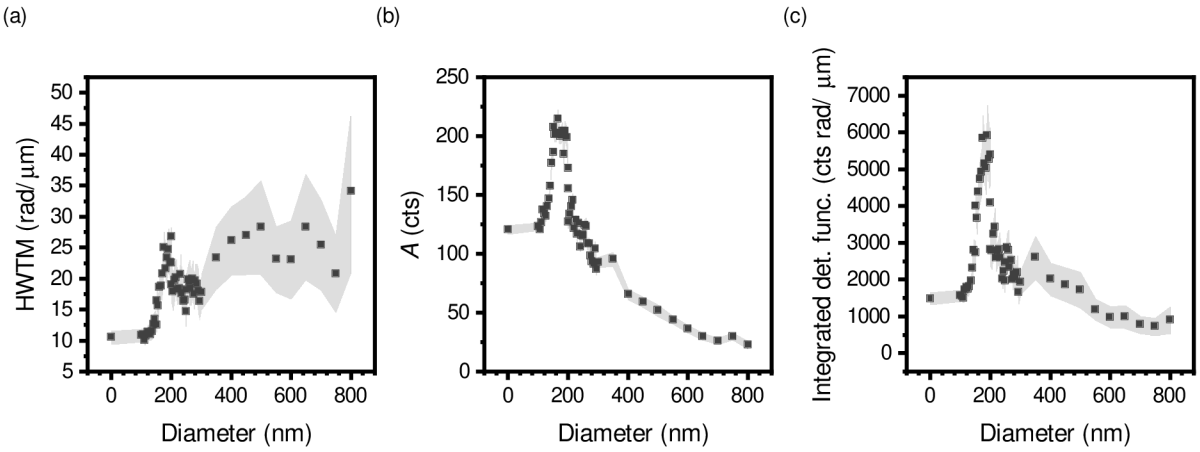

Figure 4.12: Dependence of the BLS enhancement on the silicon disk diameter at 550 mT. a, b, c Dependence of HWTM (half-width-at-tenth-maximum, maximum detectable k-vector), amplitude A, and integrated detection function (BLS signal enhancement) on the diameter of the silicon disk.

We repeated the same experiment at the field of 550 mT, see Fig. 4.12. Here, we show the data for disk diameters ranging from 100 nm to 800 nm. One can observe that HWTM is lower than in the case of lower external field (Fig. 4.11b), which is in agreement with Fig. 4.10. The amplitude (parameter A in Eq. 2.35) and integrated detection function are shown in Fig. 4.12b, c. In all three extracted parameters, we can again observe that the best performance is reached for the disks with diameter in the range from 175 nm to 200 nm, followed by sharp decrease. After approximately 300 nm, the width of the detection function (i.e. maximal detectable k-vector) raises again, see Fig. 4.12a. Here, the increase in HWTM is even bigger than in the 200 nm-wide disk. Therefore, these disks with diameters above 300 nm are not suitable for BLS measurements, as the signal is drastically reduced, see Fig. 4.12b, c.

The abrupt decrease in performance for diameters larger than 200 nm is visible in both external fields, see Figs. 4.11b, c, and 4.12. This decrease is observable in both the amplitude and widening of the detection function. Most likely, this is connected to the change of the main resonance mode in silicon disk.

To get better insights to underlaying physics, we performed the FDTD simulation of the two disks with diameters 180 nm, and 220 nm, which is before and after the abrupt decrease in performance. In the case of the 180 nm wide disk, we can observe electric dipole resonance, where the electric field hot-spots (places of high electric field intensity) are located along the edges in the axis of incident electric field polarization [204, 205], see Fig. 4.13a. In Figs. 4.13b, the cross-section in the plane of polarization is shown. We can observe asymmetry caused by the presence of the magnetic layer below the disk. Due to this, the electric field intensity is mostly located on the top of the silicon disk, see the colorbar scales in Figs. 4.13a, b. The electric field intensity also has a non-trivial distribution inside the silicon disk. On the edges, it is attracted to the magnetic layer below, while in the in-plane center is concentrated in the middle of the disk height. In plane perpendicular to the polarization axis of the incident light there are no visible hot-spots, see Fig. 4.13c.

In the case of 220 nm wide disk the resonance is of higher order, see Fig. 4.13d. The electric field intensity is no more concentrated only along the edges, but now there are

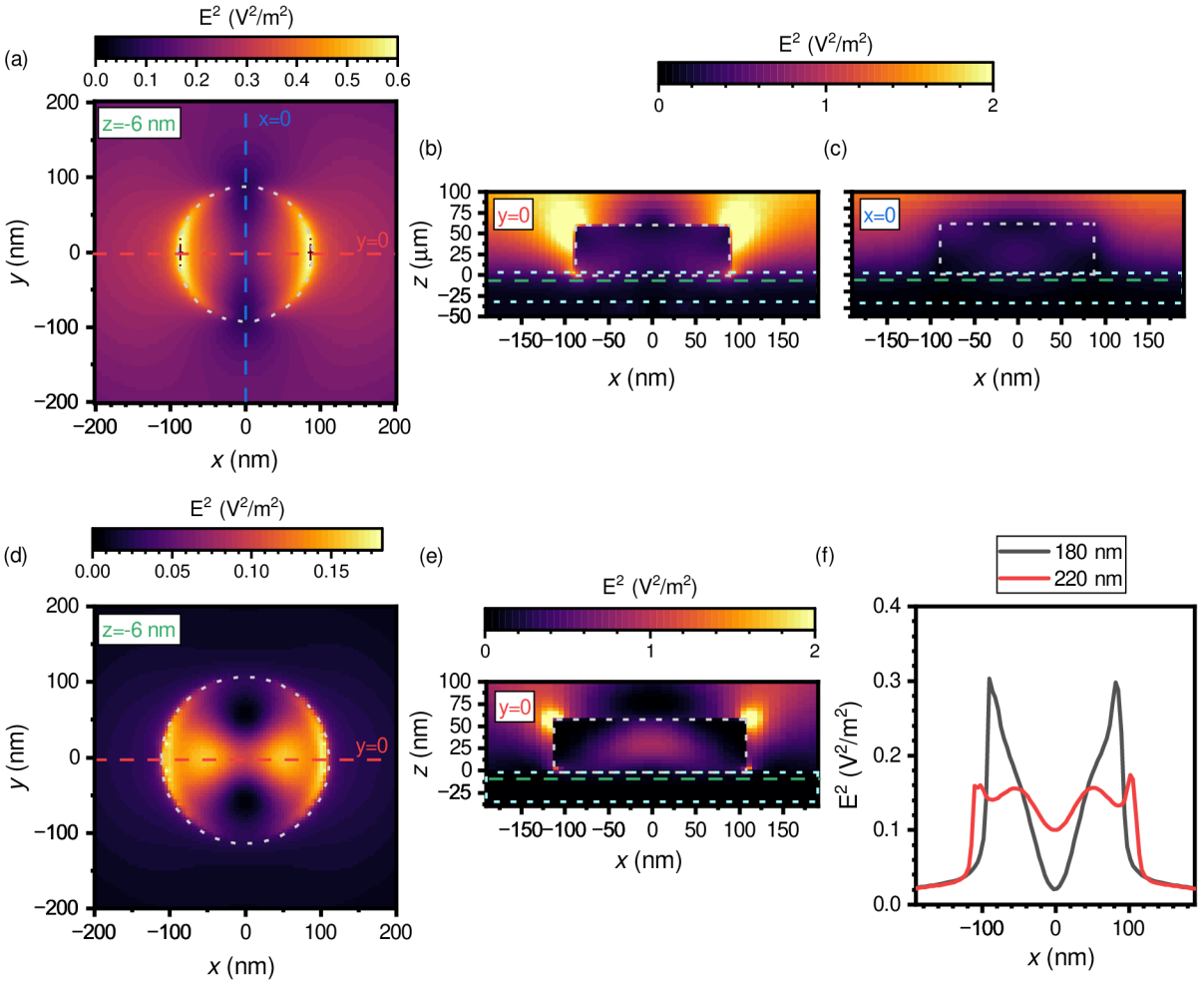

Figure 4.13: Comparison of Mie resonance in 180 nm and 220 nm wide disks. a, b, c, Squared electric field intensity maps of 180 nm wide disk on a 30 nm permalloy film, which is shown as the cyan dashed rectangle. Polarization of the incident Gaussian beam with $\lambda = 532$ nm is in the x direction.**a,** In-plane cross-sections 6 nm below the permalloy/air interface. The disk boundary is shown as a gray dotted line. The red, blue, and green dashed lines in **(a-c)** label xz, yz, and xy cross-sections, respectively. **b,** Cross-section of the xz plane. **c,** Cross-section through yz plane. **d, e,** Squared electric field intensity maps of 220 nm wide disk. **d,** In-plane cross-sections 6 nm below the permalloy/air interface. **e,** Cross-section of the xz plane. **f,** Squared electric field profile along the polarization axis 6 nm below the permalloy/air interface.

two more peaks located closer to the center of the disk. By comparing the cross-section in the plane of the incident polarization of 220 nm wide disk (Fig. 4.13e) with 180 nm wide disk (Fig. 4.13b), we can observe that the localization of the electric field intensity is way lower in the case of 220 nm-wide disk and overall, the intensity is more concentrated in the middle of the disk. By looking at the electric field profiles taken below the disk in the plane of polarization, see Fig. 4.13f we can directly see, that in the case of higher-order resonance hosted by 220 nm wide disk, the intensity is more evenly distributed, in comparison with 180 wide disk where in the center the intensity is almost zero. The more even distribution of the electric field intensity in 220 nm wide disk, can result in more absorption of the inelastically scattered light.

4.5.3. Influence of the index of refraction of dielectric disk on Mie resonances

In the previous section, we investigated the influence of the disk diameter on BLS signal enhancement and the mode of the Mie resonance. The change in disk diameter is somehow similar to the change in the wavelength of the probing light or, similarly, the material index of refraction (dielectric function). However, with the use of materials with a higher index of refraction (n), the resonance condition is fulfilled with smaller diameters, which may allow the detection of spin waves with even shorter wavelengths. The results presented in this section may serve as a guide for future material research and optimization of Mie-enhanced BLS.

We performed FDTD simulations of the disks with a diameter of 180 nm and 100 nm and index of refraction of 2.5, 4.3 (index of refraction assumed in all other simulations), and 6.0, see Fig. 4.14. The electric field is lower in the case of $n = 2.5$ (Fig. 4.14a) in comparison to the case of $n = 4.3$ (Fig. 4.14b). If the index of refraction is increased even further, a higher order radial mode occurs in 180 nm-wide disk for $n = 6.0$, see Fig. 4.14c. The influence of this higher-order mode is unclear at this moment but may have a negative effect (see Fig. 4.13). Moreover, increase in index of refraction causes decrease of electric field intensity around line $x = 0$.

In the all simulations of the smaller disk (d= 100 nm), we can observe smaller hotspots (see Fig. 4.14d-f), and thus, this miniaturization may enhance the detectable k-vectors even more. However, the experiment does not confirm this expectation, and at this moment, the explanation of this is unclear. Moreover, the electric field reaches the highest intensity for $n = 4.3$, and with further increase of index of refraction its intensity decreases, compare Fig. 4.14d-f. The onset of dark region around line $x = 0$ is visible only in the case of $n = 6.0$.

All of these observed phenomena are non-trivial, and it is very difficult to find patterns in them. This further complicates the design and optimization of the resonators for Mie-enhanced BLS. Furthermore, even after obtaining electric field distribution, it is not completely clear how this translates to the obtained signal.

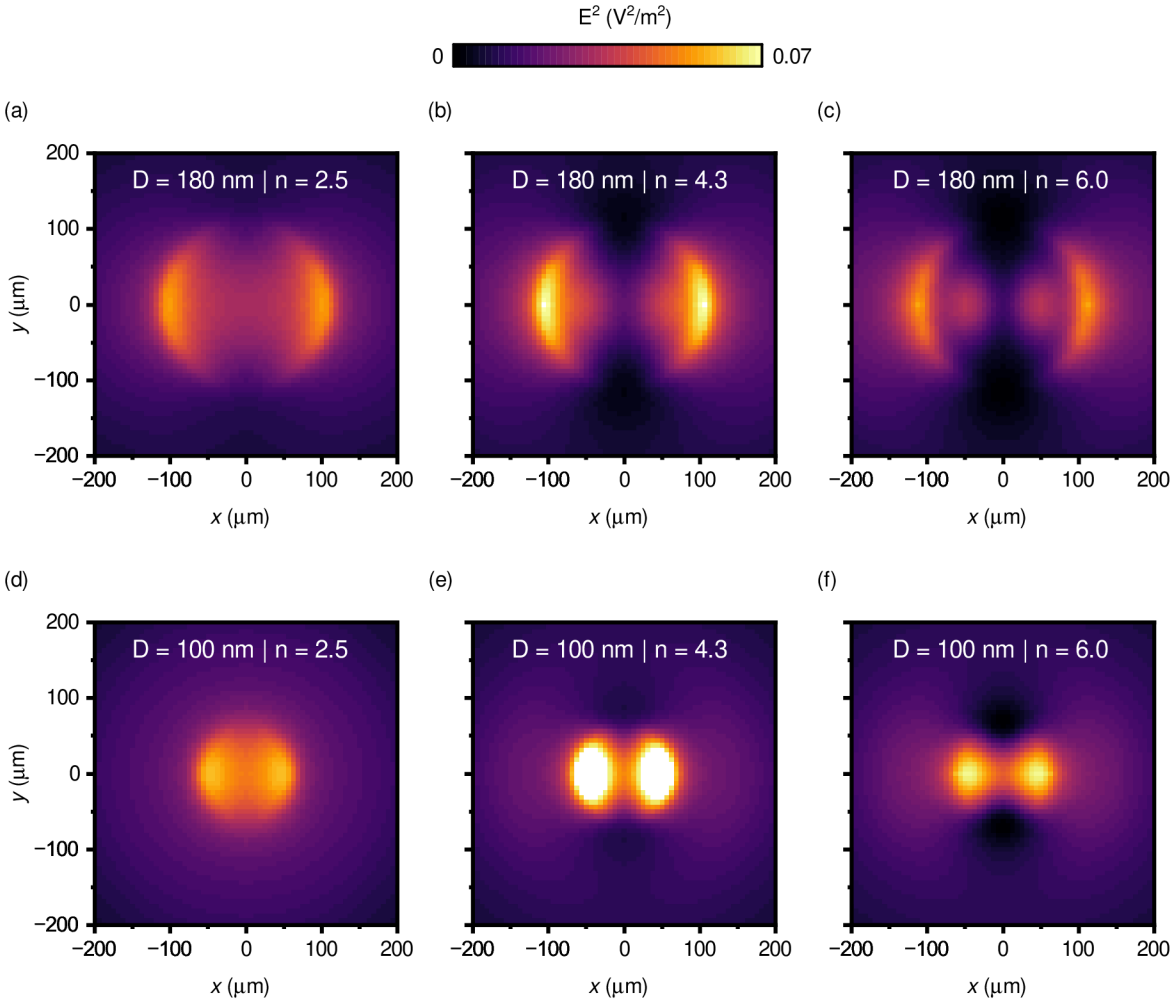

Figure 4.14: Influence of the index of refraction to Mie resonances. The squared electric field intensity is shown for disk of diameter 180 nm **(a, b,c)** and 100 nm **(d, e, f)**. The index of refraction is $n = 2.5$ **(a, d)**, $n = 4.3$ **(b, e)**, and $n = 6.0$ **(c, f)**.

4.6. Simulation of the Mie-enhanced BLS signal

This section deals with calculating the BLS signal in the presence of a scattering center. The calculation procedure was designed and implemented by Martin Hrtoň. The model gives normalized BLS intensity, and as it is based on FDTD simulation, it can account for various geometries. However, in this approach, polar symmetry is employed, which significantly reduces the amount of necessary FDTD simulations.

4.6.1. Theoretical description

We follow the approach introduced in Chapter 2. However, the situation is complicated by the fact that with the scattering center there is no analytical expression for both the electric field distribution and the dyadic Green function.

To calculate polarization vector (2.20), one has to use the results of FTDT simulation. We again assume that the profile of both the electromagnetic field and spin wave is constant across the thickness of the magnetic layer. The calculated polarization acts as a source of inelastically scattered light. However, the main difference to bare film is that now the polarization with free-light inaccessible wavevectors can be emitted to the far field and collected by the objective lens and eventually measured in the tandem-Fabry-Perot interferometer. This is allowed by the presence of perturbation (silicon disk hosting Mie resonance), which *flips-over* the wavevectors of induced polarization. Mathematically this is contained in the Green function, see Eq. 2.30.

Unfortunately, the dyadic Green function of such a system has to be calculated for each wavevector of induced polarization by FDTD simulations. The resulting BLS signal can be expressed as (the expression is similar to Eq. 2.31, but for clarity is written here again)

$$\sigma(\omega_\mathrm{m}) = \int \mathrm{d}^2 r_\parallel \int \mathrm{d}^2 k_\mathrm{m} \left| h(\mathbf{r}_\parallel) \int\limits_{k_\mathrm{p} \leq k_0 \mathrm{NA}} \mathrm{d}^2 k_\mathrm{p}\, e^{\mathrm{i}\mathbf{k}_\mathrm{p}\cdot\mathbf{r}_\parallel} \int \mathrm{d}^2 k'_\mathrm{p} \hat{\mathbf{G}}(\mathbf{k}_\mathrm{p},\mathbf{k}'_\mathrm{p})\, \hat{\boldsymbol{\chi}}(\omega_\mathrm{m},\mathbf{k}_\mathrm{m}) \mathbf{E}_\mathrm{d}(\mathbf{k}'_\mathrm{p} - \mathbf{k}_\mathrm{m}) \right|^2 . \tag{4.6}$$

Inspecting the above expression, there are apparently many factors that can affect the resulting shape of the BLS spectrum, but the ability to measure signal originating from high-k magnons has one clear prerequisite: the driving electric field also has to possess high-k components.

4.6.2. Obtained spectra for various disk diameters

From the integral inside the equation, it is visible that the possible scattering processes are determined by the spatial Fourier transform of the incident electric field. To obtain such distribution of the electric field inside the sample in real coordinates finite-difference-time-domain (FDTD) simulations have to be used, see Fig. 4.15a-d. In the bare film, the electric field has a 2D Gaussian distribution (Fig. 4.15a). However, in the case of 100 nm, 180 nm, and 220 nm wide silicon disks, we can observe the field localized in subdiffraction regions due to Mie resonances (see Figs. 4.15b-d for electric field distributions). As stated earlier, the ability to measure the spin waves with higher k-wavevector is mainly determined by the Fourier transform of the electric field distribution [i.e. by $\boldsymbol{E}(k_x,k_y)$]. In the case of bare film, the Fourier transform of the Gaussian electric field distribution is again Gaussian, see Fig. 4.15e. The extent of the intensity is determined by the width of the

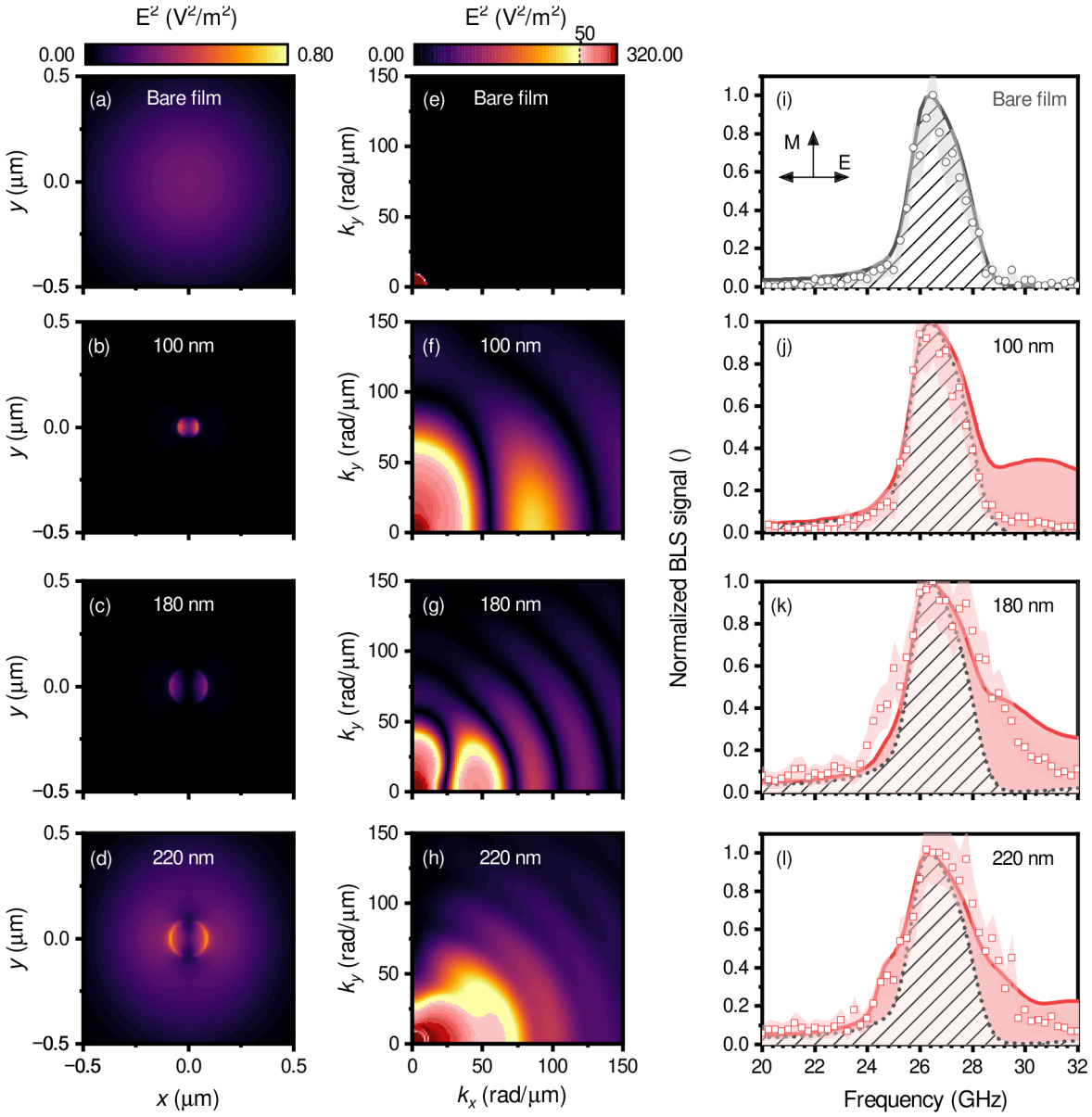

Figure 4.15: Numerical simulation of the electric field distribution and theoretically calculated BLS signal. a, b, c, d, Real-space distribution of squared electric field for **(a)** bare permalloy film and for the same permalloy film with 100 nm **(b)**, 180 nm **(c)**, and 220 nm **(d)** wide silicon disks on top. **e, f, g, h,** Reciprocal space distributions of the data shown in **(a)**, **(b)**, **(c)**, **(d)**, respectively. The colormap has two linear regions; 0–50 V^2m^{-2} and 50–320 V^2m^{-2} for better clarity. The boundary between the regions is marked by the dashed line. **i, j, k, l,** Calculated and measured BLS signal for **(i)** bare permalloy film and for the same permalloy film with **(j)** 100 nm, **(k)** 180 nm, and **(l)** 220 nm wide silicon disks.

spot in real space, see Chapter 2. In case of the Mie resonances hosted in silicon disk, and subsequent focusing to subdiffraction hot spots, the electric field spans over a larger area of the k-space exceeding values of $120\,\frac{\mathrm{rad}}{\mu\mathrm{m}}$, see Figs. 4.15f-h for their respective Fourier transform.

The Eq. 4.6 was used to calculate the BLS spectra for bare film and silicon disks with diameters of 100 nm, 180 nm, and 220 nm at external fields of 550 mT, which is shown with respective experimental data in Fig. 4.15j-l. In bare film we get perfect agreement between the Eq. 4.6 and measurement, as in agreement with Fig. 2.19. The presented model shows huge widening already in the case of 100 nm wide disk; however, in experimental data, this is barely visible, see Fig. 4.15j. In the case of 180 nm and 220 nm wide disk we can observe qualitatively similar features in both, model and experimental data. However, the good agreement between the model and experiment wasn't achieved. The origin of this discrepancy is currently unknown. This makes optimization of the Mie resonator by FDTD simulation impossible, and thus the future designs has to extensively rely on experiments.

4.7. Heating of the magnetic layer under the nanoresonator

To rule out the presence of the non-linear phenomena and self-focusing caused by the thermally-induced spatially dependent index of refraction, I performed a multiphysics simulation [206]. The system, which consists of Gaussian illumination, silicon disk, and Permalloy layer, was investigated in terms of heating caused by dissipation of the laser power and subsequent change in refractive index. The model was solved in an iterative manner until convergence was reached, accounting for the mutual effects of both phenomena. I performed all presented simulations. However, the model was designed by Jakub Zlámal. All simulations were carried out in Comsol 6.0, see section 3.4.3.

4.7.1. Multiphysics simulation

In contrast to the FDTD calculation, in Comsol, all calculations were done in the frequency domain. The electric field calculation in Comsol agrees with the FDTD, compare Figs. 4.16a,b and 4.13a,b. This confirms that there is no significant influence of the temperature-dependent index of refraction for laser power of 3 mW. This laser power was used in all presented experiments (if not stated differently). There is only small increase in temperature, see Figs. 4.16c,d. This increase is at maximum 30 K, which is approx. 10 % of the initial temperature (room temperature $\approx 293\,K$). Such increase in temperature results in the shift of index of refraction of silicon from 4.16 to 4.17.

Another aspect connected to the rise in temperature is the reduction of saturation magnetization [15, 202]. With increasing temperature, the saturation magnetization is decreased until the temperature reaches the critical value, so-called Curie temperature, where the ferromagnetism completely vanishes. We fitted this behavior with model by Kuz'min, see Eq. 4.5. The fitted dependency is used to calculate change in the FMR frequency, see Fig. 4.16e. The increase of 30 K reduces the saturation magnetization of the permalloy by 0.6 percent [see Fig. 4.16 (e)], which in turn shifts down the spin wave band by approx. 20 MHz, which is far below the resolution of our TFPi with the mirror spacing set to 3 mm [112].

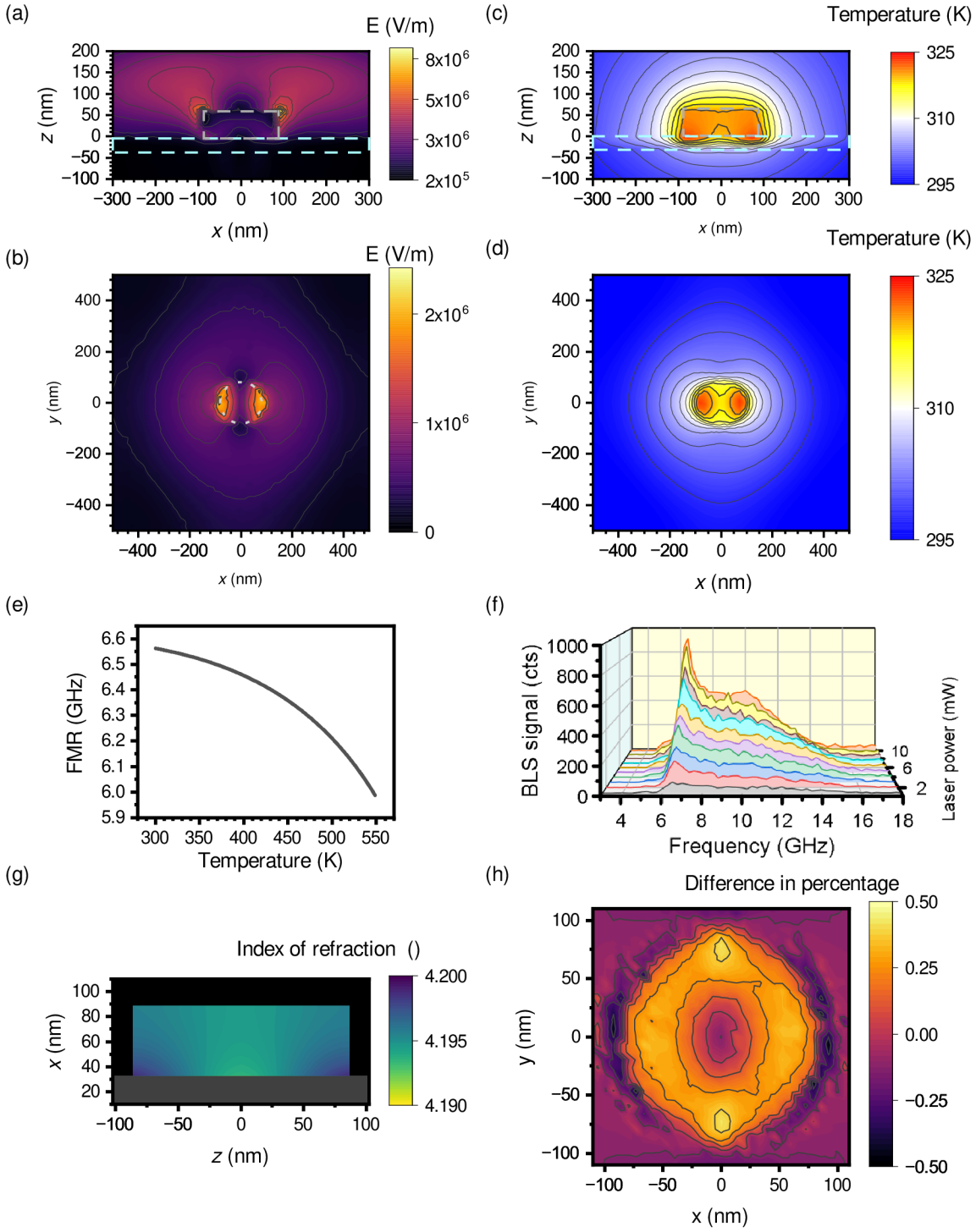

Figure 4.16: Local heating of the sample in the vicinity of the silicon disk. a, b, Simulations of squared electric field intensity in the xz plane **(a)** and xy plane **(b)**. **c, d,** The temperature distribution in the xz plane **(c)** and xy plane in $z = = -6$ nm **(d)**. **e,** FMR frequency as a function of temperature calculated from the model presented in Fig. 4.8. **f,** BLS spectra measured on a silicon disk with laser power ranging from 1 to 10 mW. **g,** Calculated index of refraction with 10 mW laser power. **h,** Difference in percentage in normalized electric field between the 3 mW and 10 mW laser power in xy-plane. **g,** Calculated temperature-dependent index of refraction for 10 mW incident power. **h,** Percentage difference between normalized electric field calculated for 10 mW and 3 mW incident power.

4.7.2. Measurement with different laser powers

We also measured the thermally excited BLS spectra with higher laser powers. The results are shown in Fig. 4.16 (f), and it can be seen that even with the highest laser power of 10 mW, there is no visible reduction of FMR frequency. However, we can see that the shape of the spectra is affected. The new peak arises at $\approx$ 11 GHz, which can be caused by change of the electric field shape induced by the local change of refraction index of silicon. This change inside the disk in xz-plane for 10 mW incident laser power is calculated in Fig. 4.16g. In the region of the hot-spots (in xz-plane on the edges) the index of refraction is elevated approx. to 4.2 from a room temperature value of 4.16. The corresponding temperature is approx. 390 K. This change in refractive index value induced subsequent changes in electric field distribution. We show the difference in shape (percentage change in normalized electric field distribution) in Fig. 4.16h. The differences reaches 0.5 %. By increasing the electric field intensity in the position of the disk and decreasing the intensity on the outer perimeter, one can judge that an elevated index of refraction causes the concentration of the electric field to a smaller area. However, it is not clear if this is solely the only reason for the change of the shape of spectra in Fig. 4.16f.

4.8. Sweeps over the edges of the silicon disk with a diameter of 1500 nm

To further explore the role of the nanoresonators' edges, I studied the enhancement of the BLS spectra on edges of 1500 nm-wide silicon disk. This diameter is roughly three times larger than the waist of the probing laser beam, and thus, the role of the finite sizes of the disk is strongly suppressed. Such a situation is very similar to the measurement on the semi-infinite film. In the following section, I demonstrate that this lack of polar symmetry around the probing beam can be utilized to achieve directional sensitivity only for spin waves propagating perpendicularly to the illuminated edge.

4.8.1. Measurement on the edges of the disk

We measured BLS spectra with the laser spot focused on the right edge and then on the top edge of a large, 1500 nm wide, disk (see Fig. 4.17a). We can see that compared to the measurement on a bare film, the overall BLS signal is lower at both laser spot positions, see Fig. 4.17b. Nevertheless, the enhancement of the maximum detectable k-vector is still present. Interestingly, when the laser beam is positioned on the right edge of the disk, we can see a broadening of the spin wave band towards higher frequencies (Fig. 4.17b, red line). This means, that wavenumber sensitivity to spin waves in Damon-Eshbach geometry was increased, see solid blue line in Fig. 4.17b. Also, the low-frequency edge is moved towards the higher frequencies, which suggests that spin waves in a backward volume direction cannot be measured in this position. When the laser beam is positioned on the top edge of the cylinder, we can see a broadening of the spin wave band towards lower frequencies (Fig. 4.17b, green line), see dashed blue line in Fig. 4.17b. In the phenomenological model (Eq. 2.35), We used different HWTM for x- and y-directions. Please note that this model does not properly describe the measured data here. This suggests that the instrumental *detection function* cannot be approximated by Gaussian function in this situation. Contrary to the situation on the right edge, the other edge

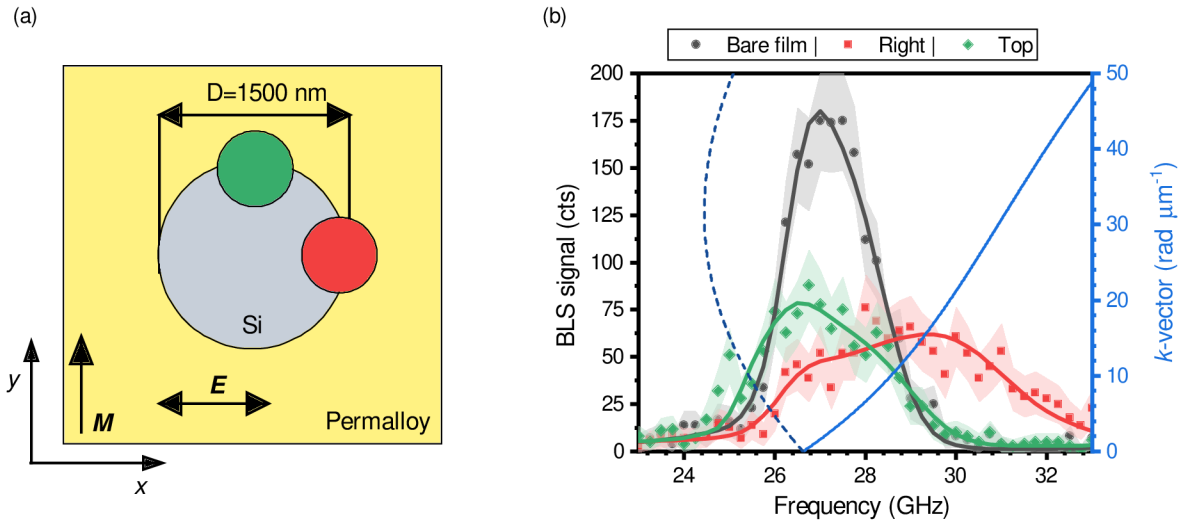

Figure 4.17: BLS enhancement at the edges of a large silicon disk. a, Schematics of the performed experiment. **b,** BLS spectra acquired in the field of 550 mT on the right edge (red line), and on the top edge (green line) of a large silicon disk compared with the spectra measured on a bare permalloy film (black line) with magnetization M pointing in the $y-$direction, see schematic. Blue line represent analytically calculated dispersion relation for DE (light blue solid line) and BV (dark blue dashed line) spin waves. The error band is calculated from the Poisson distribution.

(in this case, high frequency edge) is not moved and stays in the same position as in measurement on bare film.

These experiments suggest that it is possible to change the sensitivity to different spin wave k-vector directions. On the right edge, BLS signal was more sensitive to Damon-Eshbach spin waves ($\boldsymbol{k} \perp \boldsymbol{M}$), whereas on the top edge, it was more sensitive to backward-volume spin waves ($\boldsymbol{k} \parallel \boldsymbol{M}$). Please pay attention to the fact that during this measurement, not only the direction of the edge with respect to the magnetization was changed, but also the direction of the edge in respect to electric polarization. The better experimental scenario would be to stay on the right edge of the disk, and rotate with the magnetization by rotating the external field.

4.8.2. Linescan across the edges of the disk

To quantify this directional sensitivity and to estimate the spatial dependency, we performed a BLS linescan from the disk center across the right (Fig. 4.18a, red circle in Fig. 4.17a) and top edge of the disk (Fig. 4.18b, green circle in Fig. 4.17a). In Fig. 4.18a, the broadening of the BLS spectra towards higher frequencies around $x = 600$ nm is visible. On the other hand, the loss of the sensitivity to backward-volume spin waves (narrowing in the direction of lower frequencies) appears later, i. e., when sweeping from the direction of the bare film towards the disk center, first the sensitivity for Damon-Eshbach spin waves is increased and after another approx. 300 nm the sensitivity to backward-volume spin waves is decreased. In Fig. 4.18b, we can observe broadening towards the lower frequencies across 600 nm as expected. Contrary to the case of Fig. 4.18a, there is no decrease in sensitivity to the spin waves propagating tangentially to the disk edge (Damon-Eshbach spin waves, higher frequencies).

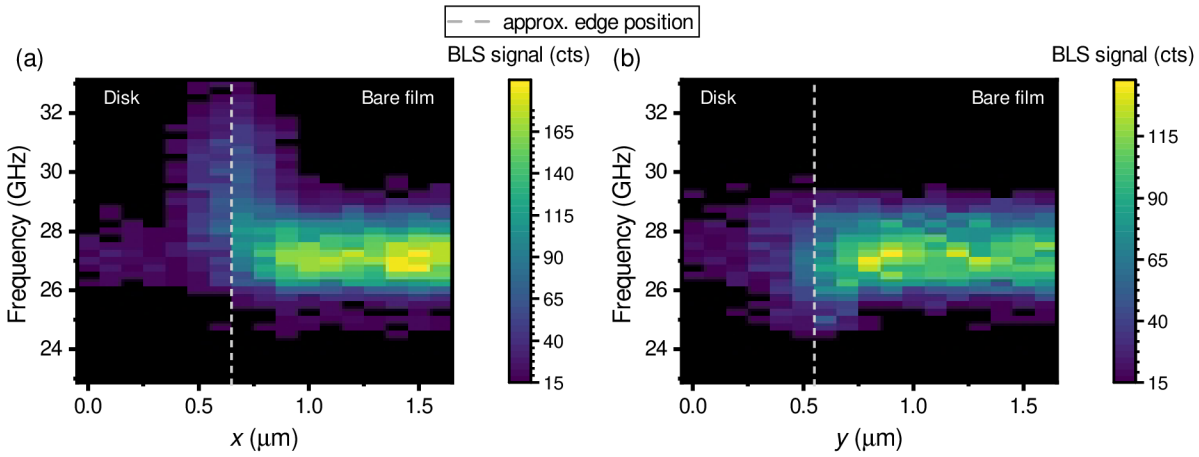

Figure 4.18: Position-frequency map on horizontal and vertical edge. a, b, BLS horizontal **(a)** and vertical **(b)** linescan across the right edge of the large silicon disk. The edge position is marked by the light gray dashed line.

The measured data shown in Fig. 4.18 were fitted for each position by the phenomenological model (Eq. 2.35) assuming different HWTM for each direction (X and Y). In Fig. 4.19a the integrated detection function for right disk edge is depicted for both perpendicular directions of spin-wave propagation. Similarly, in Fig. 4.19b, the HWTM parameters for both directions of spin-wave propagation are shown. As expected, all four fitting parameters remain contestant before the beam reaches the disk at approx. 0.9 μm. After that, HWTM in Damon-Eshbach direction (X) is approx. 5 times increased. Due to this increase, the integrated detection function in Damon-Eshbach (X) is increased as well, despite a slight decrease in amplitude parameter A. On the other hand, in the backward-volume direction (Y), we do not observe any increase, but fitting fails to emphasize the decrease of the sensitivity in the backward-volume direction (Y). After the majority of the area of the Gaussian spot reaches the silicon disk (approx. 0.3 μm) the BLS signal almost vanishes, see Fig. 4.19a.

In the case of the top edge (Fig. 4.19c, d), the enhancement of the integrated detection function and HWTM is not so pronounced (when compared to the right edge, see Fig. 4.19a, b). This is partially caused by the nature of the spin-wave dispersion in backward-volume mode. However, it seems that the geometry where electric field polarization is perpendicular to the disk's edge is much more favourable for high-k spin wave detection. Nevertheless, we still can observe a slight enhancement in the integrated detection function and HWTM at the position of the disk's edge (approx. 0.7 μm). Interestingly, this enhancement is visible in both directions of the propagation of spin waves. The best-achieved enhancements for the right and top edges are summarized in Table 4.3.

Table 4.3: Summary of the fitted parameters of the detection function for disk's right and top edges.

	A	HWTMx	HWTMy
Right edge	58 ± 4 cts	$50 \pm 5 \frac{\text{rad}}{\mu\text{m}}$	$13 \pm 2 \frac{\text{rad}}{\mu\text{m}}$
Top edge	76 ± 4 cts	$17 \pm 2 \frac{\text{rad}}{\mu\text{m}}$	$20 \pm 2 \frac{\text{rad}}{\mu\text{m}}$

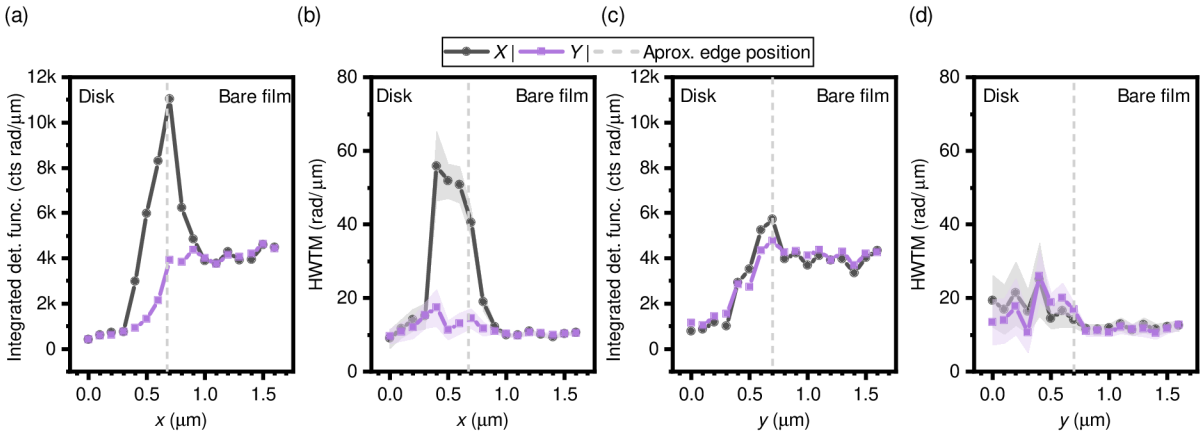

Figure 4.19: Spatially dependent fitting of BLS spectra using the phenomenological model on the right and top edge of wide silicon disk. a, b, Integrated detection function **(a)** and HWTM **(b)** of the detection function extracted from a fit to the data presented in 4.18a (scan across right disk's edge). **c, d,** Integrated detection function **(c)** and HWTM **(d)** of the detection function extracted from a fit to the data presented in 4.18b (scan across top disk's edge).

4.9. Versatility of the Mie-enhanced BLS

So far, all the experiments were performed only on a single NiFe layer with laser wavelength of 532 nm. In this chapter, I prove the wavelength versatility of this technique by measuring on the same sample with a laser wavelength of 457 nm. I have to measure on different setups, as the change of the wavelength is not trivial, and besides, the change of the laser requires a change of the Fabry-Perot mirrors as they have wavelength-specific coating. These measurements were thus carried out in the labs of Prof. Chumak at the University of Vienna. I further tested versatility by changing the material system from NiFe to CoFeB and using the 532 nm wavelength.

4.9.1. Measurement with laser wavelength of 457 nm

The electromagnet that is used in µ-BLS setup in Vienna cannot provide an external magnetic field higher than 500 mT, so I was not able to stick to 550 mT as in previous experiments, and instead, we measured BLS spectra in 450 mT.

Fig. 4.20a shows the spectra taken on bare film (black squares) and 140 nm-wide silicon disk (black squares). We can observe slight enhancement (widening of the obtained spectra). The data were fitted with the same model as in the case of the wavelength of 532 nm, and the resulting fitted curves are shown as solid lines. A good agreement between the fit and experimental data was achieved. Please note that there is a way higher background signal in comparison to the setup located in CEITEC, which is caused by the different detectors and higher levels of ambient light entering the TFPi input pinhole.

The same experiment was repeated for disks with diameters ranging from 100 nm to 300 nm[4], and all spectra was fitted. The resulting fit parameters are shown in Fig. 4.20b,c. Overall, the enhancement of both HWTM and integrated detection function is smaller in

[4]The spin-wave signal was not visible for disks with diameter above 300 nm.

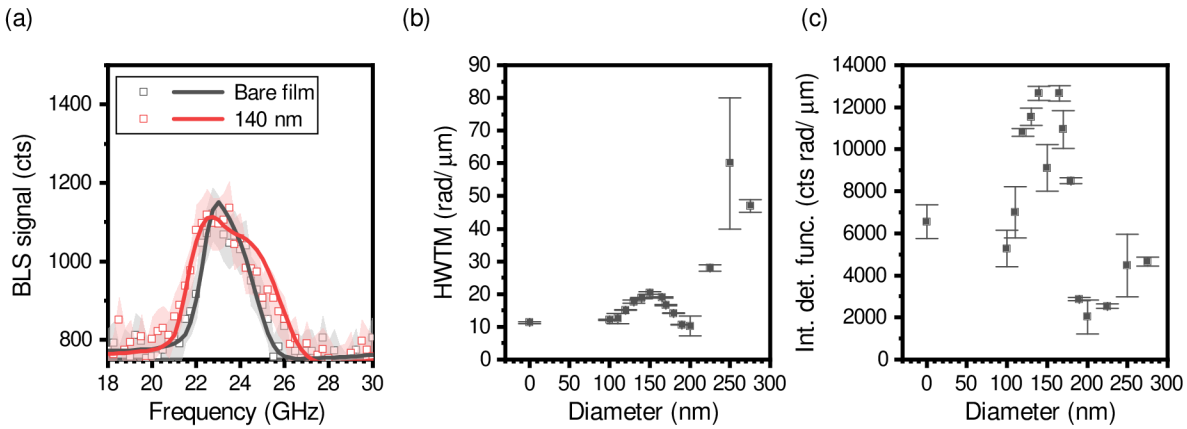

Figure 4.20: BLS enhancement with wavelength of 457 nm. a, µ-BLS spectra taken on bare film (black squares), and 140 nm-wide silicon disk (red squares). The black (red) solid line shows the fit of the data taken on bare film (silicon disk). **b, c** HWTM and integrated detection function analyzed for different disk diameters.

comparison to the case with 532 nm wavelength. The best result is achieved for a disk with a diameter of 140 nm. This is shifted by approx. 60 nm from the case of 532 nm, and is caused by the shorter used wavelength as an important parameter for resonance is a ratio between the geometrical dimension of the Mie resonator and wavelength of the light in the used material. For disk diameters larger than 200 nm, there was an abrupt decrease in BLS signal, which compromised the fitting of these spectra.

We think, that the drastic decrease of the performance of the enhancement of the BLS signal is caused by the higher absorption of silicon for wavelength of 457 nm. In order to investigate this, we have measured the dielectric function of the deposited silicon layer, see Fig. 4.21. The absorption of silicon is increased by approx. factor of 1.5 for 457 nm in comparison to 532 nm (from 1.1 to 1.8). The index of refraction changes only by approx. 1 %.

Another possible explanation for the decreased performance would be significantly lowered scattering efficiency, see Fig. 4.11a. We can observe that with decreasing wavelength, the resonance is moved towards the smaller disk diameters (which is in agreement with enhancement shown in Fig. 4.20b,c), and at the same time, the relative scattering intensity is significantly lowered. This may indicate that the electric field enhancement is lower in the case of 457 nm compared to the 532 nm wavelength.

4.9.2. Enhancement on the 100 nm thick CoFeB layer

Here, we have fabricated the same design (see Fig. 4.5) on the 100 nm thick CoFeB layer. Such thickness of the magnetic material is not ideal for studying the enhancement of wavevector detection because of the presence of the standing spin wave modes (PSSW) in the vicinity of the fundamental mode.

The experimentally measured data are shown as black squares (bare film) and red dots (245 nm wide disk) in Fig. 4.22a. We can observe broadening towards the lower frequencies of spectra taken on disk compared to the bare film measurement. Moreover, the broadening towards higher frequencies is visible in fundamental and PSSW modes. We fit the data in a similar fashion as for the NiFe layer, which is shown as a red solid

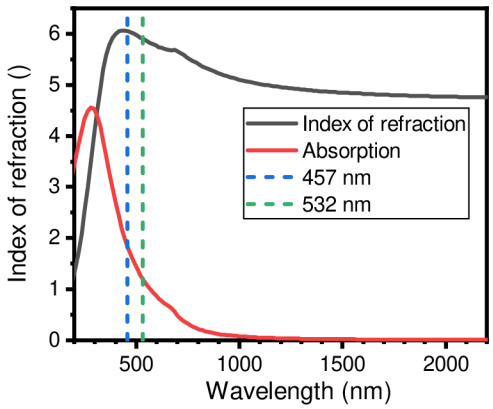

Figure 4.21: Optical properties of the used silicon. Measured index of refraction and absorption of the used silicon by ellipsometry.

line[5]. For fit, we used only the fundamental mode. This severely limits the accuracy of the fitting in comparison to the 30 thick NiFe layer, where the fundamental mode can freely broaden without interfering with the 1st PSSW mode.

The spectra were measured on disks with diameters ranging from 150 nm to 700 nm. Acquired spectra were fitted and resulting A, and HWTM parameters are shown in Fig. 4.22b, c, respectively. As previously mentioned, the uncertainty of the fits is high, but similar trends can be observed. Both HWTM and amplitude are increasing between the diameter 150 nm and 200 nm where they reach the maximum. The decrease of amplitude is visible on disks with diameters larger than 300 nm.

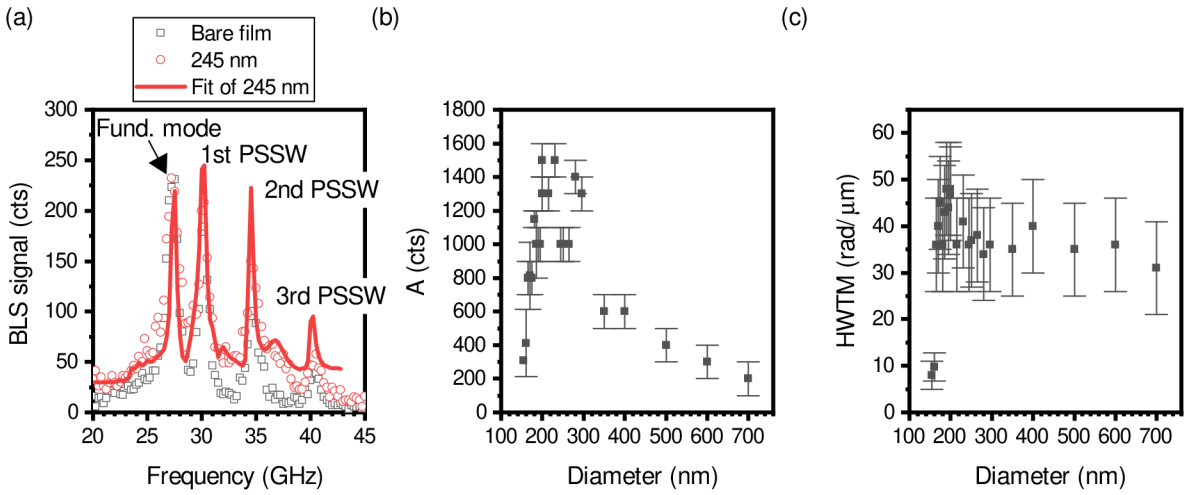

Figure 4.22: BLS enhancement on the 100 nm thick CoFeB layer. a, µ-BLS spectra taken on bare film (black squares), and 245 nm-wide silicon disk (red dots). The red solid line shows the fit of the data taken on silicon disk. **b, c** A and HWTM analysed for different disk diameters.

[5]The amplitudes of peaks associated with PSSW modes are adjusted

5. Mie-induced wavevector resolution in the micro-focused Brillouin light scattering spectroscopy

This chapter introduces the possibility to measure full in-plane wavevector (it's angle and magnitude) of spin waves based on Mie resonances in stripe arrays. The results presented in this chapter are (yet) unpublished, and thus are shown as preliminary results. Achieving wavevector resolution is topic of Jakub Krčma's bachelor's project. He made all FDTD simulations and fabricated samples in collaboration with my fellow PhD student Jakub Holobrádek.The μ-BLS experiments and data analysis presented in this chapter were performed as a joint collaboration between me and Jakub Krčma.

The chapter is structured as follows: I start with description of the basic concepts of this technique and underlying physics, then I continue with the description of the sample design and fabrication. Afterward, I discuss electric field distribution in studied structures obtained by FDTD simulations, and finally, I describe the μ-BLS experiments, data analysis, and compare the experimental results to theoretical models.

5.1. Basic concepts

Conventionally, the wavevector resolution in BLS is achieved by probing the spin-waves with large laser spots (waist of tens of microns) under different tilts of the sample [42, 207]. Such an approach has very limited spatial resolution and is complicated due to the measurement under the tilt, which makes it challenging to maintain the focus and proper position of the probing beam. This chapter shows that achieving wavevector resolution with micro-focused BLS microscopy with diffraction-limited probing spot is possible. This is achieved by inducing periodicity in the incident electric field, which allows the BLS process to occur only for spin waves with matching wavevectors. This technique can potentially allow wavevector-resolved investigation of spatially dependent behavior of incoherent spin waves (such as adiabatic parametric pumping in magnonic nanoconduits [208]), which is not possible with any other existing experimental technique.

As discussed in Sec. 2.2.1, the first step to model the BLS signal is to calculate the induced polarization

$$\boldsymbol{P}(\omega,\boldsymbol{k}) = \boldsymbol{E}_{\mathrm{d}}(\omega,\boldsymbol{k}) * \hat{\boldsymbol{\chi}}(\omega,\boldsymbol{k}). \tag{5.1}$$

This equation shows that the resulting polarization can be formed only around the k-vectors present in the electric driving field. The second step, radiation of the light to the far-field, is governed by the following equation

$$\mathbf{E}_{\mathrm{FF}}(\omega,\mathbf{k}_{\mathrm{p}}) = \hat{\mathbf{G}}(\omega,\mathbf{k}_{\mathrm{p}},\mathbf{k}'_{\mathrm{p}})\mathbf{P}(\omega,\mathbf{k}'_{\mathrm{p}}). \tag{5.2}$$

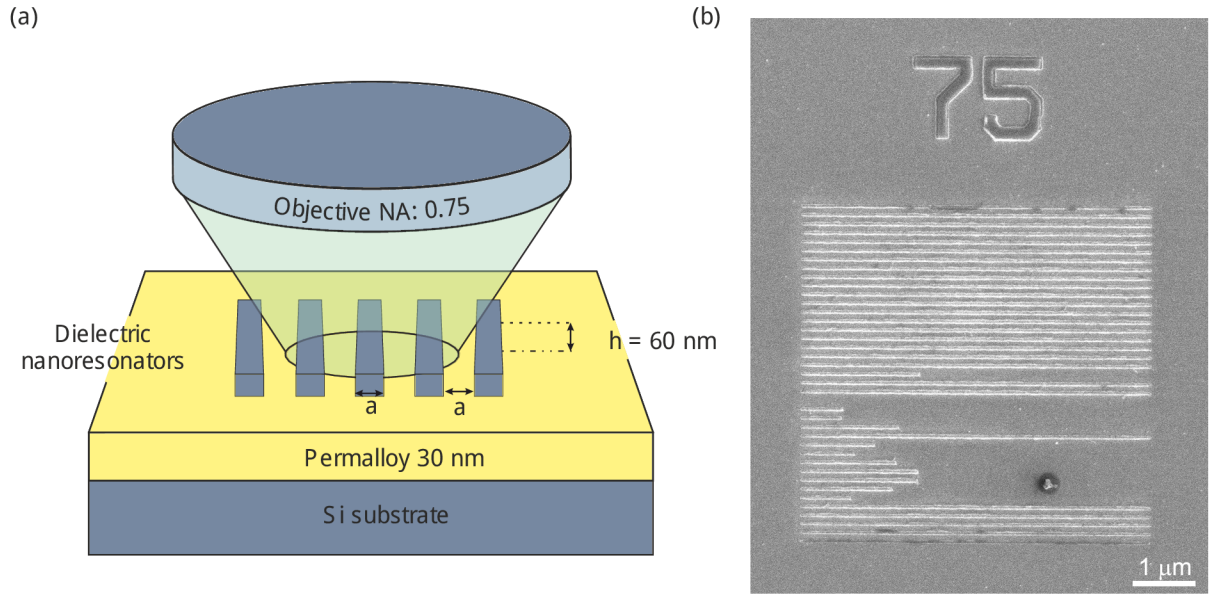

Figure 5.1: Experimental scheme of k-resolved µ-BLS measurement of thermal spin waves. a, Sketch of the experiment setting. The parameter a defines the periodicity of the structure. **b,** Scanning electron microscope image of fabricated structure.

This equation implies, that only the polarization with k-vectors on which the Green function ($\hat{\mathbf{G}}(\omega,\mathbf{k}_\mathrm{p},\mathbf{k}'_\mathrm{p})$) has non-zero elements can be measured.

Knowing these two facts, the problem of measuring specific k-vectors is reduced to inducing this specificity to (ideally both at the same) the electric driving field ($\boldsymbol{E}_\mathrm{d}$) and the Green function ($\hat{\mathbf{G}}(\omega,\mathbf{k}_\mathrm{p},\mathbf{k}'_\mathrm{p})$). As these two processes are reciprocal, we restrict our theoretical investigation only to the calculation of the incident driving electric field.

5.2. Sample design and fabrication

We achieve the k-vector specificity in both processes by placing of periodic dielectric stripes on top of the 30 nm thick NiFe layer with varying parameter a, see Fig. 5.1a. The parameter a stands for the width of the stripes and the gap between them. For good k-vector selectivity, keeping these two dimensions the same is important, as it emphasizes the given periodicity. The sample fabrication procedure was similar to the one used in Chapter 4. However, to achieve the a parameter as small as possible, and at the same time, to ensure that the gap and stripe width remain the same, we swept the electron dose and the nominal ratio between the gap and stripe width. After the fabrication was finished, we inspected the sample with a scanning electron microscope and assessed the quality of all structures. The structures, which provided a 1 : 1 ratio between the gap and stripe width and were defect-less[1], were then used for µ-BLS measurement.

An example of such fabricated structure with $a = 75$ nm is shown in Fig. 5.1b. The structure was not properly fabricated at the bottom of the stripes array. In this particular example, it was probably caused by the presence of the dust particle present in the image. Nevertheless, as the probing spot has a waist of 460 nm, this particular structure offers plenty of space in the top part for the µ-BLS measurements.

[1] at least in the area of approx. $1 \times 1\,\mu\mathrm{m}^2$

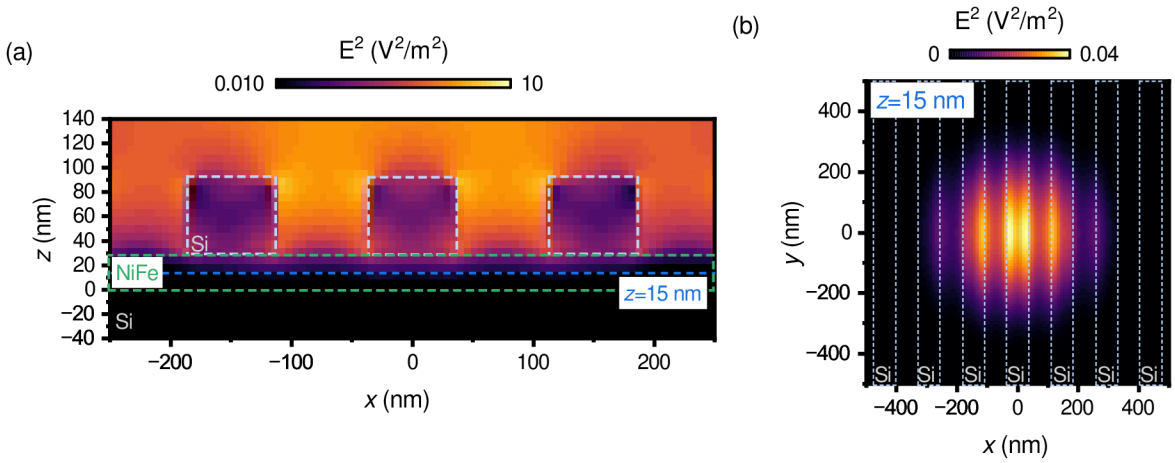

Figure 5.2: Squared electric field distribution in stripes array with $a = 75\,\mathrm{nm}$. a, The xz-cross-section of the squared electric intensity of array of silicon stripes illuminated by Gaussian beam. **b,** The xy-cross-section of the squared electric intensity under the array of silicon stripes in the middle of the NiFe layer.

5.3. Simulation of the electric field in the periodic structures

We performed the FDTD simulation of the fabricated structures, as described in Chapter 3. In Fig. 5.2a, the cross-section of the squared electric field intensity is shown in xz-plane. We can observe that the electric field intensity is periodically modulated with the period equal to $2a$. Similarly to the case of individual disks (see Chapter 4, Fig. 4.13), the majority of the intensity is concentrated on the top of the stripes. The light intensity is significantly higher in between the stripes than in the stripe. The electric field intensity is the highest in the center of the Gaussian illumination and decreases with increasing distance from the center.

In Fig. 5.2b, the squared electric field intensity in xy-cross-section is shown. Again, the periodical modulation with the period of $2a$ is visible. Contrary to the situation shown in Fig. 5.2a, the hot spots are formed under the silicon stripes, and in between them, the electric field intensity is lower. This means, that on the surface of the NiFe layer the electric field intensity is concentrated on the edges and when it penetrates towards the NiFe it gets more localized into the center of the stripes. The original shape of the Gaussian illumination envelops the whole squared electric intensity.

We transformed the data shown in Fig. 5.2b to the reciprocal space, see Fig. 5.3a. In the center of the reciprocal space ($k_x = k_y = 0$) the intensity is the highest and forms a Gaussian peak with HWTM$= (14.7 \pm 0.8)\,\frac{\mathrm{rad}}{\mu\mathrm{m}}$[2]. This originates from the Gaussian illumination, and thus, it is symmetrical. Also, additional peaks with circular shapes emerge on the cross-section $k_y = 0$, (perpendicularly to the long axis of stripes). They are centered at $\frac{\pi}{a}$, $\frac{2\pi}{a}$, and $\frac{3\pi}{a}$. From this calculation, it can be seen that by tuning the parameter a, we can measure different k-vectors. The resolution of this technique is given by the width of individual peaks in reciprocal space, which is approx. $10\,\frac{\mathrm{rad}}{\mu\mathrm{m}}$.

In Fig. 5.3b, the cross-section through $k_y = 0$ is shown. In this representation the ratio between the central peak and the peaks at $\frac{\pi}{a}$, $\frac{2\pi}{a}$, and $\frac{3\pi}{a}$ is visible. The amplitude

[2]This value is slightly higher than the value obtained in previous Chapter 4 (HWTM$\approx 10\,\frac{\mathrm{rad}}{\mu\mathrm{m}}$, due to the use of different approximation of Gaussian illumination.

of the side peaks is approx. 10 times lower. Also note, that there is a new emergent side peak between the central peak and the peak at $\frac{\pi}{a}$, which most probably originates from the shaping of the electromagnetic field by the edges of the stripes.

5.4. *k*-resolution in silicon stripes array

As described in the previous section, we have fabricated silicon stripe arrays with the parameter a ranging from 75 nm to 500 nm. This sample was measured on a standard μ-BLS setup, and BLS spectra were measured on each individual structure. We show an example for $a = 75$ nm in the inset of Fig. 5.4a. The rise of distinct peaks was only visible for structures with the parameter a between 75 nm and 175 nm. Due to the limited size of the Gaussian illumination beam and the concentration of the majority of the incident light only on individual stripes, the driving electric field does not exhibit sufficient periodicity for structures with larger a parameters.

The positions of the peaks in spectra acquired on all structures were analyzed, and the $k-$vectors (i.e. $\frac{\pi}{a}$, $\frac{2\pi}{a}$, and $\frac{3\pi}{a}$) were associated with individual peak's positions. Fig. 5.4a shows the resulting dispersion. The experimentally obtained points were simultaneously fitted with the dispersion from Slavin-Kalinikos model for $n = 0$ and $n = 1$ with two free parameters: the exchange constant A_{ex} and the thickness of the layer d. The fitting results are summarized in Table 5.1. The unprecedented k-vector span of the dispersion relation allowed simultaneous fitting of the exchange constant and the layer thickness, as the dispersion for such high wavevectors is already governed by the exchange interaction. The dependency between the exchange constant and the layer thickness reached 0.84. The exchange constant is lower than expected and differes from the value we assumed in the previous chapters. However, it agrees with various experimental studies [209, 210].

Black squares in Fig. 5.4b show the position of the peak $\frac{\pi}{a}$ acquired at different angles of the silicon stripes with respect to the external field ($B_{\text{ext}} = 50$ mT) measured on the structure with $a = 75$ nm. The solid black line shows the analytical calculation with the use of the parameters from Tab. 5.1. The agreement between the analytical model and

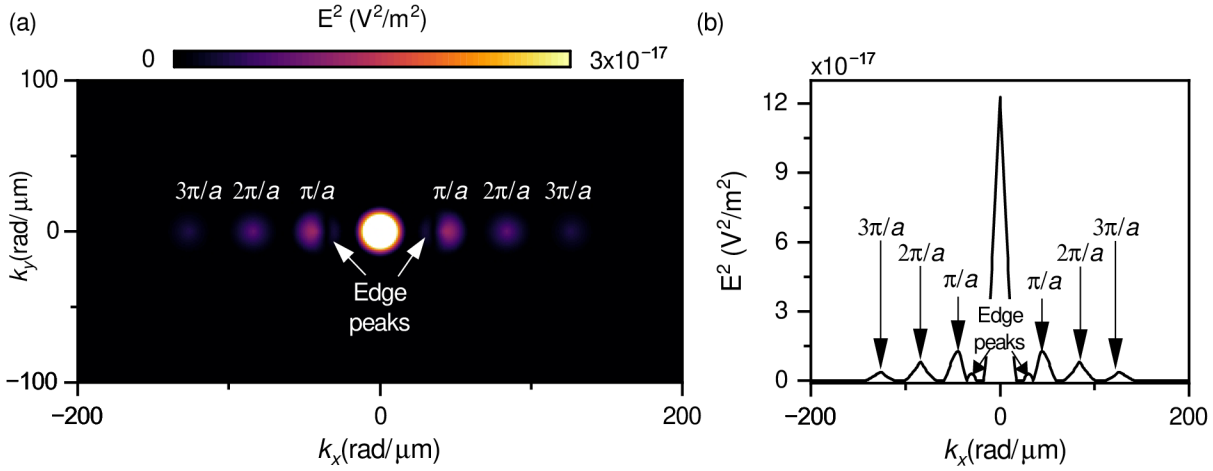

Figure 5.3: Squared electric field distribution in reciprocal space under stripes array with $a = 75$ nm. a, The squared electric intensity in the k_x,k_y reciprocal space. **b,** the cut through $k_y = 0$ line.

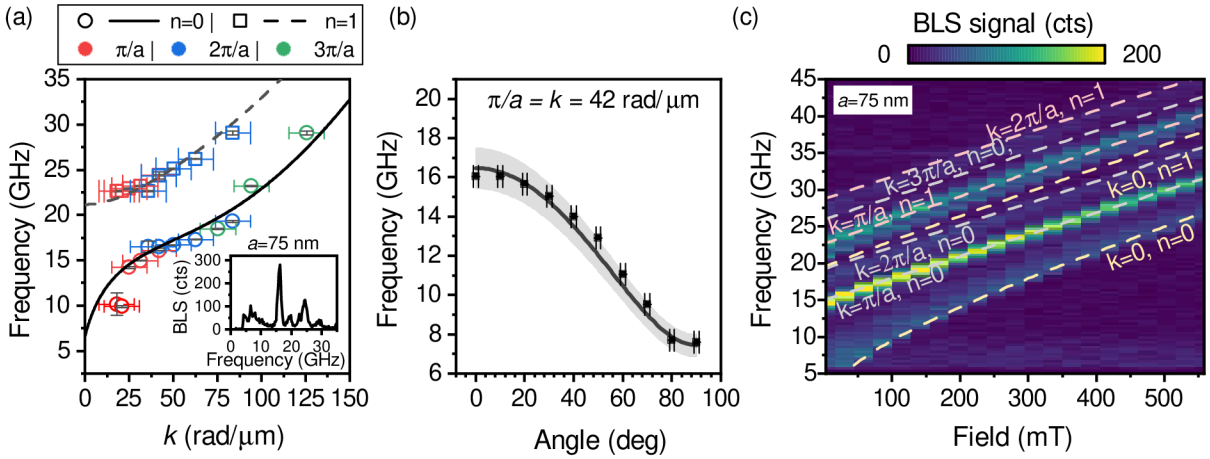

Figure 5.4: ***k*-resolved μ-BLS a,** Extracted dispersion relation at 50 mT of NiFe layer. The colors depict the order of the measured peak. Circles (squares) show $n = 0$ ($n = 1$). A solid (dashed) line shows fits of $n = 0$ ($n = 1$) experimental data. The inset shows example BLS spectra taken on structure with $a = 75$ nm. **b,** Angle resolved measurement at structure $a = 75$ nm with analyzed position of $\frac{\pi}{a}$. The solid line shows the calculation results with parameters obtained from fit in **(a)**. The shaded area shows uncertainty calculated from the uncertainty of the wavevector. **c,** Field sweep on structure $a = 75$ nm. The positions of the expected peaks are shown as dashed lines.

experimental data demonstrates the directional sensitivity of this technique and confirms the predictions based on the FDTD simulation in shown Fig. 5.3a.

Fig. 5.4c shows the spectra acquired in Damon-Eshbach-like geometry on the structure with $a = 75$ nm at external fields ranging from 550 mT down to 0 mT. We can observe a clear increase in the frequency of all modes with increasing the external field, except one constant mode at $f = 35$ GHz, whose origin is non-magnetic. The analytical model with a set of parameters from Tab. 5.1 was used to overlay the expected positions of the peaks. In this figure we can also observe very good agreement between the calculation and experimental data.

Table 5.1: Summary of the fitted parameters from Fig. 5.4a.

d (nm)	A_{ex} ($\frac{J}{m}$)	M_s ($\frac{kA}{m}$)	γ ($\frac{GHz}{T}$)
$28.4 \pm 0.9^*$	10.3 ± 0.5	$740^\dagger$	$29.5^\dagger$

* Nominal thickness was 30 nm

† Fixed, see chapter 4.

6. Mie-enhanced Brillouin light scattering microscopy

This chapter deals with the measurement of the coherent spin waves and their spatial mapping. For the experiments presented here, I have used a sample with two-step lithography containing an excitation antenna and silicon disks in its vicinity. The sample was fabricated by Jan Klíma and Meena Dhankhar. The used permalloy layer comes from the same depositions as the sample investigated in chapter 4. Therefore, I used the same magnetic parameters for data analysis. This chapter is structured as follows: I start with the introduction, followed by the experiments to prove the detection of free-light inaccessible spin-waves. Then, the technique of 2-dimensional scanning is introduced. Afterward, the phase-resolved measurement of two-wave interference and full-phase reconstruction is shown. The reconstructed dispersion relation is discussed. The found results are corroborated by FDTD simulations. Finally, the polarization of the inelastically scattered light is discussed.

In the previous chapters, I have investigated only thermal (incoherent) spin waves on one fixed position set by a silicon disk. Such investigation can be very helpful for e.g. material research or investigating fundamental physics of nanoscale spin waves. However, in applications it is completely necessary to investigate coherent spin waves, as typically these carry information. In the framework of spin waves, a lot of ideas for wave-based computing were proposed, such as directional coupler [1] or inverse-design devices [2, 211]. The biggest drawback of these devices is a large group delay caused by an unfavorably low ratio of spin-wave group velocity and wavelength. In recent years, magnonic-research community strives to overcome this drawback by moving towards nanoscale, where the spin waves propagate faster and do not need to travel long distances, thus the group delay is minimized [160].

Also, many interesting phenomena occur at nanoscale, such as spin unpinning condition [212], or generation of spin waves using parametric pumping [208, 213]. Another approach can be to use collective nanoscale spin wave dynamics [214] or use the non-collinear spin textures for manipulation [168, 215, 216]. The spin textures can also be utilized as excitation and detection perturbation in propagating spin-wave spectroscopy (PSSW) [217]. So far, to spatially investigate nanoscale spin waves one has to use x-ray radiation, a time- and resource-demanding technique [162, 218–220]. The development of an optical method for spin wave measurement capable to go beyond diffraction limit is one of the major challenges in the field of magneto-optics [221]. This chapter is mainly based on the results presented in [222].

6.1. Coherent excitation

This section deals with detecting coherently excited spin waves with free-light inaccessible wavevectors. I demonstrate the capability of measuring these spin waves by performing frequency sweep and obtaining the μ-BLS spectra on a bare film and a film with a silicon disk on top. This section is structured as follows: First, I discuss the theoretical background, especially in regard to the differences in the measurement of the thermal spin waves. Afterward, I compare measurements on the single disk and bare film and show measurements of the nanoscale spin-waves. This is followed by a demonstration of the spatial resolution by the measurement of the array of non-interacting silicon disks. Finally, I briefly discuss the polarization of the inelastically scattered light in the case of the bare film measurement and Mie-enhanced BLS.

6.1.1. Theoretical description

To prove that our approach works also for coherent spin waves a sample with 180 nm wide microwave (RF) antenna in the vicinity of 200 nm wide silicon disks on the top of the permalloy thin film was fabricated. We connected the antenna to a RF generator with the excitation power set to 10 dBm, and swept the excitation frequency from 5 GHz to 17 GHz, see Fig. 6.1a. In the first experiment we only measured on a single fixed position (silicon disk marked with the red circle in Fig. 6.1b) at the distance 1 μm from the antenna. The external magnetic field was set to 50 mT.

In this experiment the signal from monochromatic coherent spin wave is of interest. The equation for induced polarization (Eq. 2.20) can be rewritten to the following form

$$\boldsymbol{P}\left(\boldsymbol{r},\omega \pm \omega_m\right) = \hat{\chi}\left(\omega_m\right)\ e^{i\boldsymbol{k}_m\cdot\boldsymbol{r}}\ \boldsymbol{E}\left(\boldsymbol{r},\omega\right), \tag{6.1}$$

where $\boldsymbol{k}_\mathrm{m}$ and ω_m are the spin wave wavevector and the frequency, respectively. Both are defined by the frequency set on the RF generator, the experiment geometry, and the dispersion relation. The above equation (Eq. 6.1) highlights the importance of the field localization provided by the silicon disks: the spatial profile of the electric field intensity

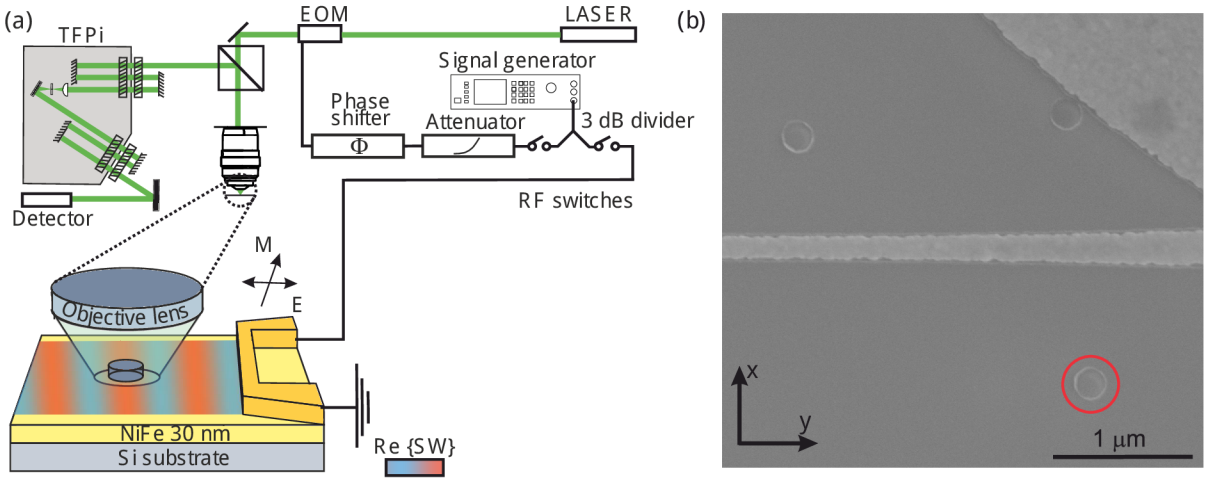

Figure 6.1: Sketch of the detection of nanoscale coherently excited spin waves. a, Sketch of the detection of coherently excited spin waves. **b,** Scanning electron microscope image of the excitation antenna and silicon disk array.

$\boldsymbol{E}$ determines the area that contributes to the collected BLS signal. Note, that the signal is collected by the detector in far-field, i.e. without any spatial information within the beam spot on the sample. It means that if the modulation of the spatial profile of the electric field intensity ($\boldsymbol{E}$) within the beam spot is larger than the spin-wave wavelength, the exponential factor $e^{i\boldsymbol{k}_m \cdot \boldsymbol{r}}$ is averaged out and the information about the spin wave is lost [113, 169].

6.1.2. Experiment on the single silicon disk

First, we performed measurement on the bare film at the same distance of 1 µm, see 6.2a. In this case, the excitation efficiency of the antenna reaches higher wavevectors than the detection sensitivity, which is confirmed by the fact that the signal from coherent spin waves ends at the lower frequency compared to the thermal background. Contrary, in the case of the measurement on the silicon disk (Fig. 6.2b), the thermal background exceeds the signal from coherent spin waves, which means that the coherent spin waves were limited by the excitation efficiency of the antenna. To directly compare the data acquired on the bare film, and on the Mie resonator we have subtracted background from the measurement and extracted the BLS signal along the diagonal using Bresenham algorithm [223], see Fig. 6.2c. By direct comparison, we can immediately observe, that on silicon disk the signal is detected also at higher frequencies. This confirms the conclusion presented in the previous chapter, that the silicon disk allows to detect free-space light inaccessible wavevectors.

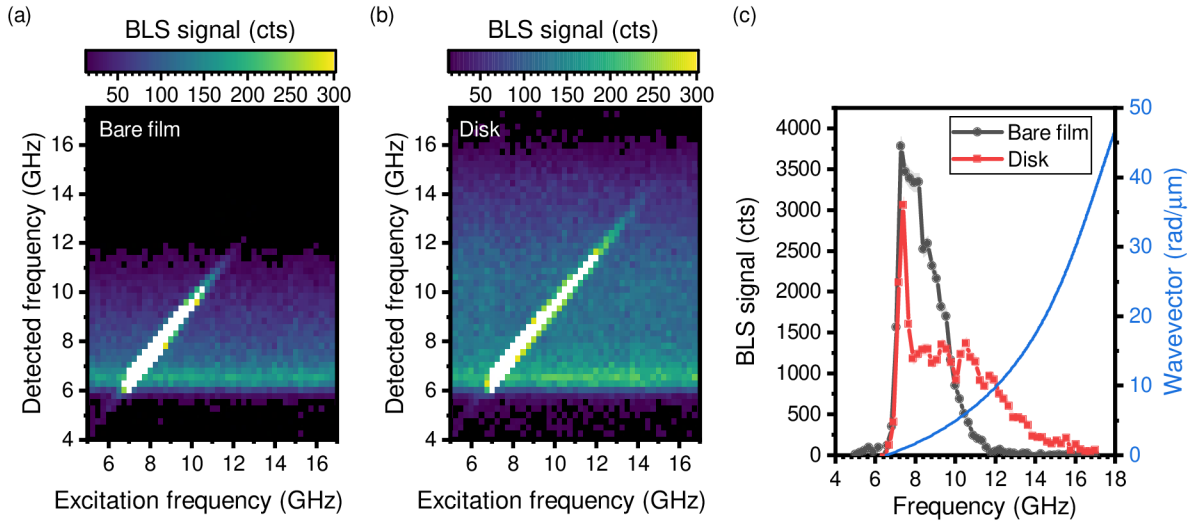

Figure 6.2: Enhancement of BLS signal from coherently excited spin waves. a, b, Spin wave spectra acquired at the distance of 1 µm away from the excitation antenna, measured on a bare film **(a)**, and on a 200 nm wide silicon disk **(b)**. Note, that the BLS signal from thermal spin waves is visible for all excitation frequencies, whereas coherently excited spin waves manifest themselves as a strong signal on the diagonal. **c,** Signal from coherent spin waves extracted from the diagonal in **(a)**, **(b)** after subtraction of the thermal background. The blue solid line shows the dispersion relation of spin waves in Damon-Eshbach geometry.

The cut-off wavevector of the used antenna with width of $w = 180\,\text{nm}$ is approximately $w/2\pi$ is $29\,\frac{\text{rad}}{\mu\text{m}}$ [73, 136]. This is consistent with the maximum detected frequency of 16 GHz, corresponding to $k = 30\,\frac{\text{rad}}{\mu\text{m}}$, see dispersion relation (blue solid line) in Fig. 6.2c.

6.1.3. Two-dimensional spatial scanning of nanoscale spin waves

The previous section only dealt with Mie-enhanced BLS measurement on a nanoresonator at a single (fixed) position. Now, we extend this approach to perform two-dimensional spatially resolved measurements. The scanning is done similarly to a standard spatially-resolved μ-BLS experiments, with the difference being that the probing beam is scanned across the array of non-interacting array of silicon disks. The positions of the disks define the spin-wave measurement positions.

The square array consisting of 200 nm-wide and 60 nm-thick sputter-deposited silicon disks was fabricated by electron beam lithography and lift-off process in the vicinity of the antenna. The array had a lattice constant of 500 nm and a tilt of 8° with respect to the antenna, see Fig. 6.3a. The SEM image of the measured structure is shown in Fig. 6.3b. The tilt was intentional to allow for subdifraction step during the linescans, see following sections.

We performed a 2D scan of the BLS intensity in the vicinity of the excitation antenna which was connected to the RF generator with frequency set to 14.5 GHz, in the external magnetic field of 50 mT, see Fig. 6.4a. The antenna thus excited coherent spin waves with the wavevector $k = 27\,\frac{\text{rad}}{\mu\text{m}}$ ($\lambda = 232\,\text{nm}$) [30, 41]. Such short-wavelength spin waves are beyond the detection limit of conventional μ-BLS (the detection limit of our μ-BLS is $k = = 11\,\frac{\text{rad}}{\mu\text{m}}$) [113], thus without any further enhancement we would see no signal. However, due to the subdiffraction localization of the E-field by the silicon disks, we observed a propagating spin wave even with a such short wavelength. The BLS signal naturally decays as the wave propagates further from the excitation antenna and it is strongly enhanced at the positions of the silicon disks. The low signal in between the positions of

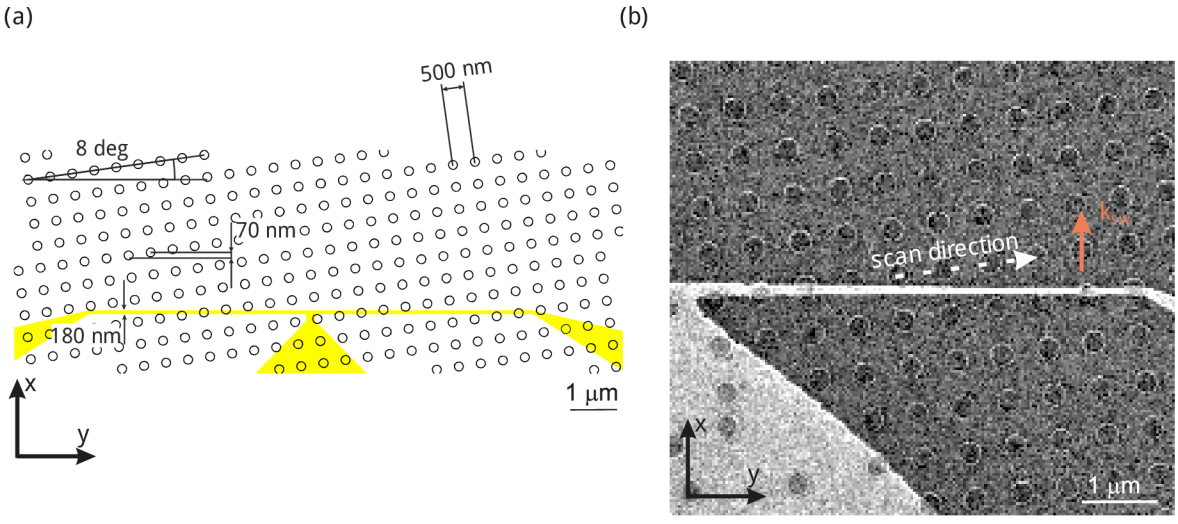

Figure 6.3: Schematics of the spatial scanning of nanoscale spin-waves. a, Schematics of the excitation antenna and silicon disks array for spatially resolved measurement. **b,** SEM image of the measured structure. The white dashed line depict scanning line used in Figs. 6.6, 6.7, and is tilted by 8° with respect to the antenna.

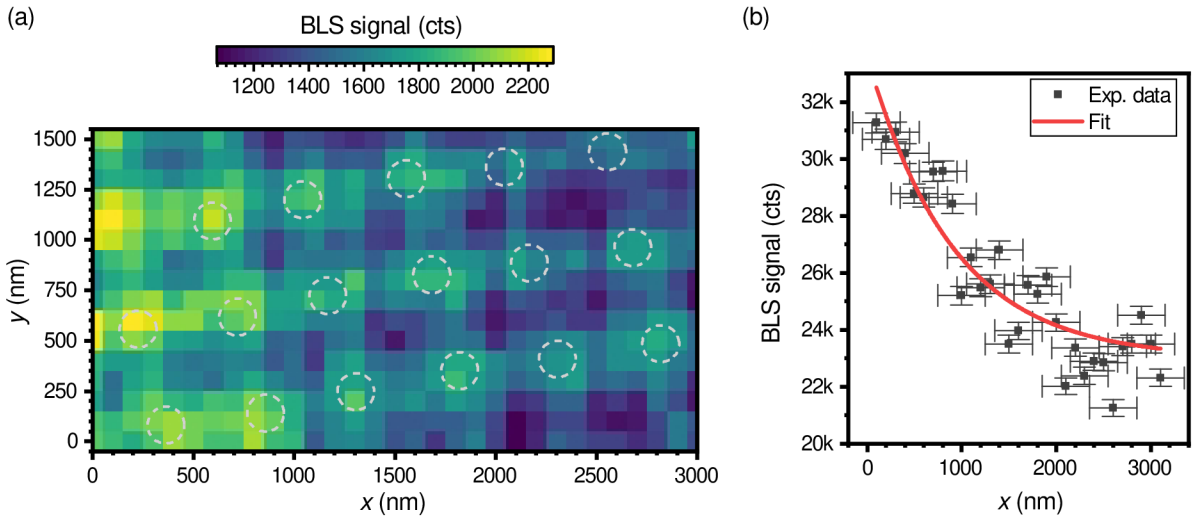

Figure 6.4: Schematics of the spatial scanning of nanoscale spin-waves. a, Schematics of the excitation antenna and silicon disks array for spatially resolved measurement. **b,** SEM image of the measured structure with shown direction of the linescans.

the silicon disks is caused by the fact that the waist of the Gaussian beam (440 nm)[113] is comparable to the lattice constant (500 nm) of the silicon disk array. These observations agree well with expectations based on Eq. (6.1).

To evaluate the decay of the spin waves, we integrate spin-wave intensity across the y-dimension, see Fig. 6.4b. The spatial step in measurement was 100 nm, but the silicon disks are separated by 500 nm, see Fig. 6.3a. As we can observe spin waves only on the fixed positions of the disks (see Fig. 6.4a and Eq. 6.1), we assumed uncertainty in the x-position of 250 nm, which is half of the array constant. The uncertainty in the BLS signal was calculated using the Poisson distribution. In the acquired data, the exponential decay is clearly visible. This decay was fitted and yielded the decay length $1.8 \pm 0.2\,\mu$m. This is in perfect agreement with the theoretically predicted value of 1.8 µm, based on Kalinikos-Slavin model.

6.1.4. Polarization of BLS light from nanoscale coherent spin waves

The polarization of the scattered light is the result of Eq. 6.1 and subsequent emitting of the light. In the case of the measurement on the bare film, we described the process governing the resulting polarization in the case of coherently excited spin waves in section 2.2.5. To experimentally check that the situation is not drastically changed in the case of measurement on a silicon disk, we analyzed the polarization of scattered light in an experiment with free-light accessible and inaccessible spin waves.

In Fig. 6.5a, we measured the spin waves at 9 GHz with wavevector $\approx 6\,\frac{\mathrm{rad}}{\mu\mathrm{m}}$. Such wavevector can also be measured by means of standard µ-BLS on bare film. We can observe that the signal is slightly enhanced on the silicon disk compared to the measurement on the bare film. However, the polarization axis remains the same.

In Fig. 6.5b, we measured the spin waves at 14 GHz with wavevector $\approx 20\,\frac{\mathrm{rad}}{\mu\mathrm{m}}$. This wavevector cannot be measured by the standard µ−BLS. This results in no signal in measurement on bare film, see red solid line in Fig. 6.5b. In the case of measurement

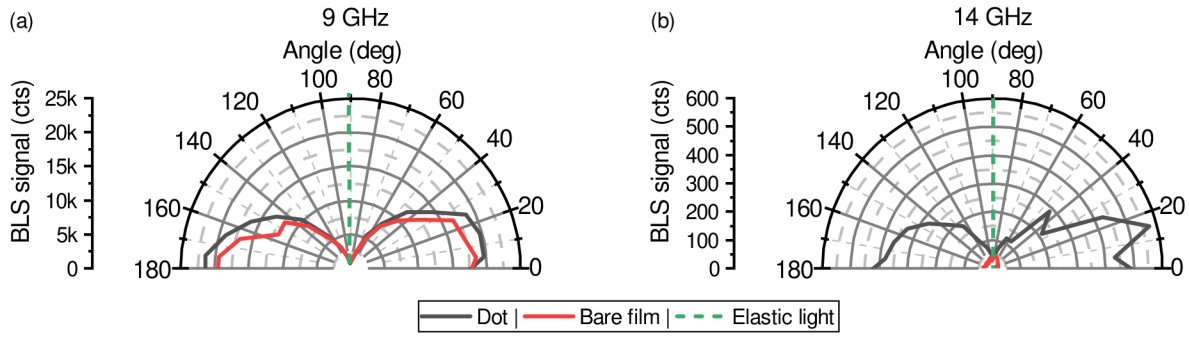

Figure 6.5: Analysis of the polarization of the BLS light on nanoscale spin waves. **a, b,** BLS signal recorder for different polarization of scattered light for free light accessible spin waves at 9 GHz **(a)** and free light inaccessible spin waves at 14 GHz **(b)** for measurement on bare film and silicon disk.

on a silicon disk, the signal remains rotated by 90 degrees with respect to the elastically scattered light.

6.2. Phase-resolved measurement

This section focuses on measuring the spatial evolution of the spin wave phase. This information provides valuable insights into the spin wave's propagation. The presented technique can enable e.g. studiyng of the phase-shifted of nanoscale spin waves after interacting with sub-diffraction magnetic structure such as skyrmion [224]. This section is structured as follows: First the technique of employing spatial symmetry of the spin waves along the excitation antenna is shown and used to obtain interference measurement. Afterward, the full-phase is reconstructed and used to measure spin-wave dispersion relation. Finally, the obtained results are discussed with use of FDTD simulations carried out by Jakub Krčma in Lumerical software with the mesh cell set to 5 nm in all directions. More details can be found in chapter 3.

6.2.1. Two wave interference linescans of nanoscale spin waves

During the BLS process, the scattered photon acquires the phase of the spin wave, and this phase can be reconstructed by observing interference between the BLS signal and reference phase signal produced by the electro-optic modulator (EOM). In this experiment, both RF switches were switched on [see Fig. 6.3a, or 3.5], and we observed the interference of the light inelastically scattered on spin-waves with the light modulated by EOM [129]. In order to acquire the phase with spatial resolution sufficient to measure spin waves with very short wavelengths, we exploited the symmetry along y-axis of the spin wave propagating perpendicularly from the excitation antenna and performed a linescan over one row of the silicon disk array (see Fig. 6.3b). As the array is tilted by 8°, the distance of the disks from the antenna increases by 70 nm for each disk in the row, see Fig. 6.3a.

This approach can be applied only in cases where the long excitation source is used and the magnetic layer is not modulated in this direction. In the case of studying magnetic waveguide or layer modulated along the excitation source, one has to prepare more structures with precisely positioned silicon disks to achieve similar resolution. E.g., in the case of the investigation of nanoscale spin waves in a narrow waveguide, the same 10

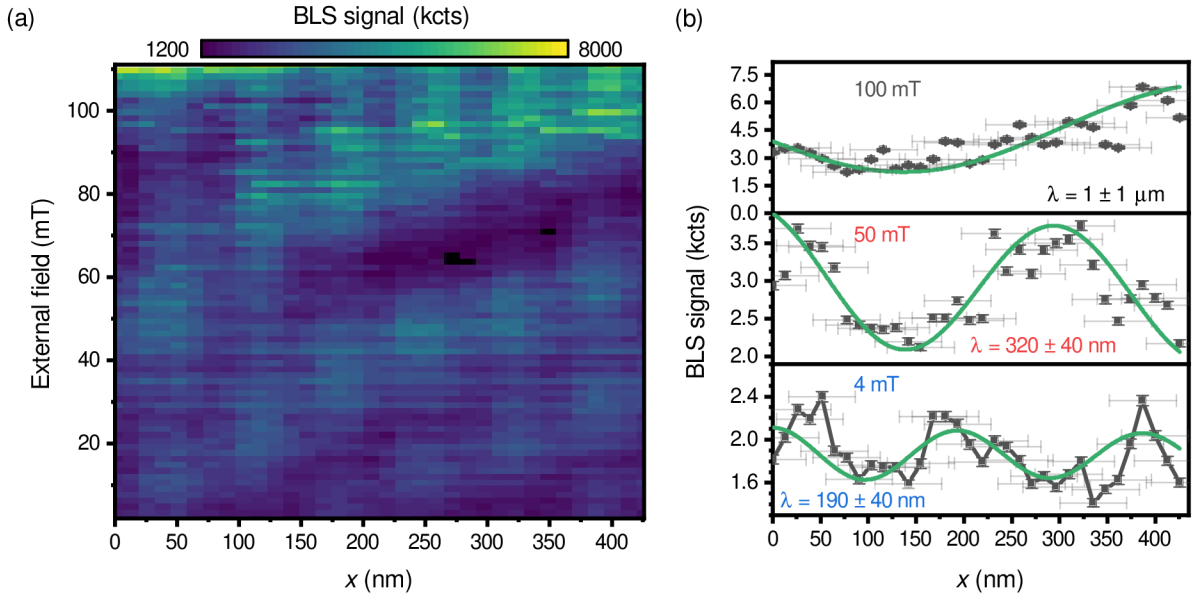

Figure 6.6: Interference BLS measurement at 14 GHz. a, The BLS intensity along the line tilted by 8° with respect to the excitation antenna in different external fields.**b, c, d,** Slices of the data presented in **(a)** for 100 mT **(b)**, 50 mT **(c)**, and 2 mT **(d)** are shown together with the corresponding fits by the two-wave interference model.

waveguide structures can be prepared, and on each structure, one will fabricate silicon disks with a spacing of 500 nm. However, the distance from the antenna to the first disk is varied by 50 nm on each structure. This way, a spatial step of 50 nm is achieved if the experiment is perfectly repeatable.

The measured dependence of the interference signal (I) on the distance from the excitation antenna and on the external magnetic field is plotted in Fig. 6.6a. The cross sections of this plot at magnetic field values of 100 mT, 50 mT, and 2 mT are shown in Fig. 6.6b, c and d, respectively. We can observe how the spin wave wavelengths get shorter for the lower values of external magnetic field, as expected. The shortening is apparent from the gradual change of the distance between the interference minima and maxima. To obtain the exact value of the spin wave wavelength, we fit the data with the two-wave interference model [129, 225]:

$$I = R_0 \exp\left(\frac{x}{\delta}\right) + E + \sqrt{E\ R_0 \exp\left(\frac{x}{\delta}\right)} \cos\left(\frac{2\pi x}{\lambda} + \varphi_0\right), \tag{6.2}$$

where R_0 and E are parameters describing the signal intensity from the spin wave and the EOM, respectively, λ is the spin-wave wavelength, δ is the spin-wave decay length, and φ_0 is the initial phase offset. The fitted wavelengths are in the corresponding panels of Fig. 6.6.

6.2.2. Full-phase reconstruction of nanoscale spin waves

Although it was possible to obtain spin-wave wavelengths from the BLS interference signal and the nonlinear fitting with the two-wave interference model, the technique of the full-phase reconstruction [128, 226] proved to be much more robust. We used this technique to obtain the full spin-wave dispersion over a broad range of frequencies and k-vectors. This

technique requires at least four measurements to fully reconstruct the spin-wave phase. In order to account for thermally excited spin waves, we added a fifth measurement, which must be taken into account if the coherent signal is comparable to the incoherent thermal background, as it is in the measured data, especially for the discussed case of short wavelengths of spin waves. To calculate the evolution of the spin-wave phase along the distance x, real $\mathrm{Re}[\Psi(x)]$ and imaginary $\mathrm{Im}[\Psi(x)]$ parts of the wave amplitude have to be calculated (see chapter 3):

$$\mathrm{Re}[\Psi(x)] = \frac{r_0 - R - E + T}{2\sqrt{E - T}}, \tag{6.3}$$

$$\mathrm{Im}[\Psi(x)] = \frac{r_{\pi/2} - R - E + T}{2\sqrt{E - T}}. \tag{6.4}$$

Here, r_0 $\left(r_{\pi/2}\right)$ is the interference signal with EOM phase shifted by 0 ($\pi/2$), R is the signal from coherent spin waves (which also includes a contribution from thermal spin waves), E is the EOM signal, and T is a signal from thermal spin waves. These signals are shown in Figs. 6.7a, b, c for 8, 12, and 15 GHz, respectively. The spin-wave phase can be calculated as

$$\Theta(x) = \mathrm{atan}\left(\frac{\mathrm{Re}(\Psi)}{\mathrm{Im}(\Psi)}\right). \tag{6.5}$$

In the case of a monochromatic spin wave, the dependence $\Theta(x)$ is linear, and its slope directly represents the spin-wave wavenumber. The phases reconstructed from the experimental data in Fig. 6.7a, b, c are shown in Fig 6.7d, together with linear fits of their slopes.

The wavevectors extracted from the phase profiles acquired in the field of 50 mT at various frequencies are compared to the theoretical dispersion relation (see Fig. 6.7e) calculated according to the Kalinikos-Slavin model [30, 41]:

The excellent agreement between the theory and the experimental data (see Fig. 6.7e) for wavevectors ranging from 4 rad/μm up to 30 $\frac{\mathrm{rad}}{\mu\mathrm{m}}$ means that we were able to reliably measure and reconstruct the spin wave phase even for spin-wave wavelengths where the BLS process had to be mediated by the silicon disk. The maximum measured wavevector corresponds to the excitation limit of the 180 nm-wide antenna [73, 136]. By utilizing another type of a spin wave source [227–229], spin waves with even shorter wavelengths could be measured.

In the linescan data, we can observe a periodic pattern in areas with an increased signal, see Fig. 6.6b, or stair-like pattern in Fig. 6.7d. This pattern has a periodicity of 70 nm, which is the same as periodicity of the positions of the individual silicon disks under the scanning tilt. The linescans were acquired with oversampling, where the spatial step in the spin-waves propagation direction ($x-$axis) was approx. 13 nm, while the distance between the silicon disks was approx. 70 nm, i.e. approximately 5 measured points per silicon disk position. This periodic pattern in the extracted phase (Fig. 6.7e) suggests that the detected phase is defined by the positions of the disks on the thin film and is not overly sensitive to the exact positioning of the laser spot relative to the position of the nanoresonator. Also note, that we were able to reliably measure the spin-wave wavelength $\lambda = 4.2\,\mu$m by scanning over a distance of 450 nm only. This would not be possible without precisely positioned detection points and without the full-phase reconstruction technique, see Fig. 6.6b at 100 mT and corresponding wavelength uncertainty.

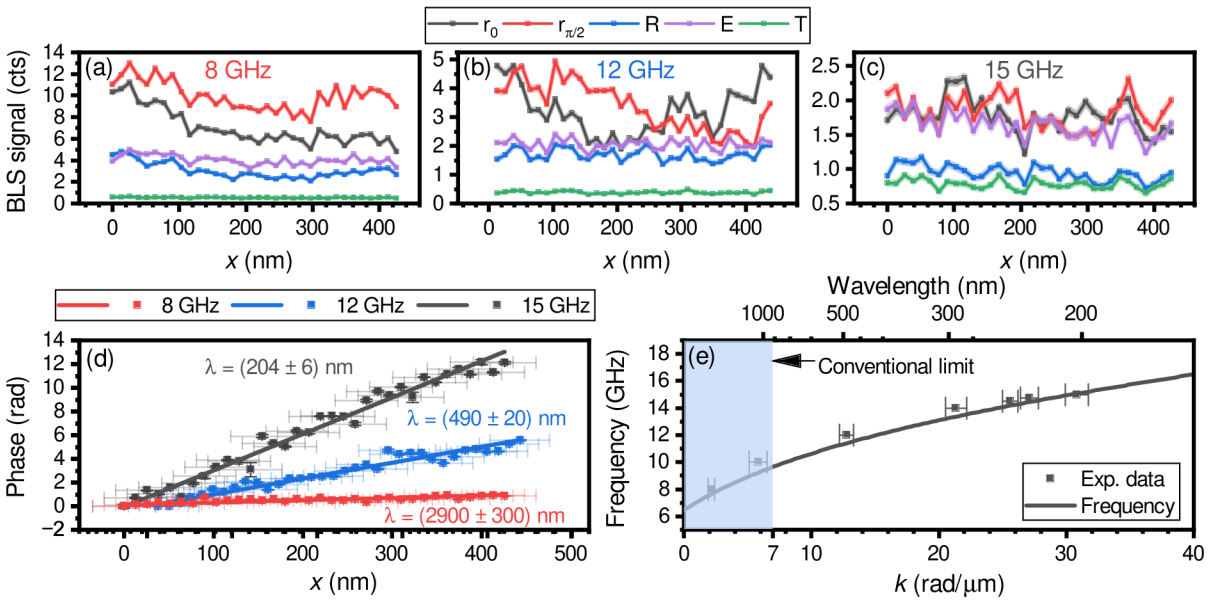

Figure 6.7: Extraction of the spin-wave dispersion relation from full phase-resolved BLS measurement. a, b, c, Five signals needed for the full phase extraction at 8, 12, 15 GHz, respectively. **d,** Evolution of the phase versus the coordinate in the direction of propagation of the spin waves at 8, 12, 15 GHz. For **(a-d)** the y-errors are calculated from Poisson distribution x-errors are 35 nm, which is given by the x-distance between the disks, see Fig. 6.3. In **(a-c)** the x-error is omitted for clarity. **e,** Extracted dispersion (squares) and analytical calculation (solid line) [30, 41]. The blue rectangle depicts the limit of conventional µ-BLS, see chapter 2.

6.2.3. FDTD simulation of silicon disks array

To clarify the phase stability when scanning over the array of silicon disks, the finite-differences-time-domain (FDTD) simulations of the sample with the same parameters as in the experiments were performed. In these simulation we swept the laser positions across the silicon-disk array to see the phase evolution and interaction between the individual disks.

Figure 6.8a shows the localization of electromagnetic field into hotspots, that allow the detection of high-k spin waves, see Eq. 6.1. In this case the Gaussian beam is precisely positioned on the silicon disk. On the other hand, if we position the beam spot directly between the silicon disks (Fig. 6.8 b-c), this localization is suppressed, and the overall light intensity is lower. This results in a decrease of the detection sensitivity to high-k spin waves and overall decrease of the BLS signal. We also extracted the phase of the electric field from the simulated data (Fig. 6.8d-f). The phase in the axis of the linear polarization of the incident light (x) is homogeneous across the high-intensity regions (hotspots), while the inner area of the disk has the opposite phase, and this is the same for all simulated positions of the beam. This independence of the electric-field phase on the exact position of the beam suggests the robustness of the phase reconstruction to external disturbances, such as mechanical vibrations.

Note that even though the two hotspots are localized on the disk edges and separated by 200 nm, this does not influence the capability of the system to detect even nanometer changes in the spin-wave wavelength. This is analogous to the case of inductive detection of spin waves by coplanar waveguides or meander antennas in propagating spin-wave

spectroscopy experiments. There, the electromagnetic field distribution under relatively large detection antennas with complex geometries is also non-trivial, and still, the spin wave phase can be measured [136, 230].

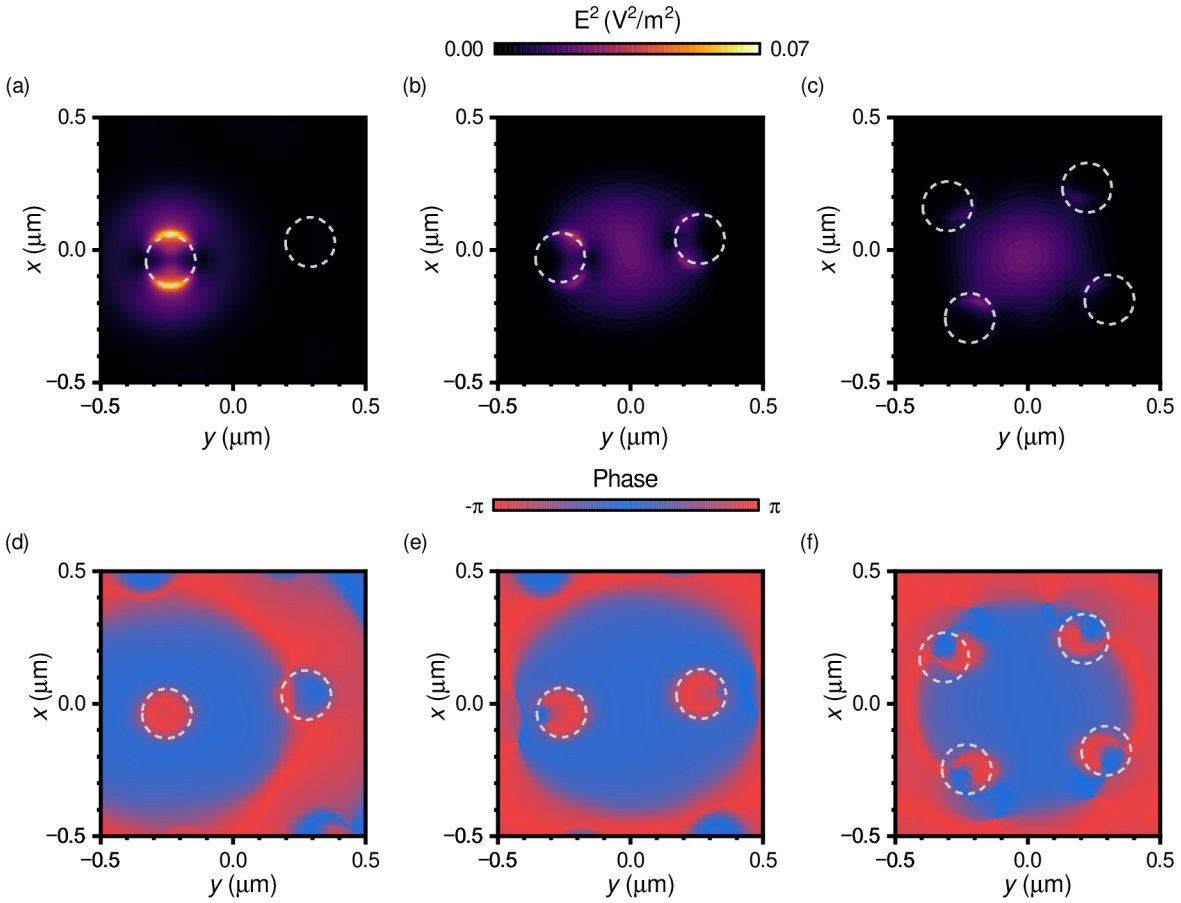

Figure 6.8: Scanning with a weakly-interacting array of silicon disks. a, b, c, d, e, f, Finite-differences-time-domain simulation of the distribution of the squared electric intensity **(a), (b), (c)** and phase **(d), (e), (f)** in the plane of the Permalloy layer. For the precisely positioned beam on the silicon disk in the array **(a), (d),** case in between two disks **(b), (e)** and the case when the beam hits the exact middle of the array **(c), (f)**. The gray dashed line depicts the positions of silicon disks.

Conclusion

During my PhD I focused on investigation of the interaction between light and magnetic excitations in the condensed matter. There are two significant contributions presented in this thesis: Mie-enhanced Brillouin light scattering technique and semi-analytical description of the micro-focused BLS.

Mie-enhanced BLS technique allows measurement of nanoscale spin waves with a *table-top* setup. Previously, imaging of nanoscale spin waves required use of large scale facilities such as synchrotrons. Presented results prove that the Mie-enhanced BLS is able to detect thermal spin waves with k-vectors exceeding 125 $\frac{\text{rad}}{\mu\text{m}}$ (corresponding to spin wave wavelength $\lambda = 50\,\text{nm}$). This is enhancement by a factor of 12 from the standard μ-BLS technique ($k \approx 10\,\frac{\text{rad}}{\mu\text{m}}$). I also demonstrated, that by utilizing the periodic stripes arrays, the resolution to spin wave's in-plane wavevector can be achieved. These findings elevate μ-BLS to the forefront of nanoscale magnonics research. Also the possibility to probe materials with high momentum photons is relevant also for other applications, e.g., for phononic studies [231], or even mechanobiology experiments [232].

Mie-enhanced BLS can also be used to study coherently excited spin waves. I have proven, that coherent spin-waves can be detected and spatially mapped with the use of weakly interacting arrays of Mie resonators. Moreover, this technique can be used in combination with phase-resolved μ-BLS, and thus can measure e.g. the dispersion of the nanoscale spin waves with nanometer precision. This precision depends on the exact positioning of the nanoresonators and on the design of the array. With modern electron beam lithography techniques, sub-10 nm precision of placement of individual array elements is achievable.

Easiness of the technique and availability of the μ-BLS setups around the world will fuel the spin-wave research and will enable fast prototyping and designing of the devices based on the nanoscale spin waves. These devices are typically way more efficient in comparison to the devices based on the microscale spin waves, and thus can be appealing for industrial applications.

The semi-analytical description of the μ-BLS allows modeling the BLS signal based on optical and magnetic configurations of the measurement. Such tool provides a whole new dimension for analysis of the acquired spectra. So far, researchers have been analysing only the positions of the BLS peaks, and were not paying much attention to their shape. With the presented semi-analytical model, the exact shape of the spin-wave spectra can reveal information which were previously hidden, for example thermodynamic properties of magnons inside the medium. Furthermore the calculation of the BLS spectra is fast (less then few seconds per spectra) and thus can be used even for fitting any optical or magnetic parameter of the system.

Moreover, the model can be used together with micromagnetic simulations to correctly interpret more complicated situations, e.g., nonlinear effects like parametric pumping. By knowing the exact the sensitivity to specific wavevectors and by modeling the exact

shape of the acquired BLS spectra a completely, new phenomena can be discovered and studied. All codes developed within this thesis (e.g. calculation of spin-wave dispersion characteristics, modeling of BLS spectra) are made publicly available on code-sharing platform Github [41, 107].

Although the achievements summarized in the thesis are already very promising, there is definitely a lot of work which needs to be done to fully exploit the potential of Mie-enhanced BLS. Below, I summarize a few directions that I think have the most promising *return of investment*, and future research should focus on them.

Optimization of resonator's shape and material can provide lot of improvement as the concept of the near-field enhanced BLS is now in the same situation as was enhancement of Raman spectra in 1977 [233]. Back then the enhancement factor was not more than 100×. Nowadays, due to thorough understanding of the involved process and its optimization the enhancement can reach a factor of 10^{12} [234].

Nano-resonators presented in this thesis were our first design without any optimization or tuning parameters such as thickness or shape. The dielectric nanoresonator's geometry and material can be further optimized to excite, e.g. higher-order Mie or anapole resonances and reduce quenching, ideally at the same time [235–237]. Even more complicated three-dimensional structures can concentrate the electromagnetic field directly into the Permalloy layer. Also, from the simulations it seems that the absorption of the dielectric material plays a crucial role. Our preliminary results suggest improvement when poly-crystalline silicon is used instead of the amorphous one.

So far, our research focused on the enhancement of the wavevector sensitivity. If we achieve also a large enhancement factors in BLS signal intensity, this can allow us to perform studies of e.g. spin wave propagation in single atomic layer magnets (2D magnets), or complicated nano structures with dimension way below 100 nm, and thus open whole new research fields.

Benchmarking with coherently excited spin waves may reveal the true potential of the Mie-enhanced BLS. My experimental estimates of the maximal detected spin-wave wavevector are based on the thermally excited spin waves, which provide only relatively weak signals. With technique, which would be able to excite coherent short-wavelength spin waves, one can benchmark true possibilities of the wavevector enhancement by Mie resonances. Even with current non-optimized design, it seems that distribution of the electric field will allow the measurement of spin waves with wavevector exceeding 150 $\frac{\mathrm{rad}}{\mu m}$, see Fig. 4.15.

For this benchmarking, a suitable spin wave source can be e.g. a spin texture (such as a domain wall) under the excitation antenna [238], grating coupler [217], or parametrically pumped spin waves [208].

Scanning Mie-enhanced BLS microscopy can open new possibilities as all presented experiments relied on the fabrication of the nanoresonator on the studied sample. Even though with modern nano-fabrication facilities, preparation of such structures is easy task, additional speed up can be provided by fabricating the Mie resonator on tip and approaching the sample surface independently. Such approach is commonly utilized in tip enhanced Raman microscopy [239] and was even demonstrated in BLS with subdiffraction aperture [168]. However, the acquisition times in the presented approach utilizing small apertures was unbearably long. If properly optimized, the on-tip Mie resonators can provide quick way for prototyping spin-wave devices and even open new directions in e.g., biological research.

References

1. Wang, Q., Kewenig, M., Schneider, M., Verba, R., Kohl, F., Heinz, B., Geilen, M., Mohseni, M., Lägel, B., Ciubotaru, F., *et al.* A magnonic directional coupler for integrated magnonic half-adders. *Nat. Electron.* **3,** 765–774. doi:10.1038/s41928-020-00485-6 (2020) (cit. on pp. 1, 105).
2. Wang, Q., Chumak, A. V. & Pirro, P. Inverse-design magnonic devices. *Nat. Commun.* **12,** 2636. doi:10.1038/s41467-021-22897-4 (2021) (cit. on pp. 1, 105).
3. Mahmoud, A., Ciubotaru, F., Vanderveken, F., Chumak, A. V., Hamdioui, S., Adelmann, C. & Cotofana, S. Introduction to spin wave computing. *J. Appl. Phys.* **128,** 161101. doi:10.1063/5.0019328 (Oct. 2020) (cit. on p. 1).
4. Körber, L., Heins, C., Hula, T., Kim, J.-V., Thlang, S., Schultheiss, H., Fassbender, J. & Schultheiss, K. Pattern recognition in reciprocal space with a magnon-scattering reservoir. *Nat. Commun.* **14,** 3954. doi:10.1038/s41467-023-39452-y (July 2023) (cit. on p. 1).
5. Kiechle, M., Papp, A., Mendisch, S., Ahrens, V., Golibrzuch, M., Bernstein, G. H., Porod, W., Csaba, G. & Becherer, M. Spin-Wave Optics in YIG Realized by Ion-Beam Irradiation. *Small* **19,** 2207293. doi:10.1002/smll.202207293 (2023) (cit. on p. 1).
6. Bejarano, M., Goncalves, F. J. T., Hache, T., Hollenbach, M., Heins, C., Hula, T., Körber, L., Heinze, J., Berencén, Y., Helm, M., Fassbender, J., Astakhov, G. V. & Schultheiss, H. Parametric magnon transduction to spin qubits. *Sci. Adv.* **10,** eadi2042. doi:10.1126/sciadv.adi2042 (2024) (cit. on p. 1).
7. Yuan, H., Cao, Y., Kamra, A., Duine, R. A. & Yan, P. Quantum magnonics: When magnon spintronics meets quantum information science. *Phys. Rep.* **965,** 1–74. doi:10.1016/j.physrep.2022.03.002 (2022) (cit. on p. 1).
8. Stancil, D. D. & Prabhakar, A. *Spin waves: theory and applications* ISBN: 9780387778648 (Springer, New York, 2009) (cit. on pp. 3, 9, 13, 14).
9. Gurevich, A. G. & Melkov, G. A. *Magnetization oscillations and waves* ISBN: 9780849394607 (CRC Press, Boca Raton, 1996) (cit. on pp. 3, 14).
10. Flajšman, L. *Magneto-optical study of the dynamic properties of magnetic nanostructures and nanostructured metamaterials* PhD thesis (Central European Institute of Technology, Brno University …, 2019) (cit. on pp. 3, 51).
11. Jungfleisch, M. B. *Spin pumping and inverse spin Hall effect in yttrium iron garnet/platinum heterostructures* PhD thesis (Technical University of Kaiserslautern, 2013) (cit. on p. 3).

12. Dmytro, B. *Spin transport in magnon and magnon-phonon gases and condensates* PhD thesis (Technical University of Kaiserslautern, 2017) (cit. on pp. 3, 60).
13. Schneider, M. *Bose–Einstein condensation of magnons by rapid cooling and its interplay with spin orbit torque* PhD thesis (Technical University of Kaiserslautern, 2021) (cit. on p. 3).
14. Vaňatka, M. *Static and dynamic properties of nanostructured magnetic materials* PhD thesis (Brno University of Technology, 2020) (cit. on pp. 3, 12, 60–62).
15. Coey, J. M. D. *Magnetism and Magnetic Materials* (Cambridge University Press, 2010) (cit. on pp. 3, 6, 91).
16. Blundell, S. *Magnetism in condensed matter* eng. ISBN: 9780585483603 (Oxford University Press, Oxford; New York, 2001) (cit. on p. 3).
17. Krishnan, K. M. *Fundamentals and applications of magnetic materials* First edition. ISBN: 9780199570447 (Oxford University Press, Oxford, United Kingdom, 2016) (cit. on p. 3).
18. Guimarães, A. P. *Principles of nanomagnetism* ISBN: 9783642014819 (Springer, Heidelberg [Germany]; New York, 2009) (cit. on pp. 3, 6).
19. Chumak, A. *Advanced Materials* Youtube. https://www.youtube.com/playlist?list=PLdD_3zCk2ykbM9undabeTR6r9tB5vRvmw (cit. on p. 3).
20. Chumak, A. *Magnonics* Youtube. https://www.youtube.com/playlist?list=PLdD_3zCk2ykbvol5nO0djNOFqXJSzJReQ (cit. on p. 3).
21. Feynman, R. P. *The Feynman lectures on physics. Volume 2: Mainly electromagnetism and matter* The new millennium edition, paperback first published. eng. ISBN: 9780465040841 (Basic Books, New York, 2011) (cit. on p. 3).
22. Griffiths, D. J. *Introduction to quantum mechanics* Second edition [2017 edition]. ISBN: 9781107179868 (Cambridge University Press, Cambridge, 2017) (cit. on p. 3).
23. Zhao, S., Stocks, G. M. & Zhang, Y. Defect energetics of concentrated solid-solution alloys from ab initio calculations: Ni0.5Co0.5, Ni0.5Fe0.5, Ni0.8Fe0.2 and Ni0.8Cr0.2. *Phys. Chem. Chem. Phys.* **18,** 24043–24056. doi:10.1039/C6CP05161H (34 2016) (cit. on p. 4).
24. Skomski, R. *Simple Models of Magnetism* ISBN: 9780198570752 (OUP Oxford, 2008) (cit. on p. 6).
25. Klíma, J. *Spin waves in non-trivial magnetic landscapes* MA thesis (Faculty of Mechanical Engineering, Brno University of Technology, 2023) (cit. on p. 6).
26. Suhl, H. *Relaxation processes in micromagnetics* ISBN: 9780198528029 (Oxford University Press, Oxford; New York, 2007) (cit. on p. 6).
27. Gilbert, T. Classics in Magnetics A Phenomenological Theory of Damping in Ferromagnetic Materials. *IEEE Trans. Magn.* **40,** 3443–3449. doi:10.1109/tmag.2004.836740 (2004) (cit. on pp. 6, 67).
28. Wegrowe, J.-E. & Ciornei, M.-C. Magnetization dynamics, gyromagnetic relation, and inertial effects. *American Journal of Physics* **80,** 607–611. doi:10.1119/1.4709188 (2012) (cit. on p. 7).
29. Saslow, W. M. Landau–Lifshitz or Gilbert damping? That is the question. en. *J. Appl. Phys.* **105,** 07D315. doi:10.1063/1.3077204 (Apr. 2009) (cit. on p. 7).

30. Kalinikos, B. & Slavin, A. Theory of dipole-exchange spin wave spectrum for ferromagnetic films with mixed exchange boundary conditions. *J. Phys. Condens. Matter.* **19,** 7013. doi:10.1088/0022-3719/19/35/014 (1986) (cit. on pp. 7, 9, 72, 82, 108, 112, 113).

31. Bloch, F. Zur theorie des ferromagnetismus. *Z. Phys.* **61,** 206–219 (1930) (cit. on p. 7).

32. Holstein, T. & Primakoff, H. Field Dependence of the Intrinsic Domain Magnetization of a Ferromagnet. *Phys. Rev.* **58,** 1098–1113. doi:10.1103/PhysRev.58.1098 (12 Dec. 1940) (cit. on p. 8).

33. Krivosik, P. & Patton, C. E. Hamiltonian formulation of nonlinear spin-wave dynamics: Theory and applications. *Phys. Rev. B* **82,** 184428. doi:10.1103/PhysRevB.82.184428 (18 Nov. 2010) (cit. on p. 9).

34. De Wames, R. E. & Wolfram, T. Dipole-Exchange Spin Waves in Ferromagnetic Films. *J. Appl. Phys.* **41,** 987–993. doi:10.1063/1.1659049 (Mar. 1970) (cit. on p. 9).

35. Sparks, M. Effect of Exchange on Magnetostatic Modes. *Phys. Rev. Lett.* **24,** 1178–1180. doi:10.1103/PhysRevLett.24.1178 (21 May 1970) (cit. on p. 9).

36. Sparks, M. Ferromagnetic Resonance in Thin Films. I. Theory of Normal-Mode Frequencies. *Phys. Rev. B* **1,** 3831–3856. doi:10.1103/PhysRevB.1.3831 (9 May 1970) (cit. on p. 9).

37. Sparks, M. Ferromagnetic Resonance in Thin Films. III. Theory of Mode Intensities. *Phys. Rev. B* **1,** 3869–3880. doi:10.1103/PhysRevB.1.3869 (9 May 1970) (cit. on p. 9).

38. Hillebrands, B. Spin-wave calculations for multilayered structures. *Phys. Rev. B* **41,** 530–540. doi:10.1103/PhysRevB.41.530 (1 Jan. 1990) (cit. on p. 9).

39. Soohoo, R. F. *Magnetic thin films* (Harper & Row, 1965) (cit. on p. 11).

40. Howell, K. B. *Ordinary differential equations: an introduction to the fundamentals* ISBN: 9781498733816 (CRC Press, Taylor & Francis Group, Boca Raton, 2016) (cit. on p. 11).

41. Wojewoda, O. *Spin-wave toolkit, GitHub* https://github.com/OndrejW (cit. on pp. 12, 13, 72, 108, 112, 113, 116).

42. Tacchi, S., Silvani, R., Carlotti, G., Marangolo, M., Eddrief, M., Rettori, A. & Pini, M. G. Strongly hybridized dipole-exchange spin waves in thin Fe-N ferromagnetic films. *Phys. Rev. B* **100,** 104406. doi:10.1103/PhysRevB.100.104406 (10 Sept. 2019) (cit. on pp. 12, 99).

43. Klíma, J., Wojewoda, O., Roučka, V., Molnár, T., Holobrádek, J. & Urbánek, M. Zero-field spin wave turns. *Appl. Phys. Lett.* **124,** 112404. doi:10.1063/5.0189394 (Mar. 2024) (cit. on pp. 13, 16).

44. Kim, J.-V., Stamps, R. L. & Camley, R. E. Spin Wave Power Flow and Caustics in Ultrathin Ferromagnets with the Dzyaloshinskii-Moriya Interaction. *Phys. Rev. Lett.* **117,** 197204. doi:10.1103/PhysRevLett.117.197204 (19 Nov. 2016) (cit. on p. 13).

45. Shiota, Y., Funada, S., Hisatomi, R., Moriyama, T. & Ono, T. Imaging of caustic-like spin wave beams using optical heterodyne detection. *Appl. Phys. Lett.* **116,** 192411. doi:10.1063/5.0010410 (May 2020) (cit. on p. 13).

46. Schneider, T., Serga, A. A., Chumak, A. V., Sandweg, C. W., Trudel, S., Wolff, S., Kostylev, M. P., Tiberkevich, V. S., Slavin, A. N. & Hillebrands, B. Nondiffractive Subwavelength Wave Beams in a Medium with Externally Controlled Anisotropy. *Phys. Rev. Lett.* **104,** 197203. doi:10.1103/PhysRevLett.104.197203 (19 May 2010) (cit. on p. 13).

47. Chumak, A. V. Fundamentals of magnon-based computing. *arXiv:1901.08934.* doi:10.48550/arXiv.1901.08934 (2019) (cit. on pp. 13, 15).

48. Faulkner, J. S. & Stocks, G. M. Calculating properties with the coherent-potential approximation. *Phys. Rev. B* **21,** 3222–3244. doi:10.1103/PhysRevB.21.3222 (8 Apr. 1980) (cit. on p. 14).

49. Misra, S., Wiendlocha, B., Tobola, J., Levinský, P., Hejtmánek, J., Migot, S., Ghanbaja, J., Dauscher, A., Lenoir, B. & Candolfi, C. Influence of In-induced resonant level on the normal-state and superconducting properties of $Sn_{1.03}Te$. *Phys. Rev. B* **106,** 075205. doi:10.1103/PhysRevB.106.075205 (7 Aug. 2022) (cit. on p. 14).

50. Verba, R., Tiberkevich, V., Guslienko, K., Melkov, G. & Slavin, A. Theory of ground-state switching in an array of magnetic nanodots by application of a short external magnetic field pulse. *Phys. Rev. B* **87,** 134419. doi:10.1103/PhysRevB.87.134419 (13 Apr. 2013) (cit. on p. 14).

51. Bertram, H., Safonov, V. & Jin, Z. Thermal magnetization noise, damping fundamentals, and mode analysis: application to a thin film GMR sensor. *IEEE Trans. Magn.* **38,** 2514–2519. doi:10.1109/tmag.2002.801909 (2002) (cit. on p. 14).

52. Sebastian, T. & Hillebrands, B. in *Heusler Alloys: Properties, Growth, Applications* (eds Felser, C. & Hirohata, A.) 321–340 (Springer International Publishing, 2016). ISBN: 978-3-319-21449-8. doi:10.1007/978-3-319-21449-8_13 (cit. on p. 15).

53. Pirro, P., Vasyuchka, V. I., Serga, A. A. & Hillebrands, B. Advances in coherent magnonics. *Nat. Rev. Mater.* **6,** 1114–1135. doi:10.1038/s41578-021-00332-w (2021) (cit. on pp. 15, 73).

54. Chumak, A., Serga, A. & Hillebrands, B. Magnonic crystals for data processing. *J. Phys. D Appl. Phys.* **50,** 244001 (2017) (cit. on p. 15).

55. Pirro, P., Brächer, T., Chumak, A., Lägel, B., Dubs, C., Surzhenko, O., Görnert, P., Leven, B. & Hillebrands, B. Spin-wave excitation and propagation in microstructured waveguides of yttrium iron garnet/Pt bilayers. *Appl. Phys. Lett.* **104,** 012402. doi:10.1063/1.4861343 (2014) (cit. on p. 15).

56. Hahn, C., Naletov, V. V., de Loubens, G., Klein, O., d'Allivy Kelly, O., Anane, A., Bernard, R., Jacquet, E., Bortolotti, P., Cros, V., Prieto, J. L. & Muñoz, M. Measurement of the intrinsic damping constant in individual nanodisks of $Y_3Fe_5O_{12}$ and $Y_3Fe_5O_{12}$| Pt. *Appl. Phys. Lett.* **104,** 152410. doi:10.1063/1.4871516 (2014) (cit. on p. 15).

57. Dubs, C., Surzhenko, O., Linke, R., Danilewsky, A., Brückner, U. & Dellith, J. Sub-micrometer yttrium iron garnet LPE films with low ferromagnetic resonance losses. *J. Phys. D Appl. Phys.* **50,** 204005. doi:10.1088/1361-6463/aa6b1c (2017) (cit. on p. 15).

58. Sun, Y., Song, Y.-Y., Chang, H., Kabatek, M., Jantz, M., Schneider, W., Wu, M., Schultheiss, H. & Hoffmann, A. Growth and ferromagnetic resonance properties of nanometer-thick yttrium iron garnet films. *Appl. Phys. Lett.* **101,** 152405. doi:10.1063/1.4759039 (2012) (cit. on p. 15).

59. Yu, H., Kelly, O. d., Cros, V., Bernard, R., Bortolotti, P., Anane, A., Brandl, F., Huber, R., Stasinopoulos, I. & Grundler, D. Magnetic thin-film insulator with ultra-low spin wave damping for coherent nanomagnonics. *Sci. Rep.* **4,** 1–5. doi:10.1038/srep06848 (2014) (cit. on p. 15).

60. Onbasli, M., Kehlberger, A., Kim, D. H., Jakob, G., Kläui, M., Chumak, A. V., Hillebrands, B. & Ross, C. A. Pulsed laser deposition of epitaxial yttrium iron garnet films with low Gilbert damping and bulk-like magnetization. *APL Mater.* **2,** 106102. doi:10.1063/1.4896936 (2014) (cit. on p. 15).

61. Liu, T., Chang, H., Vlaminck, V., Sun, Y., Kabatek, M., Hoffmann, A., Deng, L. & Wu, M. Ferromagnetic resonance of sputtered yttrium iron garnet nanometer films. *J. Appl. Phys.* **115,** 17A501. doi:10.1063/1.4852135 (2014) (cit. on p. 15).

62. Demidov, V. E. & Demokritov, S. O. Magnonic waveguides studied by microfocus Brillouin light scattering. *IEEE Trans. Magn.* **51,** 1–15. doi:10.1109/TMAG.2014.2388196 (2015) (cit. on pp. 15, 16).

63. Kalarickal, S. S., Krivosik, P., Wu, M., Patton, C. E., Schneider, M. L., Kabos, P., Silva, T. J. & Nibarger, J. P. Ferromagnetic resonance linewidth in metallic thin films: Comparison of measurement methods. *J. Appl. Phys.* **99,** 093909. doi:10.1063/1.2197087 (2006) (cit. on p. 15).

64. Patton, C. E. Linewidth and Relaxation Processes for the Main Resonance in the Spin-Wave Spectra of Ni–Fe Alloy Films. *J. Appl. Phys.* **39,** 3060–3068. doi:10.1063/1.1656733 (1968) (cit. on p. 15).

65. Křížáková, V. *Spin wave excitation and propagation in magnonic crystal prepared by focused ion beam direct writing* MA thesis (Brno University of Technology, 2018) (cit. on p. 15).

66. Brunsch, A. Magnetic properties and corrosion resistance of (CoFeB) 100- xCrx thin films. *J. Appl. Phys.* **50,** 7603–7605. doi:10.1063/1.326858 (1979) (cit. on p. 15).

67. Liu, X., Zhang, W., Carter, M. J. & Xiao, G. Ferromagnetic resonance and damping properties of CoFeB thin films as free layers in MgO-based magnetic tunnel junctions. *J. Appl. Phys.* **110,** 033910. doi:10.1063/1.3615961 (2011) (cit. on p. 15).

68. Conca, A., Greser, J., Sebastian, T., Klingler, S., Obry, B., Leven, B. & Hillebrands, B. Low spin-wave damping in amorphous $Co_{40}Fe_{40}B_{20}$ thin films. *J. Appl. Phys.* **113,** 213909. doi:10.1063/1.4808462 (2013) (cit. on p. 15).

69. Fan, Y., Gross, M. J., Fakhrul, T., Finley, J., Hou, J. T., Ngo, S., Liu, L. & Ross, C. A. Coherent magnon-induced domain-wall motion in a magnetic insulator channel. *Nat. Nanotechnol.* **18,** 1000–1004. doi:10.1038/s41565-023-01406-2 (Sept. 2023) (cit. on p. 15).

70. Demokritov, S. O., Demidov, V. E., Dzyapko, O., Melkov, G. A., Serga, A. A., Hillebrands, B. & Slavin, A. N. Bose–Einstein condensation of quasi-equilibrium magnons at room temperature under pumping. *Nature* **443,** 430–433. doi:10.1038/nature05117 (2006) (cit. on p. 15).

71. Chumak, A. V., Serga, A. A. & Hillebrands, B. Magnon transistor for all-magnon data processing. en. *Nat. Commun.* **5,** 4700. doi:10.1038/ncomms5700 (Aug. 2014) (cit. on p. 15).

72. Demidov, V. E., Urazhdin, S. & Demokritov, S. O. Control of spin-wave phase and wavelength by electric current on the microscopic scale. *Appl. Phys. Lett.* **95.** doi:10.1063/1.3279152 (2009) (cit. on pp. 16, 54).

73. Vlaminck, V. & Bailleul, M. Spin-wave transduction at the submicrometer scale: Experiment and modeling. *Phys. Rev. B* **81,** 014425. doi:10.1103/PhysRevB.81.014425 (1 Jan. 2010) (cit. on pp. 16, 108, 112).

74. Wagner, K., Kákay, A., Schultheiss, K., Henschke, A., Sebastian, T. & Schultheiss, H. Magnetic domain walls as reconfigurable spin-wave nanochannels. *Nat. Nanotechnol.* **11,** 432–436. doi:10.1038/nnano.2015.339 (2016) (cit. on p. 16).

75. Turčan, I., Flajšman, L., Wojewoda, O., Roučka, V., Man, O. & Urbánek, M. Spin wave propagation in corrugated waveguides. *Appl. Phys. Lett.* **118,** 092405. doi:10.1063/5.0041138 (Mar. 2021) (cit. on p. 16).

76. Joshi, V. K., Barla, P., Bhat, S. & Kaushik, B. K. From MTJ Device to Hybrid CMOS/MTJ Circuits: A Review. *IEEE Access* **8,** 194105–194146. doi:10.1109/ACCESS.2020.3033023 (2020) (cit. on p. 16).

77. Yuan, Y. & Jiang, Y. Review on magnetic/nonmagnetic heterojunction interface effects on spintronic MTJ devices. *Semicond. Sci. Technol.* **39,** 033001. doi:10.1088/1361-6641/ad22fd (Feb. 2024) (cit. on p. 16).

78. Landau, L. D., Bell, J., Kearsley, M., Pitaevskii, L., Lifshitz, E. & Sykes, J. *Electrodynamics of continuous media* (Elsevier, 2013) (cit. on pp. 19, 23).

79. Johnson, C. S. & Gabriel, D. A. *Laser light scattering* (Dover, 1981) (cit. on p. 20).

80. *Amyloid proteins: methods and protocols* ISBN: 9781588293374 (Humana Press, Totowa, N.J, 2005) (cit. on p. 20).

81. Phillies, G. D. J. Quasielastic Light Scattering. *Analytical Chemistry* **62,** 1049A–1057A. doi:10.1021/ac00219a712 (Oct. 1990) (cit. on p. 20).

82. Loudon, R. *The quantum theory of light* (OUP Oxford, 2000) (cit. on p. 20).

83. Malard, L., Pimenta, M., Dresselhaus, G. & Dresselhaus, M. Raman spectroscopy in graphene. *Phys. Rep.* **473,** 51–87. doi:10.1016/j.physrep.2009.02.003 (2009) (cit. on p. 21).

84. Gala, U. & Chauhan, H. Principles and applications of Raman spectroscopy in pharmaceutical drug discovery and development. *Expert Opin. Drug. Discov.* **10,** 187–206. doi:10.1517/17460441.2015.981522 (2015) (cit. on p. 21).

85. Evans, C. L. & Xie, X. S. Coherent anti-Stokes Raman scattering microscopy: chemical imaging for biology and medicine. *Annu. Rev. Anal. Chem.* **1,** 883–909. doi:10.1146/annurev.anchem.1.031207.112754 (2008) (cit. on p. 21).

86. Cottam, M. G. & Lockwood, D. J. *Light scattering in magnetic solids* (Wiley New York, 1986) (cit. on pp. 21, 23, 33, 44).

87. Cottam, M. G. Theory of light scattering off the surface of a Heisenberg ferromagnet. *J. Phys. Condens. Matter.* **9,** 2137–2150. doi:10.1088/0022-3719/9/11/020 (June 1976) (cit. on pp. 23, 33).

88. Cochran, J. Brillouin light scattering intensities for patterned magnetic thin films. *J. Magn. Magn. Mater.* **212,** 40–52. doi:10.1016/S0304-8853(99)00816-1 (2000) (cit. on p. 23).

89. Dutcher, J. R., Cochran, J. F., Jacob, I. & Egelhoff, W. F. Brillouin light-scattering intensities for thin magnetic films with large perpendicular anisotropies. *Phys. Rev. B* **39,** 10430–10432. doi:10.1103/PhysRevB.39.10430 (14 May 1989) (cit. on p. 23).

90. Wolf, E. Electromagnetic diffraction in optical systems-I. An integral representation of the image field. *Proc. Math. Phys. Sci.* **253,** 349–357. doi:10.1098/rspa.1959.0199 (1959) (cit. on p. 25).

91. Richards, B. & Wolf, E. Electromagnetic diffraction in optical systems, II. Structure of the image field in an aplanatic system. *Proc. Math. Phys. Sci.* **253,** 358–379. doi:10.1098/rspa.1959.0200 (1959) (cit. on p. 25).

92. Novotny, L. & Hecht, B. *Principles of Nano-Optics* 2nd ed. (Cambridge University Press, 2012) (cit. on pp. 25, 27, 32, 36).

93. Lindfield, G. & Penny, J. *Numerical methods: using MATLAB* (Academic Press, 2018) (cit. on pp. 26, 68).

94. Airy, G. B. On the diffraction of an object-glass with circular aperture. *Trans. Cambridge Philos.* **5,** 283 (1835) (cit. on pp. 28, 30).

95. Rubinsztein-Dunlop, H., Forbes, A., Berry, M. V., Dennis, M. R., Andrews, D. L., Mansuripur, M., Denz, C., Alpmann, C., Banzer, P., Bauer, T., Karimi, E., Marrucci, L., Padgett, M., Ritsch-Marte, M., Litchinitser, N. M., Bigelow, N. P., Rosales-Guzmán, C., Belmonte, A., Torres, J. P., Neely, T. W., Baker, M., Gordon, R., Stilgoe, A. B., Romero, J., White, A. G., Fickler, R., Willner, A. E., Xie, G., McMorran, B. & Weiner, A. M. Roadmap on structured light. *J. Opt.* **19,** 013001. doi:10.1088/2040-8978/19/1/013001 (Nov. 2016) (cit. on p. 30).

96. Dorn, R., Quabis, S. & Leuchs, G. Sharper Focus for a Radially Polarized Light Beam. *Phys. Rev. Lett.* **91,** 233901. doi:10.1103/PhysRevLett.91.233901 (23 Dec. 2003) (cit. on p. 30).

97. Dente, G. C. Polarization effects in resonators. *Appl. Opt.* **18,** 2911–2912. doi:10.1364/AO.18.002911 (1979) (cit. on p. 30).

98. Chodzko, R., Mason, S., Turner, E. & Plummer, W. Annular (HSURIA) resonators: some experimental studies including polarization effects. *Appl. Opt.* **19,** 778–789. doi:10.1364/AO.19.000778 (1980) (cit. on p. 30).

99. Thirugnanasambandam, M. P., Senatsky, Y. & Ueda, K.-i. Generation of radially and azimuthally polarized beams in Yb:YAG laser with intra-cavity lens and birefringent crystal. *Opt. Express* **19,** 1905–1914. doi:10.1364/OE.19.001905 (Jan. 2011) (cit. on p. 30).

100. Tidwell, S. C., Ford, D. H. & Kimura, W. D. Generating radially polarized beams interferometrically. *Appl. Opt.* **29,** 2234–2239. doi:10.1364/AO.29.002234 (1990) (cit. on p. 30).

101. Han, C.-Y., Wei, Z.-H., Hsu, Y., Chen, K.-H., Yeh, C.-H., Wu, W.-X. & Chen, J.-H. Generating Radially and Azimuthally Polarized Beams by Using a Pair of Lateral Displacement Beamsplitters. *Appl. Sci.* **6.** doi:10.3390/app6090241 (2016) (cit. on p. 30).

102. Machavariani, G., Lumer, Y., Moshe, I., Meir, A. & Jackel, S. Efficient extracavity generation of radially and azimuthally polarized beams. *Opt. Lett.* **32,** 1468–1470. doi:10.1364/OL.32.001468 (June 2007) (cit. on p. 30).

103. ThorLabs. *Zero-Order Vortex Half-Wave Retarders* https://thorlabs.com/newgrouppage9.cfm?objectgroup_id=9098 (2023) (cit. on p. 30).

104. Castles, F. Linear electro-optic effects due to high-order spatial dispersion. *Phys. Rev. A* **92.** doi:10.1103/physreva.92.063804 (2015) (cit. on p. 32).

105. Abel, S., Eltes, F., Ortmann, J. E., Messner, A., Castera, P., Wagner, T., Urbonas, D., Rosa, A., Gutierrez, A. M., Tulli, D. & et al. Large Pockels effect in micro- and nanostructured barium titanate integrated on silicon. *Nat. Mater.* **18,** 42–47. doi:10.1038/s41563-018-0208-0 (2019) (cit. on p. 32).

106. Qiu, Z. Q. & Bader, S. D. Surface magneto-optic Kerr effect. *Rev. Sci. Instrum.* **71,** 1243–1255. doi:10.1063/1.1150496 (2000) (cit. on p. 33).

107. Wojewoda, O. *GitHub* https://github.com/CEITECmagnonics (cit. on pp. 33, 67, 72, 116).

108. Sommerfeld, A. *Partial differential equations in physics* (Academic press, 1949) (cit. on p. 36).

109. Weyl, H. Ausbreitung elektromagnetischer Wellen über einem ebenen Leiter. *Ann. Phys.* **365,** 481–500. doi:10.1002/andp.19193652104 (1919) (cit. on p. 36).

110. Martin, H. *Semianalytical approach to simulation in nanophotonics* PhD thesis (Central European Institute of Technology, Brno University of Technology, 2021) (cit. on pp. 36, 37).

111. Mohammed, Z. H. The Fresnel Coefficient of Thin Film Multilayer Using Transfer Matrix Method TMM. *IOP Conf. Ser. Mater. Sci. Eng.* **518,** 032026. doi:10.1088/1757-899X/518/3/032026 (May 2019) (cit. on p. 36).

112. Lindsay, S. M., Anderson, M. W. & Sandercock, J. R. Construction and alignment of a high performance multipass vernier tandem Fabry–Perot interferometer. *Rev. Sci. Instrum.* **52,** 1478–1486. doi:10.1063/1.1136479 (1981) (cit. on pp. 40, 59, 91).

113. Wojewoda, O., Ligmajer, F., Hrtoň, M., Klíma, J., Dhankhar, M., Davídková, K., Staňo, M., Holobrádek, J., Krčma, J., Zlámal, J., *et al.* Observing high-k magnons with Mie-resonance-enhanced Brillouin light scattering. *Commun. Phys.* **6,** 1–10. doi:10.1038/s42005-023-01214-z (2023) (cit. on pp. 45, 73, 107–109).

114. Duh, Y.-S., Nagasaki, Y., Tang, Y.-L., Wu, P.-H., Cheng, H.-Y., Yen, T.-H., Ding, H.-X., Nishida, K., Hotta, I., Yang, J.-H., *et al.* Giant photothermal nonlinearity in a single silicon nanostructure. *Nat. Commun.* **11,** 4101. doi:10.1038/s41467-020-17846-6 (2020) (cit. on p. 45).

115. Mie, G. Beiträge zur Optik trüber Medien, speziell kolloidaler Metallösungen. *Ann. Phys.* **330,** 377–445. doi:10.1002/andp.19083300302 (1908) (cit. on p. 46).

116. Maier, S. A. *Plasmonics: fundamentals and applications* (Springer, New York, 2007) (cit. on p. 46).

117. Fujiwara, H. *Spectroscopic ellipsometry: principles and applications* (John Wiley & Sons, Chichester, England; Hoboken, NJ, 2007) (cit. on pp. 46, 47).

118. Cox, A., DeWeerd, A. J. & Linden, J. An experiment to measure Mie and Rayleigh total scattering cross sections. *American Journal of Physics* **70,** 620–625. doi:10.1119/1.1466815 (2002) (cit. on p. 47).

119. Baffou, G. *Mie Theory & Matlab Code* Oct. 2012. https://www.researchgate.net/publication/260555499_Mie_theory_Matlab_code (cit. on p. 47).

120. Terekhov, P. D., Baryshnikova, K. V., Artemyev, Y. A., Karabchevsky, A., Shalin, A. S. & Evlyukhin, A. B. Multipolar response of nonspherical silicon nanoparticles in the visible and near-infrared spectral ranges. *Phys. Rev. B* **96,** 035443. doi:10.1103/PhysRevB.96.035443 (3 July 2017) (cit. on p. 48).

121. Kuznetsov, A. I., Miroshnichenko, A. E., Brongersma, M. L., Kivshar, Y. S. & Luk'yanchuk, B. Optically resonant dielectric nanostructures. *Science* **354,** aag2472. doi:10.1126/science.aag2472 (2016) (cit. on pp. 48, 74).

122. Wojewoda, O. *Phase–resolved Brillouin light scattering: development and applications* MA thesis (Faculty of Mechanical Engineering, Brno University of Technology, 2020) (cit. on pp. 51–54).

123. Sebastian, T., Schultheiss, K., Obry, B., Hillebrands, B. & Schultheiss, H. Micro-focused Brillouin light scattering: imaging spin waves at the nanoscale. *Frontiers in Physics* **3,** 35. doi:10.3389/fphy.2015.00035 (2015) (cit. on pp. 51, 73).

124. Madami, M., Gubbiotti, G., Tacchi, S. & Carlotti, G. *Chapter Two - Application of Microfocused Brillouin Light Scattering to the Study of Spin Waves in Low-Dimensional Magnetic Systems* (eds Camley, R. E. & Stamps, R. L.) 79–150. doi:10.1016/B978-0-12-397028-2.00002-3 (Academic Press, 2012) (cit. on pp. 51, 73).

125. Table Stable ltd. *Laser Filter TCF* http://tablestable.com/en/products/view/24/ (2024) (cit. on p. 53).

126. ThorLabs. *Operating Principle of Wave Plates - Tutorial* https://www.thorlabs.com/newgrouppage9.cfm?objectgroup_id=711 (2024) (cit. on p. 54).

127. Schneider, T., Serga, A., Neumann, T., Hillebrands, B. & Kostylev, M. Phase reciprocity of spin-wave excitation by a microstrip antenna. *Phys. Rev. B* **77,** 214411. doi:10.1103/PhysRevB.77.214411 (2008) (cit. on p. 54).

128. Serga, A., Schneider, T., Hillebrands, B., Demokritov, S. & Kostylev, M. Phase-sensitive Brillouin light scattering spectroscopy from spin-wave packets. *Appl. Phys. Lett.* **89.** doi:10.1063/1.2335627 (2006) (cit. on pp. 54, 111).

129. Vogt, K., Schultheiss, H., Hermsdoerfer, S., Pirro, P., Serga, A. & Hillebrands, B. All-optical detection of phase fronts of propagating spin waves in a Ni81Fe19 microstripe. *Appl. Phys. Lett.* **95.** doi:10.1063/1.3262348 (2009) (cit. on pp. 54, 110, 111).

130. Guan, Y., Yin, B. & Dong, X. A High-Precision Method for the Determination of Cavity Length of a Fabry-Perot Interferometer. *IEEE Photonics J.* **14,** 1–6. doi:10.1109/jphot.2022.3163282 (2022) (cit. on p. 59).

131. Yao, T., Pu, S., Zhao, Y. & Li, Y. Ultrasensitive refractive index sensor based on parallel-connected dual Fabry-Perot interferometers with Vernier effect. *Sens. Actuators A Phys.* **290,** 14–19. doi:10.1016/j.sna.2019.03.011 (2019) (cit. on p. 59).

132. Cannell, D. S. & Benedek, G. B. Brillouin Spectrum of Xenon Near Its Critical Point. *Phys. Rev. Lett.* **25,** 1157–1161. doi:10.1103/PhysRevLett.25.1157 (17 Oct. 1970) (cit. on p. 59).

133. Lyons, K. B. & Fleury, P. A. Digital normalization of iodine filter structure in quasielastic light scattering. *J. Appl. Phys.* **47,** 4898–4900. doi:10.1063/1.322490 (Aug. 1976) (cit. on p. 59).

134. Table Stable ltd. *Tandem Fabry-Perot spectrometers TFP-1 and TFP-2 HC - Operator's manual* http://tablestable.com/uploads/ckeditor/TFP-2/Manual%20TFP%20unified.pdf (2024) (cit. on p. 60).

135. Roučka, V. *Spin wave propagation in structures with locally modified magnetic anisotropy* MA thesis (Faculty of Mechanical Engineering, Brno University of Technology, 2021) (cit. on p. 60).

136. Vaňatka, M., Szulc, K., Wojewoda, O., Dubs, C., Chumak, A. V., Krawczyk, M., Dobrovolskiy, O. V., Kłos, J. W. & Urbánek, M. Spin-wave dispersion measurement by variable-gap propagating spin-wave spectroscopy. *Phys. Rev. Applied* **16,** 054033. doi:10.1103/PhysRevApplied.16.054033 (2021) (cit. on pp. 60, 62, 108, 112, 114).

137. Herring, C. & Kittel, C. On the Theory of Spin Waves in Ferromagnetic Media. *Phys. Rev.* **81,** 869–880. doi:10.1103/PhysRev.81.869 (5 Mar. 1951) (cit. on p. 61).

138. Prutton, M. The structure and properties of ferromagnetic films. *British J. Appl. Phys.* **15,** 815. doi:10.1088/0508-3443/15/7/306 (July 1964) (cit. on p. 61).

139. Maksymov, I. S. & Kostylev, M. Broadband stripline ferromagnetic resonance spectroscopy of ferromagnetic films, multilayers and nanostructures. *Physica E Low Dimens. Syst. Nanostruct.* **69,** 253–293. doi:10.1016/j.physe.2014.12.027 (2015) (cit. on p. 61).

140. Bilzer, C. *Microwave susceptibility of thin ferromagnetic films: metrology and insight into magnetization dynamics* PhD thesis (Paris-Sud University, 2008) (cit. on p. 61).

141. Bilzer, C., Devolder, T., Crozat, P., Chappert, C., Cardoso, S. & Freitas, P. P. Vector network analyzer ferromagnetic resonance of thin films on coplanar waveguides: Comparison of different evaluation methods. *J. Appl. Phys.* **101,** 074505. doi:10.1063/1.2716995 (2007) (cit. on p. 63).

142. Rovenská, K. *Dieletric metasurfaces as modern optical components* MA thesis (Brno University of Technology, 2020) (cit. on p. 63).

143. Yee, K. Numerical solution of initial boundary value problems involving Maxwell's equations in isotropic media. *IEEE Trans Antennas Propag* **14,** 302–307. doi:10.1109/TAP.1966.1138693 (1966) (cit. on pp. 65, 66).

144. Taflove, A. Application of the Finite-Difference Time-Domain Method to Sinusoidal Steady-State Electromagnetic-Penetration Problems. *IEEE Trans. Electromagn. Compat.* **EMC-22,** 191–202. doi:10.1109/TEMC.1980.303879 (1980) (cit. on p. 65).

145. Kvapil, M. *Static and dynamic properties of nanostructured magnetic materials* PhD thesis (Brno University of Technology, 2015) (cit. on p. 65).

146. King, J., Wan, C., Park, T. J., Despande, S., Zhang, Z., Ramanathan, S. & Kats, M. A. Electrically tunable VO2-metal metasurface for mid-infrared switching, limiting, and nonlinear isolation. *Nat. Photon.* **18,** 74–80. doi:10.1038/s41566-023-01324-8 (2023) (cit. on p. 65).

147. Wu, T., Menarini, M., Gao, Z. & Feng, L. Lithography-free reconfigurable integrated photonic processor. *Nat. Photon.* **17,** 1–7. doi:10.1038/s41566-023-01205-0 (2023) (cit. on p. 65).

148. Tikuišis, K. K., Beran, L., Cejpek, P., Uhlířová, K., Hamrle, J., Vaňatka, M., Urbánek, M. & Veis, M. Optical and magneto-optical properties of Permalloy thin films in 0.7–6.4 eV photon energy range. *Mater. Des.* **114,** 31–39. doi:10.1016/j.matdes.2016.10.036 (2017) (cit. on p. 66).

149. Palik, E. D. *Handbook of optical constants of solids* ISBN: 9780080556307 (Academic press, 1998) (cit. on p. 66).

150. Lifshitz, E. & Landau, L. On the theory of the dispersion of magnetic permeability in ferromagnetic bodies. *Phys. Z. Sowjetunion* **8.** doi:10.1016/B978-0-08-036364-6.50008-9 (1935) (cit. on p. 67).

151. Vansteenkiste, A., Leliaert, J., Dvornik, M., Helsen, M., Garcia-Sanchez, F. & Van Waeyenberge, B. The design and verification of MuMax3. *AIP Adv.* **4,** 107133. doi:10.1063/1.4899186 (2014) (cit. on pp. 67, 68).

152. Donahue, M. J. A variational approach to exchange energy calculations in micromagnetics. *J. Appl. Phys.* **83,** 6491–6493. doi:10.1063/1.367690 (June 1998) (cit. on p. 68).

153. Donahue, M. & Porter, D. Exchange energy formulations for 3D micromagnetics. *Physica B Condens. Matter.* **343,** 177–183. doi:10.1016/j.physb.2003.08.090 (2004) (cit. on p. 68).

154. Ang, T. K. & Amir Hamzah, N. S. *Solving ordinary differential equations by the Dormand Prince method* (Penerbit UTHM, 2018) (cit. on p. 68).

155. Sukhatme, S. P. *A textbook on heat transfer* (Universities Press, 2005) (cit. on p. 68).

156. COMSOL Inc. *COMSOL* 2024. http://www.comsol.com/products/multiphysics/ (cit. on p. 69).

157. Wojewoda, O. *Dispersion relation of magnonic crystals with nontrivial spatial distribution of magnetic anisotropy* MA thesis (Faculty of Mechanical Engineering, Brno University of Technology, 2018) (cit. on p. 70).

158. Venkat, G., Kumar, D., Franchin, M., Dmytriiev, O., Mruczkiewicz, M., Fangohr, H., Barman, A., Krawczyk, M. & Prabhakar, A. Proposal for a Standard Micromagnetic Problem: Spin Wave Dispersion in a Magnonic Waveguide. *IEEE Trans. Magn.* **49,** 524–529. doi:10.1109/TMAG.2012.2206820 (2013) (cit. on p. 70).

159. Proakis, J. G. *Digital signal processing: principles, algorithms, and applications* (Pearson Education India, 2007) (cit. on p. 71).

160. Chumak, A. V. *et al.* Roadmap on Spin-Wave Computing. *IEEE Trans. Magn.* **58,** 1–72. doi:10.1109/TMAG.2022.3149664 (2022) (cit. on pp. 73, 105).

161. Liu, C., Chen, J., Liu, T., Heimbach, F., Yu, H., Xiao, Y., Hu, J., Liu, M., Chang, H., Stueckler, T., *et al.* Long-distance propagation of short-wavelength spin waves. *Nat. Commun.* **9,** 1–8. doi:10.1038/s41467-018-03199-8 (2018) (cit. on p. 73).

162. Wintz, S., Tiberkevich, V., Weigand, M., Raabe, J., Lindner, J., Erbe, A., Slavin, A. & Fassbender, J. Magnetic vortex cores as tunable spin-wave emitters. *Nat. Nanotechnol.* **11,** 948–953. doi:10.1038/nnano.2016.117 (2016) (cit. on pp. 73, 105).

163. Baumgaertl, K., Gräfe, J., Che, P., Mucchietto, A., Förster, J., Träger, N., Bechtel, M., Weigand, M., Schütz, G. & Grundler, D. Nanoimaging of Ultrashort Magnon Emission by Ferromagnetic Grating Couplers at GHz Frequencies. *Nano Lett.* **20,** 7281–7286. doi:10.1021/acs.nanolett.0c02645 (2020) (cit. on p. 73).

164. Han, X. X., Rodriguez, R. S., Haynes, C. L., Ozaki, Y. & Zhao, B. Surface-enhanced Raman spectroscopy. *Nat. Rev. Methods Primers* **1,** 1–17. doi:10.1038/s43586-021-00083-6 (2022) (cit. on p. 73).

165. Zhang, R., Zhang, Y., Dong, Z., Jiang, S., Zhang, C., Chen, L., Zhang, L., Liao, Y., Aizpurua, J., Luo, Y. e., *et al.* Chemical mapping of a single molecule by plasmon-enhanced Raman scattering. *Nature* **498,** 82–86. doi:10.1038/nature12151 (2013) (cit. on p. 73).

166. Nie, S. & Emory, S. R. Probing Single Molecules and Single Nanoparticles by Surface-Enhanced Raman Scattering. *Science* **275,** 1102–1106. doi:10.1126/science.275.5303.1102 (1997) (cit. on p. 73).

167. Utegulov, Z. N., Shaw, J. M., Draine, B. T., Kim, S. A. & Johnson, W. L. *Surface-plasmon enhancement of Brillouin light scattering from gold-nanodisk arrays on glass* in *Plasmonics: Metallic Nanostructures and Their Optical Properties V* (ed Stockman, M. I.) **6641** (SPIE, 2007), 178–187. doi:10.1117/12.735253 (cit. on pp. 73, 74).

168. Jersch, J., Demidov, V., Fuchs, H., Rott, K., Krzysteczko, P., Münchenberger, J., Reiss, G. & Demokritov, S. Mapping of localized spin-wave excitations by near-field Brillouin light scattering. *Appl. Phys. Lett.* **97,** 152502. doi:10.1063/1.3502599 (2010) (cit. on pp. 73, 74, 105, 116).

169. Freeman, R., Lemasters, R., Kalejaiye, T., Wang, F., Chen, G., Ding, J., Wu, M., Demidov, V. E., Demokritov, S. O., Harutyunyan, H. & Urazhdin, S. Brillouin light scattering of spin waves inaccessible with free-space light. *Phys. Rev. B* **2,** 033427. doi:10.1103/PhysRevResearch.2.033427 (3 Sept. 2020) (cit. on pp. 73, 74, 107).

170. Xiao, T.-H., Cheng, Z., Luo, Z., Isozaki, A., Hiramatsu, K., Itoh, T., Nomura, M., Iwamoto, S. & Goda, K. All-dielectric chiral-field-enhanced Raman optical activity. *Nat. Commun.* **12,** 1–7. doi:10.1038/s41467-021-23364-w (2021) (cit. on p. 74).

171. Genevet, P., Capasso, F., Aieta, F., Khorasaninejad, M. & Devlin, R. Recent advances in planar optics: from plasmonic to dielectric metasurfaces. *Optica* **4,** 139–152. doi:10.1364/OPTICA.4.000139 (Jan. 2017) (cit. on p. 74).

172. Alessandri, I. & Lombardi, J. R. Enhanced Raman Scattering with Dielectrics. *Chem. Rev.* **116,** 14921–14981. doi:10.1021/acs.chemrev.6b00365 (2016) (cit. on p. 74).

173. Caldarola, M., Albella, P., Cortés, E., Rahmani, M., Roschuk, T., Grinblat, G., Oulton, R. F., Bragas, A. V. & Maier, S. A. Non-plasmonic nanoantennas for surface enhanced spectroscopies with ultra-low heat conversion. *Nat. Commun.* **6,** 1–8. doi:10.1038/ncomms8915 (2015) (cit. on p. 74).

174. Yesilkoy, F., Arvelo, E. R., Jahani, Y., Liu, M., Tittl, A., Cevher, V., Kivshar, Y. & Altug, H. Ultrasensitive hyperspectral imaging and biodetection enabled by dielectric metasurfaces. *Nat. Photon.* **13,** 390–396. doi:10.1038/s41566-019-0394-6 (2019) (cit. on p. 74).

175. Tseng, M. L., Jahani, Y., Leitis, A. & Altug, H. Dielectric metasurfaces enabling advanced optical biosensors. *ACS Photonics* **8,** 47–60. doi:10.1021/acsphotonics.0c01030 (2020) (cit. on p. 74).

176. Dorrah, A. H., Rubin, N. A., Zaidi, A., Tamagnone, M. & Capasso, F. Metasurface optics for on-demand polarization transformations along the optical path. *Nat. Photon.* **15,** 287–296. doi:10.1038/s41566-020-00750-2 (2021) (cit. on p. 74).

177. Evlyukhin, A. B., Reinhardt, C. & Chichkov, B. N. Multipole light scattering by nonspherical nanoparticles in the discrete dipole approximation. *Phys. Rev. B* **84,** 235429. doi:10.1103/PhysRevB.84.235429 (23 Dec. 2011) (cit. on p. 74).

178. Staude, I. & Schilling, J. Metamaterial-inspired silicon nanophotonics. *Nat. Photon.* **11,** 274–284. doi:10.1038/nphoton.2017.39 (2017) (cit. on p. 74).

179. Koshelev, K. & Kivshar, Y. Dielectric resonant metaphotonics. *ACS Photonics* **8,** 102–112. doi:10.1021/acsphotonics.0c01315 (2020) (cit. on p. 74).

180. Bezares, F. J., Long, J. P., Glembocki, O. J., Guo, J., Rendell, R. W., Kasica, R., Shirey, L., Owrutsky, J. C. & Caldwell, J. D. Mie resonance-enhanced light absorption in periodic silicon nanopillar arrays. *Opt. Express* **21,** 27587–27601. doi:10.1364/OE.21.027587 (Nov. 2013) (cit. on p. 74).

181. Křápek, V., Konečná, A., Horák, M., Ligmajer, F., Stöger-Pollach, M., Hrtoň, M., Babocký, J. & Šikola, T. Independent engineering of individual plasmon modes in plasmonic dimers with conductive and capacitive coupling. *Nanophotonics* **9,** 623–632. doi:doi:10.1515/nanoph-2019-0326 (2020) (cit. on p. 74).

182. Hrtoň, M., Konečná, A., Horák, M., Šikola, T. & Křápek, V. Plasmonic Antennas with Electric, Magnetic, and Electromagnetic Hot Spots Based on Babinet's Principle. *Phys. Rev. Appl.* **13,** 054045. doi:10.1103/PhysRevApplied.13.054045 (5 May 2020) (cit. on p. 74).

183. Huang, T. & Xu, X.-H. N. Multicolored nanometre-resolution mapping of single protein–ligand binding complexes using far-field photostable optical nanoscopy (PHOTON). *Nanoscale* **3,** 3567–3572. doi:10.1039/c1nr10182j (2011) (cit. on p. 74).

184. Mayer, K. M. & Hafner, J. H. Localized surface plasmon resonance sensors. *Chem. Rev.* **111,** 3828–3857 (2011) (cit. on p. 74).

185. Stockman, M. I. Nanoplasmonics: The physics behind the applications. *Phys. Today* **64,** 39–44. doi:10.1063/1.3554315 (Feb. 2011) (cit. on p. 74).

186. Malinsky, M. D., Kelly, K. L., Schatz, G. C. & Van Duyne, R. P. Chain length dependence and sensing capabilities of the localized surface plasmon resonance of silver nanoparticles chemically modified with alkanethiol self-assembled monolayers. *J. Am. Chem. Soc.* **123,** 1471–1482. doi:10.1021/ja003312a (2001) (cit. on p. 74).

187. Raschke, G., Kowarik, S., Franzl, T., Sönnichsen, C., Klar, T., Feldmann, J., Nichtl, A. & Kürzinger, K. Biomolecular recognition based on single gold nanoparticle light scattering. *Nano Lett.* **3,** 935–938. doi:10.1021/nl034223+ (2003) (cit. on p. 74).

188. Wei, L., Ma, Y., Zhu, X., Xu, J., Wang, Y., Duan, H. & Xiao, L. Sub-diffraction-limit localization imaging of a plasmonic nanoparticle pair with wavelength-resolved dark-field microscopy. *Nanoscale* **9,** 8747–8755. doi:10.1039/c7nr02474f (2017) (cit. on p. 74).

189. De Angelis, F., Das, G., Candeloro, P., Patrini, M., Galli, M., Bek, A., Lazzarino, M., Maksymov, I., Liberale, C., Andreani, L. C., *et al.* Nanoscale chemical mapping using three-dimensional adiabatic compression of surface plasmon polaritons. *Nat. Nanotechnol.* **5,** 67–72. doi:10.1038/nnano.2009.348 (2010) (cit. on p. 74).

190. Kolwas, K. & Derkachova, A. Impact of the interband transitions in gold and silver on the dynamics of propagating and localized surface plasmons. *Nanomater.* **10,** 1411. doi:10.3390/nano10071411 (2020) (cit. on p. 75).

191. Barman, T., Hussain, A. A., Sharma, B. & Pal, A. R. Plasmonic hot hole generation by interband transition in gold-polyaniline. *Sci. Rep.* **5,** 18276. doi:10.1038/srep18276 (2015) (cit. on p. 75).

192. Atwater, H. A. & Polman, A. Plasmonics for improved photovoltaic devices. *Nat. Mater.* **9,** 205–213. doi:10.1038/nmat2629 (2010) (cit. on p. 75).

193. Maier, S. A., Kik, P. G., Atwater, H. A., Meltzer, S., Harel, E., Koel, B. E. & Requicha, A. A. Local detection of electromagnetic energy transport below the diffraction limit in metal nanoparticle plasmon waveguides. *Nat. Mater.* **2,** 229–232. doi:doi.org/10.1038/nmat852 (2003) (cit. on p. 75).

194. Ligmajer, F. *Odrered and disordered arrays of colloidal nanoparticles for biomolecule detection* MA thesis (Faculty of Mechanical Engineering, Brno University of Technology, 2013) (cit. on p. 75).

195. Adichtchev, S., Sirotkin, S., Bachelier, G., Saviot, L., Etienne, S., Stephanidis, B., Duval, E. & Mermet, A. High-order vibration modes of bimetallic Ag-Au nanoparticles embedded in glass. *Phys. Rev. B* **79,** 201402. doi:10.1103/PhysRevB.79.201402 (20 May 2009) (cit. on p. 76).

196. Kuok, M. H., Lim, H. S., Ng, S. C., Liu, N. N. & Wang, Z. K. Brillouin Study of the Quantization of Acoustic Modes in Nanospheres. *Phys. Rev. Lett.* **90,** 255502. doi:10.1103/PhysRevLett.90.255502 (25 June 2003) (cit. on p. 76).

197. Varghese, J., Gapiński, J. & Pochylski, M. *Chapter 3 - Brillouin spectroscopy: probing the acoustic vibrations in colloidal nanoparticles* (eds Thomas, S., Kalarikkal, N. & Abraham, A. R.) 45–72. ISBN: 978-0-12-820558-7. doi:10.1016/B978-0-12-820558-7.00010-8 (Elsevier, 2022) (cit. on p. 76).

198. Lamb, H. On the Vibrations of an Elastic Sphere. *Proc. Lond. Math. Soc.* **s1-13,** 189–212. doi:10.1112/plms/s1-13.1.189 (1881) (cit. on p. 76).

199. Sattler, K. D. *Handbook of nanophysics: nanoparticles and quantum dots* (CRC press, 2016) (cit. on p. 76).

200. Sirotkin, S. *Low frequency modes from small nanoparticles (metal nanocrystals) to large nanospheres (viruses) : an inelastic light scattering study* PhD thesis (Université Claude Bernard - Lyon, 2013) (cit. on p. 76).

201. Sirotkin, S., Cottancin, E., Saviot, L., Bernstein, E. & Mermet, A. Growth of glass-embedded Cu nanoparticles: A low-frequency Raman scattering study. *Phys. Rev. B* **85,** 205435. doi:10.1103/PhysRevB.85.205435 (20 May 2012) (cit. on p. 76).

202. Kuz'min, M. Shape of temperature dependence of spontaneous magnetization of ferromagnets: quantitative analysis. *Phys. Rev. Lett.* **94,** 107204. doi:10.1103/PhysRevLett.94.107204 (2005) (cit. on pp. 81, 91).

203. Herring, C. & Kittel, C. On the Theory of Spin Waves in Ferromagnetic Media. *Phys. Rev.* **81,** 869–880. doi:10.1103/PhysRev.81.869 (5 Mar. 1951) (cit. on p. 82).

204. Dorodnyy, A., Smajic, J. & Leuthold, J. Mie Scattering for Photonic Devices. *Laser Photon. Rev.* **17.** doi:10.1002/lpor.202300055 (2023) (cit. on p. 85).

205. Todisco, F., Malureanu, R., Wolff, C., Gonçalves, P. A. D., Roberts, A. S., Mortensen, N. A. & Tserkezis, C. Magnetic and electric Mie-exciton polaritons in silicon nanodisks. *Nanophotonics* **9,** 803–814. doi:10.1515/nanoph-2019-0444 (2020) (cit. on p. 85).

206. Wei, J., Xiao, M. & Zhang, F. Super-resolution with a nonlinear thin film: Beam reshaping via internal multi-interference. *Appl. Phys. Lett.* **89,** 223126. doi:10.1063/1.2390637 (Dec. 2006) (cit. on p. 91).

207. Holanda, J., Maior, D. S., Azevedo, A. & Rezende, S. M. Detecting the phonon spin in magnon–phonon conversion experiments. *Nat. Phys.* **14,** 500–506. doi:10.1038/s41567-018-0079-y (May 2018) (cit. on p. 99).

208. Heinz, B., Mohseni, M., Lentfert, A., Verba, R., Schneider, M., Lägel, B., Levchenko, K., Brächer, T., Dubs, C., Chumak, A. V., *et al.* Parametric generation of spin waves in nanoscaled magnonic conduits. *Phys. Rev. B* **105,** 144424. doi:10.1103/PhysRevB.105.144424 (2022) (cit. on pp. 99, 105, 116).

209. Strelkov, N., Timopheev, A., Cuchet, L., Dounia, S., Ducruet, C., Bunyaev, S. A., Kakazei, G. N. & Childress, J. R. Exchange stiffness reduction in Ta substituted NiFe alloys. *J. Phys. D Appl. Phys.* **56,** 395004. doi:10.1088/1361-6463/acdf6b (July 2023) (cit. on p. 102).

210. Nakamura, S., Umetsu, N., Quinsat, M. & Kado, M. Exchange stiffness proportional to power of magnetization in permalloy co-doped with Mo and Cu. *J. Magn. Magn. Mater.* **591,** 171674. doi:10.1016/j.jmmm.2023.171674 (2024) (cit. on p. 102).

211. Papp, Á., Porod, W. & Csaba, G. Nanoscale neural network using non-linear spin-wave interference. *Nat. Commun.* **12,** 6422. doi:10.1038/s41467-021-26711-z (2021) (cit. on p. 105).

212. Wang, Q., Heinz, B., Verba, R., Kewenig, M., Pirro, P., Schneider, M., Meyer, T., Lägel, B., Dubs, C., Brächer, T., *et al.* Spin pinning and spin-wave dispersion in nanoscopic ferromagnetic waveguides. *Phys. Rev. Lett.* **122,** 247202. doi:10.1103/PhysRevLett.122.247202 (2019) (cit. on p. 105).

213. Dreyer, R., Schäffer, A. F., Bauer, H. G., Liebing, N., Berakdar, J. & Woltersdorf, G. Imaging and phase-locking of non-linear spin waves. *Nat. Commun.* **13,** 4939. doi:10.1038/s41467-022-32224-0 (2022) (cit. on p. 105).

214. Koerner, C., Dreyer, R., Wagener, M., Liebing, N., Bauer, H. G. & Woltersdorf, G. Frequency multiplication by collective nanoscale spin-wave dynamics. *Science* **375,** 1165–1169. doi:10.1126/science.abm6044 (2022) (cit. on p. 105).

215. Che, P., Stasinopoulos, I., Mucchietto, A., Li, J., Berger, H., Bauer, A., Pfleiderer, C. & Grundler, D. Confined dipole and exchange spin waves in a bulk chiral magnet with Dzyaloshinskii-Moriya interaction. *Phys. Rev. Res.* **3,** 033104. doi:10.1103/PhysRevResearch.3.033104 (2021) (cit. on p. 105).

216. Wojewoda, O., Hula, T., Flajšman, L., Vaňatka, M., Gloss, J., Holobrádek, J., Staňo, M., Stienen, S., Körber, L., Schultheiß, K., *et al.* Propagation of spin waves through a Néel domain wall. *Appl. Phys. Lett.* **117,** 022405. doi:10.1063/5.0013692 (2020) (cit. on p. 105).

217. Yu, H., Duerr, G., Huber, R., Bahr, M., Schwarze, T., Brandl, F. & Grundler, D. Omnidirectional spin-wave nanograting coupler. *Nat. Commun.* **4,** 2702. doi:10.1038/ncomms3702 (2013) (cit. on pp. 105, 116).

218. Dieterle, G., Förster, J., Stoll, H., Semisalova, A., Finizio, S., Gangwar, A., Weigand, M., Noske, M., Fähnle, M., Bykova, I., *et al.* Coherent excitation of heterosymmetric spin waves with ultrashort wavelengths. *Phys. Rev. Lett.* **122,** 117202. doi:10.1103/PhysRevLett.122.117202 (2019) (cit. on p. 105).

219. Albisetti, E., Petti, D., Sala, G., Silvani, R., Tacchi, S., Finizio, S., Wintz, S., Calò, A., Zheng, X., Raabe, J., *et al.* Nanoscale spin-wave circuits based on engineered reconfigurable spin-textures. *Commun. Phys.* **1,** 56. doi:10.1038/s42005-018-0056-x (2018) (cit. on p. 105).

220. Sluka, V., Schneider, T., Gallardo, R. A., Kákay, A., Weigand, M., Warnatz, T., Mattheis, R., Roldán-Molina, A., Landeros, P., Tiberkevich, V., *et al.* Emission and propagation of 1D and 2D spin waves with nanoscale wavelengths in anisotropic spin textures. *Nat. Nanotechnol.* **14,** 328–333. doi:10.1038/s41565-019-0383-4 (2019) (cit. on p. 105).

221. Kimel, A., Zvezdin, A., Sharma, S., Shallcross, S., De Sousa, N., Garcia-Martin, A., Salvan, G., Hamrle, J., Stejskal, O., McCord, J., *et al.* The 2022 magneto-optics roadmap. *J. Phys. D Appl. Phys.* **55,** 463003. doi:10.1088/1361-6463/ac8da0 (2022) (cit. on p. 105).

222. Wojewoda, O., Hrtoň, M., Dhankhar, M., Krčma, J., Davídková, K., Klíma, J., Holobrádek, J., Ligmajer, F., Šikola, T. & Urbánek, M. Phase-resolved optical characterization of nanoscale spin waves. *Appl. Phys. Lett.* **122,** 202405. doi:10.1063/5.0151338 (May 2023) (cit. on p. 105).

223. Bresenham, J. E. Algorithm for computer control of a digital plotter. *IBM Systems Journal* **4,** 25–30. doi:10.1147/sj.41.0025 (1965) (cit. on p. 107).

224. Chen, S., Lourembam, J., Ho, P., Toh, A. K. J., Huang, J., Chen, X., Tan, H. K., Yap, S. L. K., Lim, R. J. J., Tan, H. R., Suraj, T. S., Sim, M. I., Toh, Y. T., Lim, I., Lim, N. C. B., Zhou, J., Chung, H. J., Lim, S. T. & Soumyanarayanan, A. All-electrical skyrmionic magnetic tunnel junction. *Nature* **627,** 522–527. doi:10.1038/s41586-024-07131-7 (Mar. 2024) (cit. on p. 110).

225. Flajšman, L., Wagner, K., Vaňatka, M., Gloss, J., Křižáková, V., Schmid, M., Schultheiss, H. & Urbánek, M. Zero-field propagation of spin waves in waveguides prepared by focused ion beam direct writing. *Phys. Rev. B* **101,** 014436. doi:10.1103/PhysRevB.101.014436 (2020) (cit. on p. 111).

226. Bouchal, P., Dvorak, P., Babocky, J., Bouchal, Z., Ligmajer, F., Hrton, M., Krapek, V., Fassbender, A., Linden, S., Chmelik, R., *et al.* High-resolution quantitative phase imaging of plasmonic metasurfaces with sensitivity down to a single nanoantenna. *Nano Lett.* **19,** 1242–1250. doi:10.1021/acs.nanolett.8b04776 (2019) (cit. on p. 111).

227. Baumgaertl, K., Gräfe, J., Che, P., Mucchietto, A., Förster, J., Träger, N., Bechtel, M., Weigand, M., Schütz, G. & Grundler, D. Nanoimaging of ultrashort magnon emission by ferromagnetic grating couplers at GHz frequencies. *Nano Lett.* **20,** 7281–7286. doi:10.1021/acs.nanolett.0c02645 (2020) (cit. on p. 112).

228. Mayr, S., Flajšman, L., Finizio, S., Hrabec, A., Weigand, M., Förster, J., Stoll, H., Heyderman, L. J., Urbánek, M., Wintz, S., *et al.* Spin-wave emission from vortex cores under static magnetic bias fields. *Nano Lett.* **21,** 1584–1590. doi:10.1021/acs.nanolett.0c03740 (2021) (cit. on p. 112).

229. Urazhdin, S., Demidov, V., Ulrichs, H., Kendziorczyk, T., Kuhn, T., Leuthold, J., Wilde, G. & Demokritov, S. Nanomagnonic devices based on the spin-transfer torque. *Nat. Nanotechnol.* **9,** 509–513. doi:10.1038/nnano.2014.88 (2014) (cit. on p. 112).

230. Lucassen, J., Schippers, C. F., Rutten, L., Duine, R. A., Swagten, H. J., Koopmans, B. & Lavrijsen, R. Optimizing propagating spin wave spectroscopy. *Appl. Phys. Lett.* **115,** 012403. doi:10.1063/1.5090892 (2019) (cit. on p. 114).

231. Smith, R. J., Pérez-Cota, F., Marques, L. & Clark, M. 3D phonon microscopy with sub-micron axial-resolution. *Sci. Rep.* **11,** 1–10. doi:10.1038/s41598-021-82639-w (2021) (cit. on p. 115).

232. Prevedel, R., Diz-Muñoz, A., Ruocco, G. & Antonacci, G. Brillouin microscopy: an emerging tool for mechanobiology. *Nat. Methods* **16,** 969–977. doi:10.1038/s41592-019-0543-3 (2019) (cit. on p. 115).

233. Jeanmaire, D. L. & Van Duyne, R. P. Surface raman spectroelectrochemistry: Part I. Heterocyclic, aromatic, and aliphatic amines adsorbed on the anodized silver electrode. *Journal of Electroanalytical Chemistry and Interfacial Electrochemistry* **84,** 1–20. doi:10.1016/S0022-0728(77)80224-6 (1977) (cit. on p. 116).

234. Le Ru, E. C., Blackie, E., Meyer, M. & Etchegoin, P. G. Surface Enhanced Raman Scattering Enhancement Factors: A Comprehensive Study. *The Journal of Physical Chemistry C* **111,** 13794–13803. doi:10.1021/jp0687908 (2007) (cit. on p. 116).

235. Kuznetsov, A. I., Miroshnichenko, A. E., Fu, Y. H., Zhang, J. & Luk'Yanchuk, B. Magnetic light. *Sci. Rep.* **2,** 1–6. doi:10.1038/srep00492 (2012) (cit. on p. 116).

236. Van de Haar, M. A., van de Groep, J., Brenny, B. J. & Polman, A. Controlling magnetic and electric dipole modes in hollow silicon nanocylinders. *Opt. Express* **24,** 2047–2064. doi:10.1364/OE.24.002047 (2016) (cit. on p. 116).

237. Yang, Y., Zenin, V. A. & Bozhevolnyi, S. I. Anapole-assisted strong field enhancement in individual all-dielectric nanostructures. *ACS Photonics* **5,** 1960–1966. doi:10.1021/acsphotonics.7b01440 (2018) (cit. on p. 116).

238. Holländer, R. B., Müller, C., Schmalz, J., Gerken, M. & McCord, J. Magnetic domain walls as broadband spin wave and elastic magnetisation wave emitters. *Sci. Rep.* **8,** 13871. doi:10.1038/s41598-018-31689-8 (Sept. 2018) (cit. on p. 116).

239. Lee, J., Crampton, K. T., Tallarida, N. & Apkarian, V. A. Visualizing vibrational normal modes of a single molecule with atomically confined light. *Nature* **568,** 78–82. doi:10.1038/s41586-019-1059-9 (Apr. 2019) (cit. on p. 116).

Selected activities performed during doctoral studies

Outputs

First-author publications

- **Wojewoda O.**, Holobrádek J., Pavelka D., Pribytova E., Krčma J., Klíma J., Michalička J., Lednický T., Chumak A. V., Urbánek M., Unidirectional propagation of zero-momentum magnons. *arXiv:2311.10044* (2024)
- **Wojewoda, O.**, Ligmajer, F., Hrtoň, M., Klíma, J., Dhankhar, M., Davídková, K., Holobrádek, J., Šikola, T., Urbánek, M. Phase-resolved optical characterization of nanoscale spin waves. *Appl. Phys. Lett.* **122**, 202405. (2023) | **Editor's pick**
- **Wojewoda, O.**, Ligmajer, F., Klíma, J., Dhankhar, M., Davídková, K., Staňo, M., Holobrádek, J., Šikola, T., Urbánek, M. Observing high-k magnons with Mie-resonance-enhanced Brillouin light scattering. *Commun. Phys.* **6**, 94. (2023)
- **Wojewoda, O.**, Hula, T., Flajšman, L., Vaňatka, M., Gloss, J., **Holobrádek, J.**, Staňo, M., Stienen, S., Körber, L., Schultheiss, K., Schmid, M., Schultheiss, H., Urbánek, M. Propagation of spin waves through a Néel domain wall. *Appl. Phys. Lett.*, **117(2)**, 022405. (2020). | **Featured article & Cover page**

Contributing-author publications

- Klíma, J., **Wojewoda, O.**, Roučka, V., Molnár, T., Holobrádek, J., Urbánek, M. Zero-field spin wave turns. *Appl. Phys. Lett.* **124**, 112404 (2024) | **Featured article**
- Wang, Q., Verba, R., Heinz, B., Schneider, M., **Wojewoda, O.**, Davídková, K., Levchenko, K., Dubs, C., Mauser, N., Urbánek, M., Pirro, P., Chumak, A. V. Deeply nonlinear excitation of self-normalised exchange spin waves. *Sci. Adv.* **11**, 9 (2023)
- Flajšman, L., **Wojewoda, O.**, Qin, H., Davídková, K., Urbánek, M., van Dijken, S., Wideband Brillouin light scattering analysis of spin waves excited by a white-noise RF generator. *App. Phys. Lett.* **121**, 232402 (2023)
- Vaňatka, M., Szulc, K., **Wojewoda, O.**, Dubs, C., Chumak, A., Krawczyk, M., Dobrovolskiy, O., Kłos, J., Urbánek, M., Spin-Wave Dispersion Measurement by Variable-Gap Propagating Spin-Wave Spectroscopy. *Phys. Rev. Applied* 16, 054033 (2021)

- Turčan, I., Flajšman, L., **Wojewoda, O.**, Roučka, V., Urbánek, M., Spin wave propagation in corrugated waveguides. *Appl. Phys. Lett.* **118**, 092405 (2021) | **Editor's pick**

- Ferreira, I, Ayre, M, Bavdaz, M, Guainazzi, M, Stefanescu, A, Komarek, M, Valenta, T, Hynek, R, Zavodnik, M, Sobotka, P, Pejchal, T,Badin, V, Kalousek, R, Bacovsky, J, Horak, M, Flajsman, L, **Wojewoda, O.**, Zlamal, J, 2018: Design of the charged particle diverter for the ATHENA mission. Space telescopes and instrumentation 2018: ultraviolet to gamma ray (2018)

Open-source code

- **SpinWaveToolkit**. Object oriented Python code for (semi)analytical calculation of spin waves in thin film and coupled bi-layers.
  Available from: github.com/OndrejW/SpinWaveToolkit

- **LABhub**. Web-based tool for laboratory book and data management.
  Available from: github.com/OndrejW/LABhub

- **BLSthermalFit**. Tool for nonlinear fitting of BLS signal in Matlab employing phenomenological model.
  Available from: github.com/CEITECmagnonics/BLSthermalFit

- **MuMaxBlBqCoupling**. Example code for implementing of biquadratic interlayer interaction in MuMax3.
  Available from: github.com/CEITECmagnonics/MuMaxBlBqCoupling

- **ModelingOfuBLS**. Semi-analytical model for calculation of micro-focused BLS spectra.
  Available from: github.com/CEITECmagnonics/ModelingOfuBLS

Projects and support

- Specific research. 2023. *Parametric amplification of magnon detected by Mie-enhanced BLS technique* . **Principal investigator**.

- Specific research. 2022. *Power-less Spin Wave Source.* **Principal investigator**.

- KInG – internal grants. 2021–2022. *Nanoscale spin waves: from waveguide transmission to competitive device.* **Principal investigator**.

- Brno PhD talent award 2020–2023. *Nanoscale Magnonics.*

Conferences and schools

- IEEE INTERnational MAGnetics conference (INTERMAG). Rio de Janeiro, Brasil. 2024. Oral and Poster contribution: *Application of Mie-enhanced BLS to study parametric pumping of spin-waves* and *Modeling of the micro-focused Brillouin light scattering signal.*

- 9th International conference on superconductivity and magnetism. Fethyie, Turkey. 2024. Invited talk: *Zero-field spin wave turns.*

- IEEE INTERnational MAGnetics conference (INTERMAG). Sendai, Japan. 2023. Oral contribution: *Measuring spatially resolved phase of nanoscale spin waves.*

- 8th Conference on Magnonics. Le Touquet-Paris-Plage, France. 2023. Oral contribution: *Phase-resolved optical characterization of nanoscale spin waves.*

- Invited seminar at Helmholtz Zentrum Dresden-Rosendorf. Dresden, Germany. 2023. Invited talk: *Optical characterization of a nanoscale spin waves.*

- CEITEC PhD retreat. Telč, Czech Republic 2022. Oral contribution: *Dielectric nanoparticle enhanced Brillouin light scattering spectroscopy of spin waves.*

- 7th Conference on Magnonics. Oxnard, California, United States of America. 2022. Poster contribution: *Observing high-k magnons with Mie-resonance-enhanced Brillouin light scattering.*

- Joint European Magnetic Symposium (JEMS) 2022. Warsaw, Poland. Oral contribution: *Dielectric nanoparticle enhanced Brillouin light scattering spectroscopy of spin waves.*

- CEITEC Nano user meeting. Brno. 2022. Poster contribution: *Observing high-k magnons with Mie-resonance-enhanced Brillouin light scattering.* **Best poster award**.

- PETASPIN 2022 School on "Spintronics: fundamentals and applications". Messina, Italy. 2022. Poster contribution: *Observing high-k magnons with Mie-resonance-enhanced Brillouin light scattering.* **Best poster award**.

- The 4$^{\text{th}}$ International Advanced School on Magnonics – MAGNETOFON. Porto, Portugal. 2022. Poster contribution: *Observing high-k magnons with Mie-resonance-enhanced Brillouin light scattering.* **Best poster award**.

- The 18$^{\text{th}}$ IUVSTA International Summer School on Physics at Nanoscale. Brno. 2021.

- European School on Magnetism (ESM). Cluj-Napoca, Romania. 2021 Poster contribution: *Spin-wave dispersion measurement by variable-gap propagatingspin-wave spectroscopy.*

- Workshop Correlative materials characterization. Brno, Czech Republic. 2021. Invited talk: *Correlative microscopy of magnetic nanostructures.*

- Joint European Magnetic Symposium (JEMS). Online. 2020. Oral contribution: *Propagation of spin waves through vortex domain wall.*

- European School on Magnetism (ESM). Saarbrücken, Germany (online). 2020

Supervising of the bachelor students

- Jan Klíma. 2023. Topic: *Spin waves in non-trivial magnetic landscapes.* Received the highest grade A and *Industrial Enterprise Price*.
- Zdeněk Nekula. 2021. Topic: *Development of the scanning time-resolved Kerr microscope..* Received the highest grade A.

Teaching

- Teaching of the laboratory practical, four semesters
  TR1 20/21L, TR1 21/22L - Mechanics for physical engineers.
  3F20/21Z, 3F21/22Z - Electricity and magnetism.
- Preparation of material for online teaching of laboratory practicals (due to the COVID19 pandemic).